AN INVESTIGATION INTO THE TORQUE CAPABILITIES OF HIGH GEAR RATIO MAGNETIC GEARBOXES

by

Kang Li

A dissertation submitted to the faculty of
The University of North Carolina at Charlotte
in partial fulfillment of the requirements
for the degree of Doctor of Philosophy in
Electrical Engineering

Charlotte

2018

Approved by:

_____
Dr. Yogendra Kakad

_____
Dr. Madhav Manjrekar

_____
Dr. Jonathan Bird

_____
Dr. Wesley Williams

ABSTRACT

KANG LI. An investigation into the torque capabilities of high gear ratio magnetic gearboxes. (Under the direction of DR. JONATHAN Z. BIRD)

Mechanical gears can be as small as those in traditional mechanical watches or as large as those in mechanical marine turbines. They can be seen in almost all transportation tools, for example, bicycles, cars, trains and airplanes. Though they have been studied and refined for centuries, there are still some disadvantages. For instance, mechanical gears often create a large amount of noise and vibration. They require regular maintenance as the gears need to be lubricated. In addition, if a gear is overloaded it can catastrophically fail.

Unlike conventional mechanical gears, magnetic gears can create speed change without physical contact. The force between magnetic gears is not created by geared teeth but instead, it is created by the magnetic poles. There will be a small air gap between different rotors which means no lubricant or maintenance is required. When one rotor rotates, the other one will also rotate driven by magnetic forces. Since the permanent magnets are used, the forces will not recede or disappear as long as the magnets are not overheated. If overloaded, a magnetic gearbox will simply slip poles. Therefore, in many applications, magnetic gears can be more reliable, efficient and safer.

The goal of this research has been to investigate the torque capabilities of high gear ratio magnetic geared devices. The performance has been investigated based on the gear ratio and torque density.

A new type of flux focusing cycloidal magnetic gear (MG) was investigated that could operate at a gear ratio of -25:1. The flux focusing topology was used because it increased the air gap flux density and therefore enabled a higher torque density. Using 2-D finite element analysis (FEA), the volume torque density was calculated to be 291 Nm/L with an outer diameter of 0.228 m. A -20:1 prototype cycloidal magnetic gear was designed. It had a calculated volumetric torque density of 260 Nm/L. The cycloidal magnetic gear was mechanically difficult to construct and therefore only the inner rotor of the cycloidal magnetic gear was constructed. In addition, the eccentric air gap will cause bearing failure.

To achieve an even higher gear ratio, a nested multistage magnetic gear (MSMG) was designed with a 2-D FEA calculated torque density of 424 Nm/L. The desired gear ratio was 59:1 so that the performance could be compared with a Sumitomo mechanical gearbox which had the same gear ratio. In order to minimize the rotor torque ripple, the harmonic field interaction between the inner stage and the outer stage of the magnetic gear had to be mitigated. A unique flux concentration Halbach rotor structure was proposed. The rotor structure was shown to shield the outer rotor from the inner rotor harmonics. The nested multistage magnetic gear contains 4 rotors and complex mechanical structure. In order to provide sufficient mechanical support, the mechanical axial length had to be very large and this negated many of the benefits of using the nested coaxial rotor structure.

A two-stage series connected 59:1 gear ratio multistage magnetic gear was also designed for wind turbines. The 6.45:1 first stage magnetic gearbox had a diameter of 0.633 m and the 3-D FEA calculated peak torque and torque density were 4.79 kNm and

159 Nm/L. The measured torque and torque density were 4.25 kNm and 141 Nm/L. While the 9.14:1 second stage magnetic gearbox had a diameter of 0.507 m and the 3-D FEA calculated peak torque and torque density were 1.04 kNm and 136 Nm/L, respectively. The series connected multistage magnetic gear had the advantage of being more modular as different gear ratios can be obtained by changing the pole pair combinations for one of the series connected magnetic gears.

A two-stage series connected 59:1 gear ratio multistage magnetic gear was also designed for a hydropower application. Non-magnetic rods were used to reduce the losses and the mechanical deflection. The 2-D calculated torque density for the stage 1 magnetic gear was 371 Nm/L. And the 2-D calculated torque density was 344 Nm/L for the stage 2 magnetic gear. A stator was also designed that was inserted inside the stage 2 magnetic gear. In order to try to reduce the torque ripple, the stator had a fractional winding distribution with 1.25 slots/pole/phase.

In order to understand the fundamental torque density capabilities of rotating magnetic devices, a 3-D analytical based model for an axial and radial magnetic coupling was developed. The models were derived using Maxwell's magnetostatic equations and by using magnetic charge boundary conditions. The Laplacian equation was solved by using the separation of variables principle. The surface charge model was then used to obtain the field and torque expressions. The results from the analytical based model were compared with commercial FEA software. A good agreement was achieved for the radial magnetic coupling. However, it was shown that in order for the axial coupling to be modelled accurately a volume charge model needed to be considered. The analytical based model was significantly faster than the FEA models as at most two integrals

needed to be numerically solved. The study of the magnetic couplings provided insight into the upper torque bound of magnetic rotary devices. The torque and torque density benefits of radial magnetic couplings relative to axial magnetic couplings were discussed.

ACKNOWLEDGMENTS

TABLE OF CONTENTS

LIST OF TABLES

LIST OF FIGURES

LIST OF ABBREVIATIONS

FEA	Finite Element Analysis
MG	Magnetic Gear
CW	Clockwise
CCW	Counter-clockwise
CMG	Coaxial Magnetic Gear
FFCMG	Flux Focusing Coaxial Magnetic Gear
AMG	Axial Magnetic Gear
FFAMG	Flux Focusing Axial Magnetic Gear
MSMG	Multistage Magnetic Gear
PMC	Permanent Magnetic Coupling

LIST OF SYMBOLS

T_v Volume torque density [Nm/L]

T_{vi} Volume torque density on the inner-stage [Nm/L]

T_{vo} Volume torque density on the outer-stage [Nm/L]

T_{Av} Volume torque density of the axial magnetic coupling [Nm/L]

T_{Rv} Volume torque density of the radial magnetic coupling [Nm/L]

T_m Mass torque density [Nm/kg]

T_{mi} Mass torque density on the inner-stage [Nm/kg]

T_{mo} Mass torque density on the outer-stage [Nm/kg]

T_{Am} Mass torque density of the axial magnetic coupling [Nm/kg]

T_{Rm} Mass torque density of the radial magnetic coupling [Nm/kg]

T_{in} Input torque [Nm]

V Total active region volume of the gearbox [L]

ω_1 Rotational speed of rotor 1 [rad/s]

ω_2 Rotational speed of rotor 2 [rad/s]

ω_3 Rotational speed of rotor 3 [rad/s]

ω_4 Rotational speed of rotor 4 [rad/s]

ω_5 Rotational speed of rotor 5 [rad/s]

ω_6 Rotational speed of rotor 6 [rad/s]

G_r Gear ratio

G_{s1} Gear ratio of the stage 1 magnetic gear

G_{s2} Gear ratio of the stage 2 magnetic gear

p_1 Number of pole pairs of rotor 1

p_2 Number of pole pairs of rotor 2

p_3 Number of pole pairs of rotor 3

n_2 Number of cage rotor 2 steel poles

p_4 Number of pole pairs of rotor 4

n_5 Number of cage rotor 5 steel poles

p_6 Number of pole pairs of rotor 6

P_{loss} Total loss of the magnetic gearbox [W]

η Efficiency of the magnetic gear [%]

η_{s1} Efficiency of the stage 1 magnetic gerarbox [%]

η_{s2} Efficiency of the stage 2 magnetic gerarbox [%]

T_1 Torque on rotor 1 [Nm]

T_2 Torque on rotor 2 [Nm]

T_3 Torque on rotor 3 [Nm]

T_4	Torque on rotor 4 [Nm]
T_5	Torque on rotor 5 [Nm]
T_6	Torque on rotor 6 [Nm]
T_A	Torque of the axial magnetic coupling [Nm]
T_R	Torque of the radial magnetic coupling [Nm]
p_A	Number of pole pairs of rotor A
p_C	Number of pole pairs of rotor C
p_I	Number of pole pairs of Halbach rotor I
p_{II}	Number of pole pairs of Halbach rotor II
ω_A	Rotational speed of of rotor A [rad/s]
ω_B	Orbital speed of of rotor B [rad/s]
ω_C	Rotational speed of rotor C [rad/s]
g	Air gap [mm]
θ_A	Pole span of the magnet and steel on rotor A [rad]
θ_C	Pole span of the magnet and steel on rotor C [rad]
θ_1	Pole span of the magnet and steel on rotor 1 [rad]
θ_2	Pole span of the magnet and steel on rotor 2 [rad]
θ_3	Pole span of the magnet and steel on rotor 3 [rad]

θ_4 Pole span of the magnet and steel on rotor 4 [rad]

θ_5 Pole span of the magnet and steel on rotor 5 [rad]

θ_6 Pole span of the magnet and steel on rotor 6 [rad]

θ_{1m} Pole span of the magnet on rotor 1 [rad]

θ_{1s} Pole span of the steel on rotor 1 [rad]

θ_{2m} Pole span of the magnet on rotor 2 [rad]

θ_{2s} Pole span of the steel on rotor 2 [rad]

θ_{3m} Pole span of the magnet on rotor 3 [rad]

θ_{3s} Pole span of the steel on rotor 3 [rad]

r_{ii} Inner radius of the inner rotor [mm]

r_{oi} Outer radius of the inner rotor [mm]

r_{io} Inner radius of the outer rotor [mm]

r_{oo} Outer radius of the outer rotor [mm]

r_{i1} Inner radius of rotor 1 [mm]

r_{o1} Outer radius of rotor 1 [mm]

r_{i2} Inner radius of rotor 2 [mm]

r_{o2} Outer radius of rotor 2 [mm]

r_{i3} Inner radius of rotor 3 [mm]

r_{o3}	Outer radius of rotor 3 [mm]
r_{i4}	Inner radius of rotor 4 [mm]
r_{o4}	Outer radius of rotor 4 [mm]
r_{i5}	Inner radius of rotor 5 [mm]
r_{o5}	Outer radius of rotor 5 [mm]
r_{i6}	Inner radius of rotor 6 [mm]
r_{o6}	Outer radius of rotor 6 [mm]
r_o	Outer radius of the axial magnetic coupling [mm]
r_i	Inner radius of the axial magnetic coupling [mm]
r_o^I	Outer radius of the radial magnetic coupling rotor I [mm]
r_i^I	Inner radius of the radial magnetic coupling rotor I [mm]
r_o^{II}	Outer radius of the radial magnetic coupling rotor II [mm]
r_i^{II}	Inner radius of the radial magnetic coupling rotor II [mm]
r_{so}	Outer radius of the stator [mm]
r_{si}	Inner radius of the stator [mm]
l_2	Radial length of rotor 2 [mm]
l_4	Radial length of rotor 4 [mm]

l_5 Radial length of rotor 5 [mm]

l_6 Radial length of rotor 6 [mm]

h_1 Rotor 1 magnet length [mm]

w_1 Rotor 1 magnet width [mm]

h_3 Rotor 3 magnet length [mm]

w_3 Rotor 3 magnet width [mm]

h_4 Rotor 4 magnet length [mm]

w_4 Rotor 4 magnet width [mm]

h_6 Rotor 6 magnet length [mm]

w_6 Rotor 6 magnet width [mm]

B_m Residual magnetic flux density [T]

ρ_m Magnet density [g/cm^3]

ρ_s Steel density [g/cm^3]

d Axial length of the magnetic gear [mm]

d_{in} Axial length of the inner-stage magnetic gear [mm]

d_{out} Axial length of the outer-stage magnetic gear [mm]

d_1 Axial length of the stage 1 magnetic gear [mm]

d_2 Axial length of the stage 2 magnetic gear [mm]

d_a^I Axial length of the axial Halbach rotor I [mm]

d_a^{II} Axial length of the axial Halbach rotor II [mm]

d_a Axial length of the rotors of the axial magnetic coupling [mm]

d_r Axial length of the rotors of the radial magnetic coupling [mm]

l Eccentricity distance [mm]

f_r Air-gap radial force density [N/cm^2]

$\mathbf{B}$ Magnetic flux density [T]

$\mathbf{H}$ Magnetic field intensity [A/m]

$\mathbf{M}$ Magnetization vector [A/m]

M Magnitude of the magnetization vector

M_f Fundamental component of the magnetization vector

B_r Radial component of magnetic flux density [T]

B_θ Azimuthal component of magnetic flux density [T]

B_z Axial component of magnetic flux density [T]

μ_0 Permeability of free space [H/m]

μ_r Relative permeability [H/m]

r Radial position [mm]

θ_s Angular span of the stator teeth lips [rad]

θ Angular position [rad]

θ_I Angular position of rotor I [rad]

θ_{II} Angular position of rotor II [rad]

z Axial position [mm]

T Angular span of the Halbach magnet array [rad]

Λ The inner radius and outer radius ratio

r_g Air gap radius [mm]

t_m Magnet radial thickness [mm]

γ_T Torque ratio between the axial and radial couplings

γ_{T_v} Volume torque density ratio between the axial and radial couplings

γ_{T_m} Mass torque density ratio between the axial and radial couplings

CHAPTER 1 : INTRODUCTION

1.1. BACKGROUND

A mechanical gear includes one rotating part which meshes with the toothed part from another gear. The rotational motion can be transmitted between two meshing gears. Mechanical gears have been extensively used in torque transmitters and speed reducers. The torque density is used to evaluate the performance of the mechanical gears. Mechanical gears have been studied for a long time and have been maturely developed [1]. The most common type of gear is the spur gear which is shown in Fig. 1-1. The spur gears are easy to install and can have a high efficiency [2,3]. Fig. 1-2 shows the worm gear, rack pinion gear and bevel gear [4]. The planetary gear is shown in Fig. 1-3.
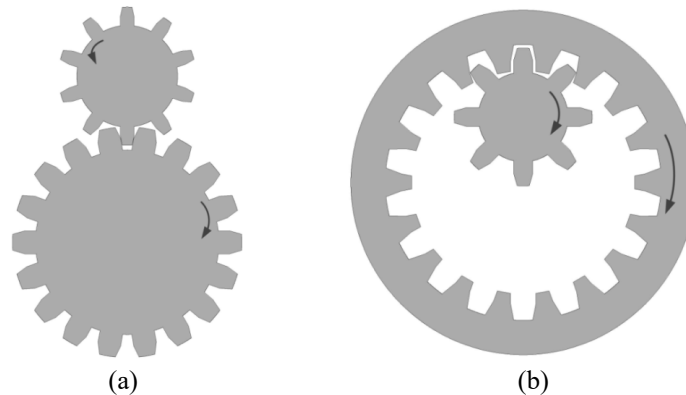
(a)   (b)
Fig. 1-1. Mechanical (a) external and (b) internal spur gear.
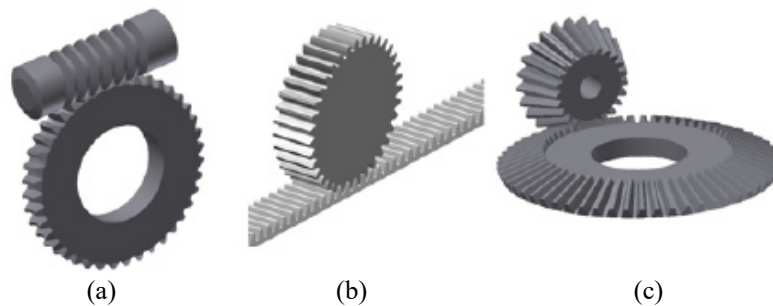
(a)   (b)   (c)
Fig. 1-2. Mechanical (a) worm gear, (b) rack pinion gear, (c) bevel gear [4].
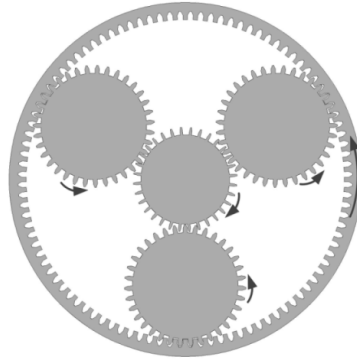
Fig. 1-3. The mechanical planetary gear.

Mechanical gearboxes are well known for their ability to have a high gear ratio and high torque density [5]. However, mechanical gears have some disadvantages such as short life time, noise and maintenance needs [5]. Therefore, magnetic gears have been proposed and studied. Magnetic gearboxes can operate with low noise and vibration and their non-contact operation means that no gear lubrication is required. In addition, magnetic gears have the unique ability to pole-slip when overloaded rather than catastrophically failing thereby providing built-in overload protection [6-9]. A magnetic gear also has the potential for high efficiency [10]. The idea of the magnetic gear dates back to at least 1901 [11] and then in 1916 [12]. At first, the magnetic gear could not operate with a very high torque density because of the limitations of the magnet material. However, with the discovery of SmCo magnets in the early 1960s and NdFeB magnets in 1982, magnetic devices could be developed with more torque. For instance, in 1987, Tsurumoto and Kikuchi used the magnetic gear topology shown in Fig. 1-4 with SmCo permanent magnets to generate higher torque density [10] than what was previously achievable using conventional magnets like ferrites and AlNiCo. However, it was not until 2001 when Atallah calculated that a coaxial magnetic gear could be developed with a 100 Nm/L torque density that active magnetic gear research became more intense.
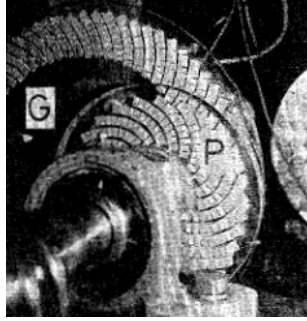
Fig. 1-4. A magnetic gear using permanent magnets [10].

In this chapter, different magnetic gear topologies are discussed, and their performance is compared based on their torque density and gear ratio.

1.2. LITERATURE REVIEW OF MAGNETIC GEARS

There are many applications in which a significantly higher gear ratio is desirable, such as in robotic and power generation applications. Therefore, in this section the gear ratio is taken into consideration when investigating the torque density performance of the magnetic gears.

The volume torque density, T_v, is often used to measure the performance of a MG. It is defined as

$$T_v = \frac{T_{in}}{V} \tag{1.1}$$

where T_{in} is the input torque and V is the total active region volume of the gearbox.

1.2.1. Magnetic Spur Gear

Fig. 1-5 (a) illustrates the external magnetic spur gear. The low speed rotor is rotating clockwise (CW) with ω_1 and has p_1 pole pairs. While the high-speed rotor is rotating counter-clockwise (CCW) with ω_2 and has p_2 pole pairs. The gear ratio, G_r can be

calculated using the speed and pole pairs [13]

$$G_r = -\frac{p_1}{p_2} = \frac{\omega_2}{\omega_1} \tag{1.2}$$

Fig. 1-5 (b) is the internal magnetic spur gear. The low-speed rotor is rotating CW with ω_1 and has p_1 pole pairs. While the high-speed rotor is also rotating CW with ω_2 and has p_2 pole pairs. The relation between speed and pole pairs is

$$G_r = \frac{p_1}{p_2} = \frac{\omega_2}{\omega_1} \tag{1.3}$$
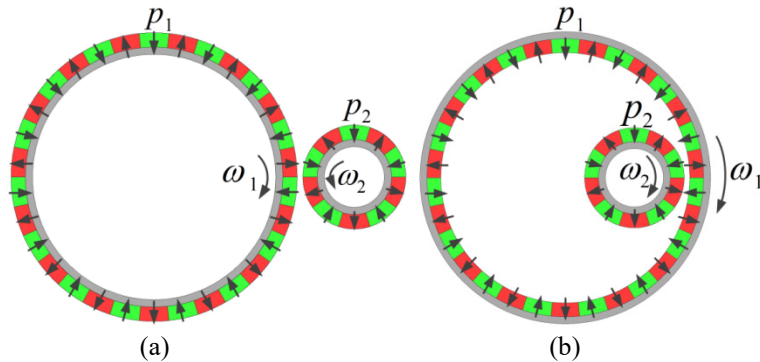
(a)   (b)
Fig. 1-5. (a) External and (b) internal magnetic gear.

The external magnetic spur gear was studied in [14,15]. In [15], Jorgensen experimentally measured the volume torque density to be 17.6 Nm/L with $G_r = -4$, $p_1 = 40$ and $p_2 = 10$. The outer radii were 100 mm and 29 mm.

1.2.2. Magnetic Planetary Gear

The concept of the magnetic planetary gear is shown in Fig. 1-6. The outer ring gear has p_3 pole pairs. The planet gear each has p_2 pole pairs and the central sun gear has p_1 pole pairs.
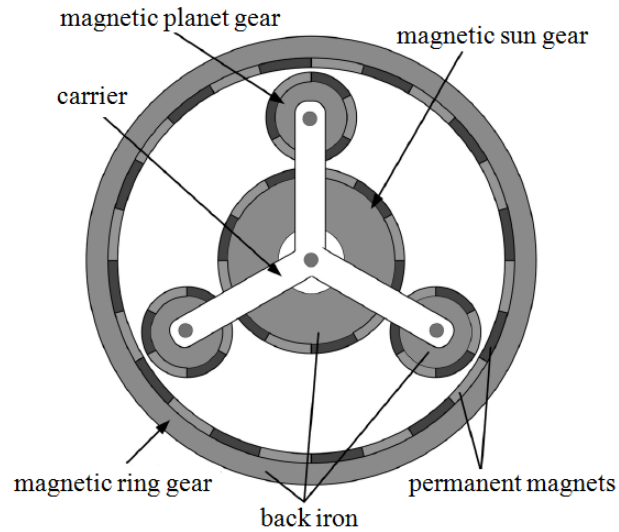
Fig. 1-6. Magnetic planetary gear with $p_1 = 6$, $p_2 = 3$, $p_3 = 12$ [16].

The magnetic planetary gear was studied in [16,17]. In [16] Huang numerically calculated a torque density of 16.9 Nm/L with a gear ratio of $G_r = 3$ and an outer radius of 47 mm. The experimental result was 16 Nm/L.

In 2015, Davey proposed a new topology of a magnetic planetary gear [18] which is shown in Fig. 1-7. The ring gear had 20 pole pairs and the sun gear had 2 pole pairs. The planet gears were replaced by 22 freely-spinning 2-pole magnetized cylinders. The corresponding gear ratio was 11 and a calculated torque density was up to 300 Nm/L with outer radius of 165 mm. However, with those free-rotating cylinders, there was much stress on the rods and it would be very difficult to assemble.
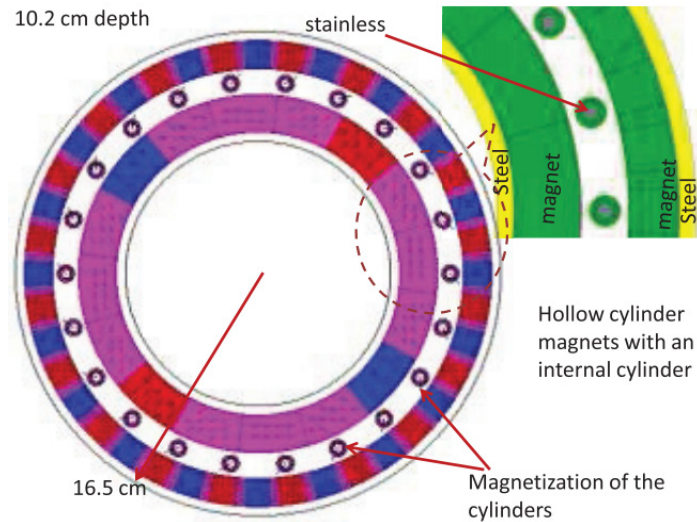
Fig. 1-7. A new magnetic planetary gear proposed by Davey with $p_1 = 2$, $p_2 = 22$, $p_3 = 20$ [18].

Wang proposed a similar topology of a magnetic planetary gear in 2016 which achieved 139.4 Nm/L [19]. Fig. 1-8 shows the topology. The ring gear had 21 pole pairs and the sun gear had 2 pole pairs. The planet gears were replaced by 23 freely-rotating 2-pole magnets. The corresponding gear ratio was -10.5 and the outer radius was 65 mm.
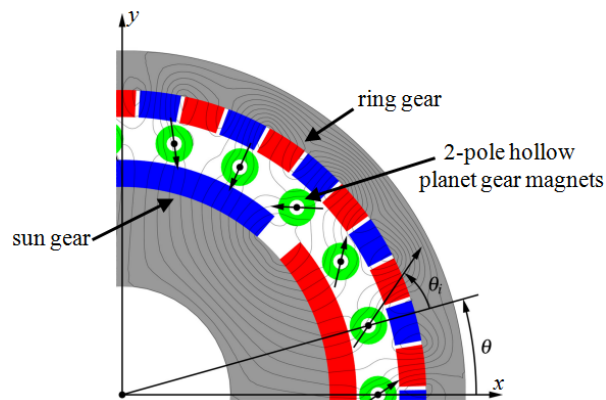
Fig. 1-8. A novel magnetic planetary gear proposed by Wang with $p_1 = 2$, $p_2 = 23$, $p_3 = 21$ [19].

1.2.3. Cycloidal MG

Fig. 1-9 illustrates the cycloidal MG which has the potential to achieve a high gear ratio at a high torque density. If both of the rotors rotate along their own centers, it will operate like an internal spur gear. For the cycloidal MG, the outer rotor is fixed and the

inner rotor has two motions. One is the rotational motion with ω_1 which allows it to rotate along its own center. The other one is an orbital motion with ω_2 which enables the cycloidal gear to move along the center of the outer rotor. The inner rotor and outer rotor have p_1 and p_2 pole pairs, respectively. The relation between these two motions is the gear ratio, G_r which can be described by

$$G_r = \frac{\omega_2}{\omega_1} = \frac{p_1}{p_1 - p_2} \qquad (1.4)$$
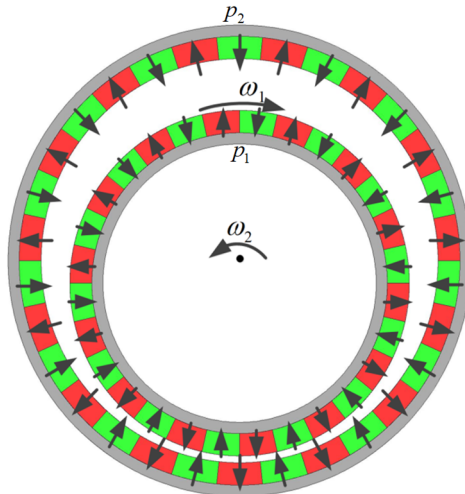
Fig. 1-9. Cycloidal MG with $p_1 = 14$ and $p_2 = 15$.

The cycloidal MG was present by Jorgensen in [20]. With $p_1 = 21$ and $p_2 = 22$ pole pairs for outer and inner rotors, respectively, the G_r was calculated to be -21. The calculated torque density from the FEA was 141.9 Nm/L and the measured value was 106.8 Nm/L. The outer radius was 61.5 mm.

In [21], Rens demonstrated another cycloidal MG with a gear ratio of -18 which is shown in Fig. 1-10. Based on this, another dual stage cycloidal MG with a high gear ratio of 360 was built in which each stage of the cycloidal MG had a 150 Nm/L torque density and the outer radius was 70 mm.
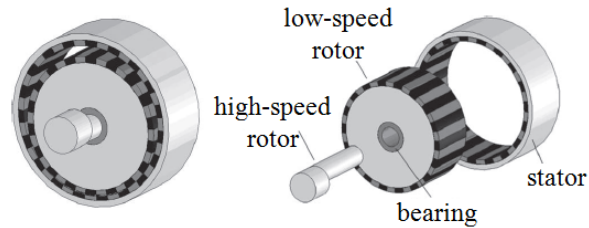
Fig. 1-10. A harmonic MG proposed by Rens with $p_1 = 18$ and $p_2 = 19$ [21].

In 2013, Chicurel-Uziel experimentally demonstrated the efficiencies of a similar type of cycloidal MG with a 26:1 gear ratio [22]. The outer radius was 81 mm.

In 2015, Li proposed a flux focusing cycloidal MG with a gear ratio of -25:1 [23] which is shown in Fig. 1-11. The calculated torque density was 291 Nm/L with an outer radius of 114 mm.
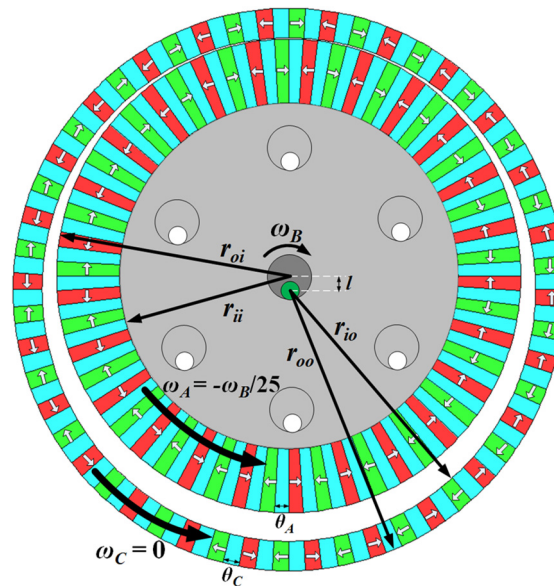
Fig. 1-11. A flux focusing cycloidal MG with $p_1 = 25$ and $p_2 = 26$ [23].

The cycloidal MG must maintain an eccentric orbit and this results in a non-uniform radial force (as discussed further in Chapter 2). This consequence will result in increased wear on the bearings. In 2014, Davey proposed solving this bearing wear issue by designing a new type of axial cycloidal MG [24]. The rotors were placed in the axial

direction and were separated by a small air gap. Davey studied the performance of a -30:1 gear ratio axial cycloidal MG which is shown in Fig. 1-12. The measured torque density was 91.5 Nm/L. However, it is very difficult to keep the air gap to be uniform for an axial cycloidal MG. The outer radius was 203.2 mm.
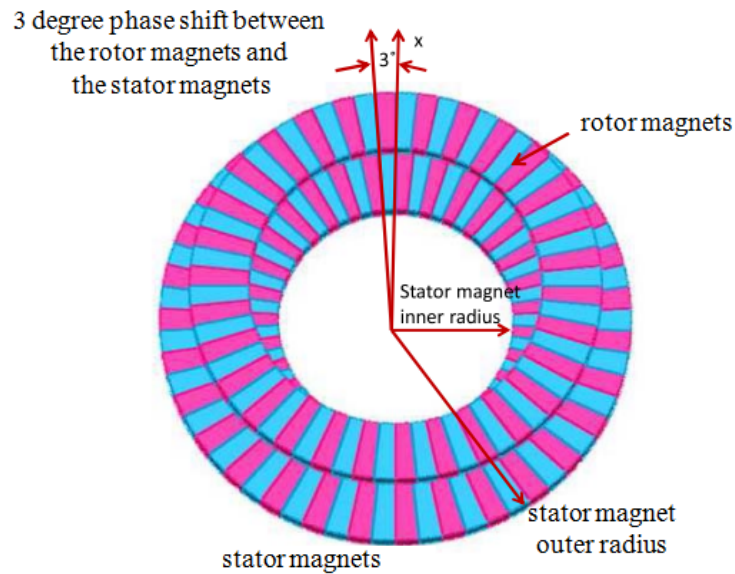
Fig. 1-12. An axial cycloidal MG proposed by Davey with $p_1 = 30$ and $p_2 = 31$ [24].

1.2.4. Coaxial Magnetic Gear (CMG)

A CMG creates speed change by inserting ferromagnetic segments between an inner and outer magnetic rotors. Such a topology is shown in Fig. 1-13.

Rotor 1: p_1 pole-pairs

Rotor 2: n_2 steel poles

Rotor 3: p_3 pole-pairs
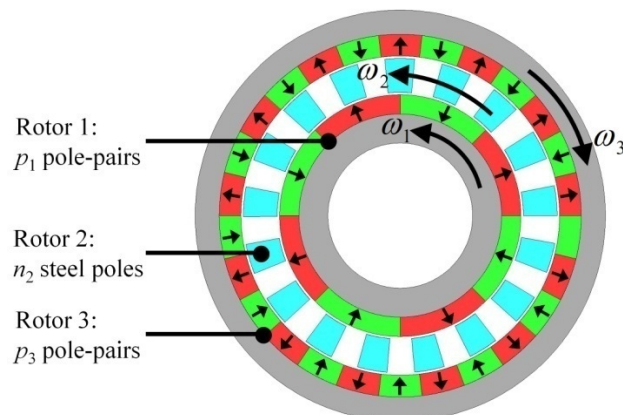
Fig. 1-13. A CMG with $p_1 = 4$, $n_2 = 17$ and $p_3 = 13$.

In order to understand the operation principle of the CMG, it is assumed that the inner rotor has p_1 pole pairs with an angular velocity ω_1 and the outer rotor has p_3 pole pairs with an angular velocity ω_3 as shown in Fig. 1-13. If the cage rotor (pole pieces) has n_2 steel pole pieces with an angular velocity ω_2, then in order to make the MG rotors to couple, the angular velocity relationship must satisfy:

$$p_1\omega_1 + p_3\omega_3 = n_2\omega_2 \tag{1.5}$$

and

$$p_1 + p_3 = n_2 \tag{1.6}$$

Fig. 1-14 shows the magnetic field plot when only the cage and outer rotors are present. The outer and the cage rotors have 13 and 17 pole pairs, respectively. It can be seen that the outer rotor generates 26 poles (13 pole pairs) at the outer region of the outer rotor. After modulated by the cage steel poles, it will generate 8 poles (4 pole pairs) at the inner side of the cage rotor. Therefore, in order to obtain a constant torque, the inner rotor must have 4 pole pairs which satisfies equation (1.6).
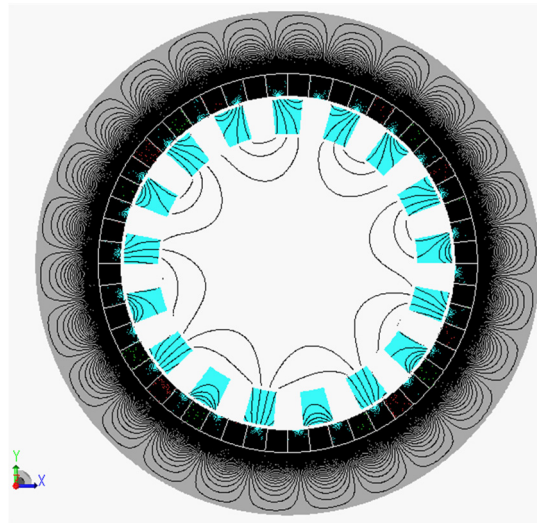
Fig. 1-14. Magnetic flux lines when only the cage and outer rotors are present.

If the outer rotor is a stationary part ($\omega_3 = 0$), then equation (1.5) becomes:

$$p_1\omega_1 = n_2\omega_2 \tag{1.7}$$

and the gear ratio, G_r is calculated as:

$$G_r = \frac{\omega_1}{\omega_2} = \frac{n_2}{p_1} = \frac{p_1 + p_3}{p_1} \tag{1.8}$$

If the cage rotor is a stationary part ($\omega_2 = 0$), then the gear ratio is calculated as:

$$G_r = \frac{\omega_1}{\omega_3} = -\frac{p_3}{p_1} \tag{1.9}$$

The power relationship between rotors is:

$$T_1\omega_1 - T_2\omega_2 = P_{loss} \tag{1.10}$$

and the efficiency can be computed from

$$\eta = \frac{|T_2|\omega_2}{|T_1|\omega_1} \tag{1.11}$$

where T_1, T_2 and T_3 are the torque on rotor 1 (input), rotor 2 (output), and rotor 3 (stationary), respectively. And the torque within the MG satisfies:

$$T_1 + T_2 + T_3 = 0 \tag{1.12}$$

The CMG topology was first proposed in 1913 by Neuland [12]. It was further modified by Chubb in 1931 [25]. In 1968, Martin invented a new magnetic transmission with coaxial topology which was able to achieve a speed increase or decrease [9]. The ferrite magnets were used on two rotors. As shown in Fig. 1-15, the torque can be

transmitted without mechanical contact.
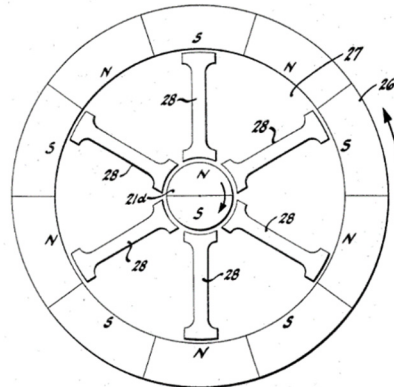
Fig. 1-15. Magnetic transmission invented by Martin [9].

In 2004, Atallah [6] proposed a CMG with gear ratio -5.75 as shown in Fig. 1-16. The calculated torque density was 111.3 Nm/L and the measured value was 77.9 Nm/L with an outer radius of 70 mm.
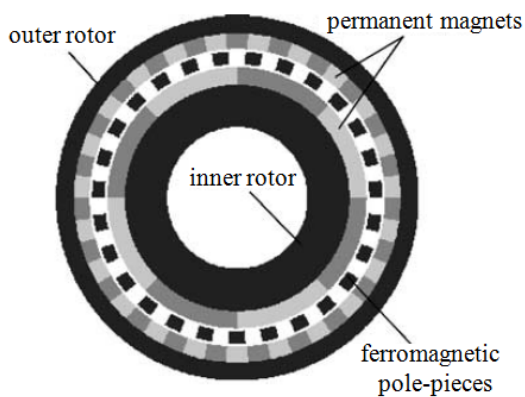
Fig. 1-16. A CMG proposed by Atallah with $p_1 = 4$, $n_2 = 19$ and $p_3 = 23$ [6].

In 2005, A CMG with buried spoke type inner magnets was proposed by Rasmussen in [8]. The topology is shown in Fig. 1-17. The FEA and experimental torque densities were 92 Nm/L and 54.5 Nm/L with a gear ratio of -5.5. The outer radius was 60 mm.
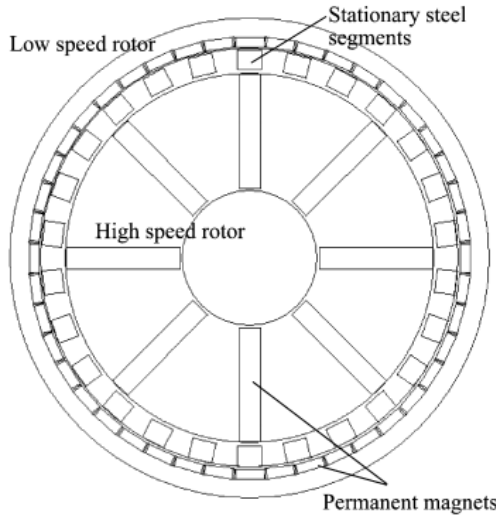
Fig. 1-17. A CMG proposed by Rasmussen with $p_1 = 4$, $n_2 = 26$ and $p_3 = 22$ [8].

In [26], Nakamura designed a CMG using the same surface mounted magnet topology as proposed by Atallah [6] but with a gear ratio of -10.33 as shown in Fig. 1-18. The torque density was measured to be 60 Nm/L with an outer radius of 85 mm.
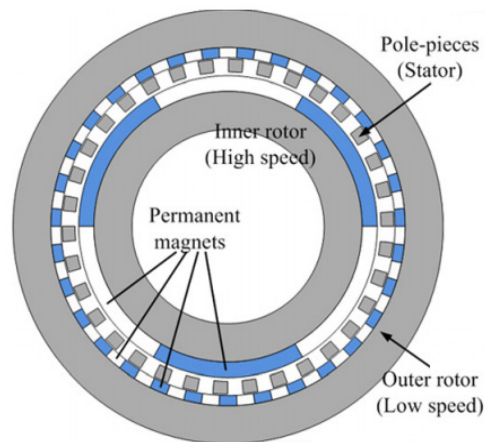
Fig. 1-18. A CMG proposed by Nakamura with $p_1 = 3$, $n_2 = 34$ and $p_3 = 31$ [26].

In Fig. 1-19, a similar topology was proposed by Shah in [27]. However, Shah proposed that by controlling the inner rotor the CMG could operate with a variable speed ratio. If the pole pieces rotor was fixed, the gear ratio was designed to be -5.5. A torque

density of 53.1 Nm/L was obtained in the FEA simulation, while the experimental result

was 41.6 Nm/L. The outer radius was 65 mm.
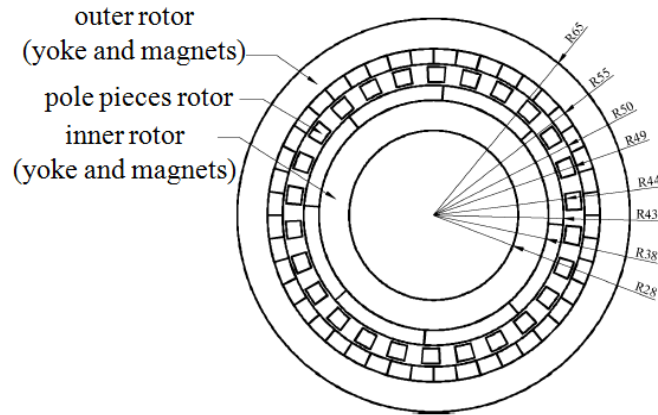
Fig. 1-19. A variable speed CMG proposed by Shah with $p_1 = 4$, $n_2 = 26$ and $p_3 = 22$ [27].

In 2009, Liu demonstrated a new topology in which the outer rotor used consequent

pole structure. The outer magnets were buried into a ferromagnetic core [28]. The

topology is shown in Fig. 1-20. The FEA and experimental torque densities were

calculated to be 55.8 Nm/L and 53.3 Nm/L with a gear ratio of -7.33. The outer radius

was 110 mm.
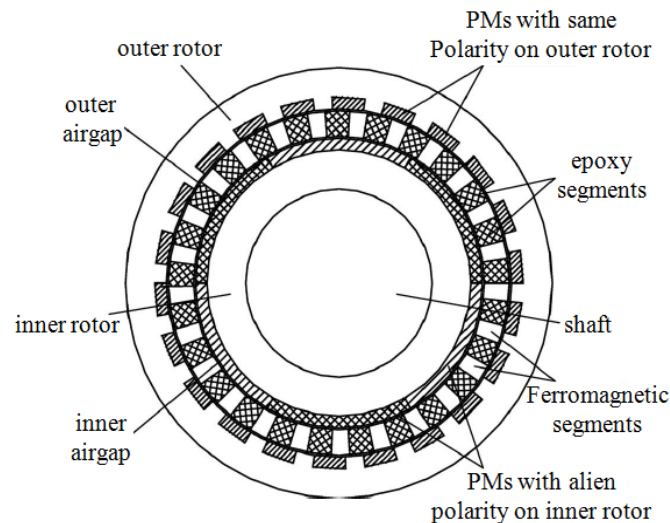
Fig. 1-20. A CMG proposed by Liu with $p_1 = 3$, $n_2 = 25$ and $p_3 = 22$ [28].

Linni designed a CMG with Halbach arrays and compared it with conventional radial magnetized CMG [29]. Fig. 1-21 shows the topologies which have a gear ratio of -4.25. The outer Halbach rotor had 2 magnets per segment and the inner Halbach rotor had 3 magnets per segment. The conventional CMG was able to achieve a calculated torque density of 97.1 Nm/L and an experimental torque density of 95.4 Nm/L. While the FEA calculated and experimental torque densities for the Halbach CMG were 110.7 Nm/L and 108.3 Nm/L, respectively. The outer radius was 107 mm. The Halbach design is able to generate higher torque but is difficult to mechanically assemble.
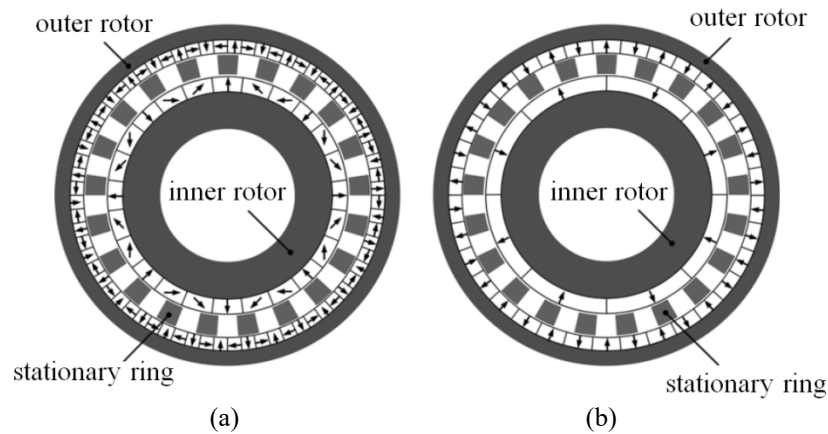
Fig. 1-21. (a) Halbach CMG and (b) conventional CMG proposed by Linni with $p_1 = 4$, $n_2 = 21$ and $p_3 = 17$ [29].

Similar to [29], Jing proposed another CMG with Halbach arrays [30] which is shown in Fig. 1-22. The gear ratio was -4.25. The outer and inner rotors of the Halbach CMG had 2 and 4 magnet segments per pole. Jing conducted an optimization of the parameters and obtained a torque density of 148.6 Nm/L when using FEA. With a load of 74 Nm, the experimental torque density was 57.2 Nm/L with an outer radius of 100 mm.
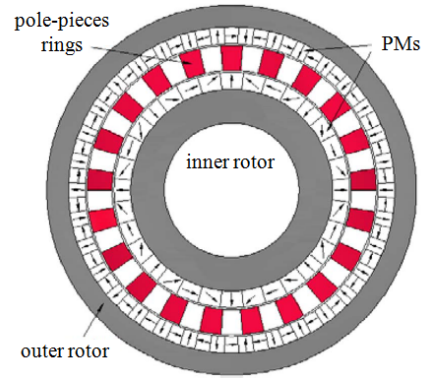
Fig. 1-22. A Halbach CMG proposed by Jing with $p_1 = 4$, $n_2 = 21$ and $p_3 = 17$ [30].

In 2010, Bronn presented a CMG which had a relatively high gear ratio of -10.5 [31]. The geometry is shown in Fig. 1-23. The inner rotor, stationary modulation rotor and outer rotor has pole pairs of 2, 23 and 21. The FEA and experimental torque densities were 80.8 Nm/L and 49.0 Nm/L. The outer radius was 57.5 mm.
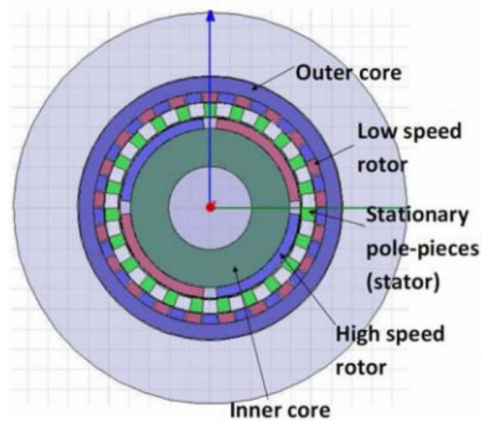
Fig. 1-23. A CMG proposed by Bronn with $p_1 = 2$, $n_2 = 23$ and $p_3 = 21$ [31].

In 2011, Frank present a CMG with a strengthened central pole modulator rotor [32]. The topology is shown in Fig. 1-24. The ferromagnetic pole modulation pieces were connected by a thin bridge and the inner rotor had interior magnets. The outer radius was 60 mm with a gear ratio of -5.5. The calculated and measured volume torque densities were 64 Nm/L and 42 Nm/L. In 2012, a similar pole modulator rotor was used by

Niguchi [33] which is shown in Fig. 1-25. The cogging torque and torque density were verified by FEA method and experiment. The torque densities from FEA and experiment were 30.2 Nm/L and 29.4 Nm/L with a gear ratio of -2.5. The outer radius was 45 mm.
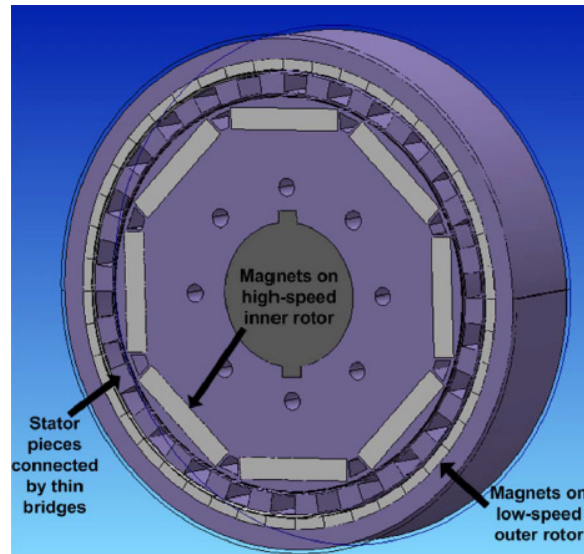
Fig. 1-24. A CMG with strengthened stator proposed by Frank with $p_1 = 4$, $n_2 = 26$ and $p_3 = 22$ [32].
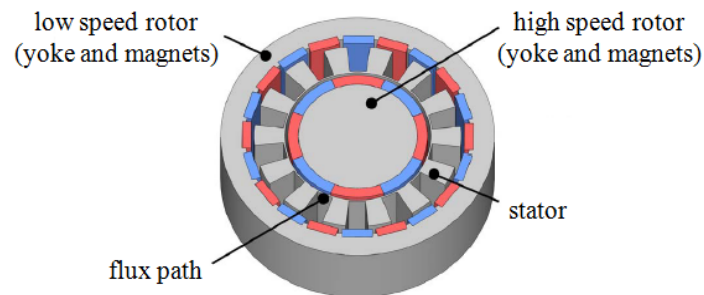
Fig. 1-25. A CMG proposed by Niguchi with $p_1 = 4$, $n_2 = 14$ and $p_3 = 10$ [33].

In 2011, Li proposed a flux focusing CMG (FFCMG) [34] as shown in Fig. 1-26. The inner rotor had surface mounted magnets which were radially magnetized while the outer rotor had a flux focusing arrangement in which the steel pieces were used between angular magnetized magnets to increase the air gap flux density. The predicted torque density was 98.1 Nm/L with a gear ratio of -5.5. The outer radius was 74 mm.
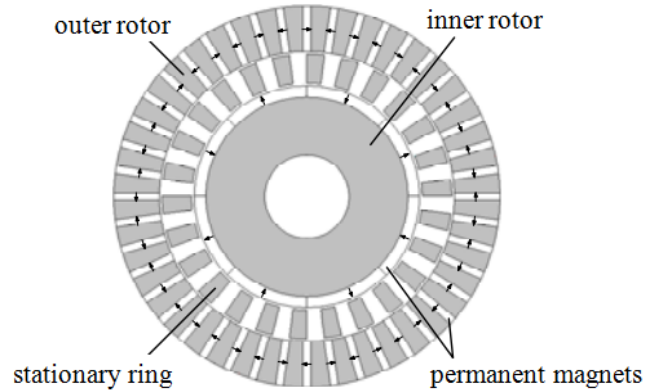
Fig. 1-26. A FFCMG proposed by Li with $p_1 = 4$, $n_2 = 26$ and $p_3 = 22$ [34].

Uppalapati present a FFCMG using high grade ferrite magnets which had a low cost [35] in 2012. The predicted torque density was 65.5 Nm/L with a gear ratio of 4.25. Both of the inner and outer rotors used the flux focusing topology which is shown in Fig. 1-27. The outer radius was 55 mm. Based on this, a FFCMG with ferrite, hybrid and NdFeB magnets was tested and compared in [36]. The torque density was 33 Nm/L, 66.3 Nm/L and 151.2 Nm/L, respectively. The outer radius was 55 mm. In 2014, Uppalapati demonstrated another FFCMG which could achieve 239 Nm/L experimentally [37]. The final design is shown in Fig. 1-28 with a gear ratio of 4.25. The outer radius was 114 mm.
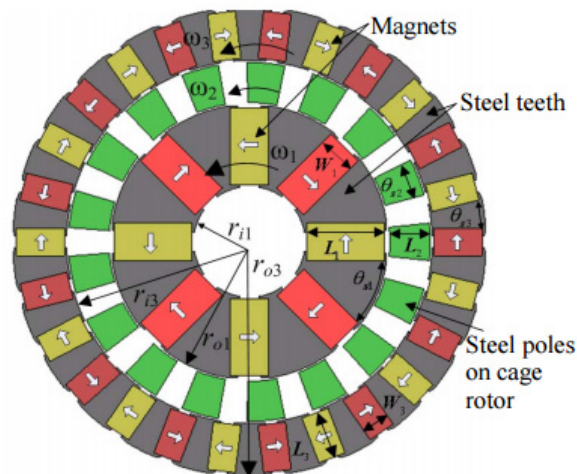
Fig. 1-27. A low-cost FFCMG proposed by Uppalapati with $p_1 = 4$, $n_2 = 17$ and $p_3 = 13$ [35].
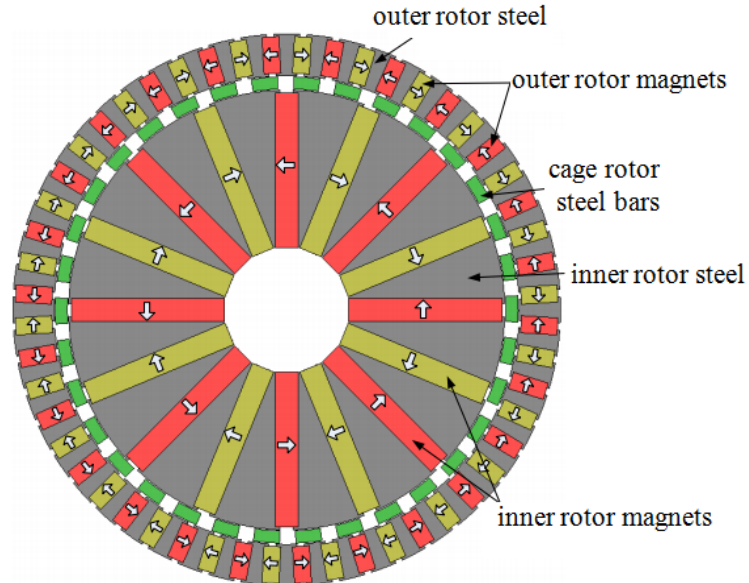
Fig. 1-28. A FFCMG proposed by Uppalapati with $p_1 = 4$, $n_2 = 17$ and $p_3 = 13$ [37].

The designs presented by Uppalapati used solid steel parts and so eddy current losses were high. A fully laminated version of the same 4.25 gear ratio flux focusing rotor typology was presented in [38] as shown in Fig. 1-29. The predicted torque density was 103.1 Nm/L and the experimentally measured value was 70.2 Nm/L when the outer radius was 56 mm.
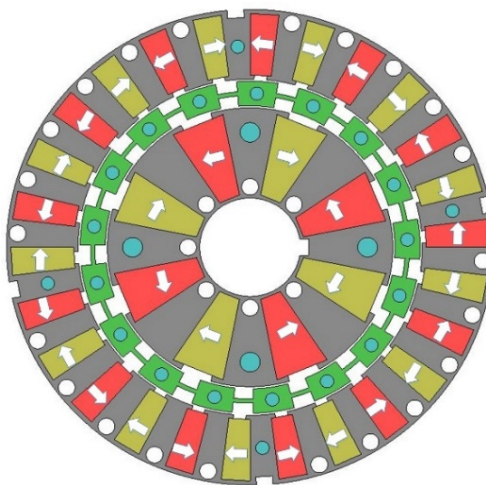
Fig. 1-29. Laminated design by Uppalapati with $p_1 = 4$, $n_2 = 17$ and $p_3 = 13$ [38].

In 2013, Fujita optimized the shape of the stationary pole pieces for a surface CMG [39] which is shown in Fig. 1-30. The initial experimental torque density was 36.9 Nm/L with a gear ratio of -5.5. After optimization, the predicted torque density was calculated to be 81.7 Nm/L. The outer radius was 45 mm. In 2015, Matthee optimized the modulator for a CMG with a gear ratio of -10.5 [40]. The geometry is shown in Fig. 1-31. The calculated torque density was 117.0 Nm/L. A measured torque density was 111.2 Nm/L with an outer radius of 57.5 mm.
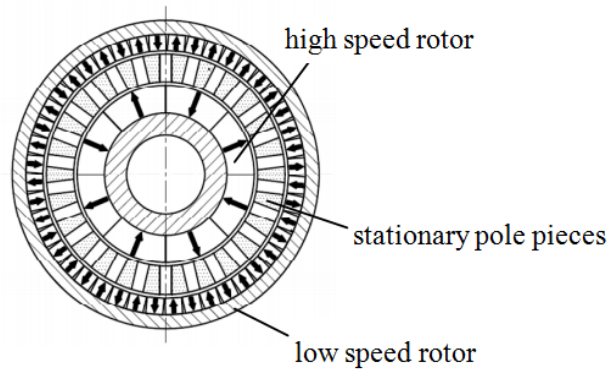
Fig. 1-30. A surface CMG proposed by Fujita with $p_1 = 4$, $n_2 = 26$ and $p_3 = 22$ [39].
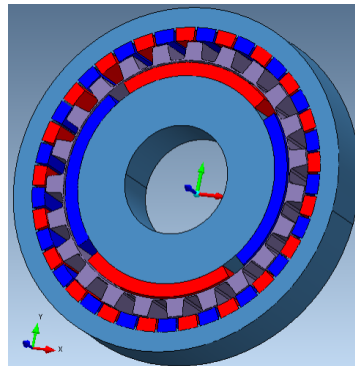
Fig. 1-31. A CMG with an optimized shape of modulator proposed by Matthee with $p_1 = 2$, $n_2 = 23$ and $p_3 = 21$ [40].

In 2016, an improved FFCMG was present by Fu [41]. New arrangements of magnets were used as shown in Fig. 1-32. A predicted torque density of 382.7 Nm/L was

calculated with a gear ratio of -7.33. The outer radius was 92 mm. A similar design was present in [42] which was calculated to be able to achieve a torque density of 226 Nm/L. The outer radius was 92 mm. These designs would be difficult to construct due to the many small magnet pieces.
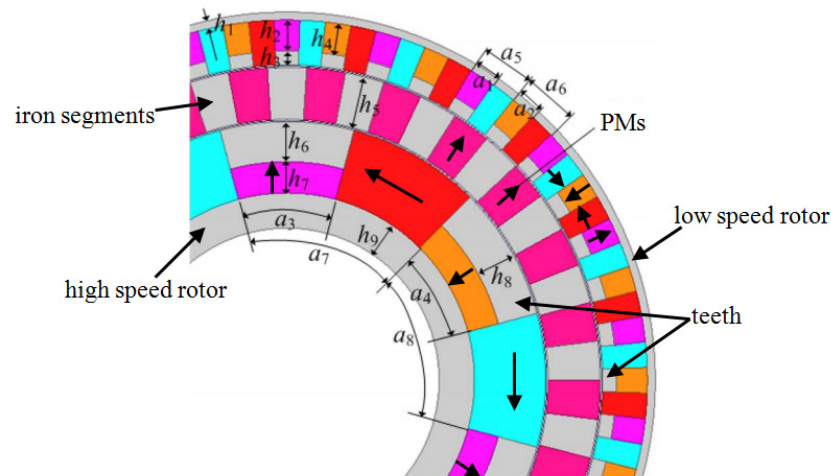
Fig. 1-32. An improved FFCMG proposed by Fu with $p_1 = 3$, $n_2 = 25$ and $p_3 = 22$ [41].

Som also proposed a coaxial MG with flux concentration topology in 2017 [43]. This design is shown in Fig. 1-33. The primary difference was that the central rotor did not contain magnets. The calculated and measured volume torque density was 142.2 Nm/L and 82.8 Nm/L, respectively. The gear ratio was 4.25 and the outer radius was 57 mm.
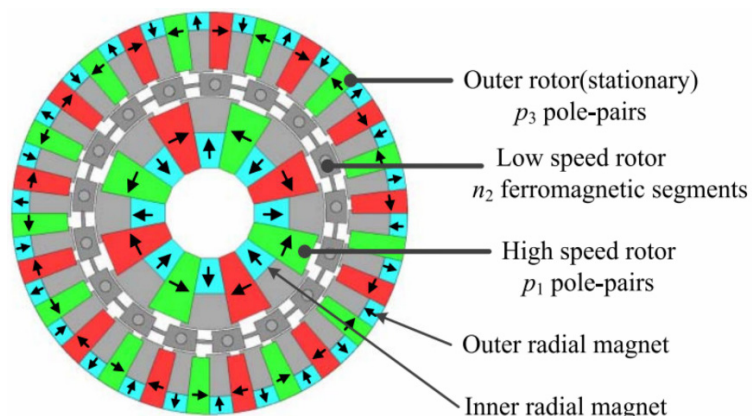
Fig. 1-33. A flux concentration Halbach MG with $p_1 = 4$, $n_2 = 17$ and $p_3 = 13$ [43].

1.2.5. Axial Magnetic Gear (AMG)

The AMG has the same operating principle as the CMG, the only difference is that the rotors of the AMG are aligned axially and there is an axial air gap between each rotor. In 2006, Mezani proposed an AMG [44] with a gear ratio of -5.75 as shown in Fig. 1-34. A torque density in excess of 70 Nm/L was calculated. The outer radius was 100 mm.
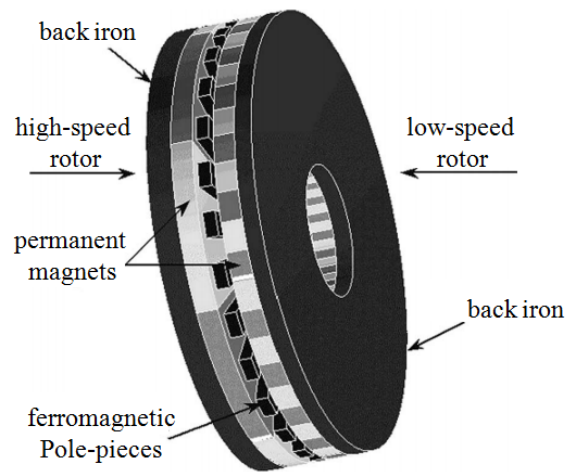
Fig. 1-34. An AMG proposed by Mezani with $p_1 = 4$, $n_2 = 27$ and $p_3 = 23$ [44].

In 2014, Johnson built an AMG with a gear ratio of -8 [45]. Since only one pole pair was used for the high-speed rotor, the torque density was only 22.4 Nm/L. Fig. 1-35 shows the geometry of the AMG. In 2015, Johnson [46] utilizeda Halbach magnet array in the axial rotor topology. With the Halbach arrays, higher torque density could be achieved. For a gear ratio of 4.14, the predicted torque density was 183.9 Nm/L. For a gear ratio of 9.2, the predicted torque density was 155.8 Nm/L with an outer radius of 167 mm.
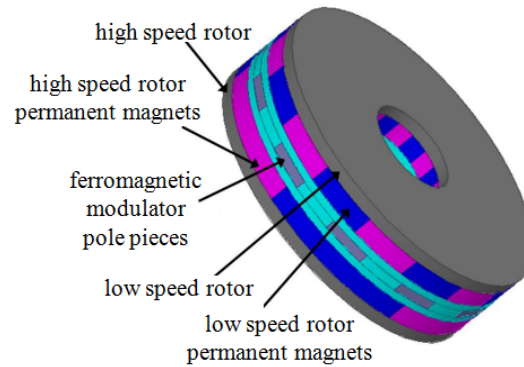
Fig. 1-35. An AMG proposed by Johnson with $p_1 = 1$, $n_2 = 9$ and $p_3 = 8$ [45].

A flux focusing AMG (FFAMG) was demonstrated by Acharya [47] in 2014. As shown in Fig. 1-36, the high-speed rotor and the stationary rotor used a flux focusing topology. The gear ratio was 4.17 and the predicted torque density was 289.8 Nm/L. The outer radius was 140 mm.
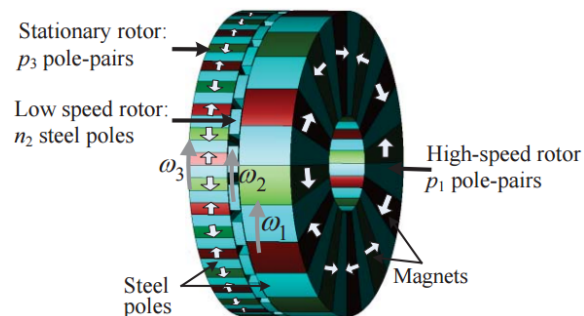
Fig. 1-36. A FFAMG proposed by Acharya with $p_1 = 6$, $n_2 = 25$ and $p_3 = 19$ [47].

1.2.6. Hybrid Magnetic Gear

In 2008, Yong proposed the 6.5:1 gear ratio transverse flux MG [48] which is shown in Fig. 1-37. The rotor flux passes through the modulation ferromagnet segments in an axial direction, whilst this rotor arrangement should make fabrication significantly easier, Yong showed that the torque density was very low, only 2.4 Nm/L when the outer radius was 110.7 mm.
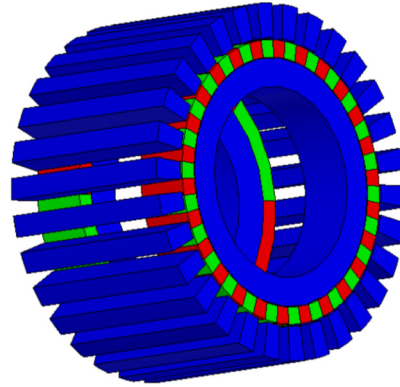
Fig. 1-37. A transverse flux MG proposed by Yong with $p_1 = 4$, $n_2 = 30$ and $p_3 = 26$ [48].

In 2014, Bomela proposed a transverse flux MG [49] which is shown in Fig. 1-38. In this approach, the modulation flux passes through the ferromagnetic steel axially and the flux from the rotors is created radially. The gear ratio was -3.75 and the predicted torque density was 80.6 Nm/L. The outer radius was 80 mm. An axial topology version was present in [50] which is shown in Fig. 1-39. A predicted torque density of 77 Nm/L was achieved with a gear ratio of -4.25. The outer radius was 82 mm.
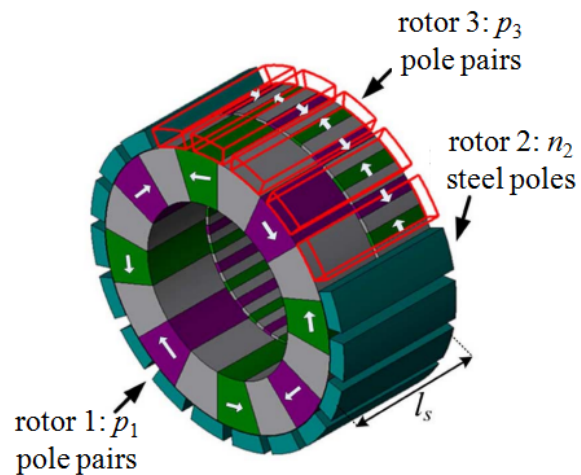
Fig. 1-38. A transverse MG proposed by Bomela with $p_1 = 4$, $n_2 = 19$ and $p_3 = 15$ [49].
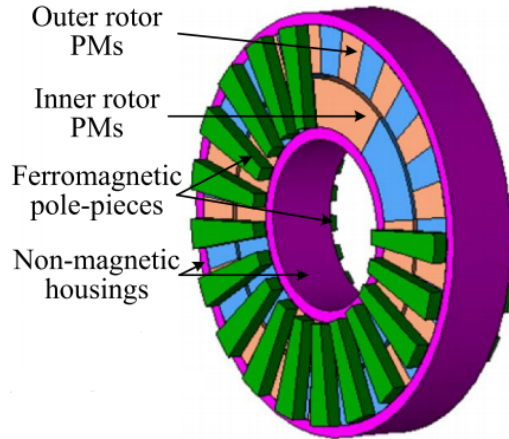
Fig. 1-39. An axial-field MG proposed by Zhu with $p_1 = 4$, $n_2 = 21$ and $p_3 = 17$ [50].

Peng proposed a MG combing the transverse and axial MGs together [51] as shown in Fig. 1-40. The gear ratio was -5.5 and the predicted torque density was 181.2 Nm/L with an outer radius of 154 mm. Though the performance of the MG was improved, the topology would to be very difficult to construct.
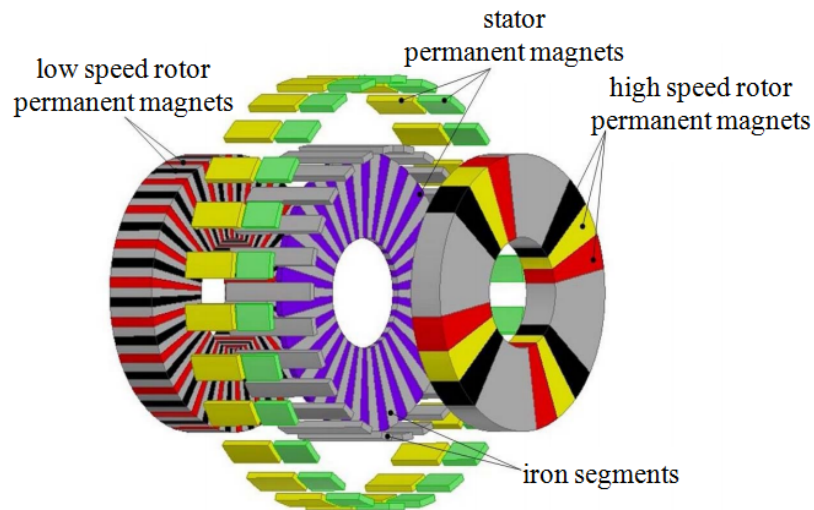
Fig. 1-40. A hybrid MG proposed by Peng with $p_1 = 4$, $n_2 = 26$ and $p_3 = 22$ [51].

Yin [52] and Chen [53] proposed an alternative hybrid MG topology which is shown in Fig. 1-41 and Fig. 1-42, respectively. For Yin's design, a calculated torque density of

268.4 Nm/L was obtained with a gear ratio of 4.17. The outer radius was 140 mm. While Chen predicted that a torque density of 108 Nm/L could be obtained with a gear ratio of - 5.5. The outer radius was 150 mm. Both designs would be extremely difficult to mechanically construct.
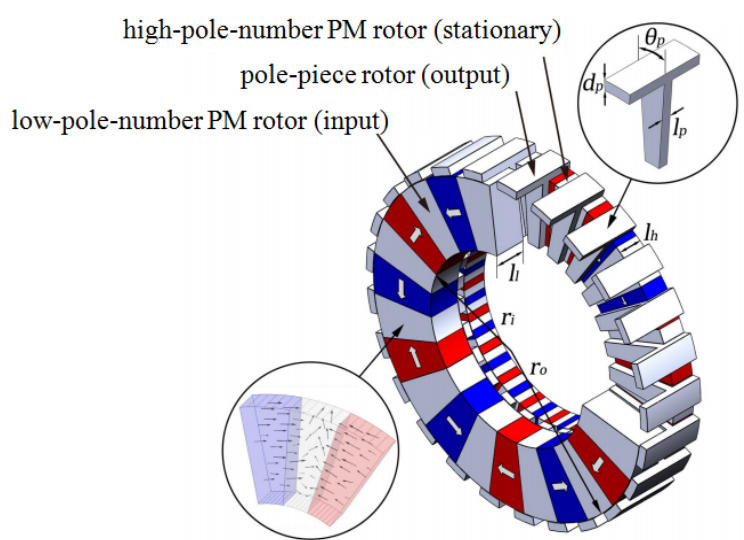
Fig. 1-41. A simplified hybrid MG proposed by Yin with $p_1 = 6$, $n_2 = 25$ and $p_3 = 19$ [52].
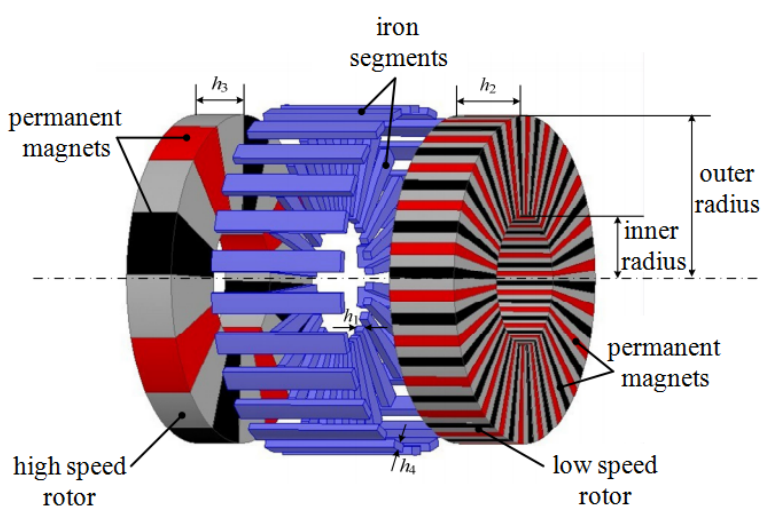
Fig. 1-42. A simplified hybrid MG proposed by Chen with $p_1 = 4$, $n_2 = 26$ and $p_3 = 22$ [53].

1.2.7. Stator Integrated Magnetic Gear

A stator can be integrated with a MG. For instance, in 2008, Atallah proposed a CMG with an integrated stator and a gear ratio of 11.5 [54]. The topology is shown in Fig. 1-43 with an outer radius of 89 mm. The outer stator integrated with the high speed inner rotor and Attallah experimentally showed that it could operate at a torque density of 53 Nm/L.
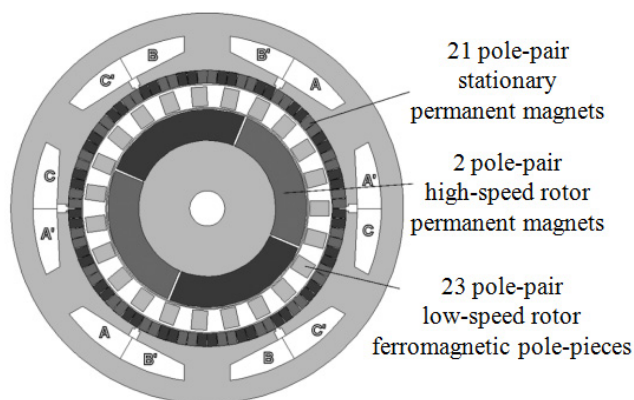
Fig. 1-43. A CMG combined with an electrical machine proposed by Atallah with $p_1 = 2$, $n_2 = 23$ and $p_3 = 21$ [54].

A motor integrated CMG with a wide speed range was present by Rasmussen in 2009 which is shown in Fig. 1-44 [55]. A torque density of 130 Nm/L was calculated with a gear ratio of 8.67. The outer radius was 132 mm.
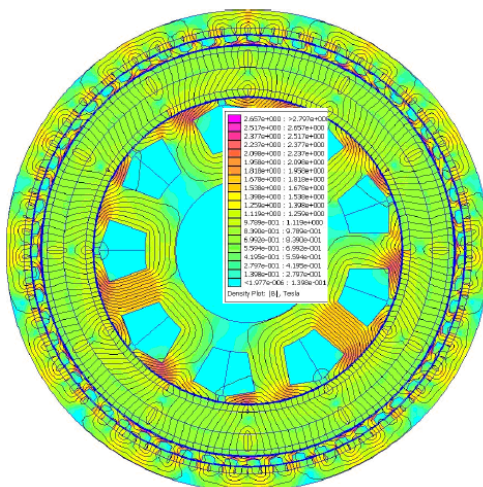
Fig. 1-44. A CMG with an integrated stator proposed by Rasmussen [55].

In 2011, Rasmussen experimentally built a motor integrated CMG with a gear ratio of -8.83 as shown in Fig. 1-45 [56] which was based on the design in [55]. The FEA and measured torque densities were 113 Nm/L and 92 Nm/L, respectively. The outer radius was 134.25 mm. In 2012, Frandsen further improved the CMG present in [56] by reducing the rotational losses [57] which is shown in Fig. 1-46. A predicted torque density of 107.4 Nm/L was obtained with a gear ratio of 9. The outer radius was 120 mm.
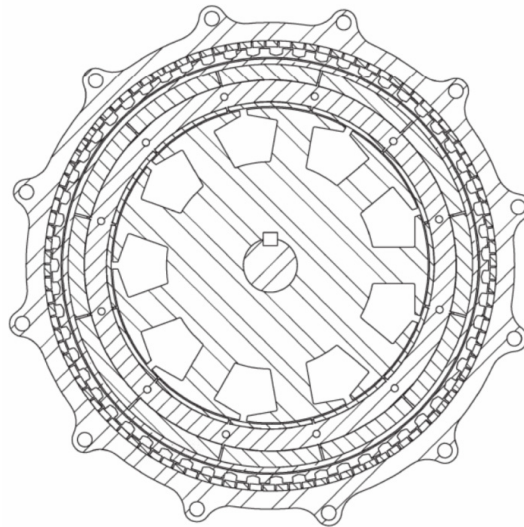
Fig. 1-45. A motor integrated CMG proposed by Rasmussen with $p_1 = 6$, $n_2 = 59$ and $p_3 = 53$ [56].
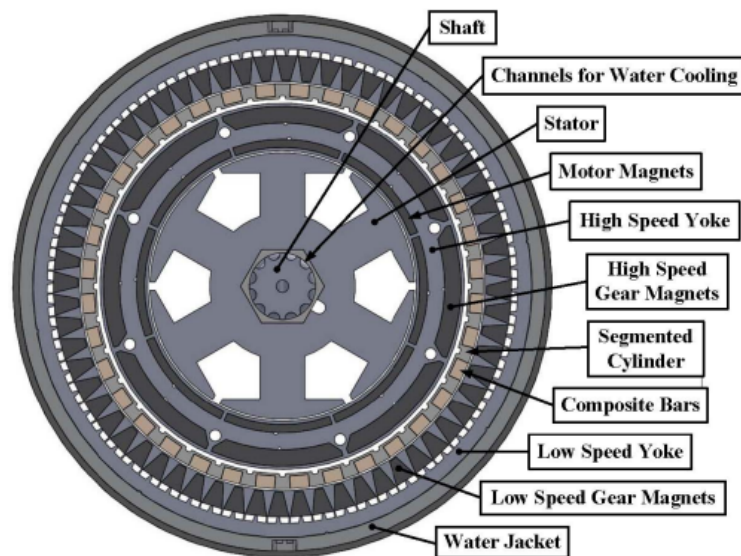
Fig. 1-46. An improved motor integrated CMG proposed by Frandsen with $p_1 = 4$, $n_2 = 36$ and $p_3 = 32$ [57].

Gerber demonstrated a magnetically geared permanent magnet machine with a gear ratio of 9.5 in [58]. Fig. 1-47 shows the inner-stator machine which had a calculated torque density of 73.5 Nm/L. The outer radius was 70 mm.
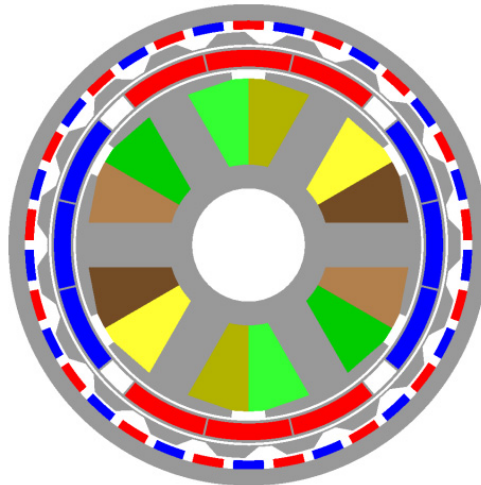
Fig. 1-47. A magnetically geared PM machine proposed by Gerber with $p_1 = 2$, $n_2 = 19$ and $p_3 = 17$ [58].

A summary of published single stage experimentally verified MGs with different gear ratios and volume torque densities is given in Fig. 1-48. For the dual stage MGs, the highest reported torque density is 75 Nm/L with a gear ratio of 360 [21]. Table 1-I summarizes the performances of the previous MGs.
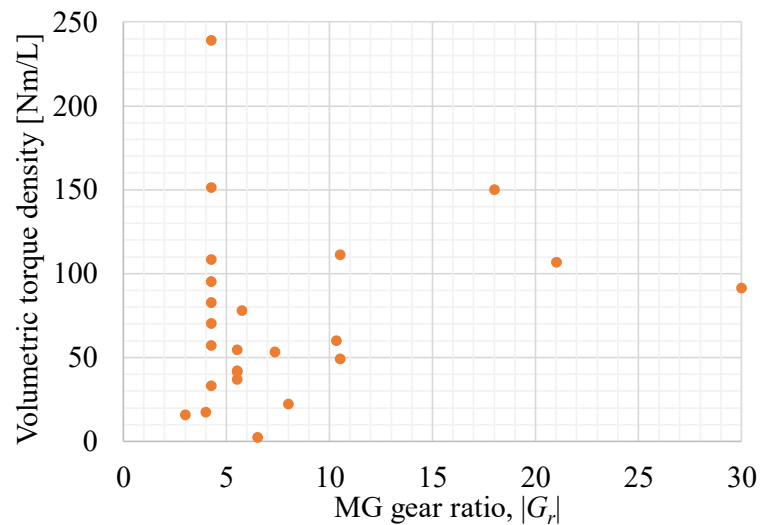
Fig. 1-48. Experimental verified MGs with different gear ratios and torque densities.

Table 1-I. SUMMARY OF MGS WITH DIFFERENT GEAR RATIO AND TORQUE DENSITY

Gear ratio	Outer radius [mm]	Measured torque density [Nm/L]	MG topology
4.25	114	239	Coxial
4.25	55	151.2	Coaxial
18	70	150	Cycloidal
10.5	57.5	111.2	Coaxial
4.25	107	108.3	Coaxial
21	61.5	106.8	Cycloidal
4.25	107	95.4	Coaxial
30	203.2	91.5	Cycloidal
4.25	57	82.8	Coaxial
5.75	70	77.9	Coaxial
4.25	56	70.2	Coaxial
10.33	85	60	Coaxial
4.25	100	57.2	Coaxial
5.5	60	54.5	Coaxial
7.33	110	53.3	Coaxial
10.5	57.5	49	Coaxial
5.5	60	42	Coaxial
5.5	65	41.6	Coaxial
5.5	45	36.9	Coaxial
4.25	55	33	Coaxial
8	-	22.4	Axial
4	100	17.6	Spur
3	47	16	Planetary
6.5	110.7	2.4	Hybrid

1.3. RESEARCH AIM

Though previous work has demonstrated either high gear ratio MGs or high torque density MGs, no MGs have been proposed to be capable of achieving both a high gear ratio and a high torque density. Potential research can be done to make improvements regarding torque density and gear ratio while also paying attention to assembly complexity. This research focuses on designing a multistage magnetic gearbox and magnetically geared generator with both a high gear ratio and a high torque density. In addition, this research develops analytical models of magnetic couplings in order to investigate the fundamental torque density limits of rotary magnetic devices.

1.4. DISSERTATION LAYOUT

Chapter 1: Introduction

This chapter gives a literature review of the previously published research on MGs. Different types of MGs are compared based on the torque density, gear ratio and outer radius.

Chapter 2: A Flux Focusing Cycloidal Magnetic Gear

The operating principle of a flux focusing cycloidal magnetic gear is discussed. Parameter sweeping is applied in order to achieve the peak torque density. Different designs for retaining the magnets in place were investigated for reducing the MG's mechanical assembly difficulty.

Chapter 3: A Nested Multistage Magnetic Gearbox

A multistage MG with a gear ratio of 59:1 was designed and is present. Six rotors are placed coaxially. The torque ripple has been studied and improved. The mechanical issues with such a design are highlighted.

Chapter 4: A Series Connected Multistage Magnetic Gearbox for Wind Turbine

In this chapter, two MGs are connected in series to obtain a gear ratio of 59:1. The two stages are put axially in series and therefore there will be no magnetic interaction between the two MG stages. The parameter sweeping analysis has been done to optimize the performance. The flux concentration topology has been chosen to improve the torque performance. The performance is tested and compared with FEA results.

Chapter 5: A Series Connected Multistage Magnetic Gearbox Generator for a Hydropower Application

In this chapter, a series connected multistage MG has been designed for a hydro application. The operating principle is the same as the MG discussed in chapter 4 and different structures have been evaluated with respect to the mechanical strength. The stator design has also been discussed and improved.

Chapter 6: An Analytical Based Model for the Axial Magnetic Coupling

A 3-D analytical model is developed when the surface and volume charge values are considered. There is a good agreement between the analytical model and the FEA model. The analytical based model is significantly faster and is useful for understanding the fundamental scaling relationship and limits for MGs.

Chapter 7: An Analytical Based Model for the Radial Magnetic Coupling

A 3-D analytical model of a radial magnetic coupling is developed. The results are compared with FEA calculations and a good agreement is reached. The performance of the axial and radial magnetic couplings is compared.

Chapter 8: Conclusions and Future Work

This chapter gives a summary of the research contributions and presents suggested future research.

Appendix A: An Alternative Charge Sheet Model for the Axial Magnetic Coupling

An analytical model is developed using the surface charge sheet model. The model

was developed and did not consider the volume charge prior to the model in Chapter 6. This model is only accurate for some of the geometry parameters. An improved model is discussed in Chapter 6.

CHAPTER 2 : A FLUX FOCUSING CYCLOIDAL MAGNETIC GEAR

2.1. BACKGROUND

There are many applications in which a high gear ratio, greater than 20:1, is required. For instance, in factory robots with a gear ratio of 60 or greater is often used and in large wind turbines a 90:1 gearbox is often used. Ships often rely on a large gear ratio gearbox to drive their main propeller.

This chapter investigates the potential for creating a high gear ratio magnetic gearbox by using a cycloidal motion rotor. The performance of a -25:1 gear ratio cycloidal magnetic gearbox with a new type of flux-focusing rotor topology will be investigated. The performance of the cycloidal magnetic gearbox is investigated by conducting an iterative parameter sweep analysis. Very little research has been published which looks at the capabilities of the cycloidal MG.

The purpose of this chapter is to demonstrate that a cycloidal MG is capable of achieving a volumetric torque density greater than 200 Nm/L while also operating with a high gear ratio.

2.2. A FLUX FOCUSING CYCLOIDAL MAGNETIC GEAR

The flux-focusing cycloidal MG under investigation is shown in Fig. 2-1 which has a gear ratio of -25:1. Unlike previously published cycloidal MG designs [20-22] the magnets are azimuthally magnetized and steel poles are placed between each magnet. The flux-focusing cycloidal MG consists of an eccentric inner rotor and a stationary outer rotor. In this design, the inner rotor has $p_A = 25$ pole pairs and the outer rotor has $p_C = 26$ pole pairs. The inner rotor has both a rotational motion, ω_A and an orbital motion, ω_B. For

the rotational motion, the inner rotor rotates along its center, while for the orbital motion, the inner rotor moves along an orbit with a fixed minimum air gap between the rotors which is $g = 0.5$ mm. When the inner rotor moves along the orbit for 2π in the clockwise direction, it will only rotate $-2\pi/25$ in the counter clockwise direction. The process of the movement is schematically demonstrated in Fig. 2-2 (a-i). With the outer rotor held stationary ($\omega_C = 0$), the gear ratio, G_r, can be calculated

$$G_r = \frac{p_A}{p_A - p_C} \tag{2.1}$$
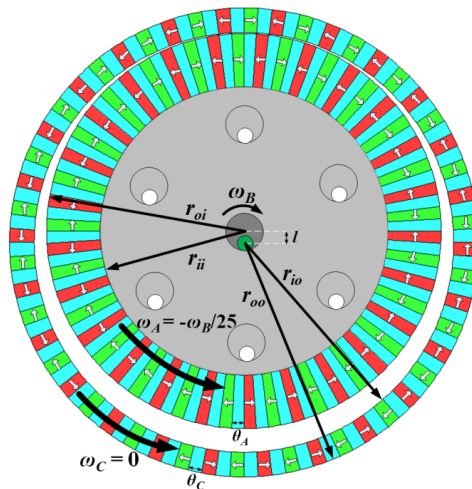
Fig. 2-1. Cross-sectional view of the flux focusing cycloidal magnetic gearbox.
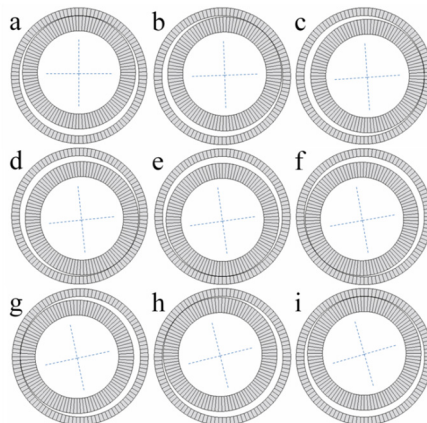
Fig. 2-2. The motion of a cycloidal gearbox [20].

2.3. PARAMETER SWEEP ANALYSIS

An iterative parameter sweep analysis has been used to investigate the performance capabilities of the flux focusing cycloidal MG topology. The fixed material and dimensional properties are shown in Table 2-I while the initial parameter sweep dimensions are shown in Table 2-II. An outer rotor radius r_{oo} = 114 mm has been chosen so that a direct comparison to the coaxial MG presented in [37] can be made. By looking at Fig. 2-1 it can be noted that $r_{oi}+g+l = r_{io}$ and therefore since r_{io} and r_{oi} are interrelated; there are only three "independent" variables which are inner radius of the inner rotor, r_{ii}, eccentricity distance, l and inner radius of the outer rotor, r_{io}. The iterative process shown in Fig. 2-3 has been used and T_{in} is the input torque.

Table 2-I. FIXED DIMENSIONS AND MATERIAL PROPERTIES

Description		Value	Unit
Inner rotor	Pole pairs, p_A	25	-
	Pole span, θ_A	$\pi/(2p_A)$	radians
Outer rotor	Outer radius, r_{oo}	114	mm
	Pole pairs, p_C	26	-
	Pole span, θ_C	$\pi/(2p_C)$	radians
Material	NdFeB magnet, NMX41SH, B_m	1.27	T
	1018 steel, resistivity	15.9	$\mu\Omega$-cm
	Magnet density, ρ_m	7.6	g/cm^3
	Steel density, ρ_s	7.85	g/cm^3
Minimum air gap, g		0.5	mm
Axial length, d		75	mm

Table 2-II. PARAMETER SWEEP DIMENSIONS

Description		Initial [mm]	Final [mm]
Inner rotor	Inner radius, r_{ii}	70	75
	Outer radius, r_{oi}	96	93.75
	Eccentricity distance, l	5.5	3.75
Outer rotor	Inner radius, r_{io}	102	98
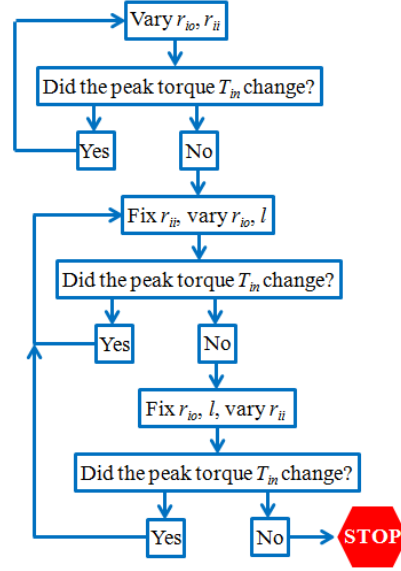
Fig. 2-3. The iterative process of the parameter sweeping.

Using JMAG's magnetostatic FEA solver, the volumetric torque density plot is obtained which is shown in Fig. 2-4. The volumetric torque density can be calculated from (1.1):

$$T_v = \frac{T_{in}}{\pi r_{oo}^2 d}$$

(2.2)

where T_{in} = input torque. In this plot both the inner radius of the outer rotor, r_{io}, and the inner radius of the inner rotor, r_{ii}, were changed whilst keeping all other dimensions fixed. Fig. 2-4 shows that there is a diminishing return when decreasing r_{ii} and the peak torque occurs when r_{io} = 102 mm. By holding r_{io} fixed Fig. 2-5 shows that there is a clear trade-off with respect to maximizing the active region volume and mass torque density. The active region mass torque density is calculated by

$$T_m = \frac{2T_{in}}{\pi\left[\left(r_{oo}^2 - r_{io}^2\right) + \left(r_{oi}^2 - r_{ii}^2\right)\right]\left(\rho_m + \rho_s\right)d}$$

(2.3)

where ρ_m and ρ_s are the material densities of the magnets and steels.

In this analysis r_{ii} = 70 mm has been chosen in order to maximize the volumetric torque density. This dimension gives a volumetric and mass torque density of 262 Nm/L and 64 Nm/kg, respectively.
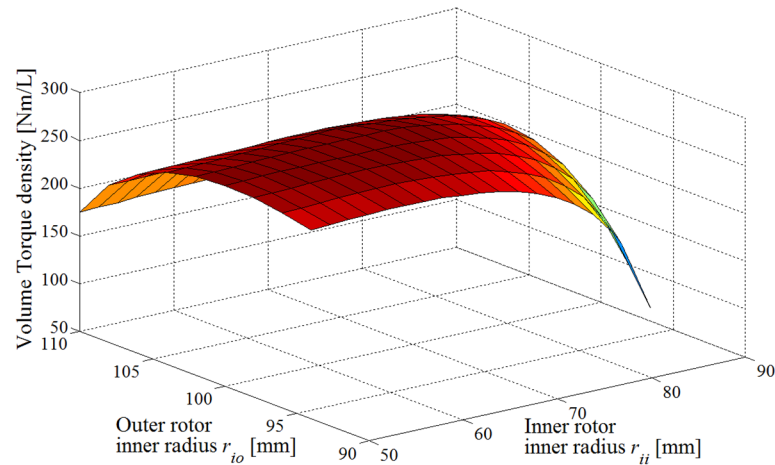
Fig. 2-4. 3-D volumetric torque density when the inner rotor inner radius, r_{ii} and outer rotor inner radius, r_{io}, are varied.
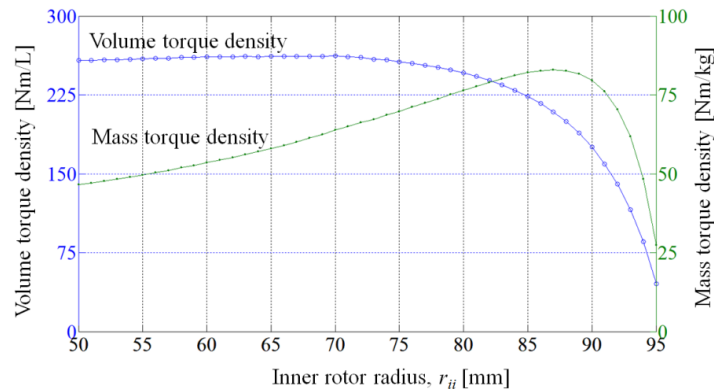
Fig. 2-5. Volume and mass torque density with different inner radii, r_{ii}.

The eccentricity distance l will also have a big impact on the torque density. Fig. 2-6 and Fig. 2-7 show how the volume and mass torque density change when varying both eccentricity distance l and inner radius of the outer rotor r_{io}. A peak torque occurs when

r_{io} = 98 mm and l = 3.75 mm. With r_{io} = 98 mm and l = 3.75 mm fixed, the inner radius

of the inner rotor r_{ii} was then again varied. The calculated volume and mass torque

density are shown in Fig. 2-8. The peak volume torque density occurs when r_{ii} = 70 mm

while the peak mass torque density occurs at r_{ii} = 84 mm. Most MG papers exclusively

look at maximizing the volumetric torque density, but Fig. 2-8 indicates that by minimize

volumetric size the active material mass will be higher than needed. In order to provide a

clearer comparison with prior-art work the volume torque density was chosen to be

maximized. Therefore, an inner radius value of r_{ii} = 75 mm was selected and this then

gave a volume torque density of 291 Nm/L. Selecting r_{ii} = 70 mm will give a slightly

higher volume torque density but this would result in an 8 % decrease in mass torque

density. Further iterations do not yield significant gains. The final selected dimensions

are shown in Table 2-II.
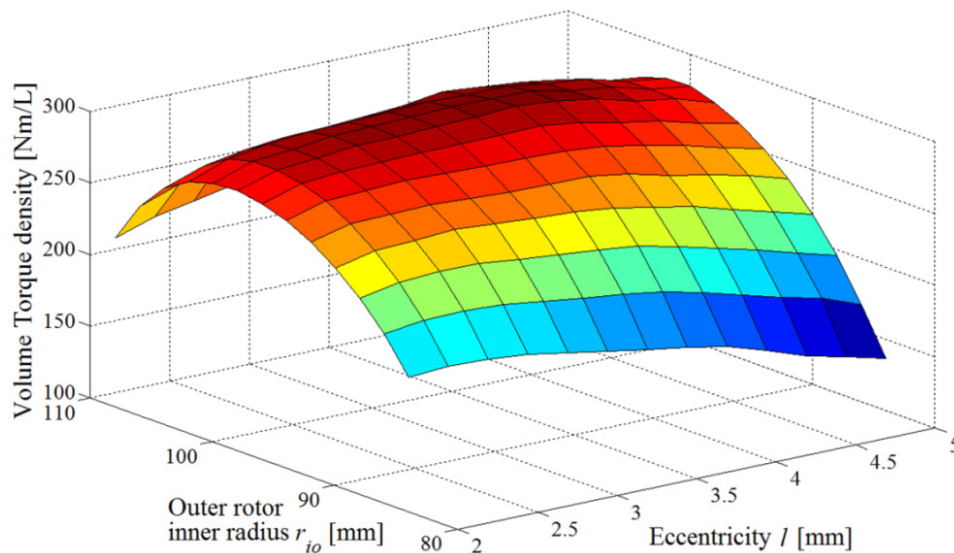
Fig. 2-6. Volume torque density when the inner radius of the outer rotor r_{io} and the eccentricity distance l are varied.
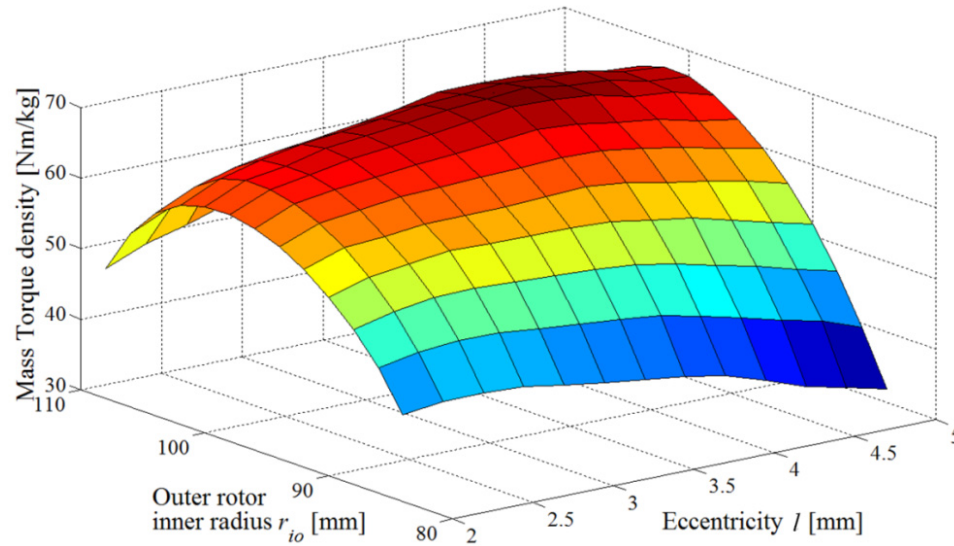
Fig. 2-7. Mass torque density when the inner radius of the outer rotor r_{io} and the eccentricity distance l are varied.
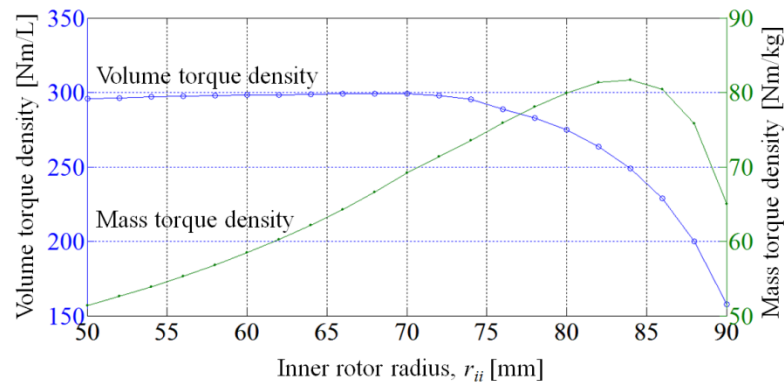
Fig. 2-8. Influence of inner rotor radius on the active region volume and mass torque density.

Using the dimensional parameters shown in Table 2-I and Table 2-II a 2-D transient FEA simulation was conducted using Infolytica MagNet. The simulation results for the torque on the inner rotor are shown in Fig. 2-9. The calculated torque ripple was 0.46 % and the efficiency when the input speed was ω_B = 20 RPM was calculated to be 99 %. The electrical efficiency is high due to the low input speed and the high segmentation of the magnets and steel. A comparison between the flux focusing cycloidal MG and a flux

focusing coaxial MG with the same volumetric dimensions is shown in Table 2-III [23]. The results presented indicate that the flux focusing cycloidal MG is highly competitive. Table 2-III also shows the calculated torque density (after conducting a parameter sweep analysis) for a surface mounted magnet cycloidal MG. It can be noted that the flux focusing topology outperforms the surface mounted design.

Table 2-III. COMPARISON BETWEEN FLUX FOCUSING COAXIAL AND CYCLOIDAL MAGNETIC GEARBOXES

Parameter	Flux focusing cycloidal MG	FFCMG [37]	Surfacemounted cycloidal MG	Units
Volume torque density	291	239	179	Nm/L
Mass torque density	75	35	47	Nm/kg
Efficiency @ 20 RPM	99	96	-	%
Torque ripple @ peak torque	0.46	0.3	-	%
Gear ratio	-25	4.25	-25	-
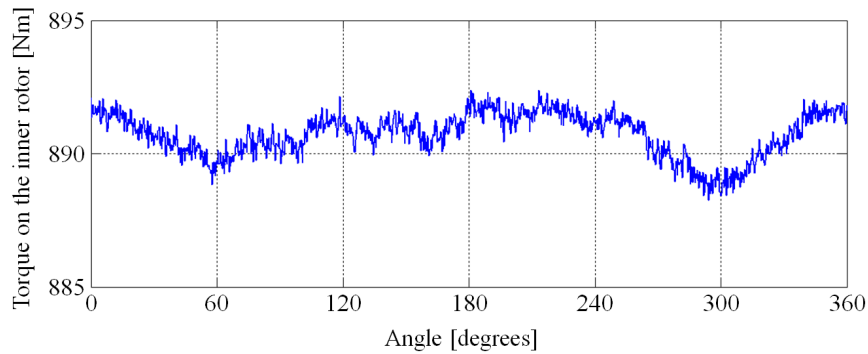
Fig. 2-9. Torque on inner rotor when flux focusing cycloidal MG has both an orbital and rotational motion. The input speed used in this simulation is 20 RPM.

It must be noted that the cycloidal MGs operation relies on the use of a non-uniform air gap and this results in a large non-uniform radial force distribution. The air gap radial force density, f_r, in the flux focusing cycloidal MG can be computed using Maxwell's stress tensor [59]

$$f_r = \frac{1}{2\mu_0}(B_r^2 - B_\theta^2) \qquad (2.4)$$

where B_r = radial component of magnetic flux density and B_θ = azimuthal component of magnetic flux density.

When this force distribution is plotted as a function of angular position, it can be seen from Fig. 2-10 that the flux focusing cycloidal MG creates a highly unsymmetrical radial force distribution. This will create increased stress on the mechanical bearings. Therefore, although the torque production is non-contact, mechanical design approaches need to be considered that balance out these force pulsations otherwise the bearing life expectancy will be degraded. This non-symmetric radial force is not present in the CMG topology and therefore this is one of the primary challenges that needs to be resolved before the cycloidal MG can be seen to be competitive with the CMG. One possibility is to cancel the forces by using an axial cycloidal MG topology [24]. However, the axial cycloidal MG is challenging to design due to the difficulty in mechanically maintaining a small axial air gap.
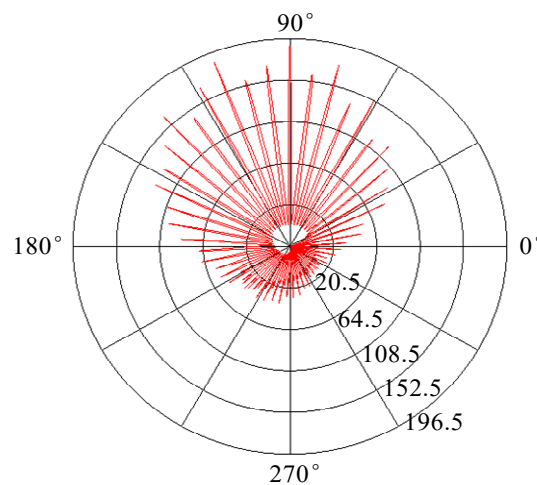
Fig. 2-10. Radial force density distribution [N/cm^2].

2.4. HARMONIC ANALYSIS

Using the final dimensions an air gap harmonic analysis was conducted. Fig. 2-11 shows the radial flux density, B_r, and the corresponding spatial harmonic in the air gap when both rotors were present. Because of the number of pole pairs for the magnets, the 25th harmonic and the 26th harmonic are dominant. Fig. 2-12 shows the flux density and the corresponding spatial harmonic when the magnets of the outer rotor were not present. It can be seen that a 26th harmonics is still present. This demonstrates how the non-uniform air gap creates the additional harmonics needed for the angular speed change.

(a)

(b)
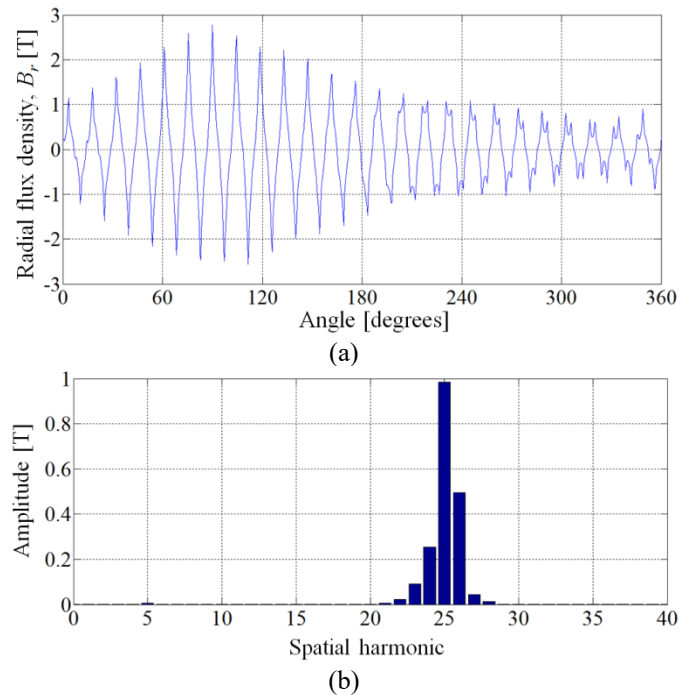
Fig. 2-11. (a) Flux density in the air-gap at $r = 94$ mm when both rotors are present and (b) the corresponding spatial harmonic.
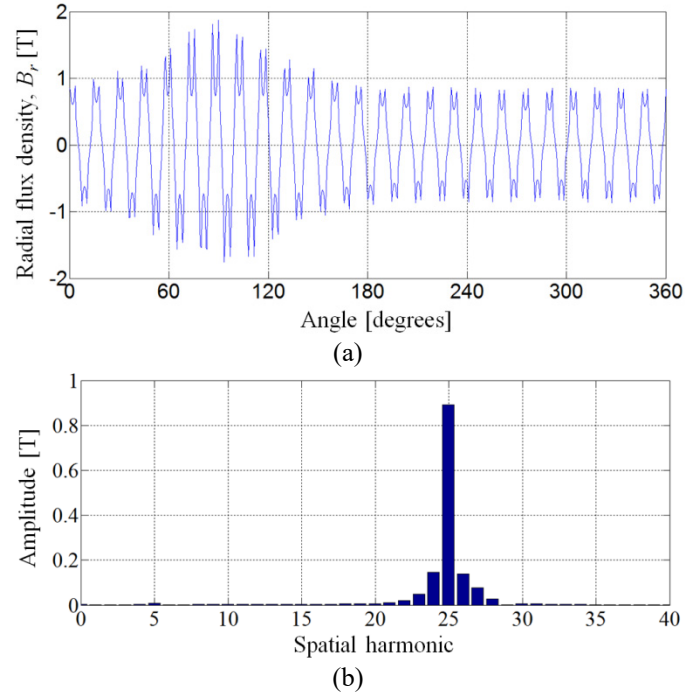
Fig. 2-12. (a) Flux density in the air-gap when the magnets of the outer rotor are not present and (b) the corresponding spatial harmonic.

2.5. MAGNET RETAINING DESIGNS

In order to fabricate a cycloidal MG, magnet retaining lips need to be added so as to hold the magnets in place. However, by adding the lips the performance of the MG will be degraded. Different magnet retaining topologies were designed and compared for the cycloidal MG. The results are shown in Table 2-IV. The original design which had no retaining lips had a peak torque of 892 Nm. Design XII was chosen for the final design as it would give a relative high torque and was easier to construct. The inner magnets are prevented from moving radially outwards by the taper while the outer rotor magnets can be held in place with an outer retaining non-magnetic plate.

Table 2-IV. Different Magnet RetainingTopologies

I (Original)	II	III
892 Nm	673 Nm	788 Nm
IV	V	VI
780 Nm	853 Nm	755 Nm
VII	VIII	IX
834 Nm	624 Nm	774 Nm
X	XI	XII
807 Nm	782 Nm	850 Nm
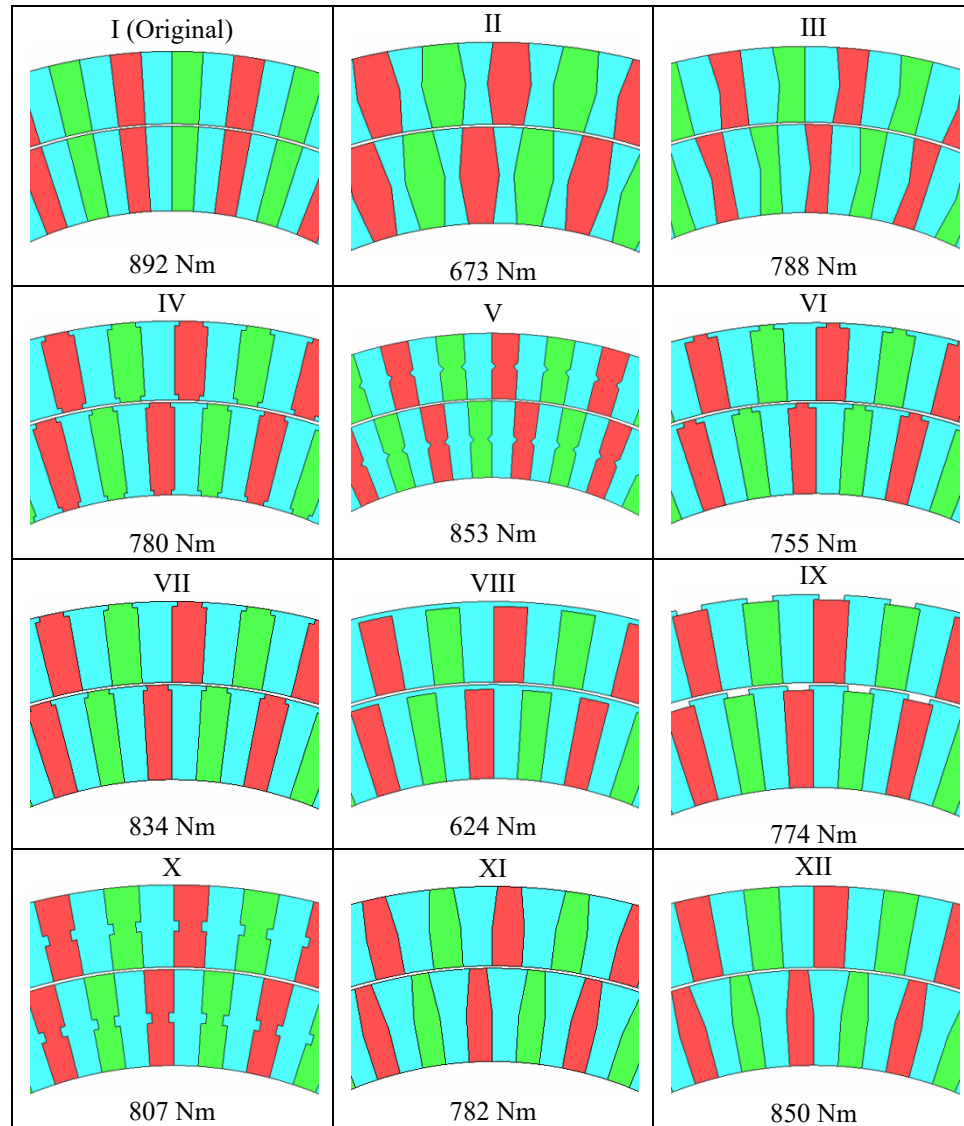
However, the steel poles will be too thin to add steel skews for above designs. Therefore, the gear ratio was reduced to -20:1 to increase the sizes of the steel pole pieces. Fig. 2-13 shows the final design for the flux focusing cycloidal MG with -20:1 gear ratio. The final dimensions are shown in TABLE 2-V. The torque is shown in Fig. 2-14 which is obtained from the JMAG FEA model. The peak torque of the inner rotor is 795 Nm which gives a volume torque density of 260 Nm/L.
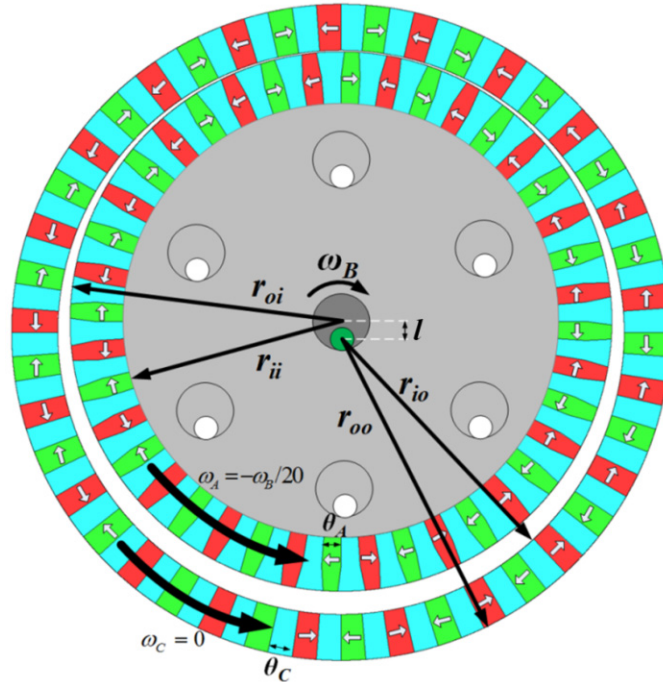
Fig. 2-13. Cross-sectional view of the flux focusing cycloidal magnetic gearbox with lips.

TABLE 2-V. DIMENSIONS AND MATERIAL PROPERTIES

Description		Value	Unit
Inner rotor	Inner radius, r_{ii}	75	mm
	Outer radius, r_{oi}	93.75	mm
	Pole pairs, p_A	20	-
	Pole span, θ_A	$\pi/(2p_A)$	radians
Outer rotor	Inner radius, r_{io}	98	mm
	Outer radius, r_{oo}	114	mm
	Pole pairs, p_C	21	-
	Pole span, θ_C	$\pi/(2p_C)$	radians
Materials	NdFeB magnet, NMX41SH, B_m	1.27	T
	1018 steel, resistivity	15.9	$\mu\Omega$-cm
Eccentricity distance, l		3.75	mm
Minimum air gap, g		0.5	mm
Axial length, d		75	mm
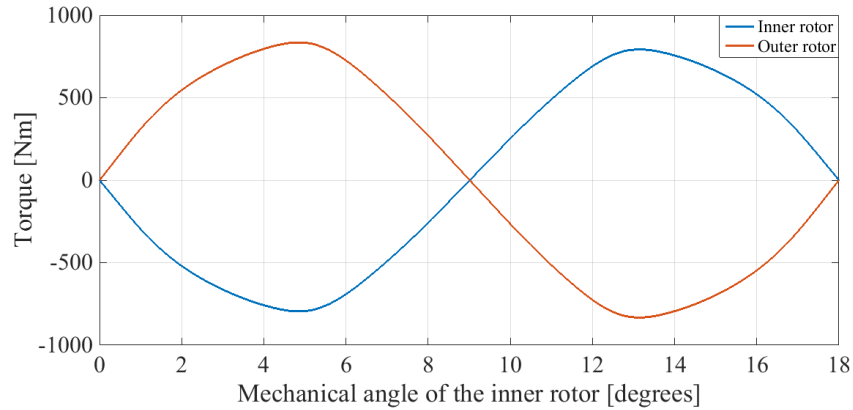
Fig. 2-14. Torque on the inner and outer rotors.

The mechanical assembly is shown in Fig. 2-15 and the inner rotor of the cycloidal gearbox is shown in Fig. 2-16. The inner rotor had two parts and each of them had an axial length of 37.5 mm. The position of the minimum air gap for the two inner rotors was shifted by 180 degrees so that the radial force could be evened out. Due to significant mechanical issues with regard to maintaining the cycloidal motion, this design was discontinued and focus was placed on developing a multistage MG approach which would be able to achieve an even higher gear ratio.
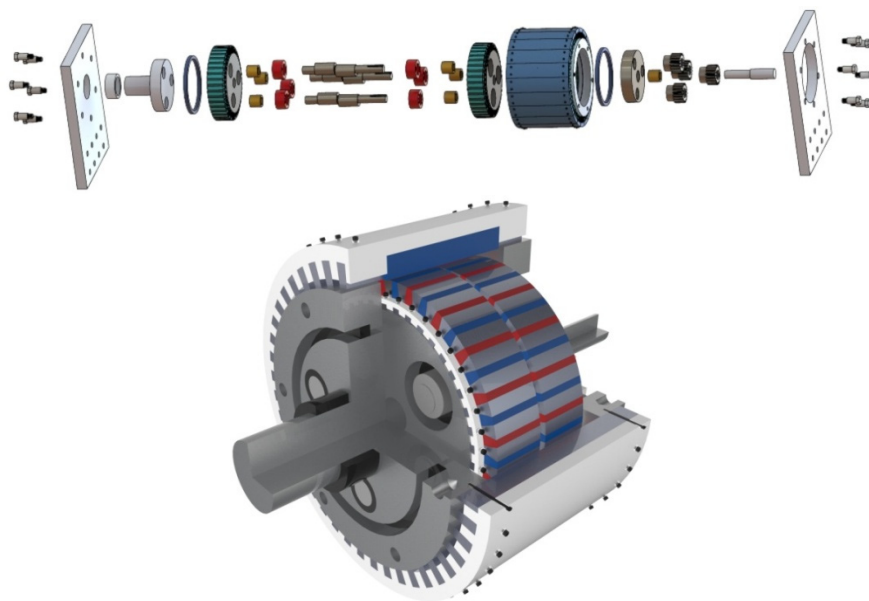
Fig. 2-15. Experimental prototype [figure from Joshua Kadel].

<center>(a)   (b)</center>
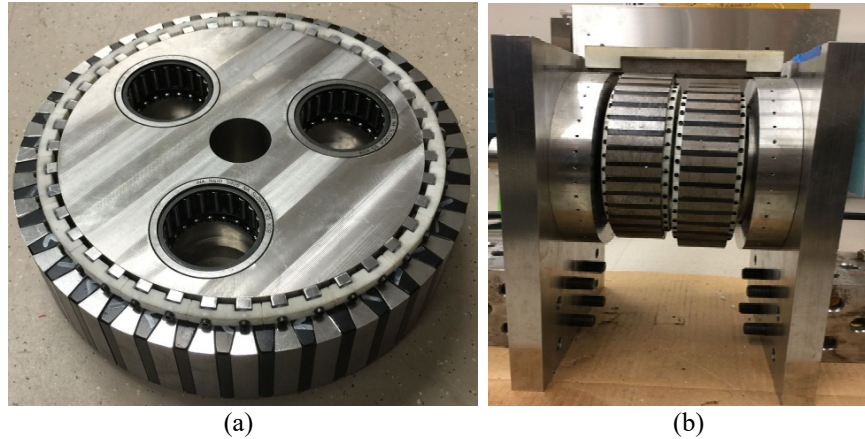
Fig. 2-16. (a) One inner rotor assembled and (b) both of the inner rotors assembled.

2.6. CONCLUSION

A flux focusing cycloidal MG design has been presented that was calculated to be capable of operating at a peak volumetric torque density of 291 Nm/L and a high gear ratio of -25:1. The torque ripple is only 0.46 %. However, in order to operate, the flux focusing cycloidal MG must have a non-uniform air gap and it has been shown that this will result in large non-symmetric radial forces. An experimental prototype with a gear ratio of -20:1 has been designed and the inner rotor has been assembled. This design has been calculated using 2-D FEA to have a peak torque and torque density of 795 Nm and 260 Nm/L, respectively. This design was not able to be tested because of unsolved mechanical assembly issues.

CHAPTER 3 : A NESTED MULTISTAGE MAGNETIC GEARBOX

3.1. OPERATING PRINCIPLE

In this chapter, a nested multistage magnetic gear (MSMG) has been designed which has a gear ratio of 59:1. The design of the MSMG is shown in Fig. 3-1. Rotor 3 and rotor 4 are the coupling rotors which have the same speed. The MSMG is being designed to have a 59:1 gear ratio so that the performance of the MSMG can be directly compared with a 59:1 Sumitomo mechanical cycloidal gearbox which is shown in Fig. 3-2.

Rotor 1: p_1 pole pairs
Rotor 2: n_2 steel poles
Rotor 3: p_3 pole pairs
Rotor 4: p_4 pole pairs
Rotor 5: n_5 steel poles
Rotor 6: p_6 pole pairs
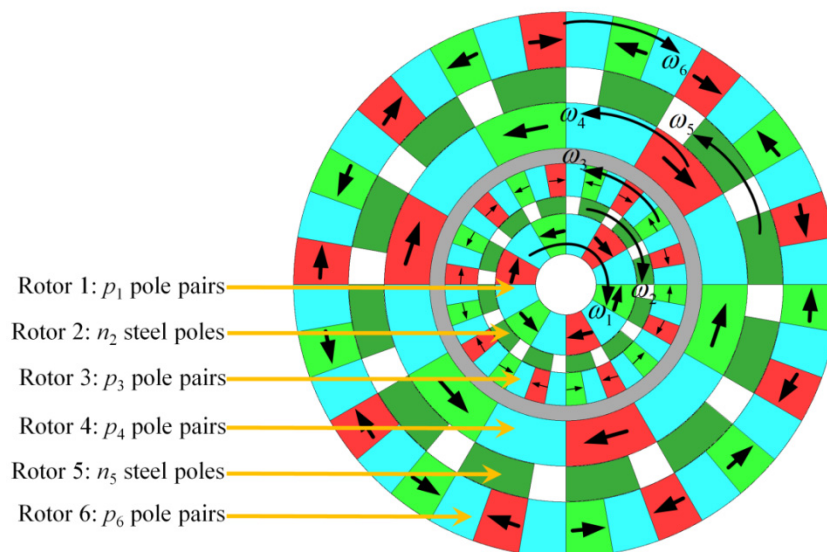
Fig. 3-1. A nested multi-stage MG.
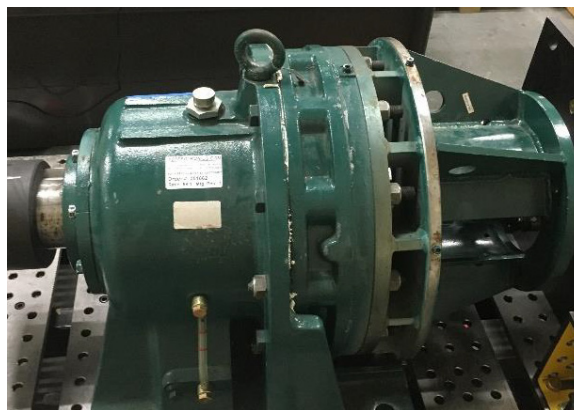
Fig. 3-2. Sumitomo cyclo inline 59:1 ratio mechanical gearbox reducer model CHHJ-4225Y-59-320TC.

The pole pairs of the three inner rotors are related by (1.6) while the pole pairs of the three outer rotors have to satisfy the condition

$$n_5 = p_4 + p_6 \tag{3.1}$$

The three inner rotors (rotor 1, 2 and 3) are governed by (1.5) while the three outer rotors (rotor 4, 5 and 6) are related by

$$p_4\omega_4 = n_5\omega_5 - p_6\omega_6 \tag{3.2}$$

where the speed terms are shown in Fig. 3-1. Rotor 3 and rotor 4 are connected together which means $\omega_4 = \omega_3$. Then equation (3.2) can be substituted into (1.5) to get

$$\omega_1 = \frac{n_2}{p_1}\omega_2 - \frac{p_3}{p_1}\frac{n_5}{p_4}\omega_5 + \frac{p_3}{p_1}\frac{n_6}{p_4}\omega_6 \tag{3.3}$$

In this design rotor 2 and rotor 6 are held as a stationary part ($\omega_6 = \omega_2 = 0$) and so (3.3) simplifies to

$$\omega_1 = -\left(\frac{p_3 n_5}{p_1 p_4}\right)\omega_5 \tag{3.4}$$

Therefore, the overall gear ratio is

$$G_r = -\left(\frac{p_3 n_5}{p_1 p_4}\right) \tag{3.5}$$

Neglecting losses the general power flow relationship is then

$$T_1\omega_1 + T_2\omega_2 + T_3\omega_3 + T_4\omega_4 + T_5\omega_5 + T_6\omega_6 = 0 \tag{3.6}$$

where T_i is the torque on rotor i (i = 1, 2, 3, 4, 5, 6).

With $\omega_6 = \omega_2 = 0$ and $\omega_4 = \omega_3$ equation (3.6) simplifies down to

$$T_1\omega_1 + (T_3 + T_4)\omega_4 + T_5\omega_5 = 0 \tag{3.7}$$

The coupling rotor will freely rotate (it has no shaft) and therefore no power can come in/out of the coupling rotor. The torque on the coupling rotor must be zero. Therefore, with $T_3+T_4 = 0$ the power flow equation simplifies down to

$$T_1\omega_1 + T_5\omega_5 = 0 \tag{3.8}$$

The torque relationship between all the rotors at equilibrium is then

$$T_1 + T_2 + T_5 + T_6 = 0 \tag{3.9}$$

3.2. DESIGN ANALYSIS

The material properties used in the MSMG are shown in Table 3-I.

Table 3-I. MATERIAL PROPERTIES FOR THE MSMG

Description	Value	Units
Remnant flux density, B_m	1.28	T
416 steel (cage rotor), resistivity	57.0	$\mu\Omega$-cm
1018 steel (inner/middle/outer rotors), resistivity	15.9	$\mu\Omega$-cm
Magnet density, ρ_m	7.6	g/cm^3
Steel density, ρ_s	7.85	g/cm^3

The active region mass torque density on the outer-stage MG, T_{mo}, is assessed by computing

$$T_{mo} = 2T_5 / \{[(\rho_m + \rho_s)][(r_{o6}^2 - r_{i6}^2) + (r_{o4}^2 - r_{i4}^2)] + (r_{o5}^2 - r_{i5}^2)\rho_s n_5 / p_6]\pi d_{out}\} \quad (3.10)$$

where the radii shown in (3.10) are defined in Table 3-II.

Table 3-II. DEFINITION OF THE RADII

Radius [mm]	Description
r_{i4}	The inner radius of rotor 4.
r_{o4}	The outer radius of rotor 4.
r_{i5}	The inner radius of rotor 5.
r_{o5}	The outer radius of rotor 5.
r_{i6}	The inner radius of rotor 6.
r_{o6}	The outer radius of rotor 6.

The outer stage volumetric torque density is computed from

$$T_{vo} = T_5 / (\pi r_{o6}^2 d_{out}) \quad (3.11)$$

where d_{out} = outer stage MG stack length.

The active region mass torque density on the inner-stage MG, T_{mi}, is assessed by computing

$$T_{mi} = 2T_3 / \{[(\rho_m + \rho_s)][(r_{o3}^2 - r_{i3}^2) + (r_{o1}^2 - r_{i1}^2)] + (r_{o2}^2 - r_{i2}^2)\rho_s n_2 / p_3]\pi d_{in}\} \quad (3.12)$$

where the radii shown in (3.12) are defined in Table 3-III.

Table 3-III. DEFINITION OF THE RADII

Radius [mm]	Description
r_{i1}	The inner radius of rotor 1.
r_{o1}	The outer radius of rotor 1.
r_{i2}	The inner radius of rotor 2.
r_{o2}	The outer radius of rotor 2.
r_{i3}	The inner radius of rotor 3.
r_{o3}	The outer radius of rotor 3.

The outer stage volumetric torque density is computed from

$$T_{vi} = T_2 / (\pi r_{o3}^2 d_{in})$$ (3.13)

where d_{in} = inner stage MG stack length.

The torque ripple on rotor 1 is mainly due to the interaction between the inner stage and the outer stage. Rotor 4, which is the closest rotor to the inner stage, plays an important role in the torque ripple. In order to study the torque ripple further, the pole combination for the inner stage was selected as $p_1 = 5$, $n_2 = 53$, $p_3 = 48$ and torque ripple on rotor 1 was simulated in JMAG with different pole pairs on rotor 4. Only the inner stage and rotor 4 were present and the results are shown in Table 3-IV.

Table 3-IV. TORQUE RIPPLE ON ROTOR 1

p_4	10	11	12	13
Torque ripple	33%	11%	16%	4%

From Table 3-IV, it can be seen that the lowest torque ripple occurs when $p_4 = 13$. n_5 and p_6 were chosen to be 80 and 67and the corresponding gear ratio G_r was 59.08. The design with final choice of pole pairs is shown in Fig. 3-3. The parameters for that design are shown in Table 3-V. The torque plots are shown in Fig. 3-4 and Fig. 3-5.

Outer stage

Rotor 6: 67 pole pairs

Rotor 5: 80 pole pairs

Rotor 4: 13 pole pairs

Inner stage

Rotor 3: 48 pole pairs

Rotor 2: 53 pole pairs

Rotor 1: 5 pole pairs
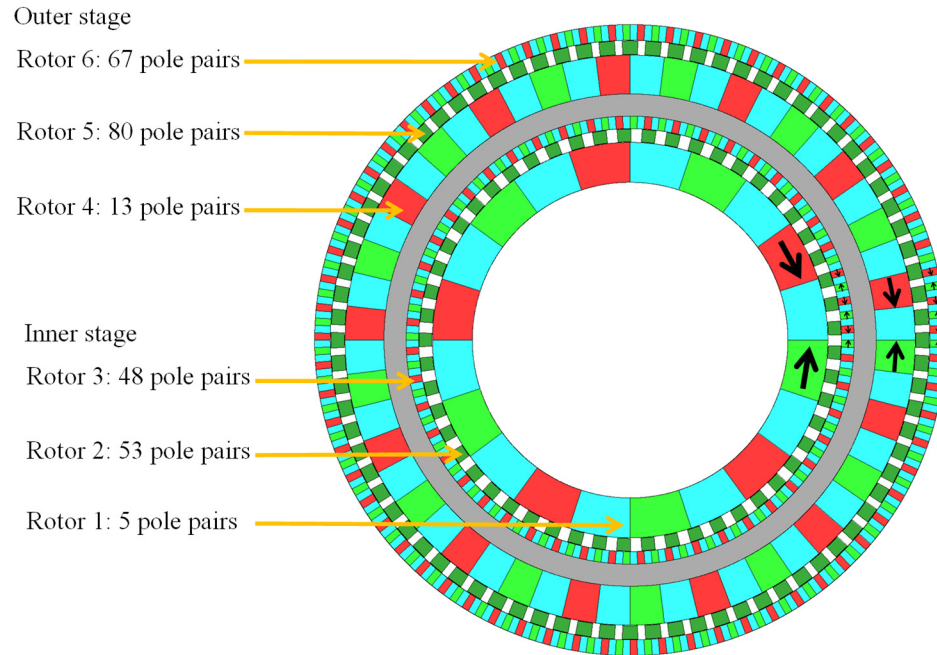
Fig. 3-3. Geometry of the final design VI of the nested MSMG with a gear ratio of 59:1.
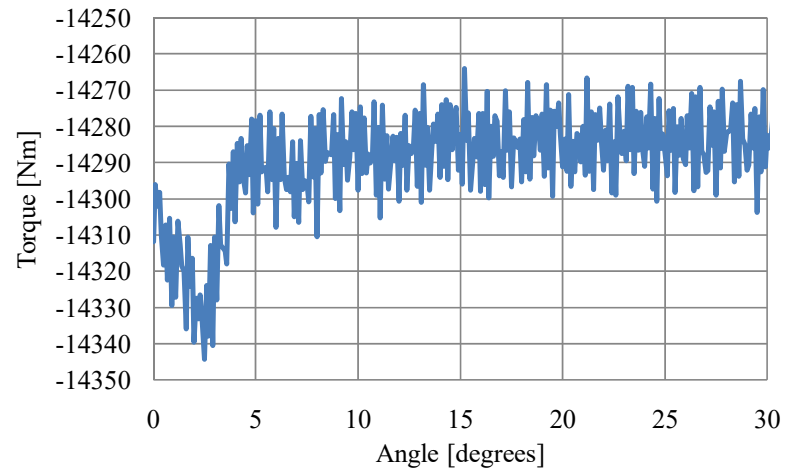
Fig. 3-4. Torque as a function of angle for low-speed input rotor 5.
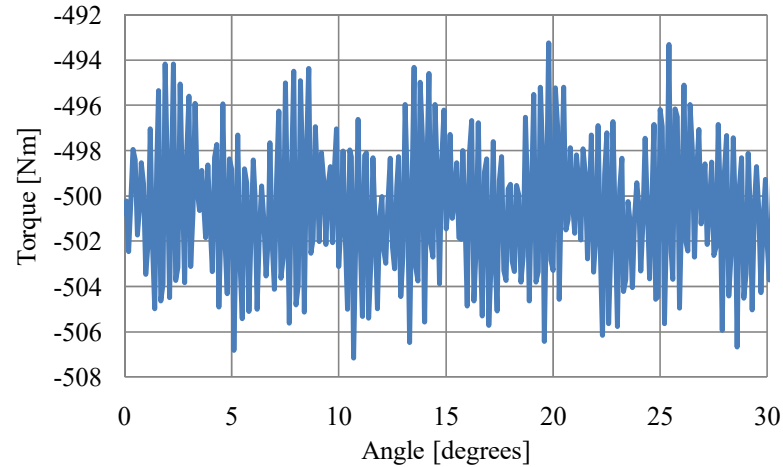
Fig. 3-5. Torque as a function of angle for high-speed output rotor 1.

Table 3-V. PARAMETERS FOR THE DESIGN WITH FINAL CHOICE OF POLE PAIRS

Description	Outer stage			Inner stage			Units
	Outer rotor	Cage rotor	Inner rotor	Outer rotor	Cage rotor	Inner rotor	
Rotor number, n	6	5	4	3	2	1	-
Pole pair number	67	80	13	48	53	5	-
Outer radius, r_{on}	300	284.5	271	213	200.5	188	mm
Inner radius, r_{in}	285	271.5	234	201	188.5	150	mm
Axial length, d	114	114	114	114	114	114	mm

The simulated torque ripple for the MSMG design shown in Fig. 3-5 was still considered too high. Therefore, a range of different geometries were considered to reduce the torque ripple further. Design VI is the original design. Design VII and VIII add air regions between the inner and outer stages. Design IX-XIII adds more magnets to make the rotors to be Halbach magnetized. Therefore, less flux from rotor 4 will interact with the inner stage. Design XIII shows the final design with magnet retaining lips and back irons. This design was chosen because it gave the lowest torque ripple and a relatively high torque density. Both rotor 3 and rotor 4 use the flux concentration topology so that more magnetic flux will be created in the air gap and a higher torque can be obtained.

Table 3-VI. Different Designs to Reduce Torque Ripple

VI	VII
VIII	IX
X	XI
XII	XIII
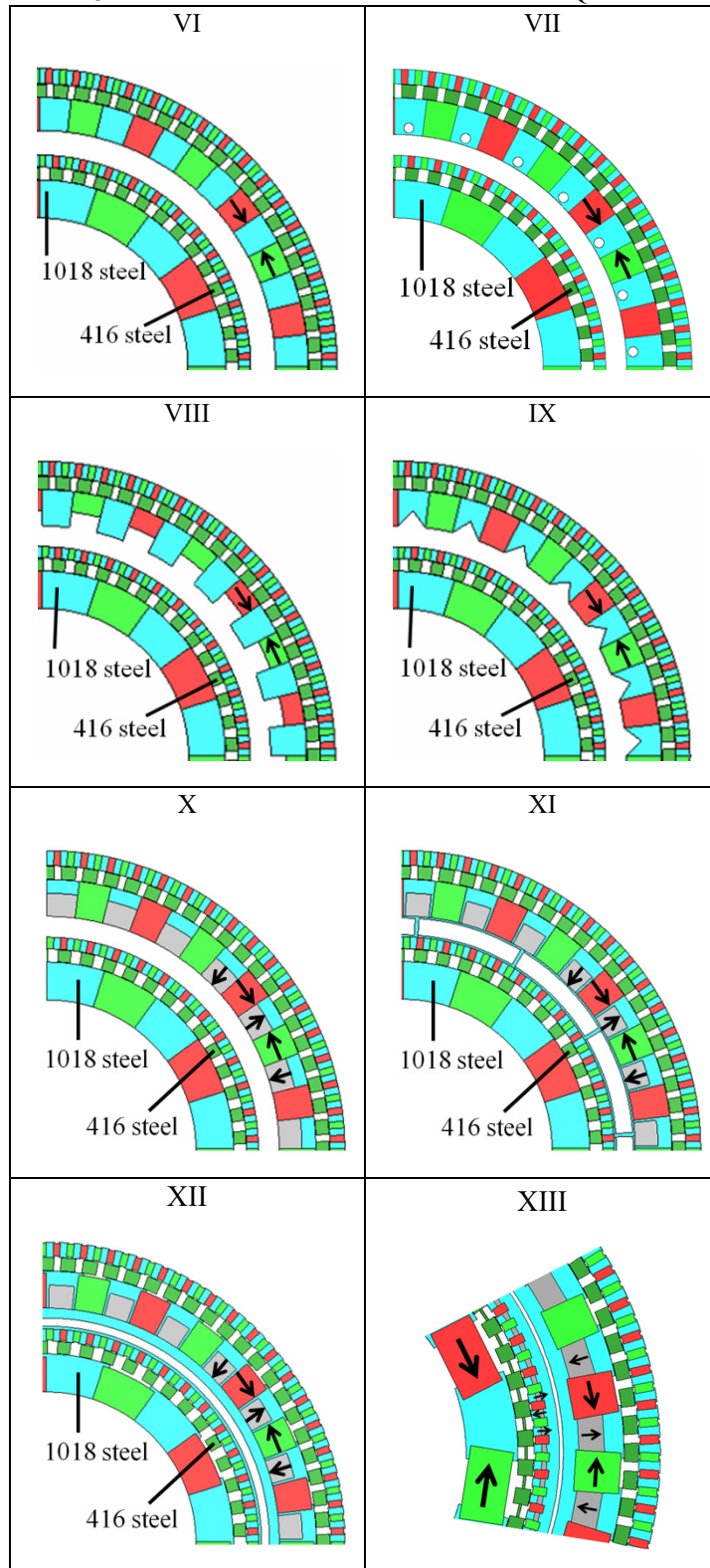
The results for the designs in Table 3-VI are shown in Table 3-VII. The final design with magnet retaining lips is shown in Fig. 3-6. To maintain the torque above 10 kNm and also to reduce total weight and volume, the axial length of the MSMG was reduced from 114 mm to 95 mm. The torque plots are shown in Fig. 3-7 and the field lines of this flux concentration MSMG is shown in Fig. 3-8.

Table 3-VII. PERFORMANCE OF DIFFERENT DESIGNS.

Design VI	Design VII	Design VIII	Design IX	Design X	Design XI	Design XII	Design XIII
Peak torque [kNm]							
14.3	14.3	14.7	14.5	16.6	15.6	12.8	13.7
Torque density [Nm/L]							
443	443	456	451	514	483	397	424
Torque ripple on rotor 1 [%]							
2.8	2.7	2.3	2.5	1.3	9.8	2.8	1.1
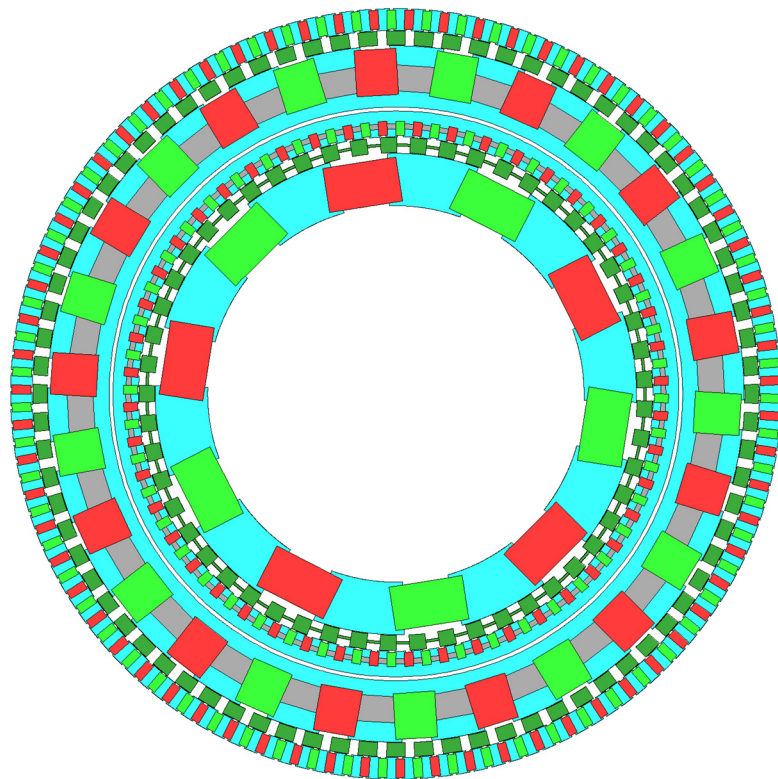
Fig. 3-6. Final design of the nested MSMG.
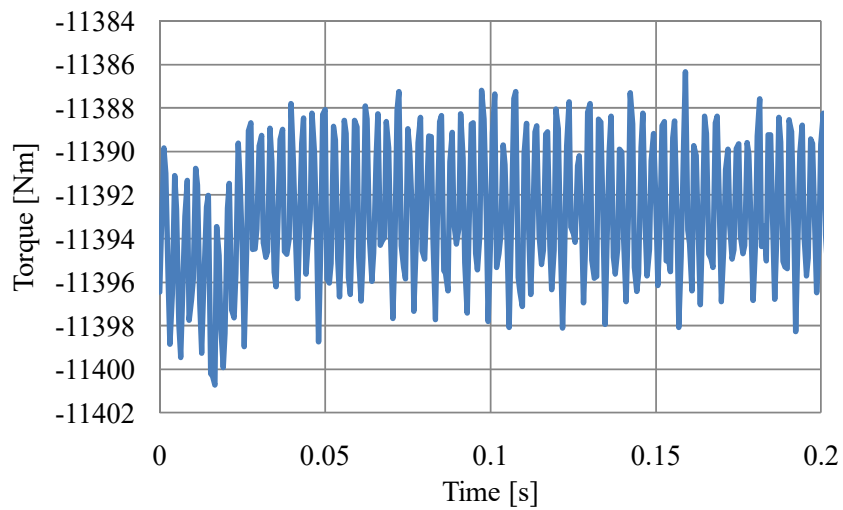
(a)
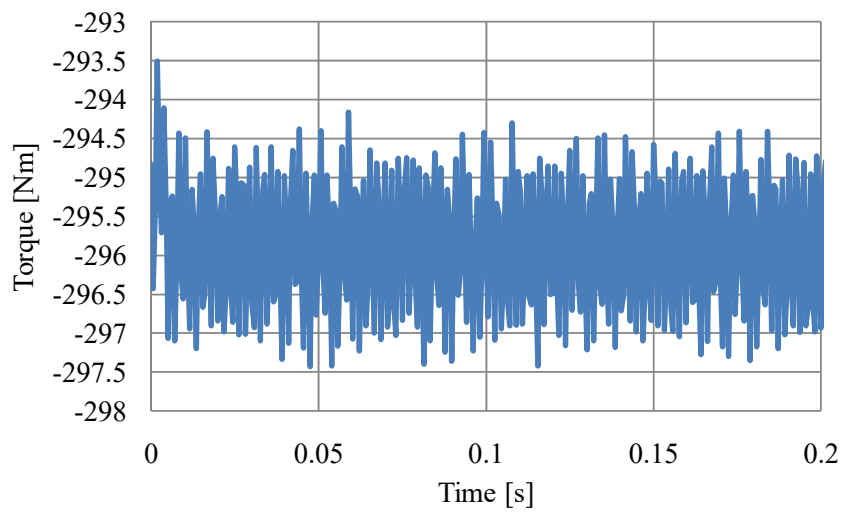
(b)

Fig. 3-7. Torque as a function of time on (a) low speed input rotor 5 and (b) high speed output rotor 1 with an axial length of 95 mm.
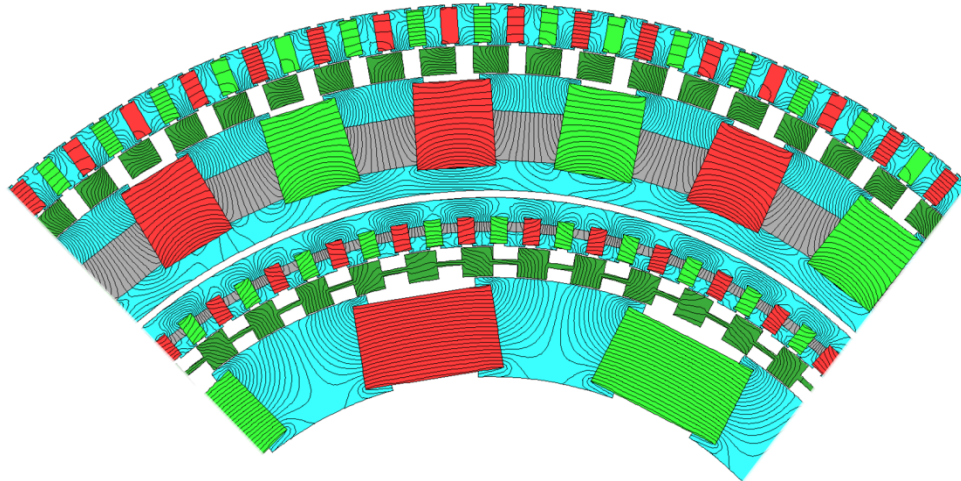
Fig. 3-8. Magnetic flux lines of the MSMG.

The mechanical design of this nested MSMG is shown in Fig. 3-9. However, this work was not continued because the mechanical structure needed to support the 6 rotors as well as to add space for an inner stator. This would make the axial length very large as shown in Fig. 3-9. Furthermore, the nesting of the two gear stages would make the assembly and disassembly process very difficult. For these reasons, the series connected MSMG was studied.
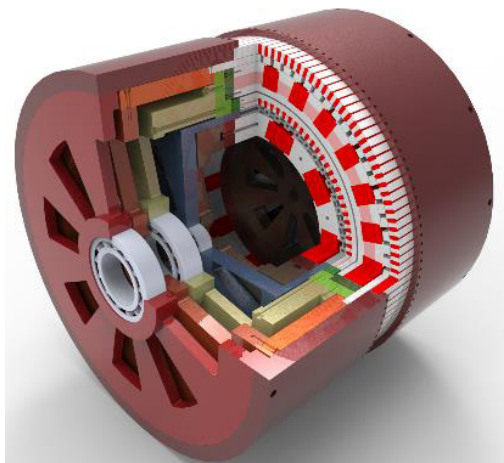
Fig. 3-9. Mechanical design for the nested MSMG [figure from Sina Modaresahmadi].

3.3. CONCLUSION

This chapter provides a summary of the 2-D FEA design analysis approach for a high gear ratio MSMG (59:1) with a peak torque capability greater than 10 kNm. Different designs have been simulated to reduce the torque ripple. The volumetric torque density has been calculated to be 424 Nm/L with a low torque ripple after optimization. However, this design was not constructed because it would be extremely difficult to assemble.

CHAPTER 4 : A SERIES CONNECTED MULTISTAGE MAGNETIC GEARBOX FOR
WIND TURBINE

4.1. OPERATING PRINCIPLE

In this chapter, a two-stage series connected MSMG is investigated. Stage 1 MG is connected to the high-torque low-speed input and stage 2 MG is connected to the low-torque high-speed output. This is shown in Fig. 4-1.
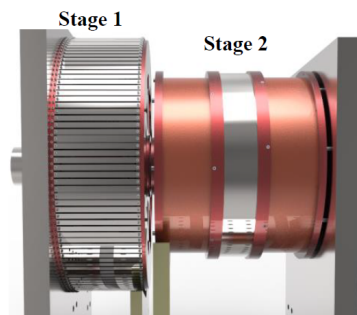
Fig. 4-1. Stage 1 is connected to the high-torque low-speed input and stage 2 is connected to the low-torque high-speed output [figure from Sina Modaresahmadi].

The gear ratio of a MG can be increased by connecting the two gearboxes in series as illustrated in Fig. 4-1. In this analysis, both stage 1 and stage 2 MGs use the FFCMG topology as described in Fig. 4-2.

Rotor 1: p_1 pole pairs
Rotor 2: n_2 pole pairs
Rotor 3: p_3 pole pairs
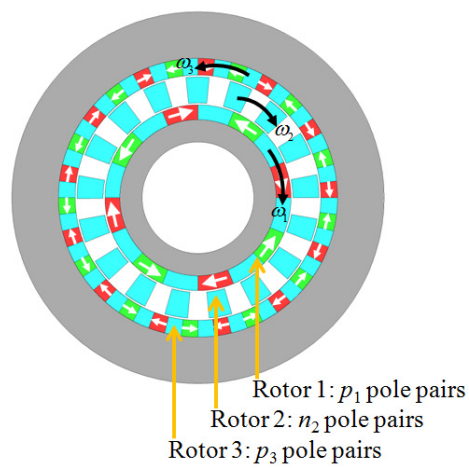
Fig. 4-2. An example of the FFCMG with $p_1 = 4$, $n_2 = 17$ and $p_3 = 13$.

Assuming that for the stage 1 MG, the inner rotor has p_1 pole pairs with angular speed ω_1, the cage rotor has n_2 pole pairs with angular speed ω_2 and the outer rotor has p_3 pole pairs with $\omega_3 = 0$. Then the gear ratio of stage 1 MG can be calculated from (1.8):

$$G_{s1} = \frac{n_2}{p_1} = \frac{\omega_1}{\omega_2} \tag{4.1}$$

The efficiency of stage 1 MG can be determined from

$$\eta_{s1} = \frac{|T_1|}{|T_2|} \cdot \frac{n_2}{p_1} \tag{4.2}$$

where T_1 and T_2 are the torque on the inner rotor and cage rotor, respectively.

Similarly, assuming that for the stage 2 MG, the inner rotor has p_4 pole pairs with angular speed ω_4, the cage rotor has n_5 pole pairs with angular speed ω_5 and the outer rotor has p_6 pole pairs and is stationary ($\omega_6 = 0$). Then the gear ratio of the stage 2 MG will be:

$$G_{s2} = \frac{n_5}{p_4} = \frac{\omega_4}{\omega_5} \tag{4.3}$$

The output of stage 1 is connected to the input of stage 2 such that $\omega_1 = \omega_5$. Then (4.1) and (4.3) can be combined to get a MSMG gear ratio given by:

$$G_r = G_{s1}G_{s2} = \frac{\omega_4}{\omega_2} = \frac{n_2 n_5}{p_1 p_4} \tag{4.4}$$

The efficiency of stage 2 MG can be determined from

$$\eta_{s2} = \frac{|T_4|}{|T_5|} \cdot \frac{n_5}{p_4} \tag{4.5}$$

where T_4 and T_5 are the torque on the inner rotor and cage rotor, respectively.

4.2. INITIAL DESIGN OF STAGE 1 MAGNETIC GEARBOX

Based on the analysis in Table 3-IV, the torque ripple will be low when rotor 1 has an odd number of pole pairs. The goal is to obtain more than 10 kNm torque value. Considering the mechanical sizes of the magnets and ferromagnetic steels, the number of pole pairs for rotor 1 was chosen to be 11. The initial parameters and torque values for stage 1 are shown in Table 4-I. The material properties are shown in Table 4-II. In this initial analysis, the cage rotor used 416 ferromagnetic steel and the inner and outer rotors were assumed to be made of 1018 steel. Fig. 4-3 and Fig. 4-4 show the initial Design I of stage 1 MG.
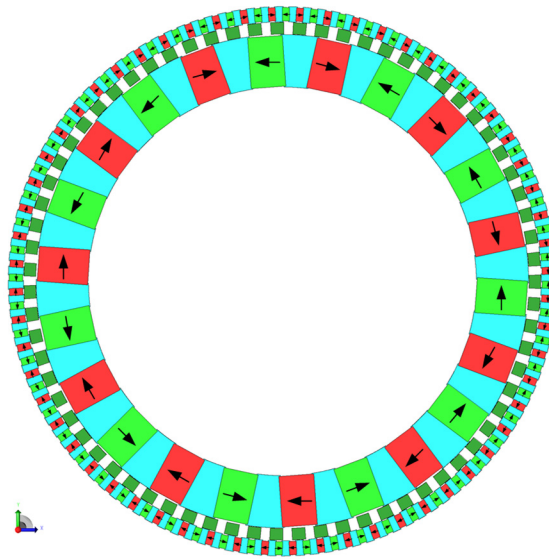
Fig. 4-3. Initial Design I of stage 1 magnetic arrangement for the series connected magnetic gearbox.
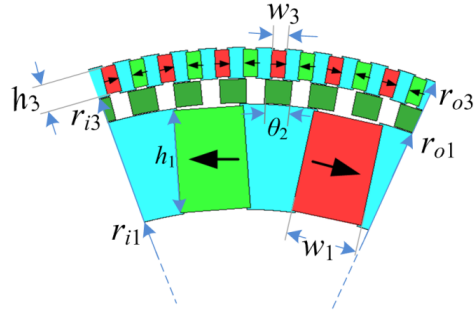
Fig. 4-4. Geometry definitions of initial Design I.

Table 4-I. INITIAL PARAMETERS FOR STAGE 1

Description		Value	Unit
Inner rotor	Inner radius, r_{i1}	215	mm
	Outer radius, r_{o1}	273	mm
	Pole pairs, p_1	11	-
	Angular span, θ_1	$\pi/(2p_1)$	radians
	Magnet length, h_1	56.2	mm
	Magnet width, w_1	38.8	mm
	Torque, T_1	1536.7	Nm
Cage rotor	Inner radius, r_{i2}	273.5	mm
	Outer radius, r_{o2}	286.5	mm
	Pole pairs, n_2	71	-
	Angular span, θ_2	$\pi/(p_3)$	radians
	Torque, T_2	-9916.6	Nm
Outer rotor	Inner radius, r_{i3}	287	mm
	Outer radius, r_{o3}	304	mm
	Pole pairs, p_3	60	-
	Angular span, θ_3	$\pi/(2p_3)$	radians
	Magnet length, h_3	15.0	mm
	Magnet width, w_3	7.9	mm
	Torque, T_3	8328.2	Nm
Axial length, d		75	mm

Table 4-II. MATERIAL PROPERTIES

Description	Value	Unit
416 steel density	7.75	g/cm^3
1018 steel density	7.85	g/cm^3
Magnet density	7.60	g/cm^3
Total magnet mass	35.48	kg
Total steel mass	40.47	kg
Total mass	75.95	kg
Total volume	21.78	L
Torque, T_2	-9916.64	Nm
Volume torque density	455.42	Nm/L
Mass torque density	130.57	Nm/kg
Torque-per-kg magnet	279.50	Nm/kg
Magnet cost @ $40/kg	1419.20	$
Steel cost @ $2/kg	80.94	$
Total estimated cost	1500.14	$

The torque ripple was calculated to be only 0.16 % on the cage rotor and the torque was 9917 Nm for the cage rotor when the losses were not considered. Therefore, in order to maintain the torque above 10 kNm after including eddy current losses, three approaches were used:

1. The radial length of the magnets on the outer rotor was increased from 15 mm to 25 mm to increase the peak torque value.

2. Lamination parts were used for all the steel parts to reduce the eddy current losses and increase the efficiency.

3. The magnets were segmented into four parts along the axial direction to reduce losses.

To make the mechanical assembling easier, a bridge has been used for the outer rotor instead of magnet retaining lips. The new Design II is shown in Fig. 4-5. The peak torque value on the cage rotor becomes 10652 Nm (without losses).
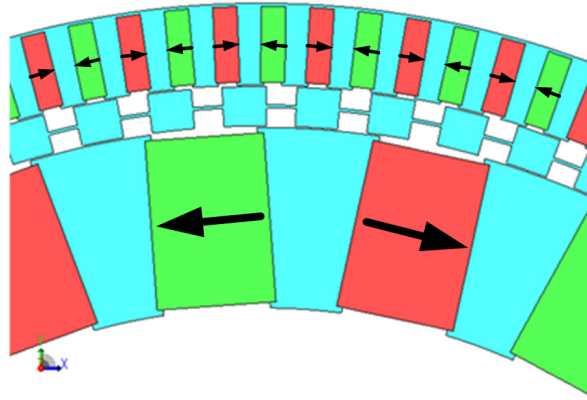
Fig. 4-5. Design II Stage 1 MG with magnet retaining lips and bridges. The pole pair numbers for the inner, cage and outer rotors are $p_1 = 11$, $n_2 = 71$ and $p_3 = 60$.

Before choosing the design shown in Fig. 4-5, several different designs were simulated and compared. The general idea was to force more magnetic flux to go into the two air gaps so that higher torque can be achieved. However, none of the alternative designs had an appreciably higher torque value. The different geometries are shown in Table 4-III and the description is given in Table 4-IV.

Table 4-III. Comparison of Different Designs.
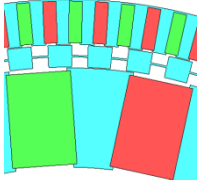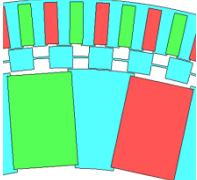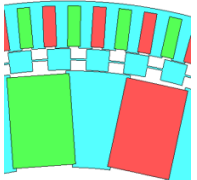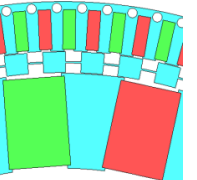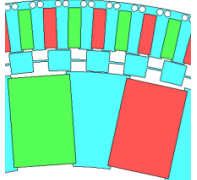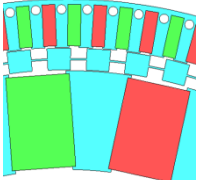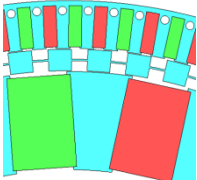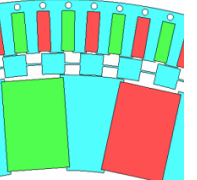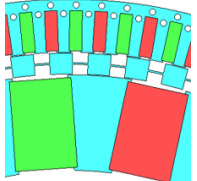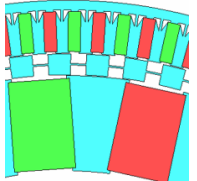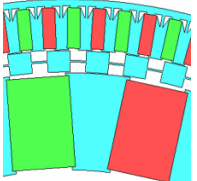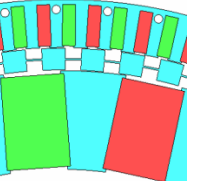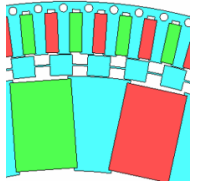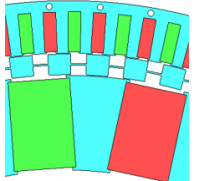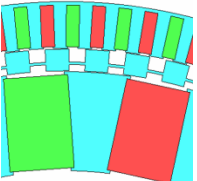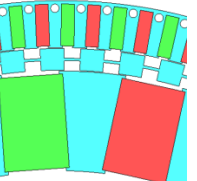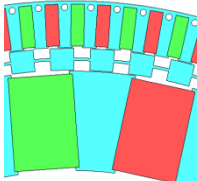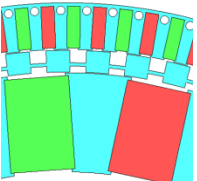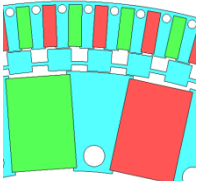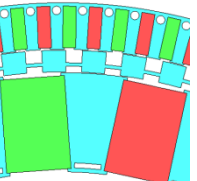
II	III	IV	V
10652 Nm	10194 Nm	9826 Nm	10018 Nm
VI	VII	VIII	IX
9806 Nm	10545 Nm	10451 Nm	9280 Nm
X	XI	XII	XIII
9625 Nm	9746 Nm	10144 Nm	10189 Nm
XIV	XV	XVI	XVII
9561 Nm	9207 Nm	9993 Nm	10359 Nm
XVIII	XIX	XX	XXI
10176 Nm	10221 Nm	10221 Nm	10261 Nm

Table 4-IV. Descriptions for Different Designs

Design II	The original design.
Design III	2 mm thickness bridge for the outer rotor.
Design IV	3 mm thickness bridge for the outer rotor.
Design V	5 mm thickness bridge for the outer rotor with air holes.
Design VI	5 mm thickness bridge for the outer rotor with more air holes.
Design VII	3 mm thickness bridge for the outer rotor with air holes (2.8 mm radius).
Design VIII	3 mm thickness bridge for the outer rotor with air holes (2.54 mm radius).
Design IX	7 mm thickness bridge for the outer rotor with air holes (1.905 mm radius).
Design X	7 mm thickness bridge for the outer rotor with more air holes (1.905 mm radius).
Design XI	7 mm thickness bridge for the outer rotor with rectangular air regions.
Design XII	5 mm thickness bridge for the outer rotor with rectangular air regions.
Design XIII	3 mm thickness bridge for the outer rotor with fewer air holes (2.54 mm radius).
Design XIV	7 mm thickness bridge for the outer rotor with air holes (2.54 mm radius).
Design XV	7 mm thickness bridge for the outer rotor with air holes (1.905 mm radius).
Design XVI	2.302 mm thickness bridge for the outer rotor. 1.524 mm thickness bridge for the cage rotor. The cage rotor bridge was shifted radially inward by 2 mm.
Design XVII	2.302 mm thickness bridge for the outer rotor with air holes (2.54 mm radius). 1.524 mm thickness bridge for the cage rotor.
Design XVIII	2.302 mm thickness bridge for the outer rotor with air holes (1.905 mm radius). 1.524 mm thickness bridge for the cage rotor.
Design XIX	2.302 mm thickness bridge for the outer rotor. 2.302 mm thickness bridge for the cage rotor. The cage rotor bridge was shifted radially inward by 2 mm.
Design XX	Air holes were added on the inner rotor (based on design XIX).
Design XXI	Rectangular air regions were added on the inner rotor (based on design XIX).

After adding magnet retaining supports, bridges and rods, the Design XXII of stage 1 MG is shown in Fig. 4-6. The zoomed in view is shown in Fig. 4-7. The inner rotor laminations are not connected by bridges. They only have magnet retaining lips. The cage rotor consists of 4 segment pieces while the outer rotor consists of 10 segments. The flux lines are also present in Fig. 4-6 and the magnetic flux density is shown in Fig. 4-8.
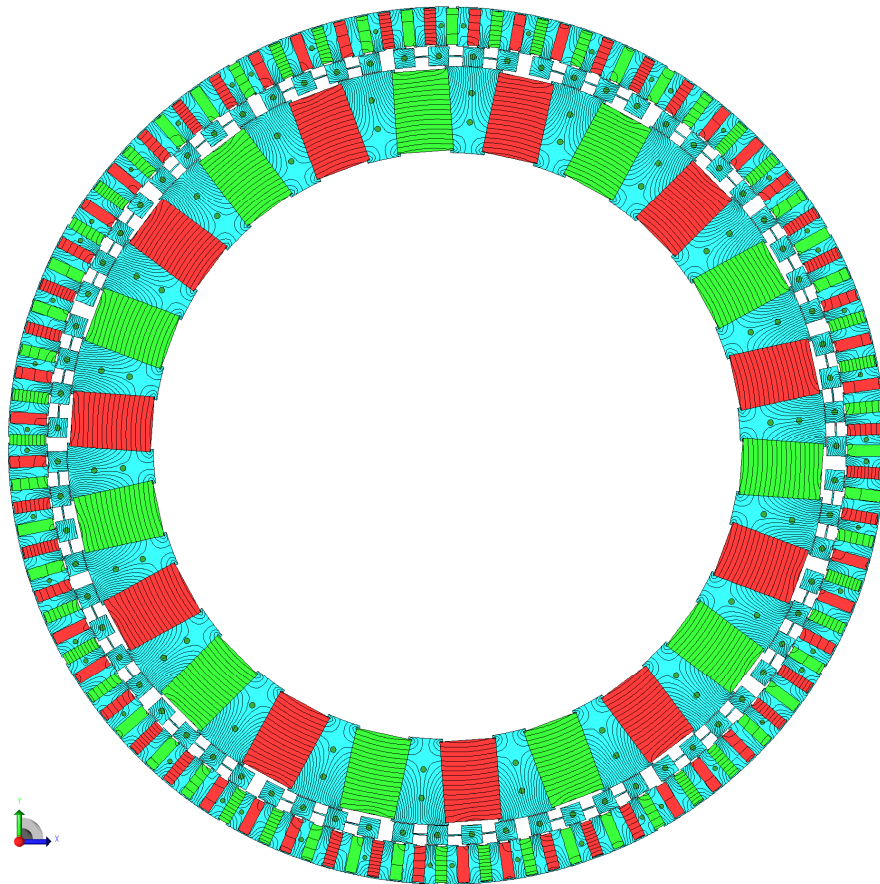
Fig. 4-6. Design XXII of stage 1 MG.
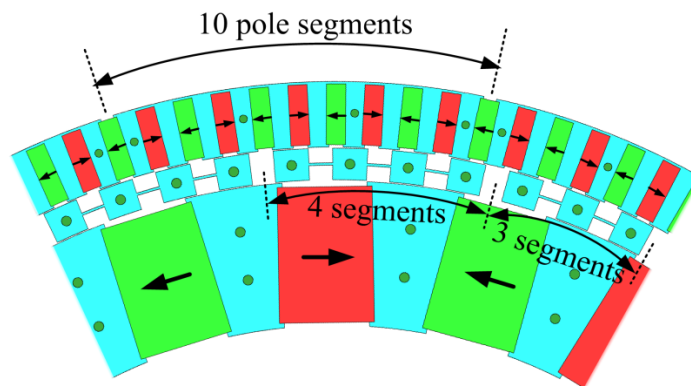
Fig. 4-7. Zoomed in view showing the bridges on the stationary outer rotor and cage rotor. The outer (stationary) rotor is made up of 10 segments while the cage rotor is made up of 4 segment pieces and one 3 segment section. The inner rotor steel poles are no connected by bridges.

(a)   (b)
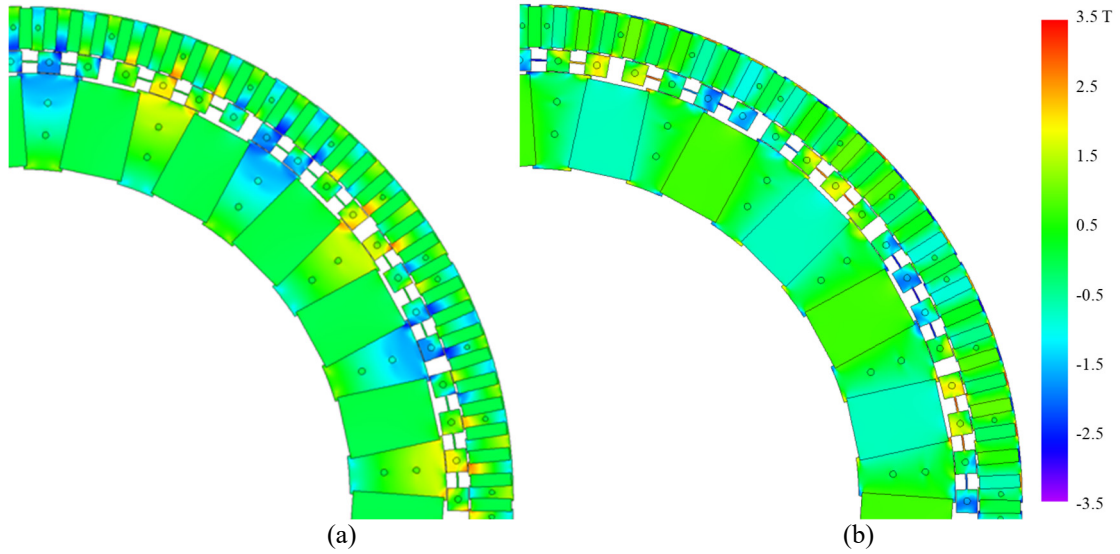
Fig. 4-8. (a) Radial flux density, B_r and (b) azimuthal flux density, B_θ .

The MG torque plots on the inner and cage rotor when operating at peak torque condition is shown in Fig. 4-9 and Fig. 4-10 (without losses). It can be noted that the percentage torque ripple is low.
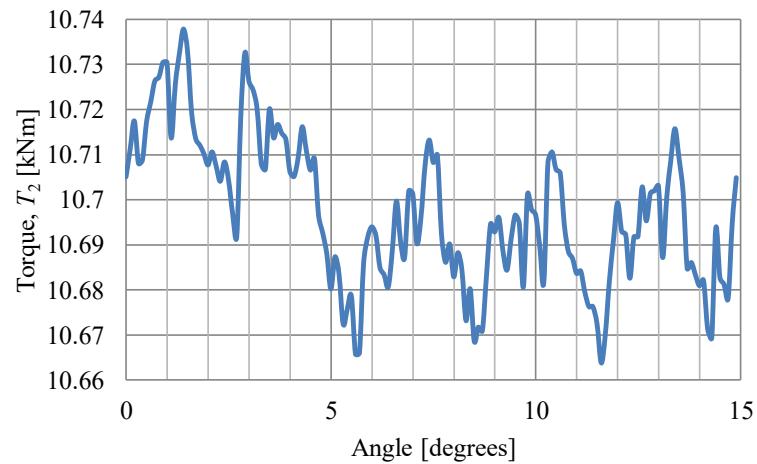
Fig. 4-9. Calculated torque using 2-D FEA on low-speed cage rotor.
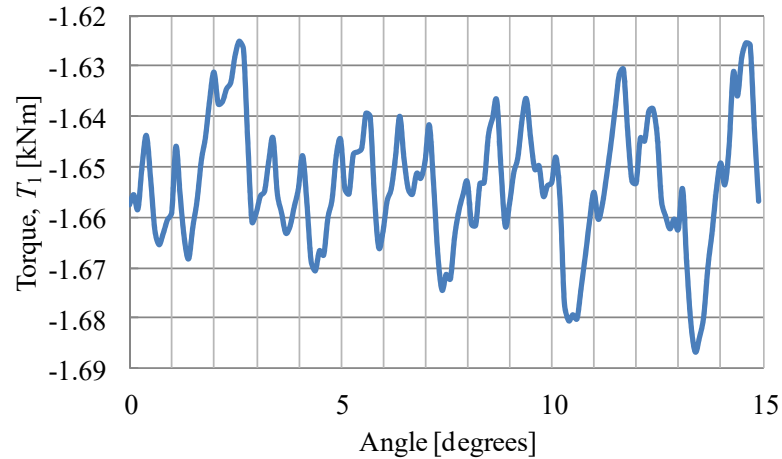
Fig. 4-10. Calculated torque using 2-D FEA on high-speed inner rotor.

The experimental lamination parts for stage 1 MG Design XXII are shown in Fig. 4-11. Since the diameters are quite large, the lamination parts could not be made as one single part. They were separated into 18 segments for the cage rotor and 12 segments for the outer rotor. The bridges on the middle of the cage laminations are 1-mm thick. There are also 1-mm thick bridges at the outer radius of the outer laminations.
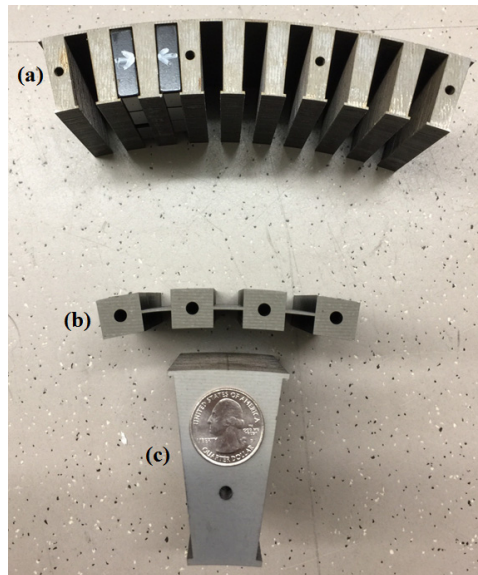
Fig. 4-11. Rotor lamination parts for (a) outer rotor (b) cage rotor and (c) inner rotor.

The magnetic fields of the inner and outer magnets have been measured and compared with 3-D FEA results. The comparison is shown in Fig. 4-12 and they have a good agreement. The assembled inner rotor is shown in Fig. 4-13 and the inner rotor field comparison is shown in Fig. 4-14. Fig. 4-15 shows the harmonic analysis for the inner rotor field. The discrepancy of the fundamental value between the measurement and 3-D FEA is 5.41 %.

(a)

(b)
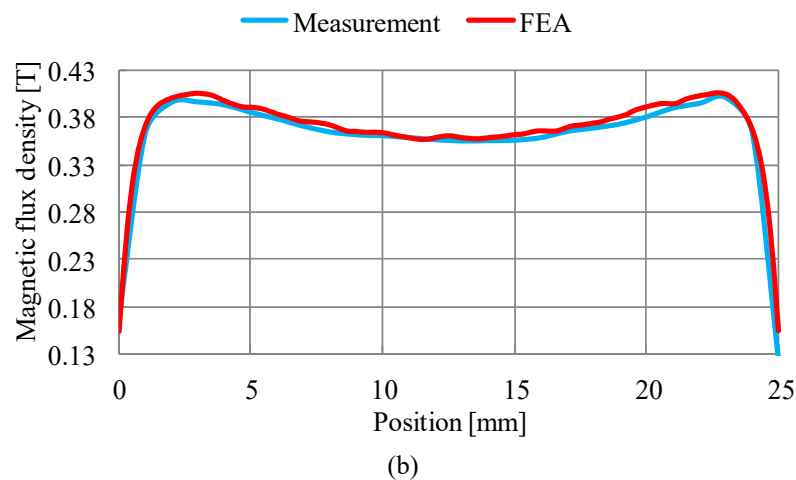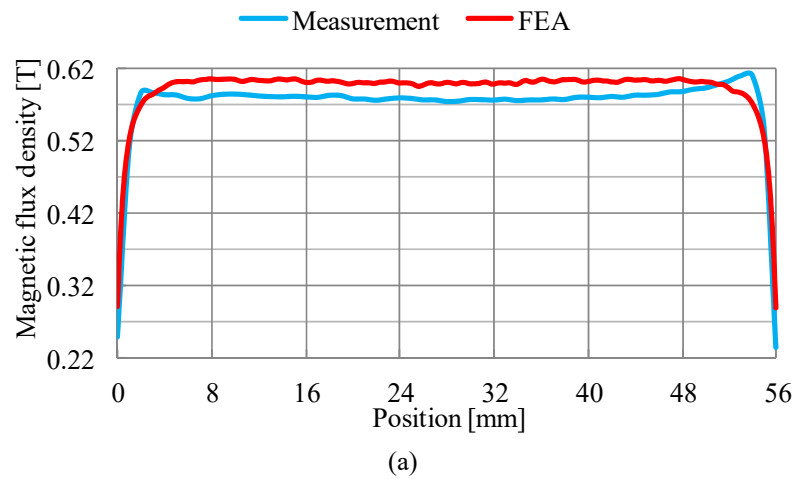
Fig. 4-12. Fields comparison for the (a) inner magnets and (b) outer magnets when magnet is surrounded by air.

Fig. 4-13. Assembled inner rotor.
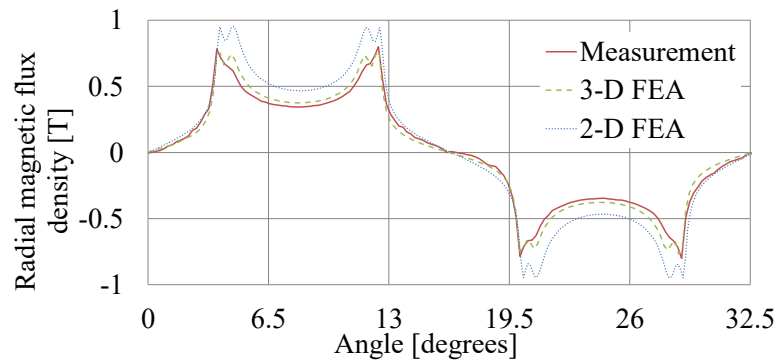
Fig. 4-14. Inner rotor field comparison between measurement and FEA.
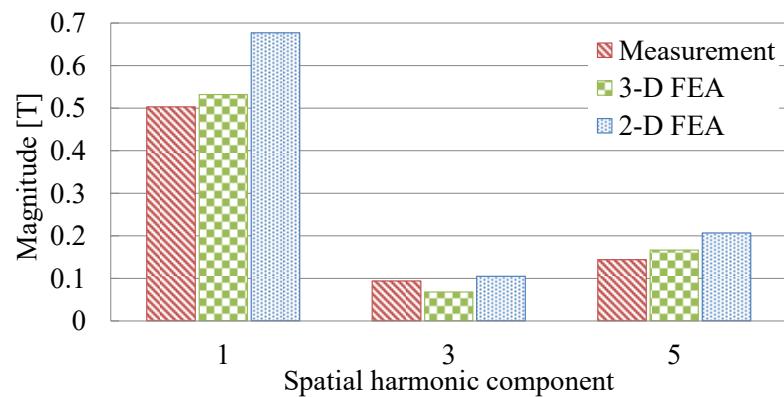
Fig. 4-15. Harmonic analysis for the inner rotor field.

However, when the cage laminations were assembled, they were attached to the inner rotor instead of maintaining a 0.5 mm air gap as shown in Fig. 4-16. That was because the radial forces for the cage laminations were so large that the cage rods were deflected.

(a)   (b)
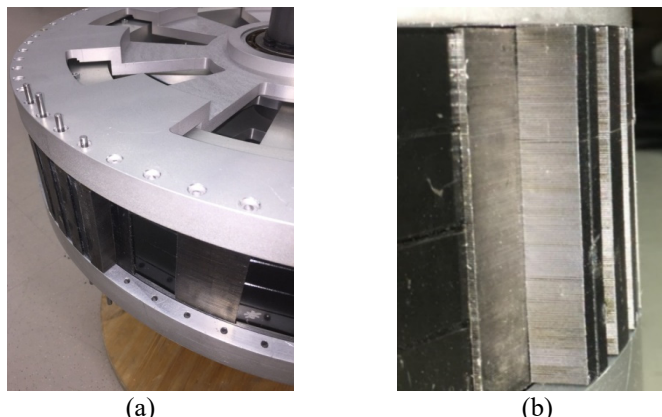
Fig. 4-16. (a) Low-speed cage rotor assembly and (b) deflection of a cage rotor laminated segment.

In order to solve the deflection issue, the radial forces on each rotor have been calculated as a function of time when the cage rotor was rotating at 5 RPM. The forces were calculated on a single lamination segment for inner, cage and outer rotor as shown in Fig. 4-17-Fig. 4-19 which consists of 1, 4 and 10 ferromagnetic teeth, respectively.
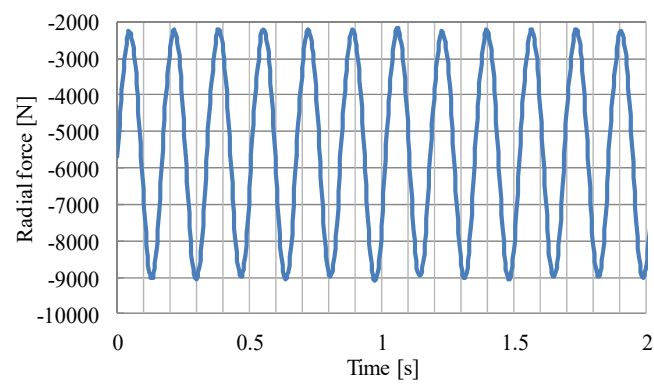
Fig. 4-17. The radial force on a single lamination segment for the outer rotor.
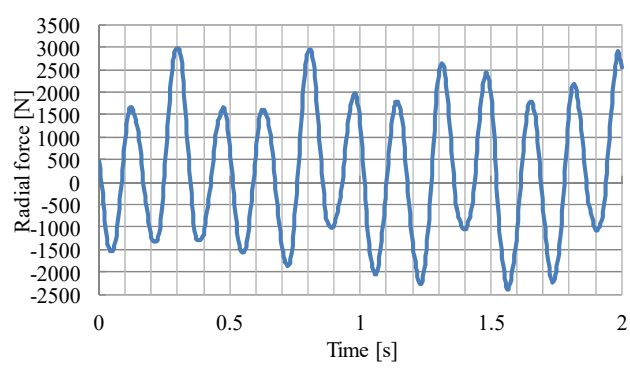
Fig. 4-18. The radial force on a single lamination segment for the cage rotor
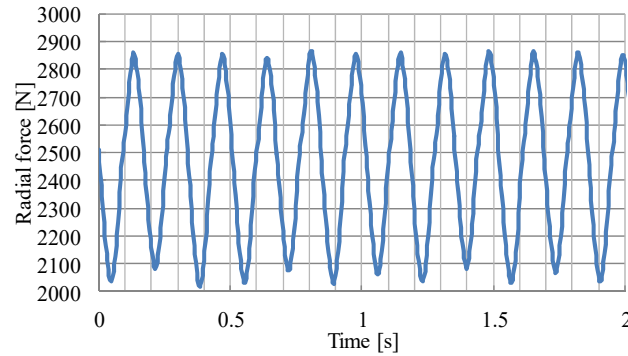
Fig. 4-19. The radial force on a single lamination segment for the inner rotor.

It can be seen that the maximum radial forces on the cage rotor and the outer rotor segments are 3 kN and 9.0 kN, respectively. The radial and tangential force on each segmented rod as a function of angular position was also computed at different time steps, and an example of the force profile at one time-step is shown in Fig. 4-20. The negative value means the force direction is radially inwards. Fig. 4-20 (a) shows the radial force distribution applied to the inner rotor rods are all positive values, meaning the forces are all directed radially outwards, but Fig. 4-20 (b) shows that for the cage rotor, the force values vary between -0.2 kN to 1.6 kN and for the outer rotor, all the values are directed inwards which means the force is in negative radial direction. This means that only the cage rotor experiences oscillating deflective inward and outward forces at different rotor angular positions. The maximum reduction of the inner air gap is therefore the summation of the deflection values for the inner rotor and cage rotor rods, and the reduction of the outer air gap is the summation of deflection values for the cage rotor and outer rotor rods.
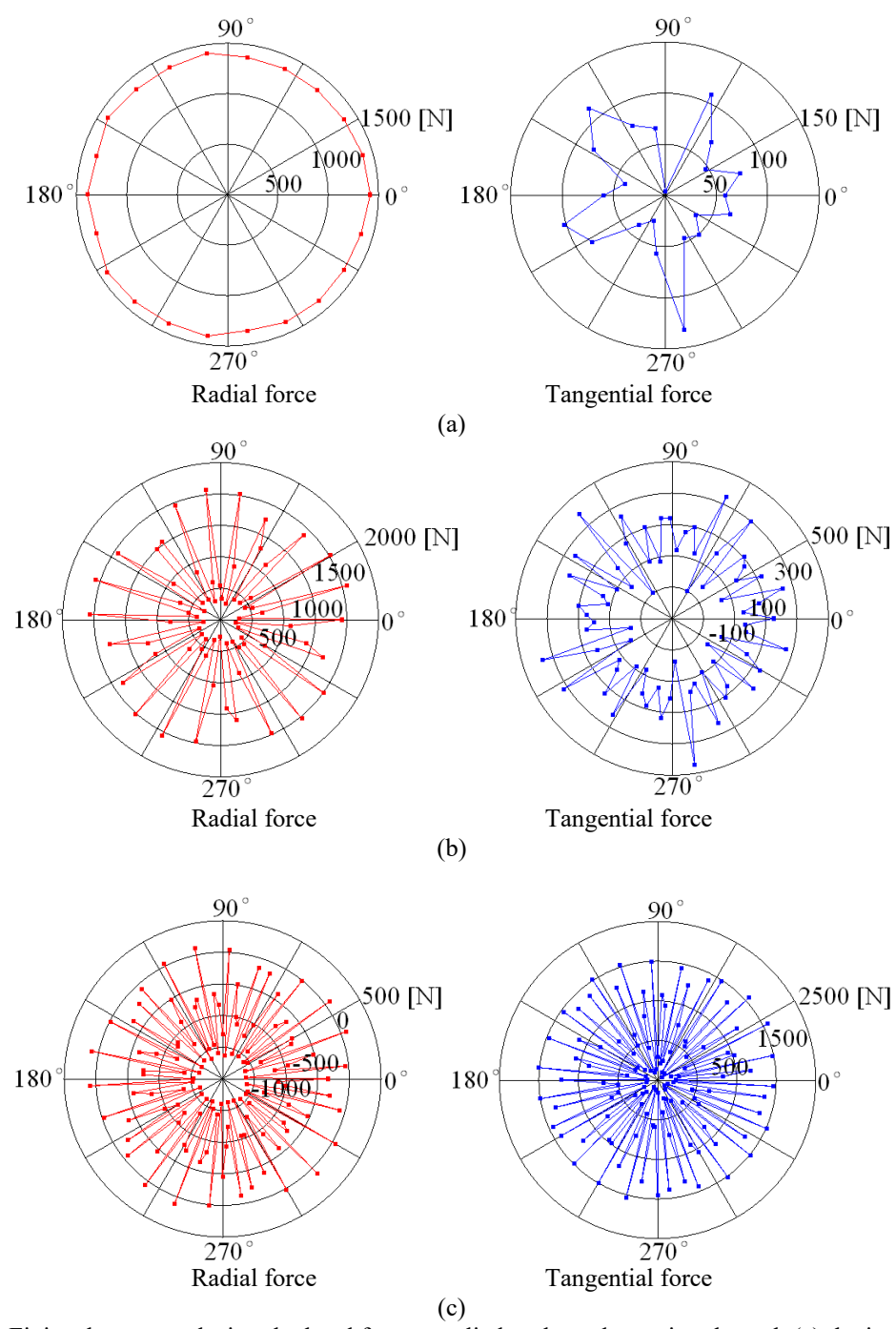
Fig. 4-20. Finite element analysis calculated forces applied to the rods passing through (a) the inner rotor (b) cage rotor and (c) outer rotor.

To understand the deflection issue further, the amount of rod deflection was calculated based on the force value. The initial diameter for the support rods was 4.07 mm. However, using the peak force provided in Fig. 4-19 it was calculated that the maximum rod

deflection was 1.4 mm. Since the air gap is only 0.5 mm, the cage laminations will definitely be attached to the inner rotor. The deflection of a cage rod with different diameters is shown in Fig. 4-21 along with the approximate 2-D FEA calculated eddy current loss. It can be noted that increasing the rod diameter will significantly increase the eddy current loss. For instance, the increased rod size needed to reduce the deflection to less than 0.1 mm will result in approximately 6 times higher eddy current loss relative to the initial design.
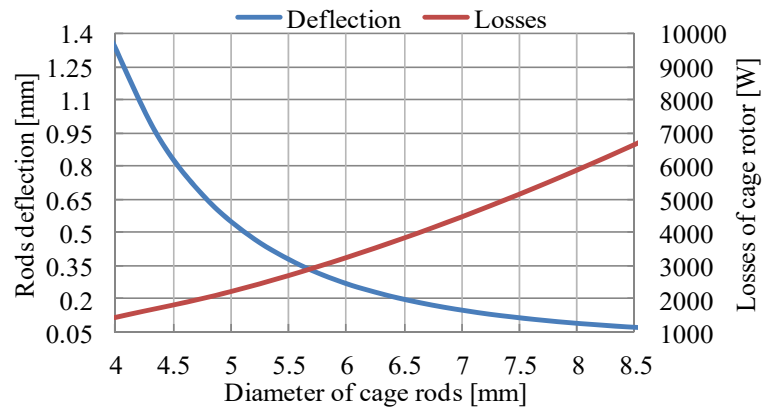
Fig. 4-21. Calculated radial deflection and estimated eddy current loss for different diameter cage rotor support rods.

4.3. IMPROVED DESIGN OF STAGE 1 MAGNETIC GEARBOX

In order to reduce the deflection down to an acceptable value, three circular aluminum support rings were added at three positions along the axial direction of the MG. This Design XXIII is illustrated in Fig. 4-22. To minimize the circulating currents between the support rods and the support rings, non-conductive spacer rings have been used which are shown in Fig. 4-23.
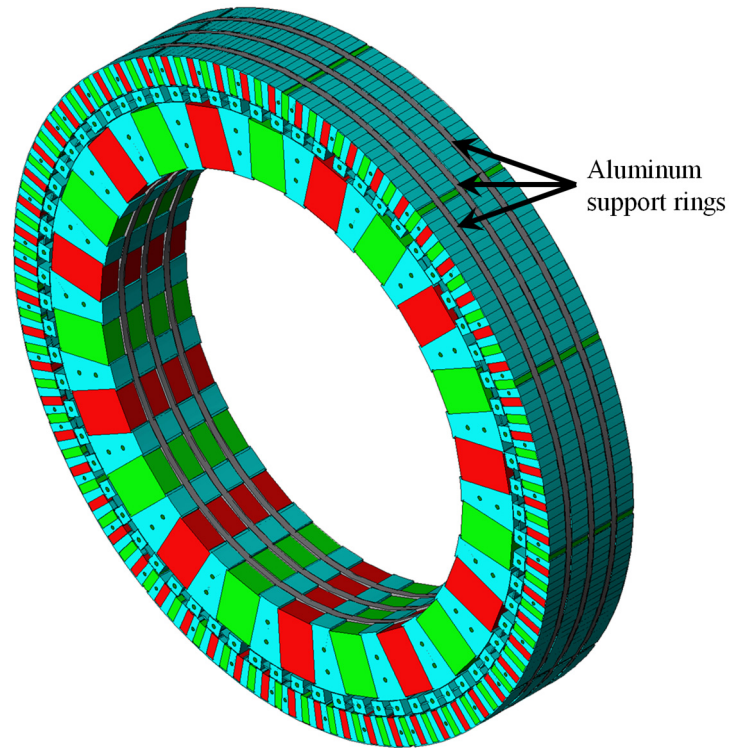
Fig. 4-22. 3-D FEA model with three supporting aluminum rings of Design XXIII.
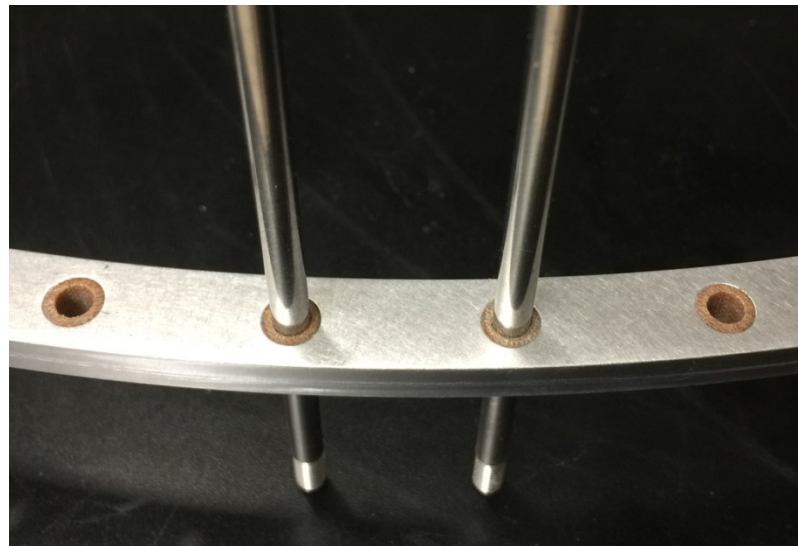
Fig. 4-23. Non-conductive spacers placed in the support ring.

Fig. 4-24 (a) shows the deflection of outer rods at different locations with and without support rings. The improvement of deflection is significant. The amount of deflection

with support rings is more clearly seen in Fig. 4-24 (b). The maximum deflection is within 0.1 mm.
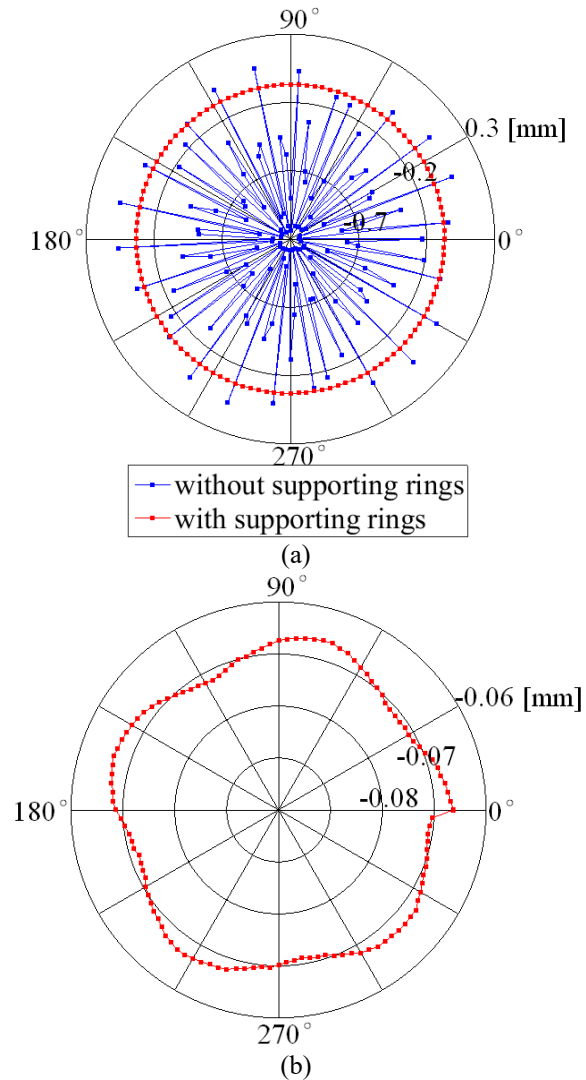
Fig. 4-24. (a) Comparison of FEA calculated deflection of the outer rotor rods with and without supporting rings. The supporting ring has an axial thickness of 6.35mm (b) Deflection plot showing level of deflection only on outer rotor rods in the presence of supporting rings. [data from Sina Modaresahmadi]

A summary of the maximum deflection for each rotor for the case when the axial support rings are present and not present is shown in Table 4-V [calculated by Sina Modaresahmadi]. It should be noted that in these FEA deflection calculations, the effect of laminations is neglected because the stiffness of the bonding between the lamination

layers is very small in comparison with the forces applied to them. It is assumed that the laminations do not provide significant mechanical support.

Table 4-V. CALCULATED MAXIMUM DEFLECTION OF RODS WITH/WITHOUT THREE 6.35 MM THICKNESS RINGS [CALCULATED BY SINA MODARESAHMADI]

Rotor	Deflection with three rings [µm]	Deflection with no rings [µm]
Inner Rotor	23.2	514
Cage Rotor	44.5	574
Outer Rotor	78.3	1140

The addition of the support rings reduces the expected peak calculated torque. Using 3-D magnetostatic FEA the calculated peak torque reduced to 8.27 kNm (298 Nm/L and 88 Nm/kg). A larger air gap has also been considered because of the deflection issue. If the air gap was increased from 0.5 mm to 1 mm, then the peak torque was further reduced down to 6.76 kNm.

The assembled new inner rotor with support rings is shown in Fig. 4-25. The magnetic field around the inner rotor was measured and compared with the FEA model which is shown in Fig. 4-26. The harmonic analysis is present in Fig. 4-27. The discrepancy of the fundamental component between measurement and 3-D FEA model is 2.32 %.

Fig. 4-25. Fully assembled inner rotor with three support rings.
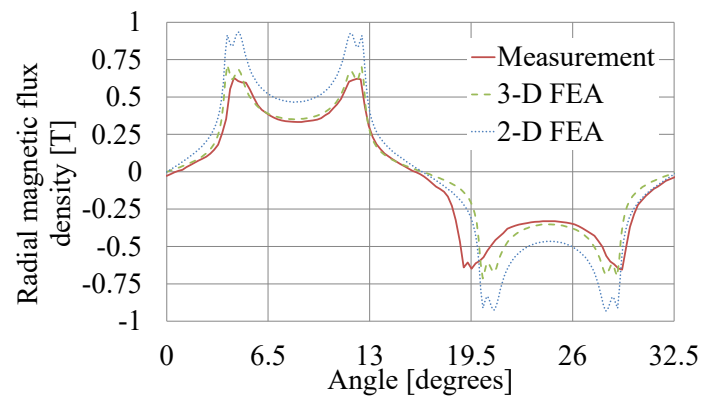
Fig. 4-26. Inner field comparison between the measurement and FEA model when support rings are present.
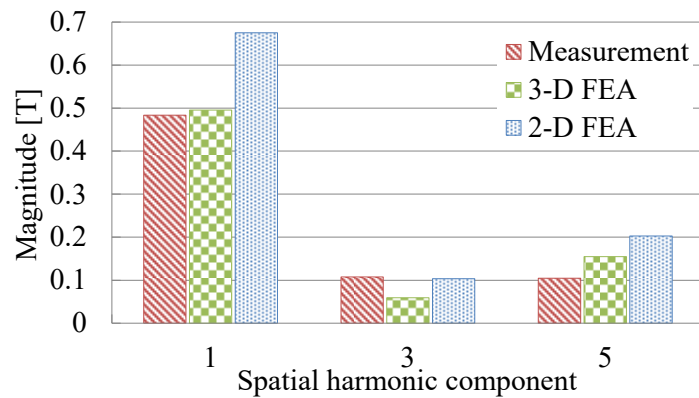
Fig. 4-27. Harmonic analysis of the inner rotor field.

The deflection analysis has been done with the support rings. The cage rotor was assembled with only laminations at three different positions with 120 degrees apart. Therefore, the radial force would be uniform. Fig. 4-28 shows the 3-D FEA model and Fig. 4-29 shows the experimental setup. The cage rotor also has three support rings to help reduce the deflection. However, some of the cage laminations were still attached to the inner rotor. One possible reason was that the 1-mm thick bridge on the cage lamination did provide enough support so that the cage bars could tilt along the cage rods. Another reason was that the cage support rings were deformed because only a small amount of cage rods had been inserted as shown in Fig. 4-29.
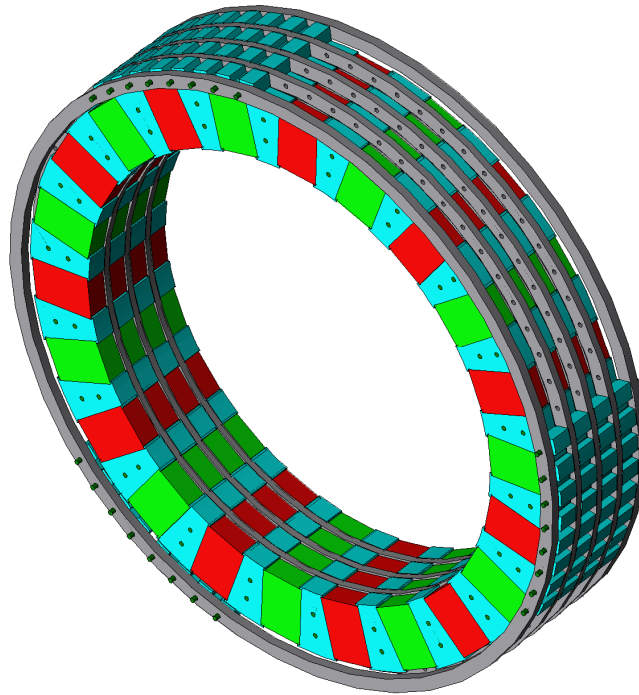
Fig. 4-28. Deflection test setup in FEA model.
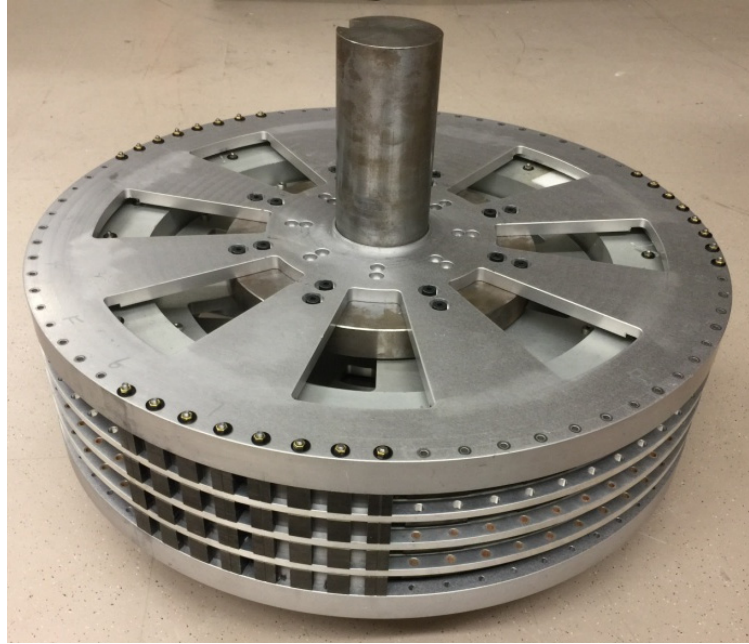
Fig. 4-29. Deflection test setup in experiment.

It can be seen from Fig. 4-30 that the magnetic field was non-uniform on that individual cage lamination bar. In this FEA model, one piece of inner magnet and two pieces of inner laminations were present. The 3-D model is displayed in Fig. 4-31 (a), while the distribution of the non-uniform radial nodal force is shown in Fig. 4-31 (b) which can explain the tilting of the cage bar.
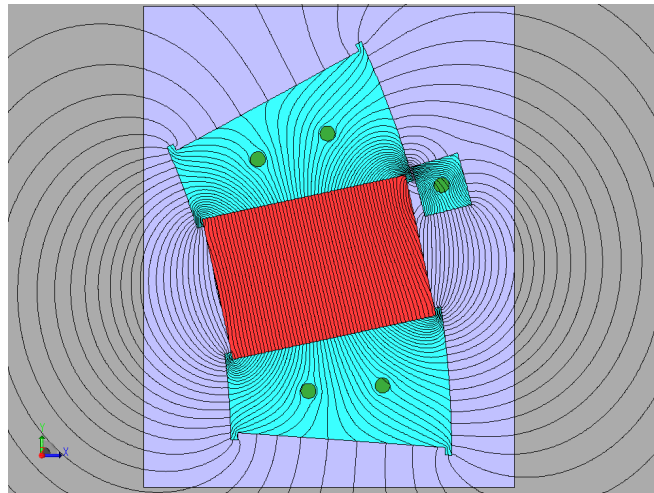
Fig. 4-30. Magnetic flux lines for one individual cage lamination bar.

(a)   (b)
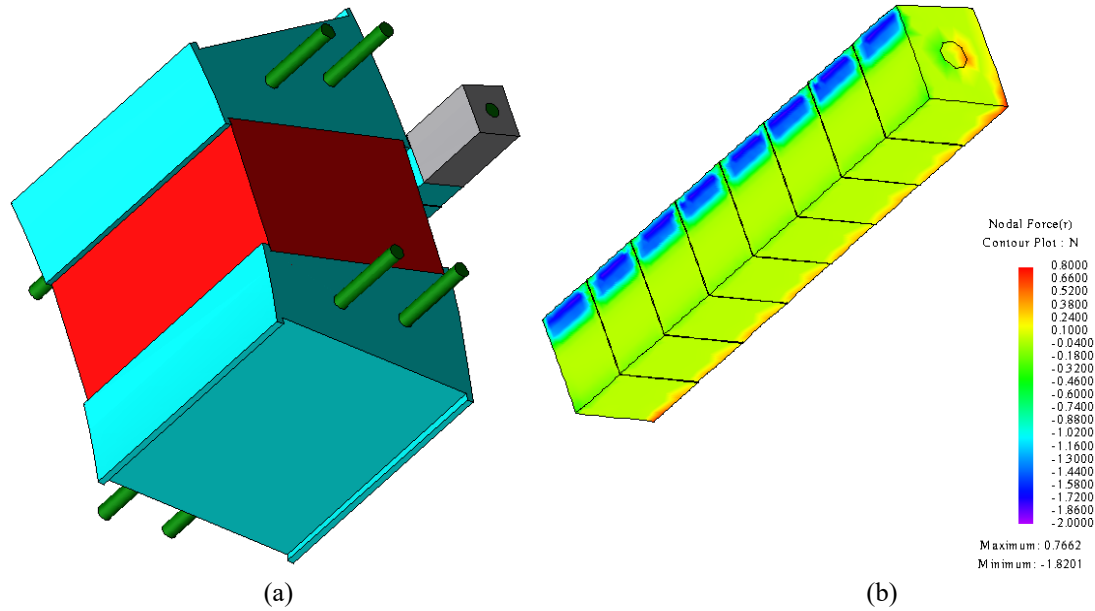
Fig. 4-31. (a) 3-D FEA model and (b) radial force distribution.

As a result, the cage lamination design shown in Fig. 4-11 was not structural strong enough as the 1-mm thick bridges did not provide much support. Also, with one bridge at the middle of the lamination, the single lamination bars would be rotated along the cage rods which may cause the cage lamination contacting the inner rotor. The outer laminations had the same issue as the cage ones. Another issue for the outer laminations is that there were only 4 rods on the 10 segments which means 6 segments would be only supported by the outer 1-mm thick bridges. Apparently, that was not enough support and the outer laminations would be attached to the cage rotor as well. Therefore, new cage and outer laminations have been designed and compared which is shown in Table 4-VI. The description for each design is present in Table 4-VII. All the designs shown in Table 4-VI were simulated in 2-D with an axial length of 75 mm. The topology of Design XXXXV was chosen as it had a mechanically robust structure for both assembly purposes and mechanical support. Design XXXXVII was selected as the final design (the

size of the radial magnets on the outer rotor was increased slightly from 6×4.5 mm^2 to

6.2×5.2 mm^2) and is shown in Fig. 4-32. The calculated torque in 2-D was 7.1 kNm.

With this design, those rods and bridges will provide more support than the previous

design. Another advantage of this design is that the outer rods on the outer rotor can rest

on the cage end plates which will make the assembly process much easier. The

parameters are provided in Table 4-VII. Since the cage rotor has 71 steel poles, it cannot

get an integer if the number is divided by 3. Therefore, there are 21 segments that consist

of 3 cage single bars and 2 segments that consist of 4 cage single bars.

Table 4-VI. Different Topologies for Stage 1

XXII	XXIV	XXV	XXVI
10.7 kNm	9.0 kNm	8.0 kNm	7.5 kNm
XXVII	XXVIII	XXIX	XXX
7.8 kNm	7.2 kNm	7.4 kNm	5.5 kNm
XXXI	XXXII	XXXIII	XXXIV
6.1 kNm	5.2 kNm	6.7 kNm	6.7 kNm

XXXV	XXXVI	XXXVII	XXXVIII
7.0 kNm	7.8 kNm	7.7 kNm	7.6 kNm
XXXIX	XXXX	XXXXI	XXXXII
6.4 kNm	6.7 kNm	7.6 kNm	7.1 kNm
XXXXIII	XXXXIV	XXXXV	XXXXVI
6.7 kNm	7.0 kNm	6.8 kNm	7.0 kNm
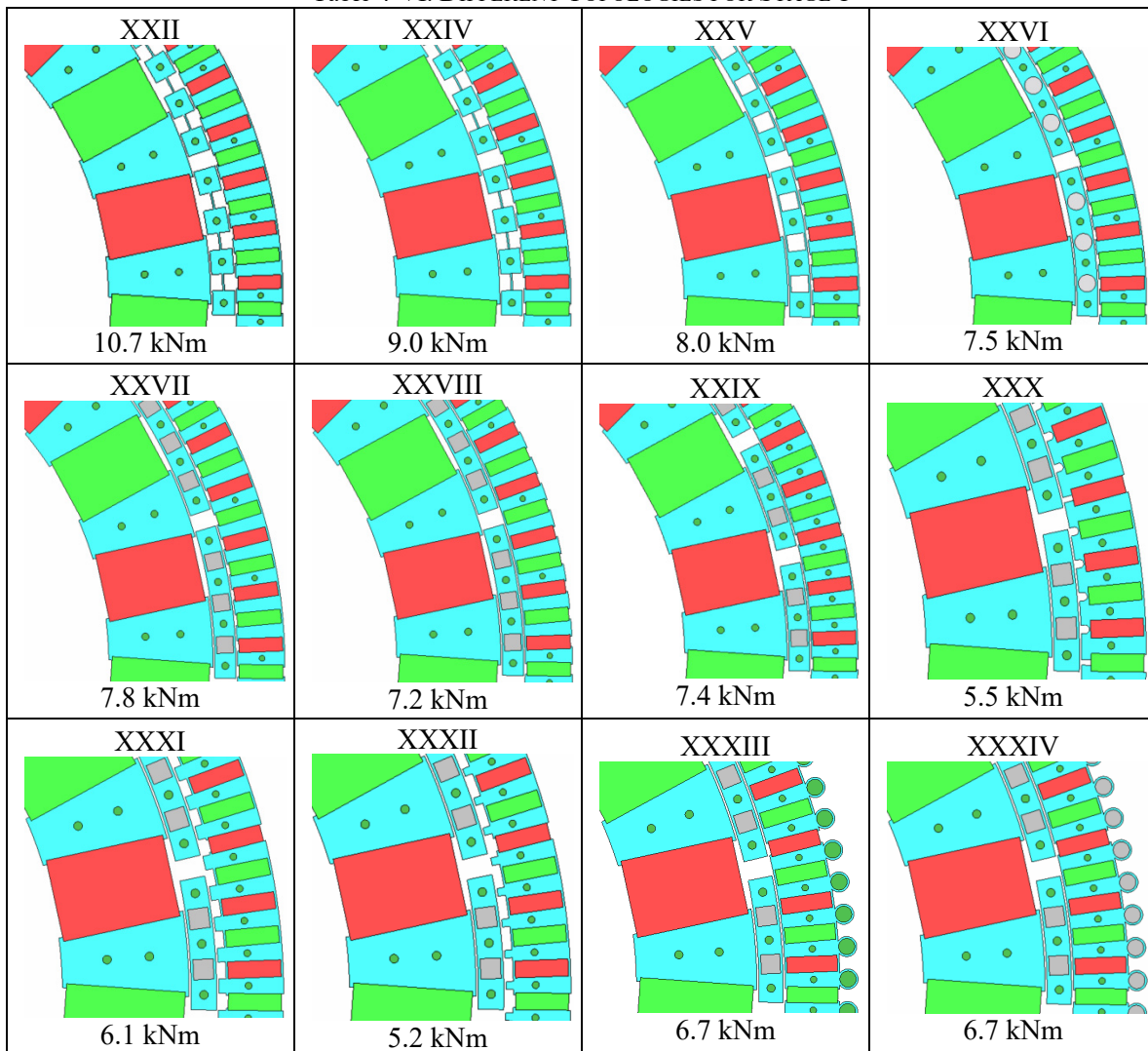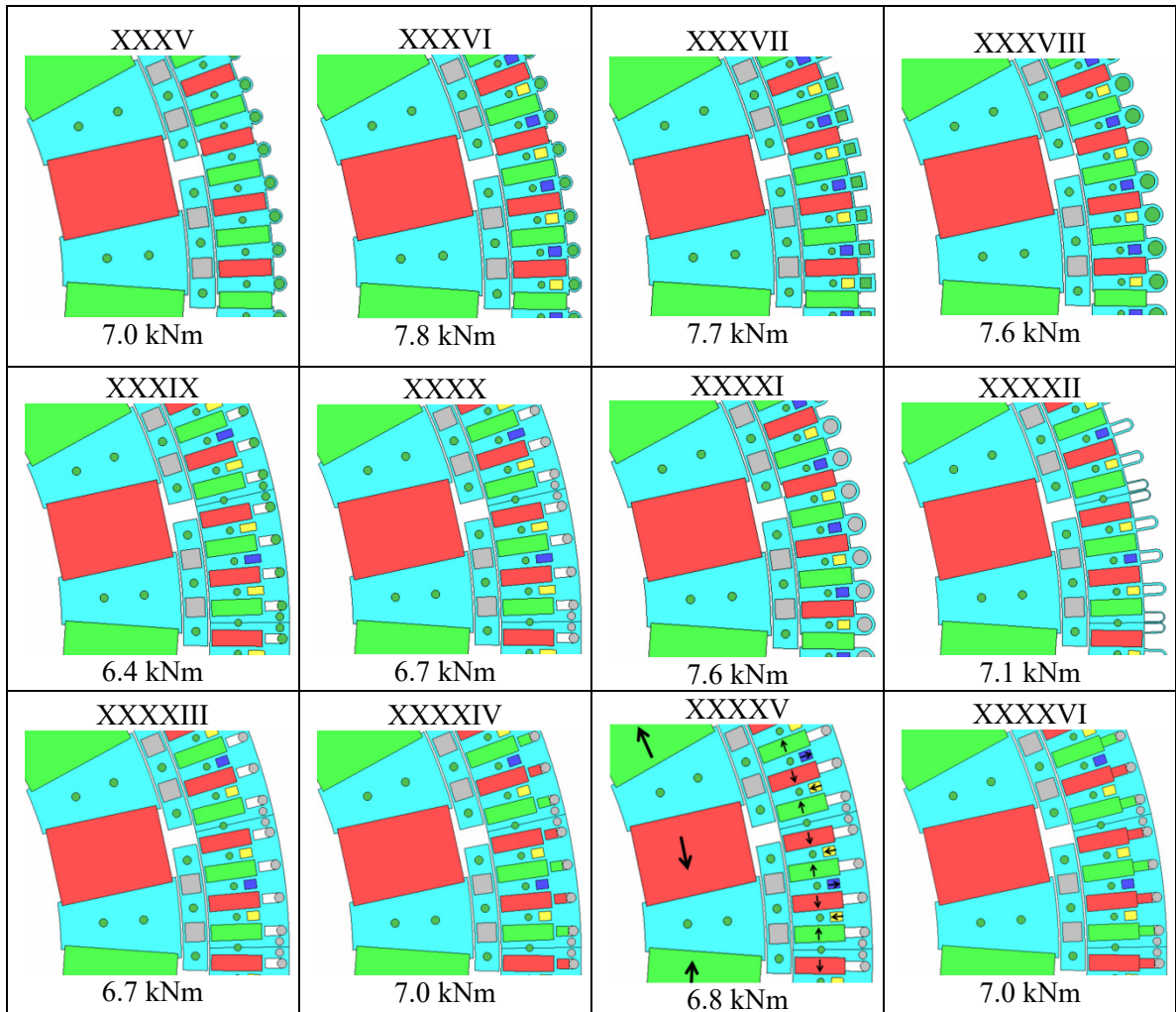
Table 4-VII. Descriptions for Different Designs

Design XXII	0.5 mm air gap, one bridge on cage rotor
Design XXIV	1 mm air gap, one bridge on cage rotor
Design XXV	1 mm air gap, two bridges on cage rotor
Design XXVI	1 mm air gap, two bridges and more rods on cage rotor
Design XXVII	1 mm air gap, two bridges on cage rotor, 3/8" square plastic inserts for cage lamination
Design XXVIII	Modified bridges for the outer rotor from design XXVII
Design XXIX	Modified number of segments for cage lamination, two bridges on outer rotor
Design XXX	Modified outer rotor from design XXIX
Design XXXI	Modified outer rotor from design XXIX
Design XXXII	Modified outer rotor from design XXIX
Design XXXIII	Modified outer rotor from design XXIX
Design XXXIV	Modify design XXXIII (plastic outer rods)
Design XXXV	Modify design XXXIII (smaller outer rods)
Design XXXVI	Modify design XXXV (radial magnets on outer rotor)
Design XXXVII	Modify design XXXVI
Design XXXVIII	Modify design XXXVI
Design XXXIX	Modified outer rotor lamination
Design XXXX	Modify design XXXIX (plastic outer rods)
Design XXXXI	Modify design XXXVIII (plastic outer rods)
Design XXXXII	Modified outer rotor lamination
Design XXXXIII	Modify design XXXX
Design XXXXIV	Modify design XXXXI (more magnets on outer rotor)
Design XXXXV	Modify design XXXXIII (The final design was chosen based on this design)
Design XXXXVI	Modify design XXXXV
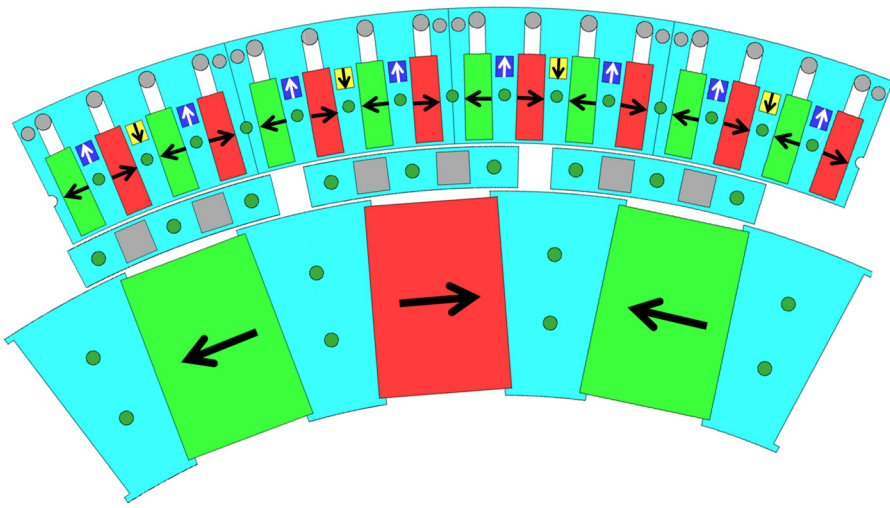
Fig. 4-32. Zoomed in view of the improved design for cage and outer laminations for Design XXXXVII.

The 2-D model of Design XXXXVII is shown in Fig. 4-33. The plots of B_r and B_θ are shown in Fig. 4-34 and the torque plots as a function of time are shown in Fig. 4-35. The torque ripples for inner, cage and outer rotors are 12.7 %, 2.1 % and 1.6 %, respectively.
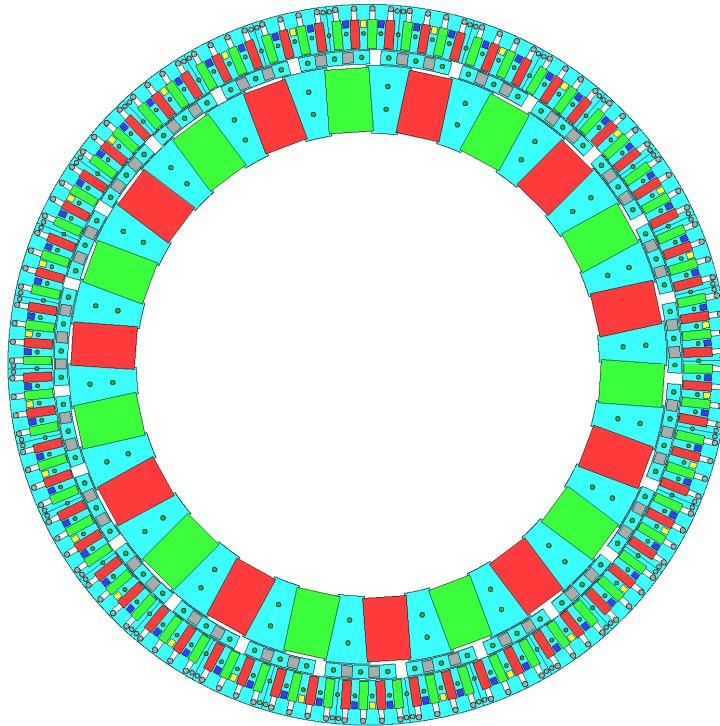
Fig. 4-33. Final choice for the improved design of stage 1 MG.
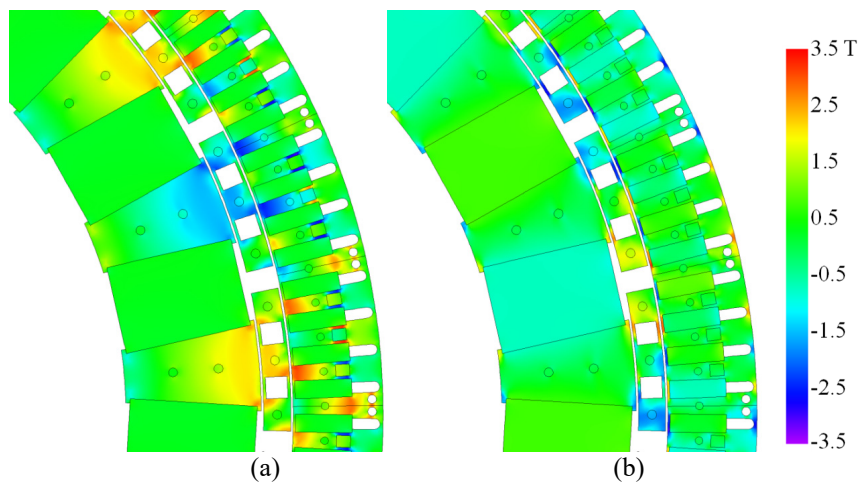
(a)   (b)
Fig. 4-34. Contour plot of (a) B_r and (b) B_θ.
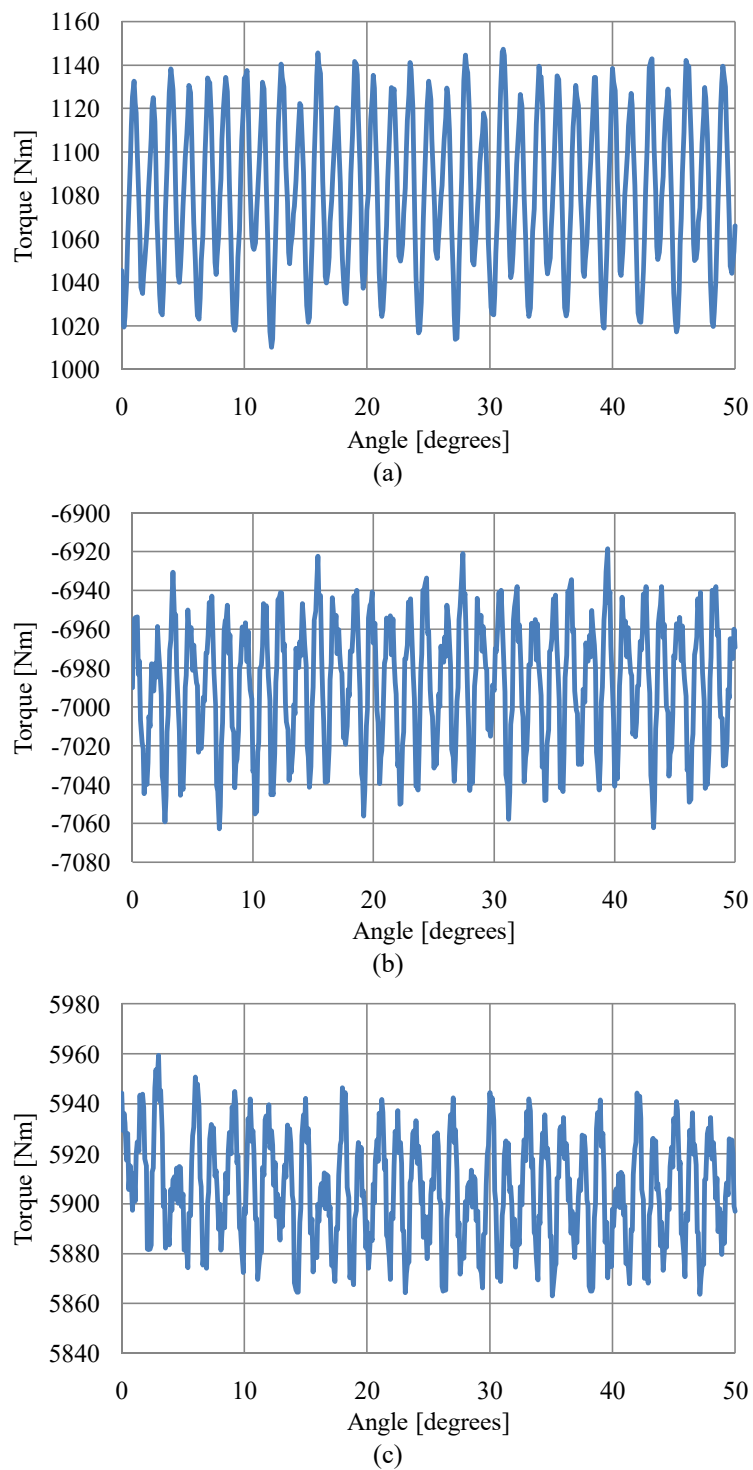
Fig. 4-35. Torque plot for the (a) inner rotor (b) cage rotor and (c) outer rotor.

The new BH curve of the M19 lamination has been used when calculating the inner rotor field. The comparison of the old and new M19 BH curves is shown in Fig. 4-36. The comparisons of peak torque and torque ripple are present in Table 4-VIII.
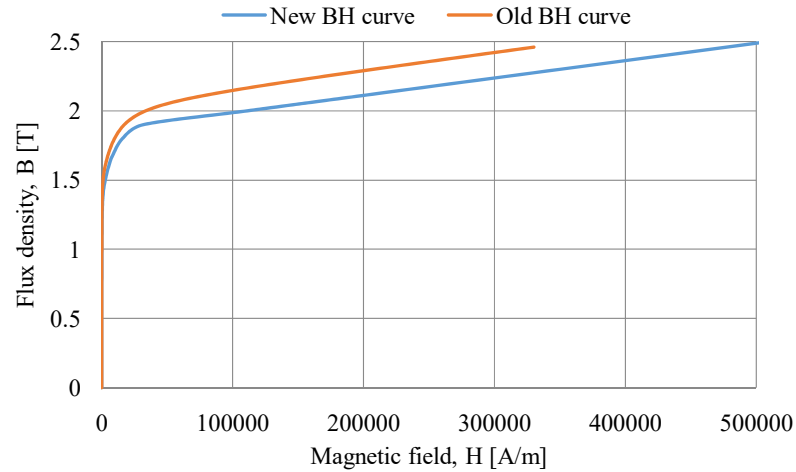
Fig. 4-36. Comparison between the old and new M19 BH curves.

Table 4-VIII. PERFORMANCE COMPARISON USING OLD AND NEW M19 BH CURES

	Old BH curve		New BH curve	
	Torque [kNm]	Torque ripple [%]	Torque [kNm]	Torque ripple [%]
Inner rotor	1.0	12.7	1.0	12.0
Cage rotor	-7.0	2.1	-6.8	1.9
Outer rotor	6.0	1.6	5.8	1.6

In the previous simulation the grade of the magnets was N40 CH. However, when ordering the magnets, the grade was chosen as N45 SH. The final 3-D geometry of the MG is shown in Fig. 4-37 which has a peak torque of 4.79 kNm with the new BH curve. The final geometry parameters are shown in Table 4-IX.
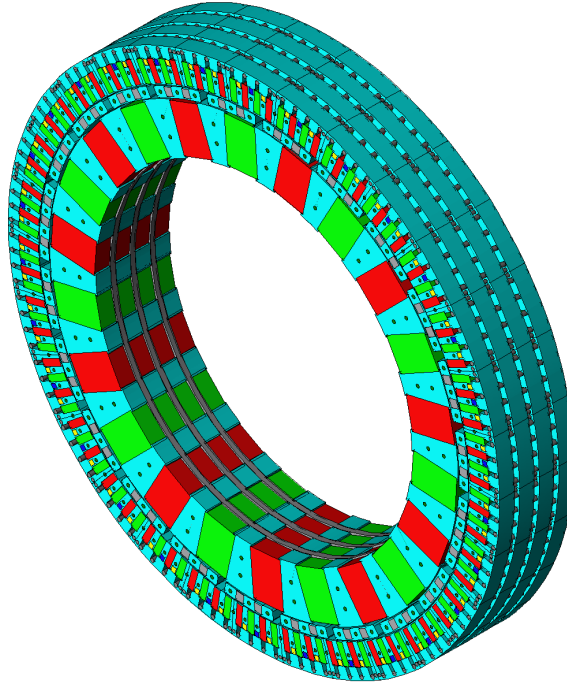
Fig. 4-37. Final geometry of the stage 1 MG.

Table 4-IX. GEOMETRIC AND MATERIAL PROPERTIES FOR FINAL STAGE 1 MAGNETIC GEARBOX DESIGN.

Description		Final value	Unit
Inner rotor	Inner radius, r_{i1}	203.5	mm
	Outer radius, r_{o1}	263	mm
	Radial length of magnet	56	mm
	Width of magnet	38.8	mm
Cage rotor	Inner radius, r_{i2}	264	mm
	Outer radius, r_{o2}	276	mm
Outer rotor	Inner radius, r_{i3}	277	mm
	Outer radius, r_{o3}	316.5	mm
	Radial length of angular magnet	25	mm
	Width of angular magnet	7.9	mm
	Radial length of radial magnet	5	mm
	Width of radial magnet	5	mm
Axial length of each support ring		6.35	mm
Axial length (magnets and laminations)		76.2	mm
Axial length (with support rings), d		95.25	mm
Air gap, g		1	mm

The addition of support rings creates quite severe edge effects which can be seen in Fig. 4-38. Fig. 4-38 (a) and (b) show that the radial and azimuthal magnetic flux were reduced by adding the support rings. Fig. 4-38 (c) shows that more flux will go into the

regions between each layer along the axial direction. This was the reason that the peak torque was reduced from 5.70 kNm (without support rings) to 4.79 kNm (with support rings).
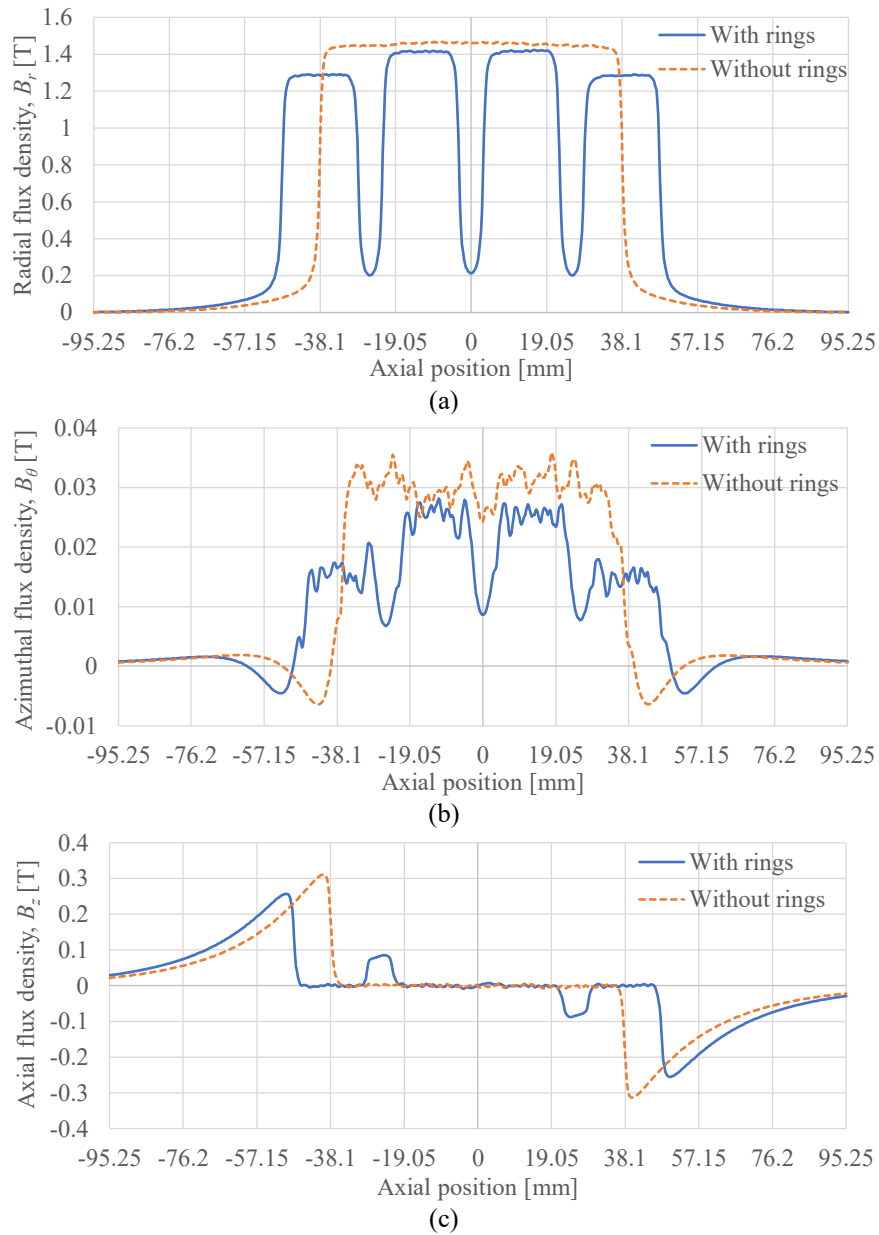
Fig. 4-38. (a) Radial (b) azimuthal and (c) axial magnetic flux distribution in the air gap between the cage and inner rotors at $r = 263.5$ mm. The axial position is from -38.1 mm to 38.1 mm without support rings. Whilst it is from -47.625 mm to 47.625 mm with support rings.

To make the cage rods to deflect less, square plastic bars were inserted into the air region between the two bridges. The cage lamination parts are shown in Fig. 4-39 (a). The corners of the cage lamination pieces were rounded during fabrication. Fig. 4-39 (a) also shows the plastic inserts that have been put in the air region which can provide more support. Fig. 4-39 (b) shows the outer lamination with inserted magnets (both azimuthal and radial magnetized magnets). Fig. 4-40 (a) shows the fully assembled inner rotor and Fig. 4-40 (b) shows the assembled inner and cage rotors. The fully assembled stage 1 MG is shown in Fig. 4-40 (c). The material properties are shown in Table 4-X. Table 4-XI gives a summary of the calculated torque density for the active material region. The mass torque density value shown when the support rings are present includes the mass of the support rings in the calculation.

(a)

(b)
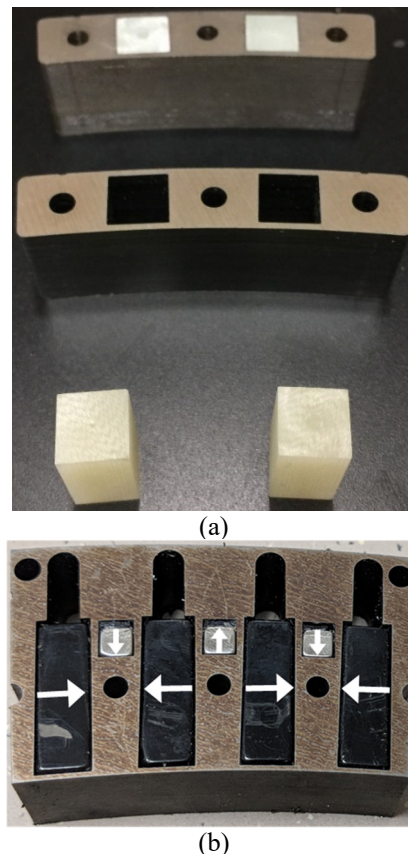
Fig. 4-39. (a) Cage lamination with plastic inserts and (b) outer lamination with magnets
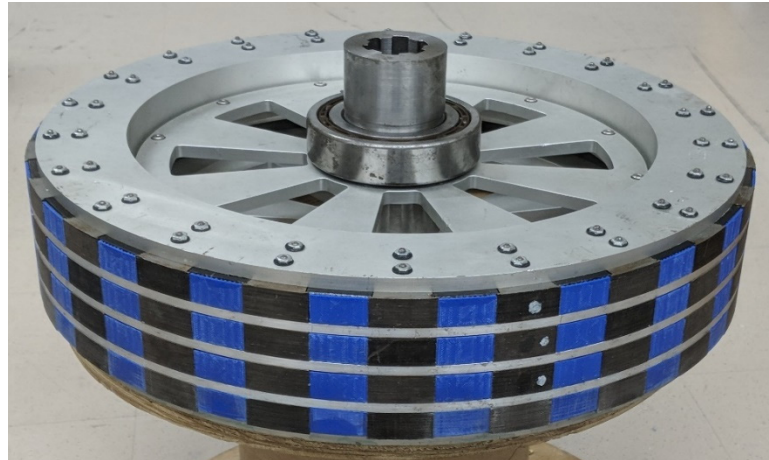
(a)
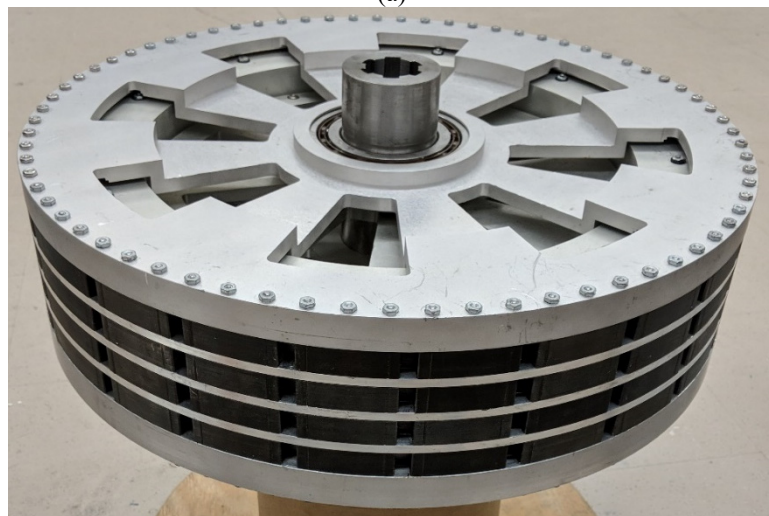
(b)
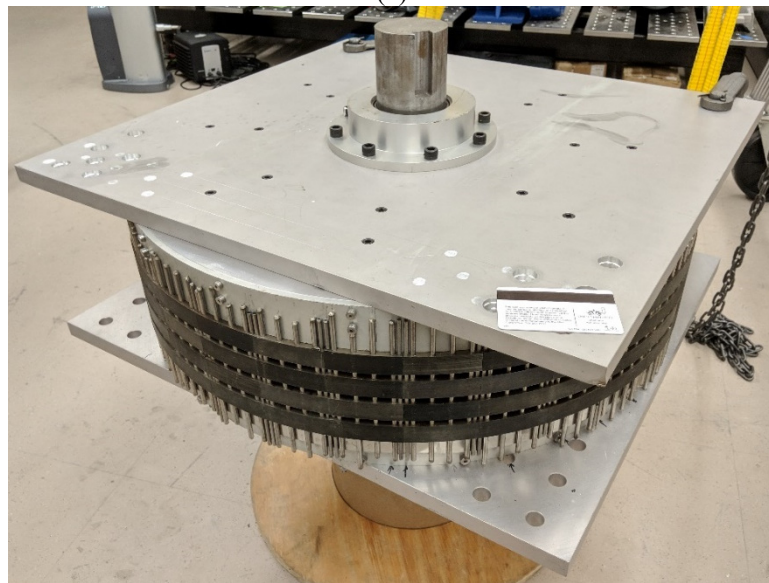
(c)

Fig. 4-40. (a) Assembled inner rotor (b) assembled inner and cage rotors (c) fully assembled stage 1 MG.

Table 4-X. Material Properties.

Description		Initial value	Final value	Unit
Material	NMX-40CH, B_m	1.28	1.28	T
	M19 conductivity	0	0	S/m
	Steel rod 416 resistivity	57	57	μΩ-cm
Axial length, d		38.1	38.1	mm
Air gap, g		0.5	1	mm

Table 4-XI. Summary of Calculated Active Material Region Torque Density

Analysis type	Air gap [mm]	Support rings	Peak torque [kNm]	Torque density Volume [Nm/L]	Torque density Mass [Nm/kg]
Magnets grade: N40 CH (B_m = 1.28 T)					
2-D FEA, design I	0.5	No	9.92	448	129
3-D FEA, design XXII	0.5	No	9.90	447	115
3-D FEA, design XXIII	0.5	Yes	8.27	298	88
3-D FEA, design XXIV	1	Yes	6.76	243	72
2-D FEA, design XXXXVII	1	No	7.07	295	72
3-D FEA, design XXXXVII	1	Yes	4.34	144	41
3-D FEA, design XXXXVII (New M19 BH curve)	1	Yes	4.26	141	40
Magnets grade: N45 SH (B_m = 1.35 T)					
3-D FEA of design XXXXVII (New M19 BH curve)	1	Yes	4.79	159	45
Measurement	1	Yes	4.25	141	40

The stage 1 MG torque was first measured using a static test as shown in Fig. 4-41. The input shaft of the stage 1 MG was locked while the output of the MG was connected to a torque transducer, mechanical gearbox and an aluminum bar. The output shaft of the MG could be rotated by rotating the aluminum bar. Therefore, the torque values at different mechanical angles have been measured and compared with the 3-D FEA model. The results are shown in Fig. 4-42.

Torque
transducer

Aluminum
bar
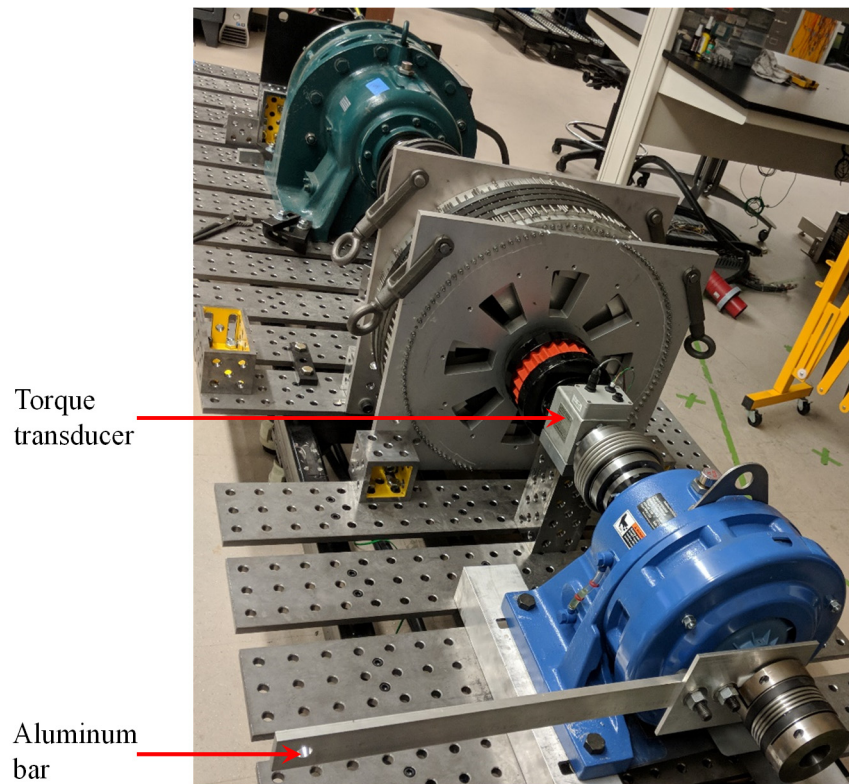
Fig. 4-41. Static test of the stage 1 MG.
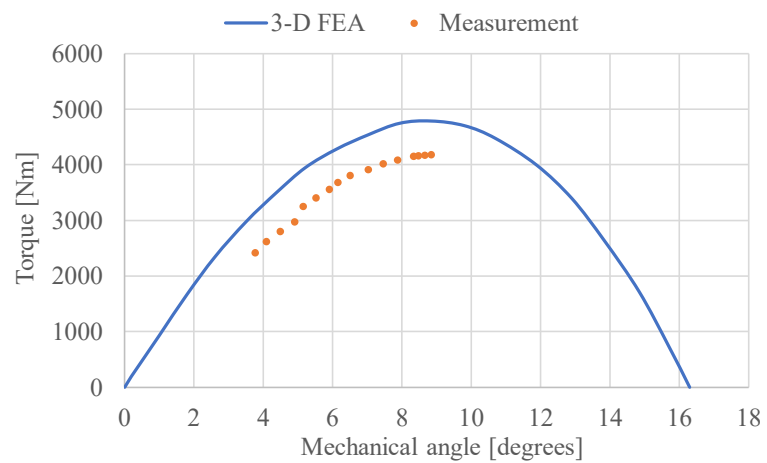
Fig. 4-42. Torque comparison between FEA and measurement (static test)

The measured peak torque was 11.3 % lower than the FEA. The possible reasons could be:

1. In the simulation, 5 mm by 5 mm radial magnets were used for the outer rotor while in reality only 3/4 of them were 5 mm by 5 mm magnets and 1/4 of them are 4 mm by 4 mm magnets.

2. After finishing the assembly of the outer rotor, it was not aligned perfectly along the axial direction (around 2 mm offset).

3. From the inner rotor field comparison result, the measured value was 2.32 % lower than the 3-D FEA. Therefore, a 4.58 % discrepancy of the torque should be expected even if everything else was perfect.

The transient setup to test the stage 1 MG is shown in Fig. 4-43. The low-speed input side of the stage 1 MG was connected to a 59:1 mechanical gearbox. The high-speed output side was connected to a 11:1 mechanical gearbox and a generator.
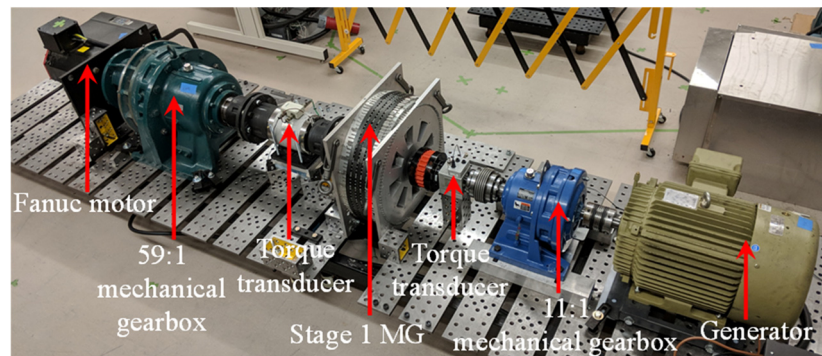
Fig. 4-43. Transient test setup for the stage 1 MG.

When the generator did not apply any load on the output side, the input and output torque were measured at different speeds. The corresponding losses are shown in Fig. 4-44. The input and output torque have been measured with different loads. The results are shown in Fig. 4-45 when the input speed is 5 RPM. The absolute and percentage torque ripple values are shown in Fig. 4-46 for the inner and cage rotors. It can be seen

that the calculated and measured torque ripple values do not change significantly with load. With the torque values in Fig. 4-45, the efficiency can be calculated using (4.2) and the results are shown in Fig. 4-47.
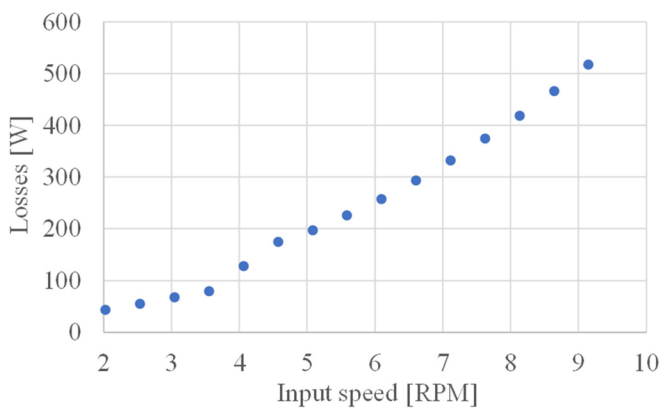
Fig. 4-44. Loss values for different speeds (with no load).
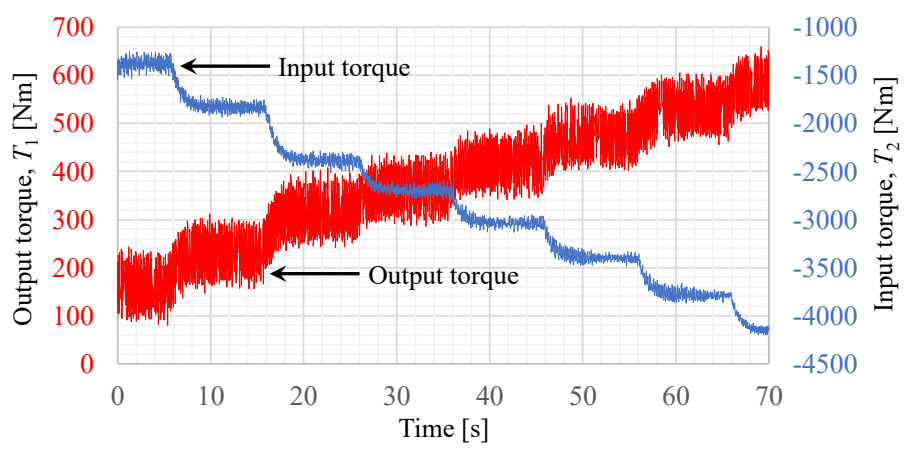
Fig. 4-45. Transient torque on the cage rotor and inner rotor with different loads when the input speed is 5 RPM.
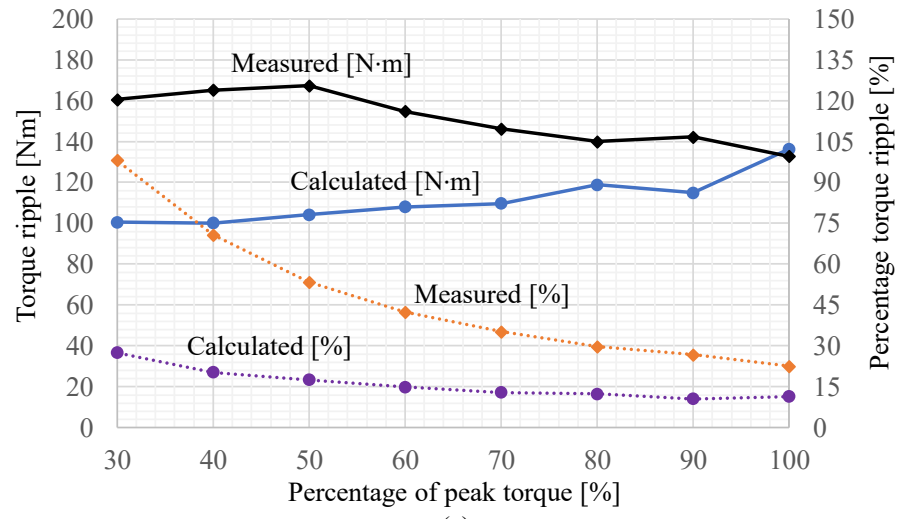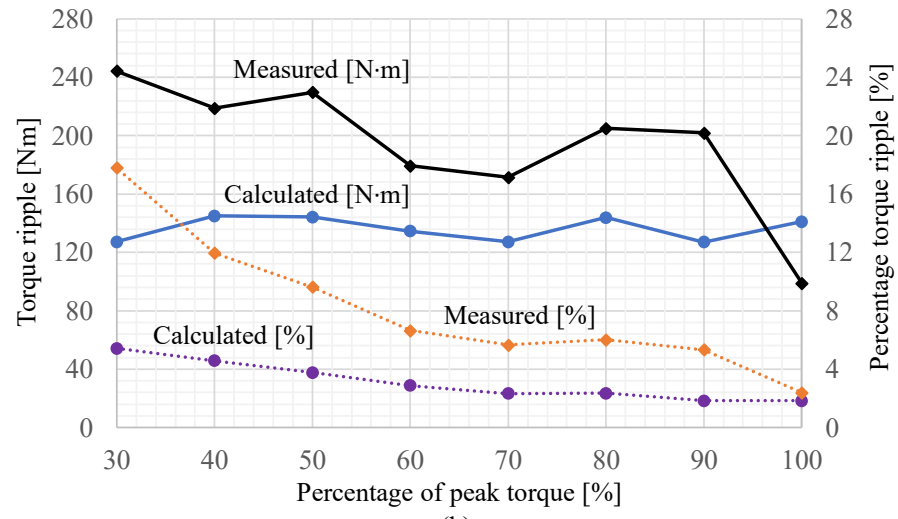
Fig. 4-46. Measured and calculated torque ripple on the (a) inner and (b) cage rotors as a percentage of load.
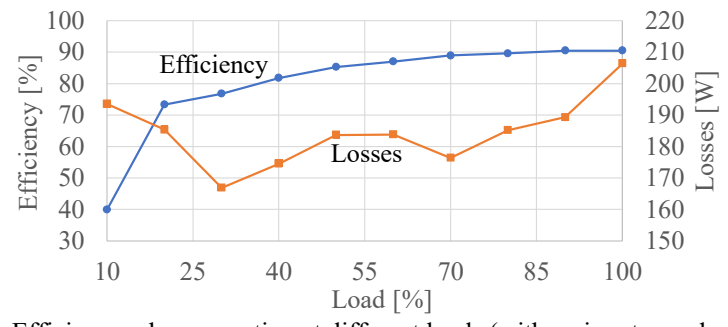
Fig. 4-47. Efficiency when operating at different loads (with an input speed of 5 RPM).

4.4. INITIAL DESIGN OF STAGE 2 MAGNETIC GEARBOX

In order to achieve an overall 59:1 gear ratio, the pole pair combination of stage 2 was initially chosen to be $p_4 = 6$, $n_5 = 55$ and $p_6 = 49$. The outer rotor was fixed giving a gear ratio of 9.17. The initial Design #1 is shown in Fig. 4-48.

(a)

(b)
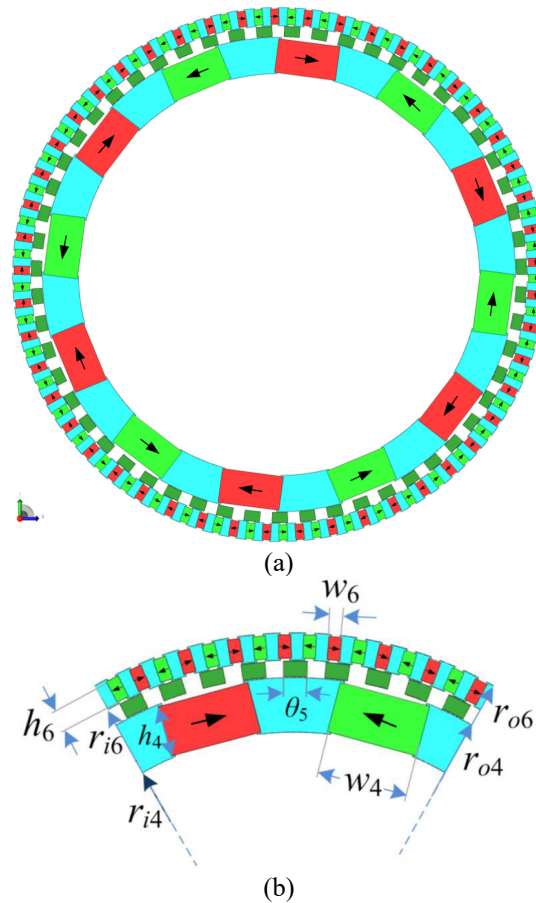
Fig. 4-48. (a) Initial Design #1 of stage 2 magnetic arrangement for the series connected magnetic gearbox (b) geometry definitions.

In order to optimize the performance and obtain a high torque value, a parameter sweep analysis was conducted. The inner radius of the inner rotor was fixed at a constant $r_{i4} = 155$ mm so that there is enough space for adding a stator inside. The outer radius of the outer rotor, r_{o6} was first fixed. Then the radial length of the cage rotor, l_5 and the outer radius of the inner rotor, r_{o4} were varied to obtain the peak mass torque density. Then

another value of r_{o6} was chosen and the process was repeated. Fig. 4-49-Fig. 4-51 show the parameter sweep results when $r_{o6} = 200$ mm, $r_{o6} = 205$ mm and $r_{o6} = 210$ mm. The peak value was chosen for each value of r_{o6}. Fig. 4-52 shows the mass and volume torque densities when r_{o6} was varied from 200 mm to 240 mm.
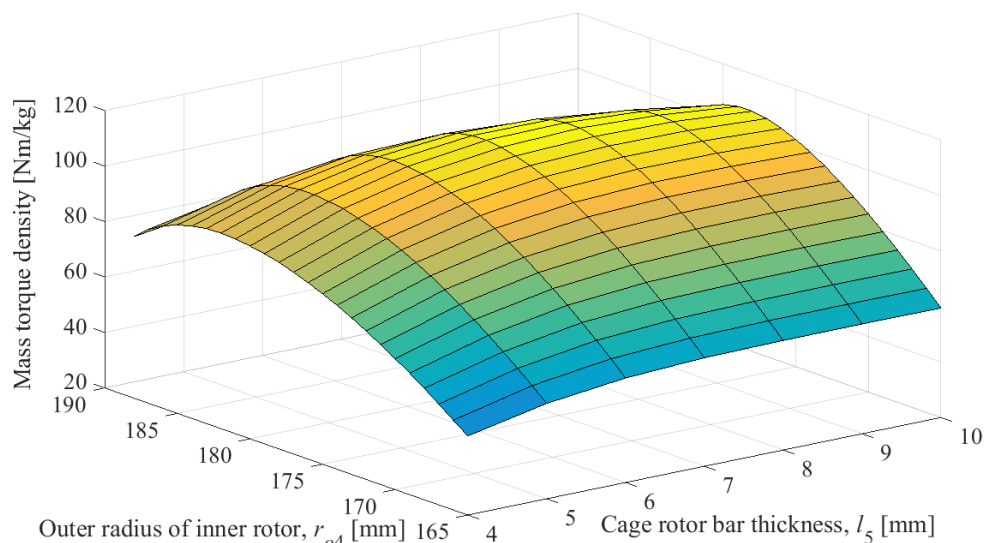
Fig. 4-49. Parameter sweep results when $r_{o6} = 200$ mm.
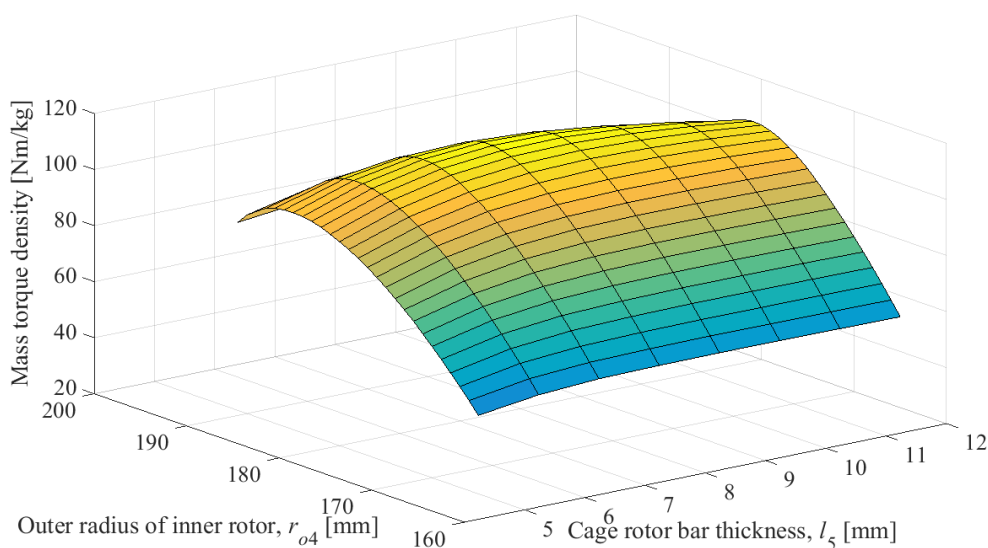
Fig. 4-50. Parameter sweep results when $r_{o6} = 205$ mm.
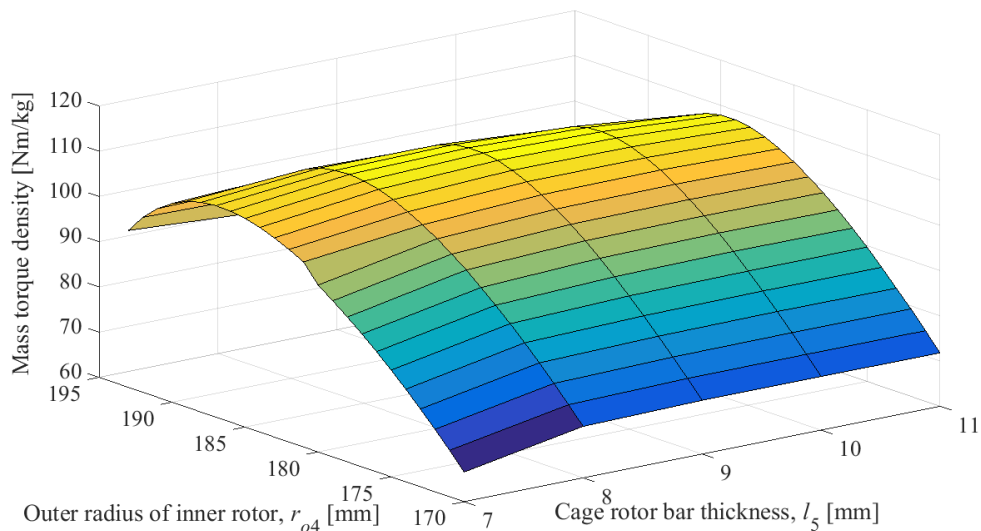
Fig. 4-51. Parameter sweep results when r_{o6} = 210 mm.
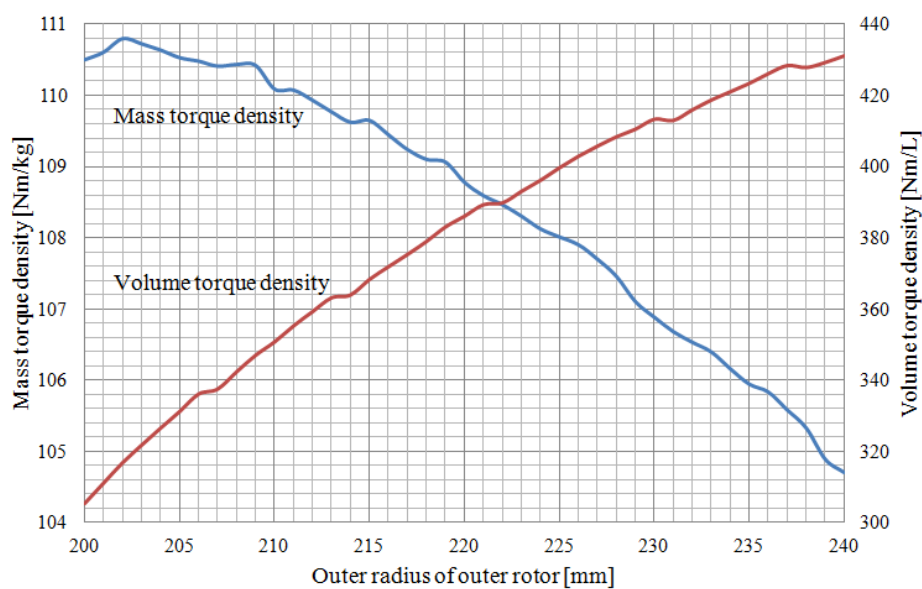
Fig. 4-52. Torque density plot when the outer radius of the outer rotor was varied.

It can be seen that the volume torque density keeps increasing with r_{o6} increasing, while the mass torque density is decreasing. To achieve a high volume torque density and a relatively high mass torque density, the outer radius, r_{o6} was chosen to be 240 mm. The 2-D and 3-D geometries of Design #2 with magnet retaining lips and 1-mm bridges are shown in Fig. 4-53 and Fig. 4-54. The parameters are described in Table 4-XII.
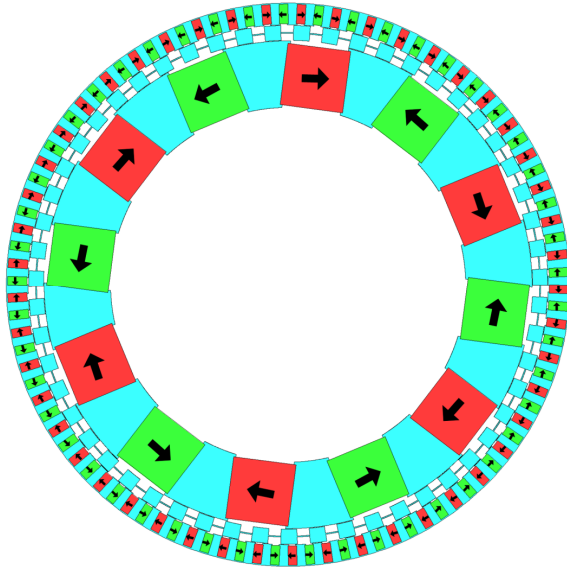
Fig. 4-53. 2-D FEA model with magnet retaining supports and bridges for Design #2.
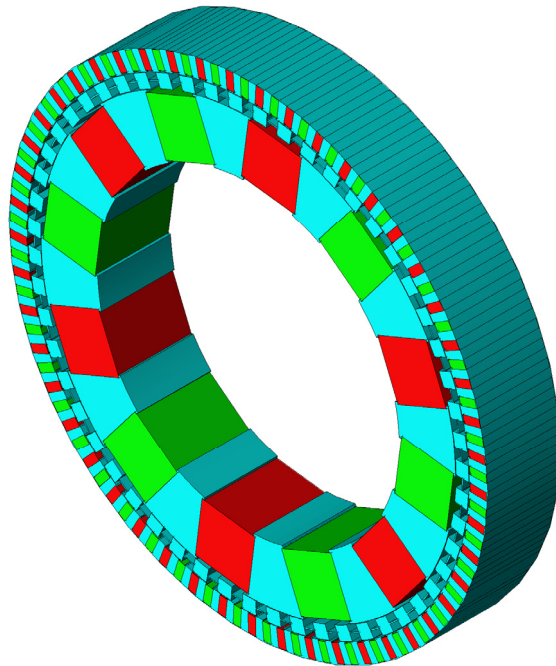
Fig. 4-54. 3-D FEA model with magnet retaining supports and bridges for Design #2.

Table 4-XII. PARAMETERS OF STAGE 2 MG

Description		Value	Unit
Inner rotor	Inner radius, r_{i4}	155	mm
	Outer radius, r_{o4}	213	mm
	Magnet length, h_4	54.0	mm
	Magnet width, w_4	55.1	mm
	Torque, T_4	325.5	Nm
	Speed, ω_4	1952.5	RPM
Cage rotor	Inner radius, r_{i5}	213.5	mm
	Outer radius, r_{o5}	226.5	mm
	Torque, T_5	-5463.9	Nm
	Speed, ω_5	213	RPM
Outer rotor	Inner radius, r_{i6}	227	mm
	Outer radius, r_{o6}	246	mm
	Magnet length, h_6	17.0	mm
	Magnet width, w_6	7.8	mm
	Torque, T_6	5131.7	Nm
Axial length, d		75	mm
Air gap, g		0.5	mm

As mentioned in the previous chapters, a MG will have a higher torque with a higher number of pole pairs. Therefore, in order to increase the torque further, a pole pair combination of 7-64-57 has been chosen with the same radii provided in Table 4-XII. The 2-D geometry of this Design #3 is shown in Fig. 4-55. Since the torque on the inner rotor of the stage 1 MG is less than 2 kNm, the torque on the cage rotor of the stage 2 MG only needs to be higher than 2 kNm. Therefore, the axial length of stage 2 MG can be reduced down to be half (38.1 mm) to reduce the material cost and weight. The torque plots on the inner, cage and outer rotors are shown in Fig. 4-56-Fig. 4-58.
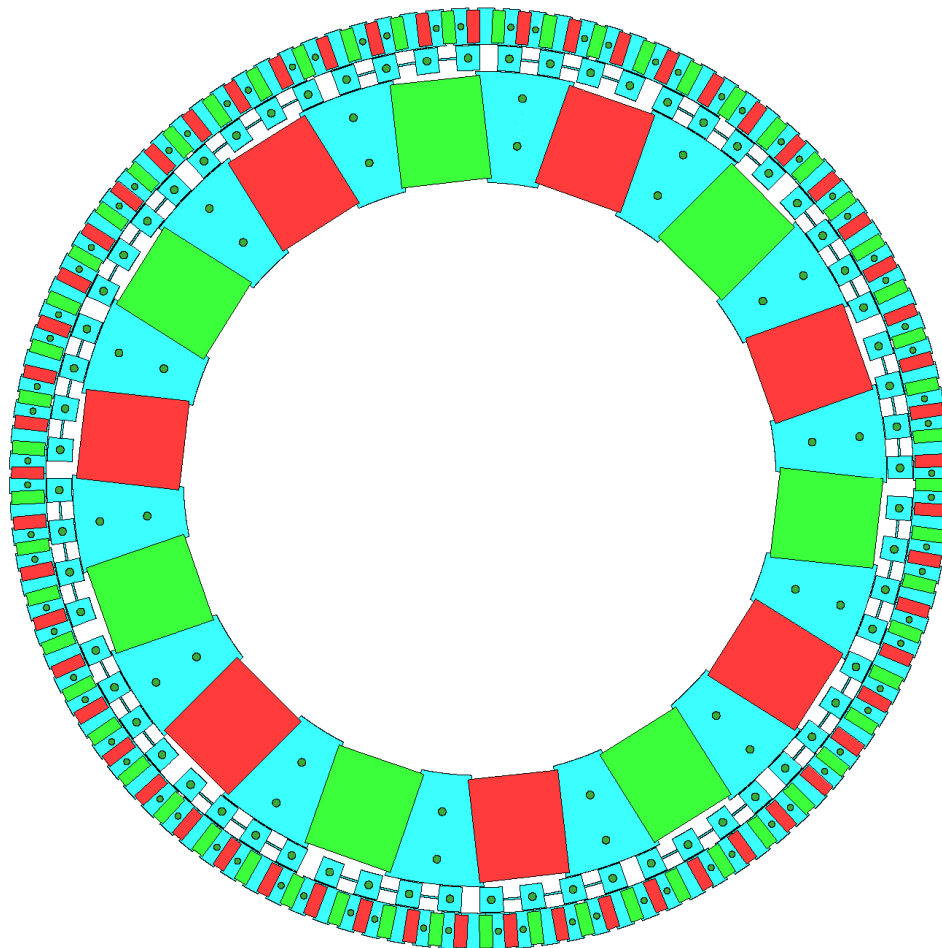
Fig. 4-55. Design #3 of stage 2 MG with bridges and rods.
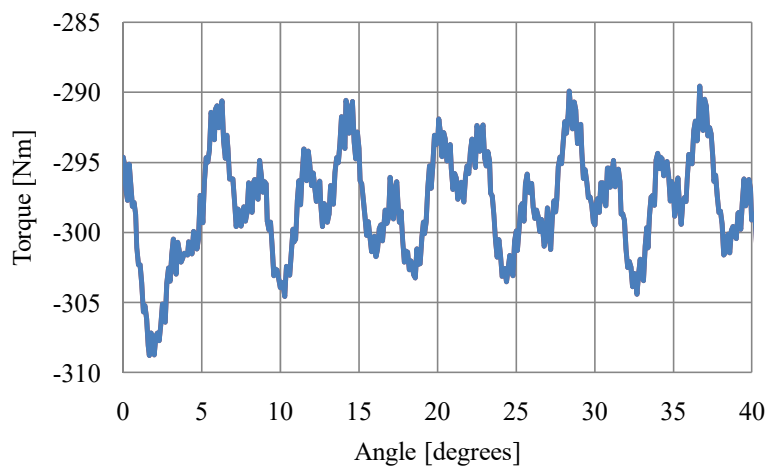
Fig. 4-56. Torque on the inner rotor.
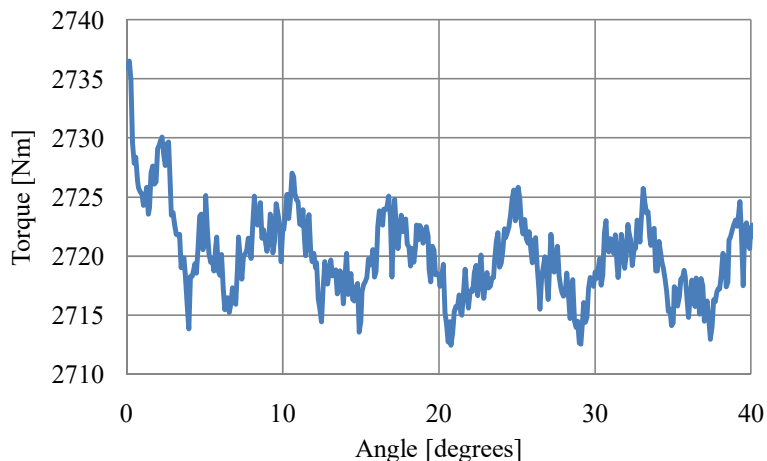
Fig. 4-57. Torque on the cage rotor.
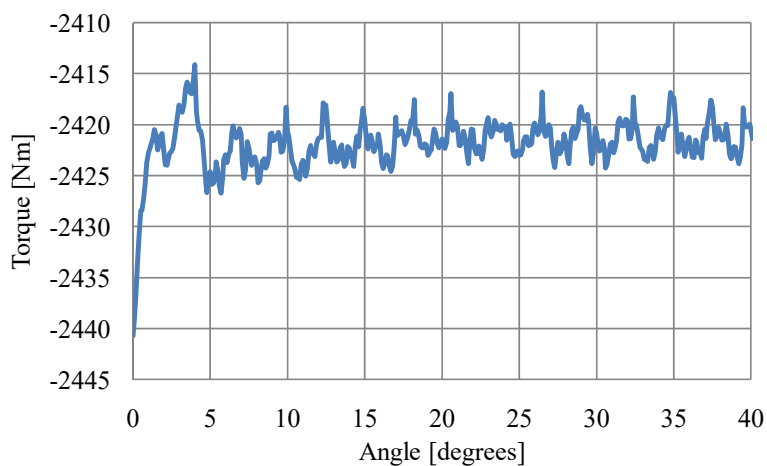
Fig. 4-58. Torque on the outer rotor.

Because of the deflection issue that happened to the stage 1 MG, the radial and tangential forces were calculated on each single lamination bar when the cage rotor was rotating at 5 RPM. The force values are shown in Fig. 4-59-Fig. 4-64. Since the force on the cage lamination is applied to one single rod, while the force on the inner lamination is applied to two rods. For the outer lamination, the force is applied to the rod as well as the 1-mm thick bridge. Therefore, the inner rods will not have deflection issue while the cage and outer rods will have the same deflection issue that were with the stage 1 MG. To

solve the deflection issues, the air gap has been increased from 0.5 mm to 1 mm. The outer and cage laminations have been re-fabricated in order to provide more support and make the assembling process easier.
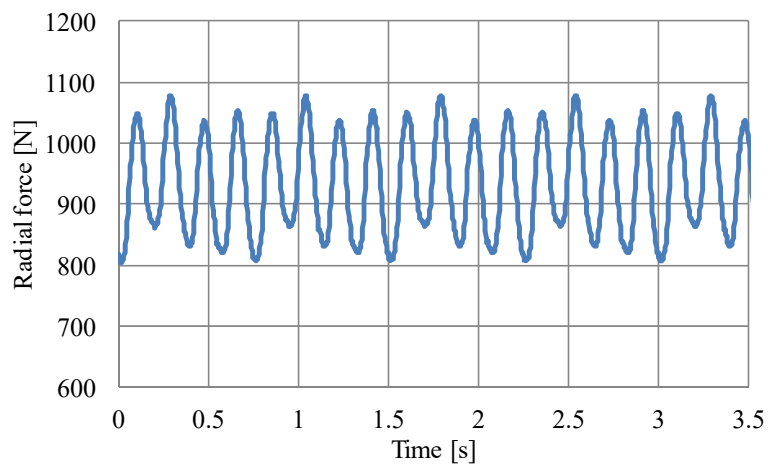
Fig. 4-59. Radial force on one single inner lamination bar.
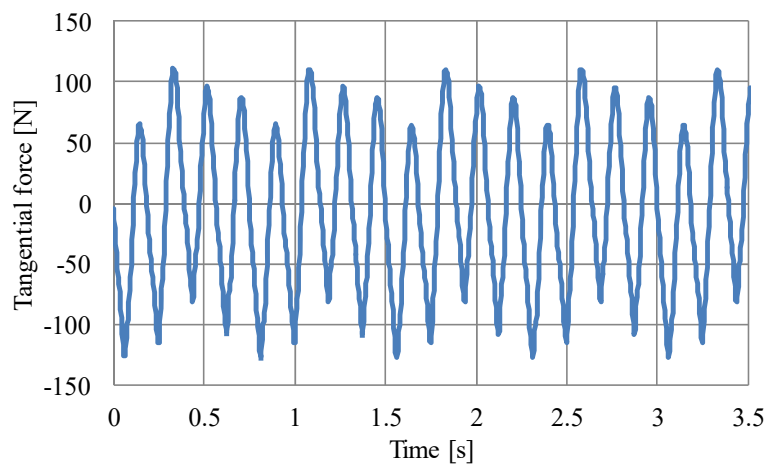
Fig. 4-60. Tangential force on one single inner lamination bar.
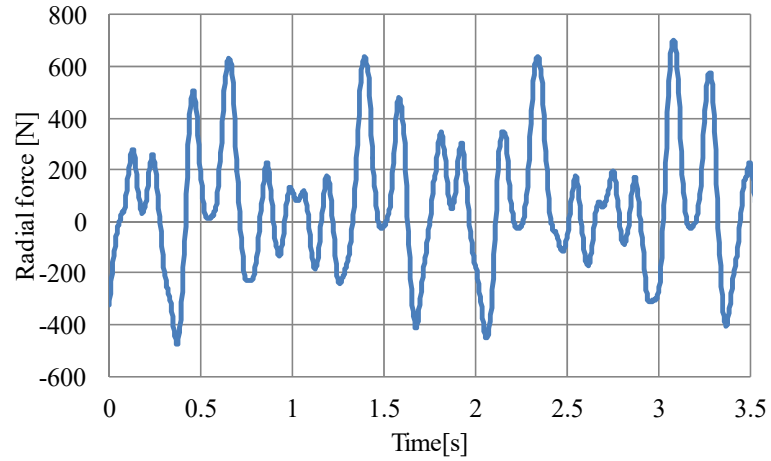
Fig. 4-61. Radial force on one single cage lamination bar
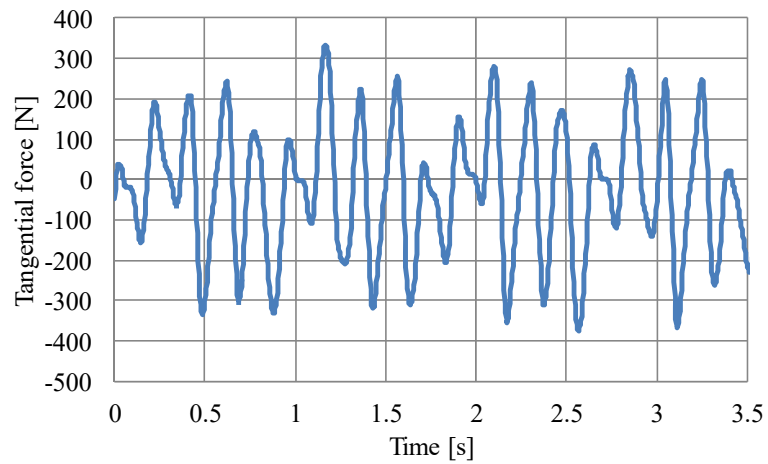
Fig. 4-62. Tangential force on one single cage lamination bar.
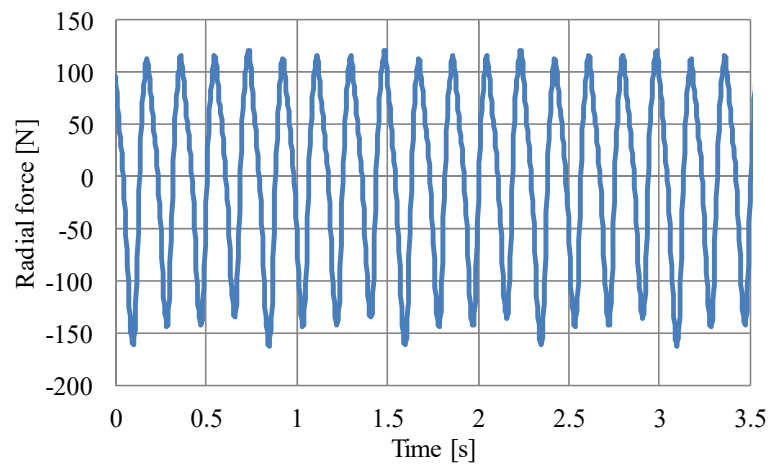
Fig. 4-63. Radial force on one single outer lamination bar.
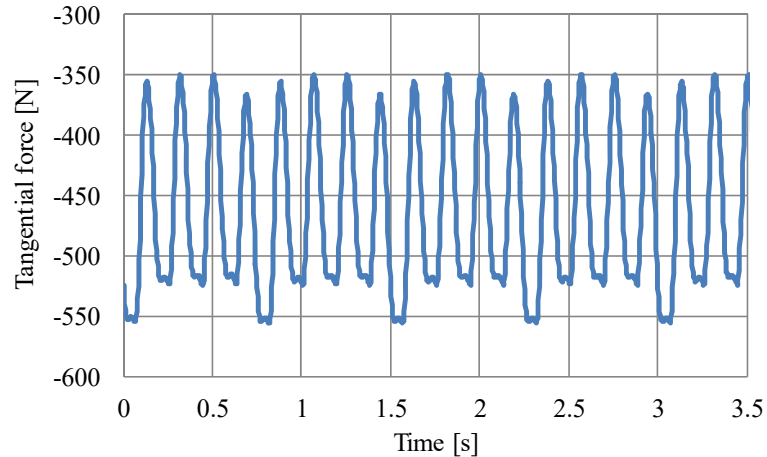
Fig. 4-64. Tangential force on one single outer lamination bar.

4.5. IMPROVED DESIGN OF STAGE 2 MAGNETIC GEARBOX

As the stage 1 MG has met deflection and assembly issues [60], a more robust structural design was sought for stage 2 MG. As the inner rotor does not experience significant radial deflection forces for the stage 1 MG design, the inner rotor laminations and magnet design was unchanged from what is shown in Fig. 4-55. Therefore $(r_{i4}, r_{o4}) =$ (155, 213) mm is fixed. This decision was made to reduce re-fabrication costs.

An ideal outer and cage rotor typology was first considered in which the airgaps were increased to 1 mm, this Design #4 is shown in Fig. 4-65. The ideal design gives the upper torque capability limit for this design. The air gap was increased in order to provide more tolerance robustness.
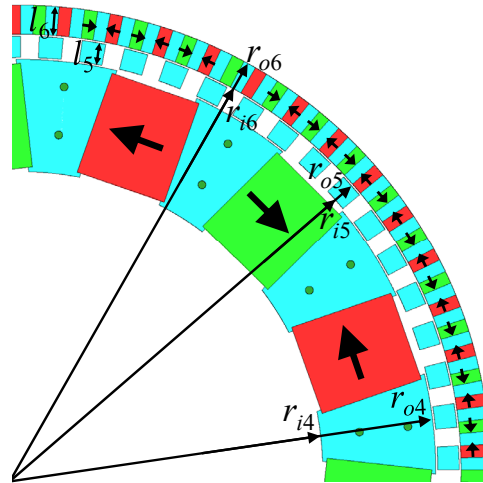
Fig. 4-65. Idealized Design #4 of stage 2 magnetic gearbox with a 1 mm air gap.

To maximize torque density, the cage rotor and the outer rotor radial lengths were varied. The radial length of the cage rotor is defined as:

$$l_5 = r_{o5} - r_{i5}$$ (4.6)

and the radial length of the outer rotor is:

$$l_6 = r_{o6} - r_{i6}$$ (4.7)

The cage rotor length was varied from l_5 = 7 mm to l_5 = 16 mm at 1 mm intervals. The outer rotor length was also varied from l_6 = 15 mm to l_6 = 35 mm at 1mm step intervals. The results for the 210 different 2-D FEA simulation cases have been plotted in Fig. 4-66 where the active region volumetric and mass torque density are compared. The equations used to compute the torque density are defined in (3.10) and (3.13). The radial length of the cage rotor, l_5, is shown in the legend of Fig. 4-66. Fig. 4-66 shows that a peak exists for maximizing the volumetric torque density and this is at the expense of a non-optimal

mass torque density. Table 4-XIII gives a summary of the peak torque density values for each cage bar length l_5. The peak torque density occurs when $l_5 = 10$ mm.
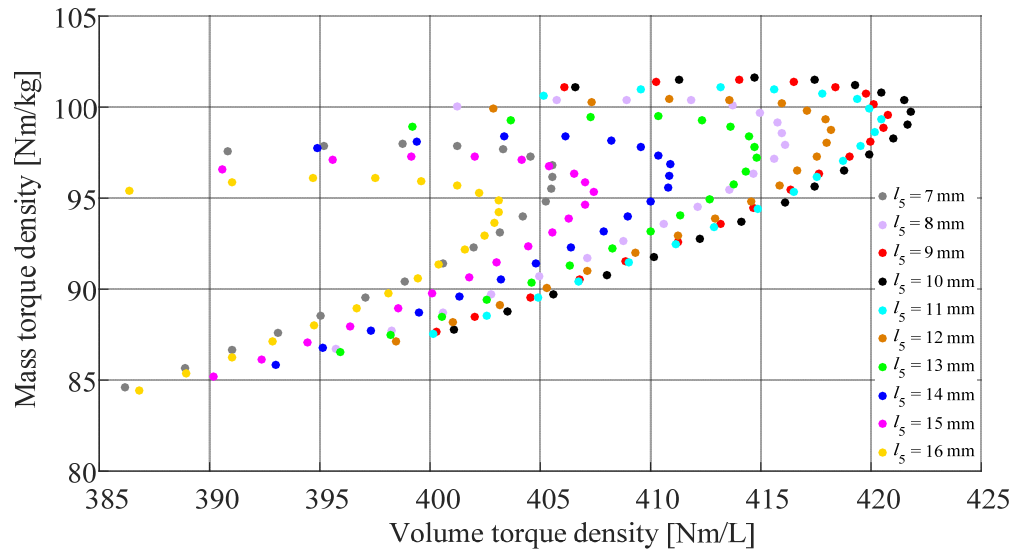
Fig. 4-66. Mass and volume torque density analysis plot when l_5 and l_6 were both varied for the idealized stage 2 MG design.

Table 4-XIII. 2-D Calculated Peak Torque Density at Respective Cage Bar Lengths.

l_5 [mm]	l_6 [mm]	Volume torque density [Nm/L]	Mass torque density [Nm/kg]
7	21	405.5	96.8
8	23	416.1	97.9
9	22	420.7	99.6
10	22	421.8	99.8
11	22	420.5	99.4
12	22	418.2	98.7
13	23	414.8	97.2
14	22	410.9	96.9
15	23	407.4	95.3

In order to make the MG have higher mechanical strength a 1-mm bridge was added on both radial sides of the cage rotor and outer rotor as shown in Fig. 4-67 for Design #5. The radial length of the cage rotor and outer rotor was then again varied. The resultant torque density plot and results are shown in Fig. 4-68 and Table 4-XIV. The bridges

introduce significant additional flux leakage, as shown in Fig. 4-69, and this greatly reduce the peak torque density. From studying Table 4-XIV it can be noted that the peak torque density now occurs when l_5 = 12 mm.
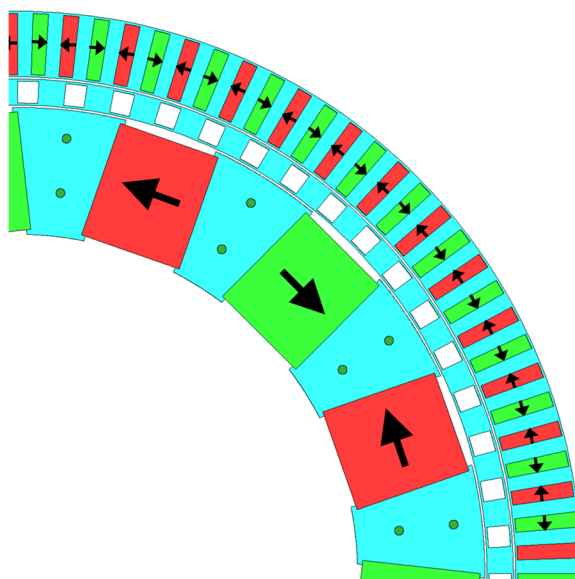
Fig. 4-67. Design #5 of stage 2 MG with 1 mm bridges on the cage and outer rotors.
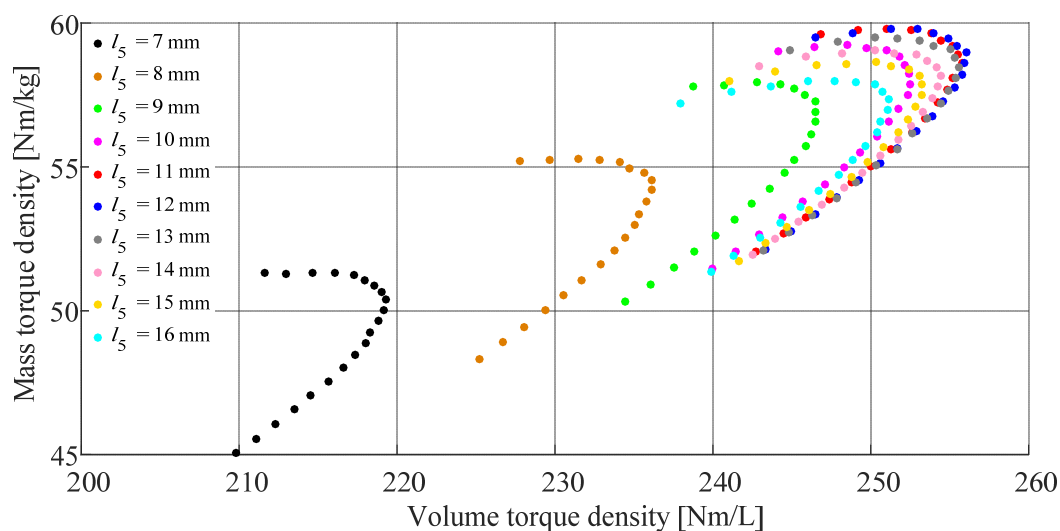
Fig. 4-68. Mass and volume torque density analysis plot when l_5 and l_6 were both varied for the MG bridge design. The length l_6 was varied from 17 mm to 37 mm at 1mm intervals.

Table 4-XIV. Peak Torque Density at Respective Cage Bar Lengths

l_5 [mm]	l_6 [mm]	Volume torque density [Nm/L]	Mass torque density [Nm/kg]
7	25	219.3	50.4
8	25	236.2	54.2
9	25	246.5	56.6
10	25	252.5	57.9
11	25	255.8	58.6
12	24	256.1	59.0
13	25	255.6	58.5
14	25	254.4	58.2
15	26	253.2	57.5

(a)   (b)
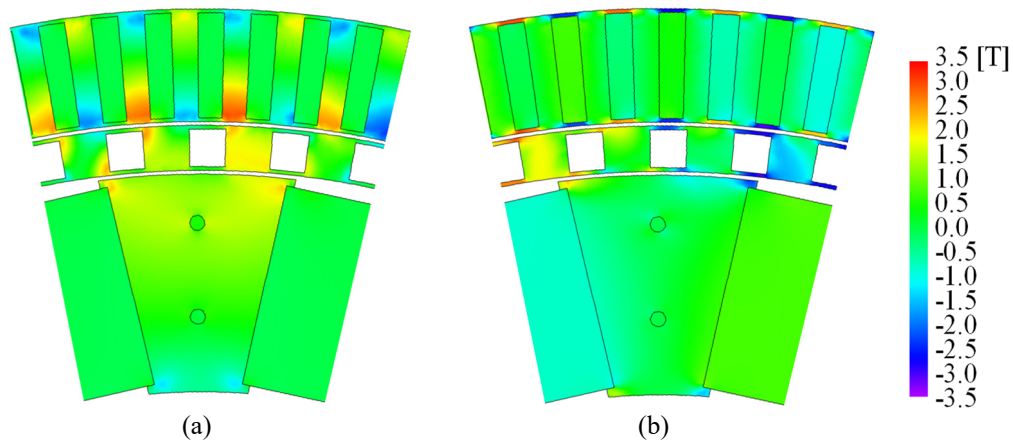
Fig. 4-69. (a) Radial flux density B_r and (b) azimuthal flux density B_θ for the bridge support MG design when $(l_5, l_6) = (12, 30)$ mm. The bridge leakage flux is clearly evident.

In order to fabricate the laminated parts, the cage and outer rotor has to be segmented. The radial size is too large to be manufactured as one piece. The analysis in Fig. 4-65 and Fig. 4-67 was repeated for the case when the cage and outer lamination steels were segmented as shown in Fig. 4-70 for Design #6.
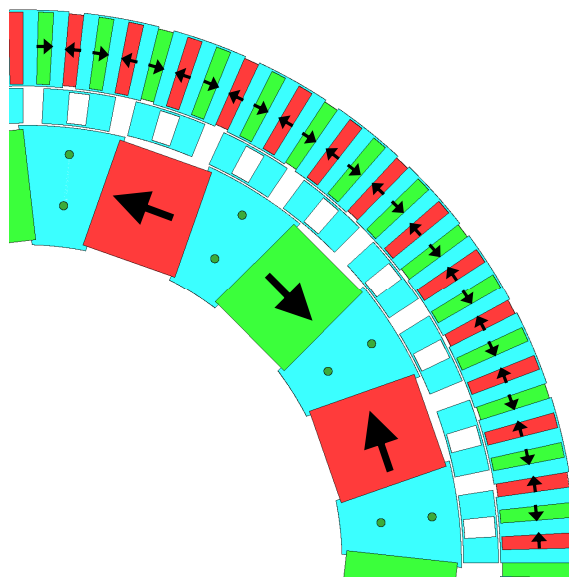
Fig. 4-70. Design #6 of stage 2 MG with 1-mm bridges on the cage and outer rotors and segmented sections.

The sweep analysis results for all length combinations are shown in Fig. 4-71. It can be noted that the peak torque density increases. Fig. 4-72 shows the torque vs. mass torque density and volume torque density for the segmented design. The peak volume torque density values for the different cage bar radial lengths, l_5, are summarized and shown in Table 4-XV.
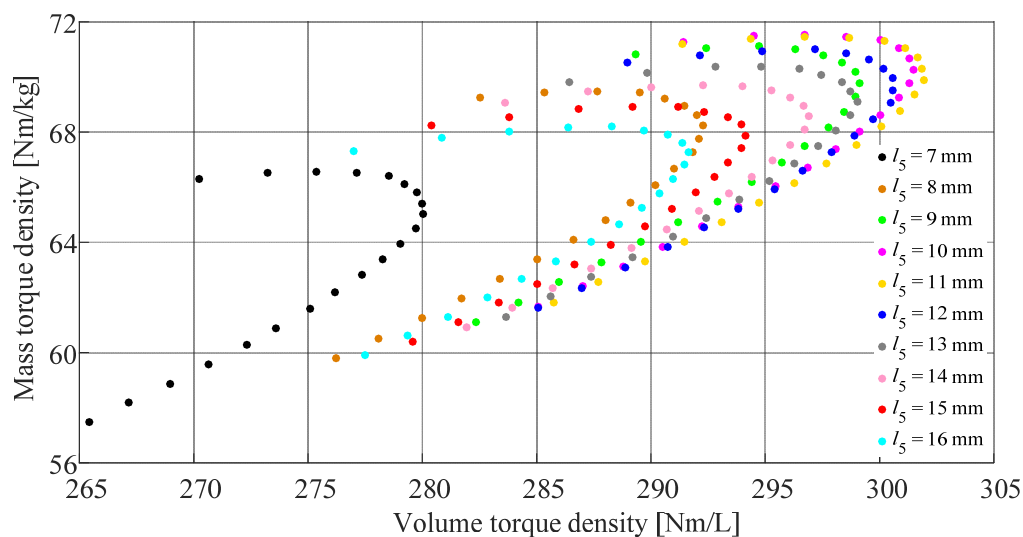
Fig. 4-71. Mass and volume torque density analysis plot when l_5 and l_6 were both varied for the segmented bridge design. The length l_6 was varied from 17 mm to 37 mm.
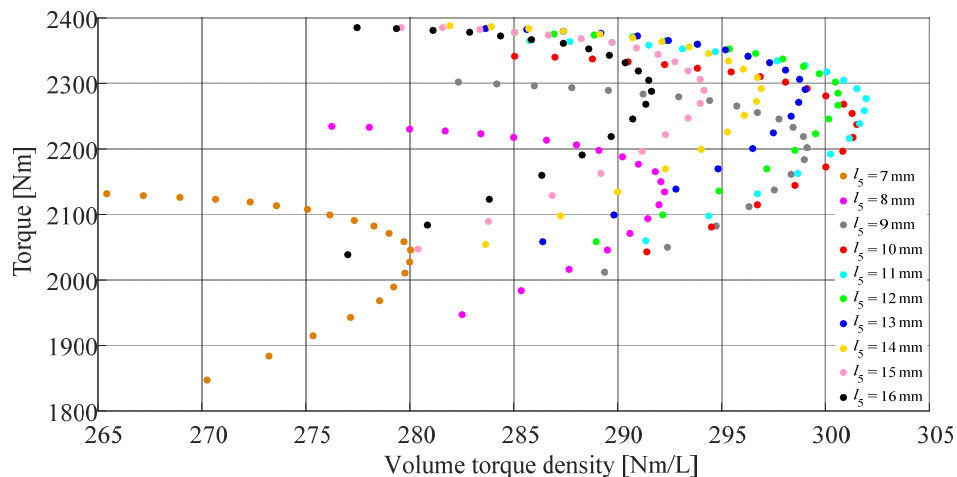
(a)
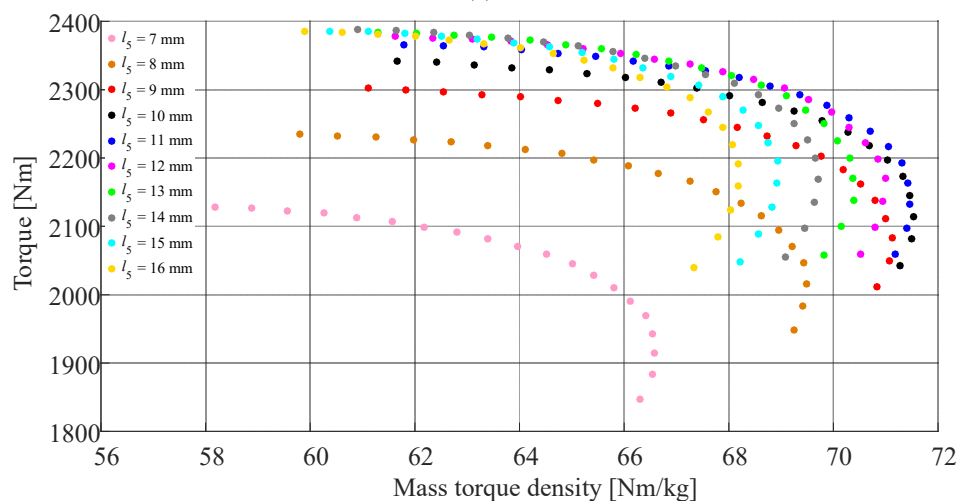
(b)

Fig. 4-72. (a) Torque vs. volumetric torque density and (b) torque vs. mass torque density when l_5 and l_6 were varied.

Table 4-XV. PEAK TORQUE DENSITY AT RESPECTIVE CAGE BAR LENGTHS.

l_5 [mm]	l_6 [mm]	Volume torque density [Nm/L]	Mass torque density [Nm/kg]
7	25	280.0	65.0
8	24	292.2	68.2
9	24	299.1	69.7
10	24	301.4	70.2
11	25	301.9	69.8
12	24	300.5	69.9
13	25	299.0	69.1
14	25	296.8	68.5
15	25	294.1	67.8

From Fig. 4-72, the peak torque density does not occur at the peak torque. It is because higher torque values are only achieved when the outer rotor radius, r_{o6} is increased.

In order to use larger rods to reduce the deflection, the outer rotor typology was modified to be Design #7 as shown in Fig. 4-73. The outer rotor is still supported by bridges like in the prior design. However, the outer rotor radius now has support holes for retaining rods but no bridges. This design change mitigates some of the outer leakage flux whilst still providing mechanical support to both sides of the outer rotor. Furthermore, it moves the outer rotor support rods away from the air-gap thereby significantly reducing eddy current losses. The reduction in outer radius leakage is evident as shown in Fig. 4-74 and the final 3-D geometry is shown in Fig. 4-75.
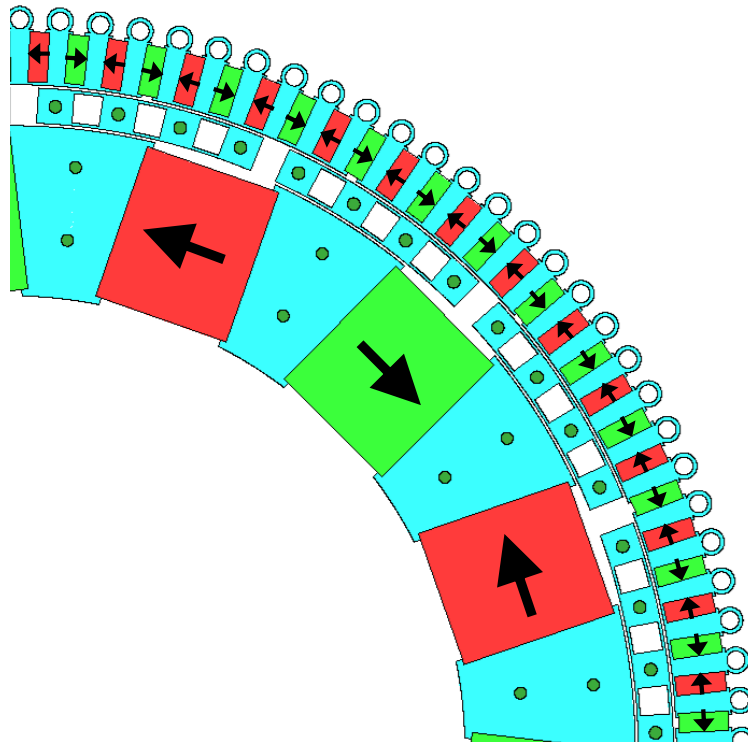
Fig. 4-73. Final design of the stage 2 MG.
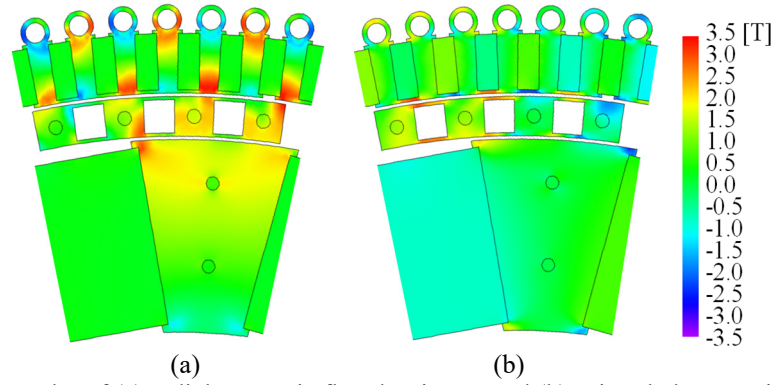
Fig. 4-74. Surface plot of (a) radial magnetic flux density, B_r and (b) azimuthal magnetic flux density, B_θ.
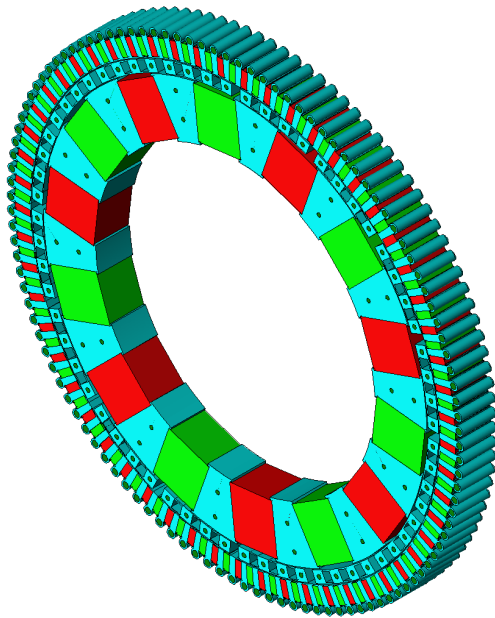
Fig. 4-75. Final 3-D geometry of the stage 2 MG.

The magnetic fields for the inner and outer magnets have been measured and compared with the 3-D FEA results. The comparison is shown in Fig. 4-76 and a good agreement has been achieved.

(a)

(b)
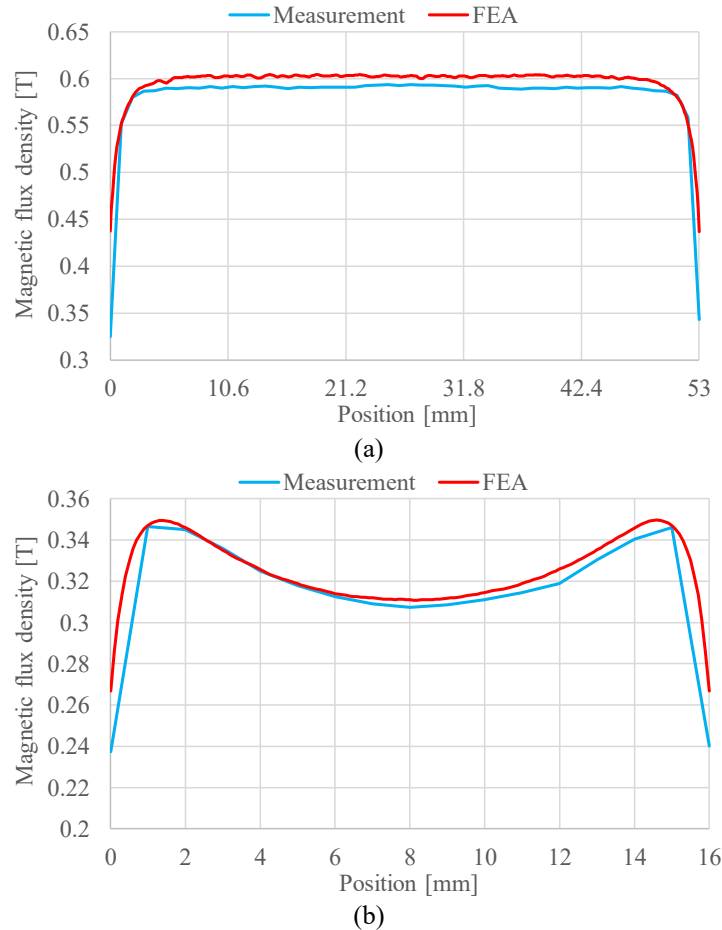
Fig. 4-76. Magnetic field comparison for the (a) inner magnets and (b) outer magnets.

It should also be noted that in this final design the outer rotor radial length was reduced to enable existing outer magnets to be used which have a length of l_{om} =17 mm. A summary of the final MG design parameters is given in Table 4-XVI. The 2-D calculated volume and mass torque density (with magnet grade N40 CH) are 232 Nm/L and 57 Nm/kg, respectively. The torque ripple in 2-D is shown in Fig. 4-77. However, the 3-D calculated volume and mass torque density (with magnet grade N40 CH) are only 124 Nm/L and 30 Nm/kg, respectively. The reduction of the torque value in 3-D is because of the small axial length (compared to the outer radius). The field edge effects across the cross-section are clearly apparent in Fig. 4-78. This explains the discrepancy

between the 2-D and 3-D models. When ordering the magnets, the magnet grade was

chosen as N45 SH. This increased the 3-D calculated volume and mass torque density

(with magnet grade N45 SH) to be 135 Nm/L and 33 Nm/kg.

Table 4-XVI. GEOMETRIC AND MATERIAL PROPERTIES FOR INITIAL AND FINAL STAGE 2 MAGNETIC GEARBOX DESIGN.

Description		Initial value	Final value	Unit
Inner rotor	Inner radius, r_{i4}	155	155	mm
	Outer radius, r_{o4}	213	213	mm
	Radial magnet length	54	54	mm
	Magnet width	47.25	47.25	mm
Cage rotor	Inner radius, r_{i5}	213.5	214	mm
	Outer radius, r_{o5}	226.5	226	mm
Outer rotor	Inner radius, r_{i6}	227	227	mm
	Outer radius, r_{o6}	246	253.675	mm
	Radial magnet length	17	17	mm
	Magnet width	6.75	6.75	mm
Material	NMX-40CH, B_m	1.28	1.28	T
	M19 conductivity	0	0	S/m
	Steel rod 416 resistivity	57	57	μΩ-cm
Axial length, d		38.1	38.1	mm
Air gap, g		0.5	1	mm
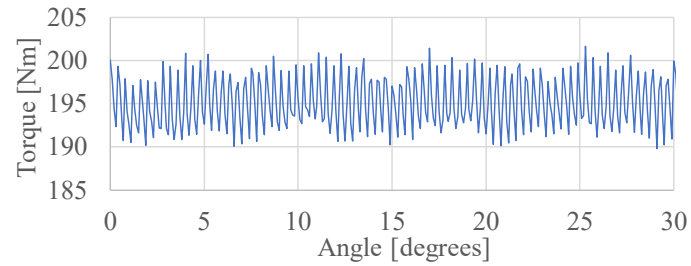
(a)
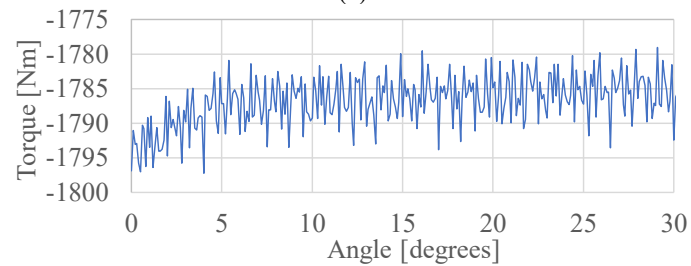
(b)

Fig. 4-77. Calculated 2-D transient FEA torque on (a) the inner rotor and (b) cage rotor when neglecting losses.
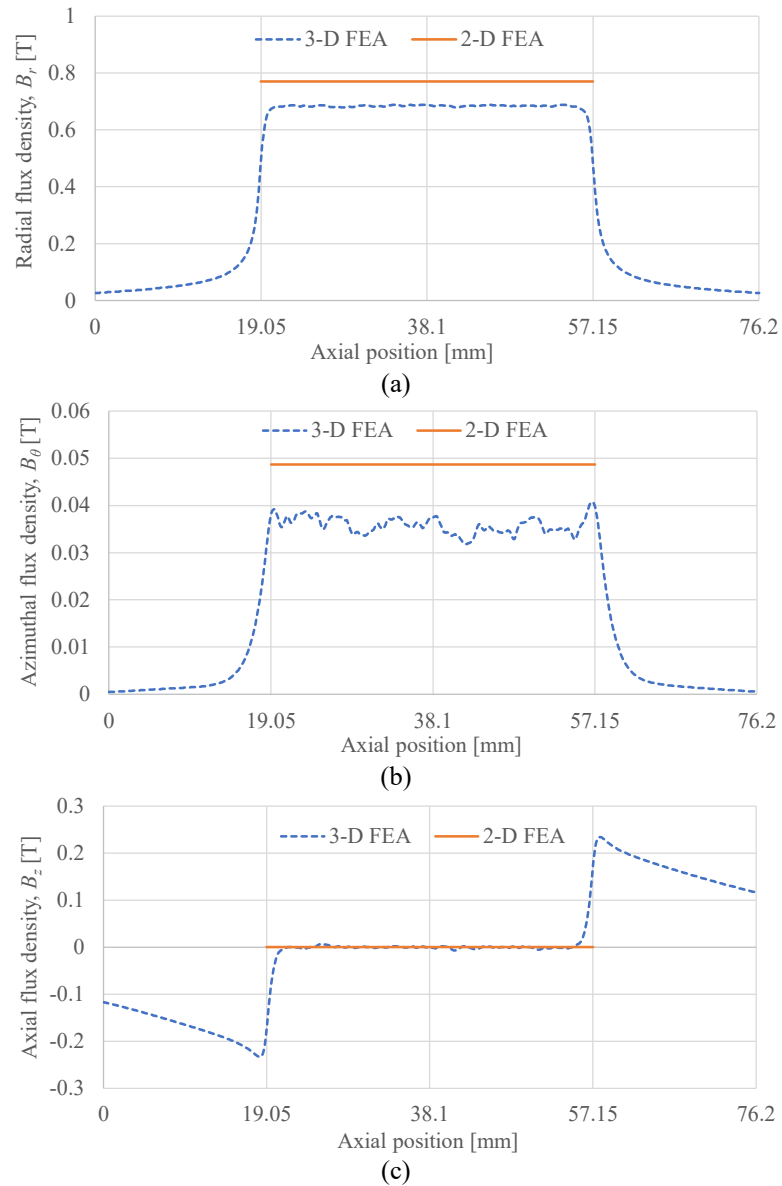
Fig. 4-78. (a) Radial (b) azimuthal and (c) axial magnetic field components along the axial length from 2-D and 3-D models. The values were calculated at $r = 213.5$ mm. The stage 2 MG region is from 19.05 mm to 57.15 mm

The mechanical assembly is shown in Fig. 4-79 and Fig. 4-80. The assembled inner rotor is shown in Fig. 4-81. The magnetic field has been measured at 0.66 mm above the surface and compared with FEA result which is shown in Fig. 4-82. The 1st, 3rd and 5th harmonic components have been calculated and compared as shown in Fig. 4-83. The

discrepancy of the fundamental component between measurement and 3-D FEA is only

1.42 %.
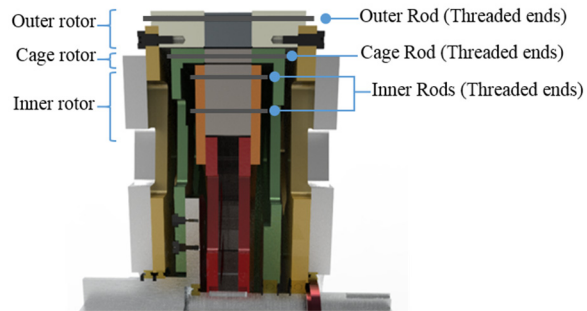
Fig. 4-79. Positioning of inner, cage and outer rotor connecting components of stage 2 MG [figure from Sina Modaresahmadi].
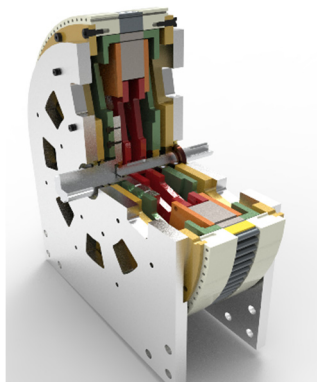
Fig. 4-80. A 90-degree cut-away view of the stage 2 MG showing all the interior mechanical components [figure from Sina Modaresahmadi].
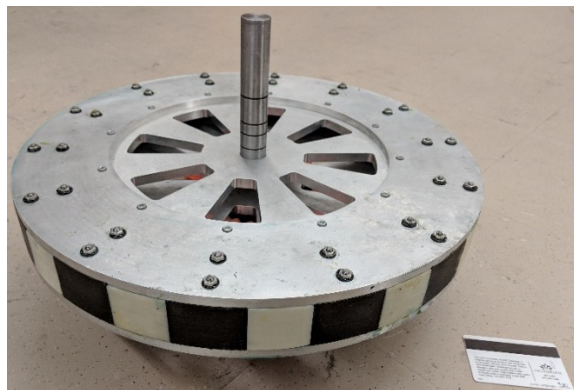
Fig. 4-81. Assembled inner rotor of stage 2 MG.
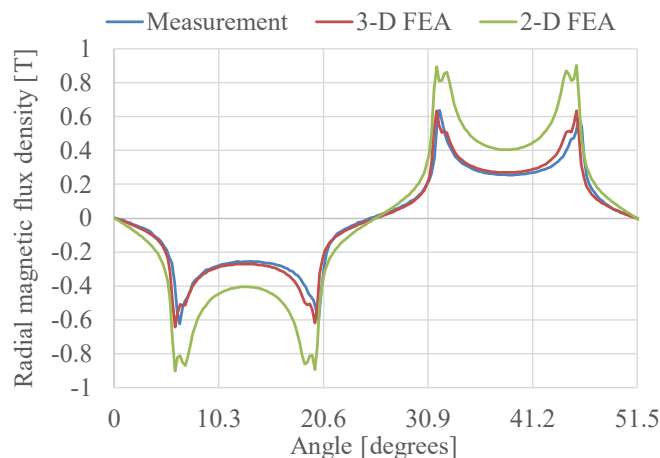
Fig. 4-82. The comparison of the inner rotor field between measurement and FEA.
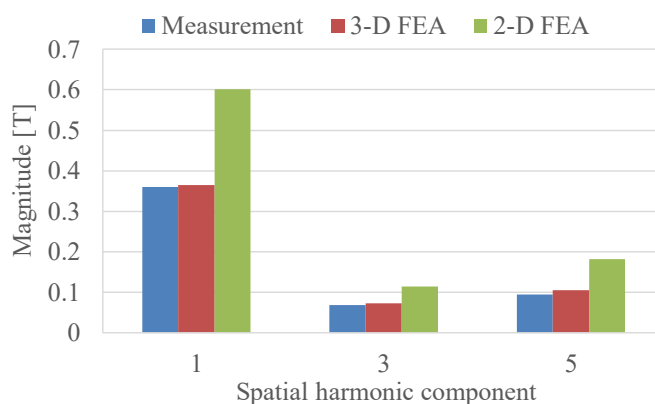
Fig. 4-83. Harmonic analysis of the inner rotor field.

Initially, there were no insulation between the rods and the aluminium endplates. This will result in a significant increase in the eddy current losses. Therefore, the gearbox was disassembled and the plastic insulation inserts were added on the ends of the rods as shown in Fig. 4-84.

(a)   (b)

Fig. 4-84. (a) rods with plastic inserts and washers and (b) plastic inserts between the rod and the endplate.

Fig. 4-85 shows the assembled inner and cage rotors. Fig. 4-86 shows the outer lamination segment with inserted magnets. The fully assembled stage 2 MG is shown in Fig. 4-87.

Fig. 4-85. Fully assembled inner and cage rotors.

Fig. 4-86. Outer lamination with inserted magnets.
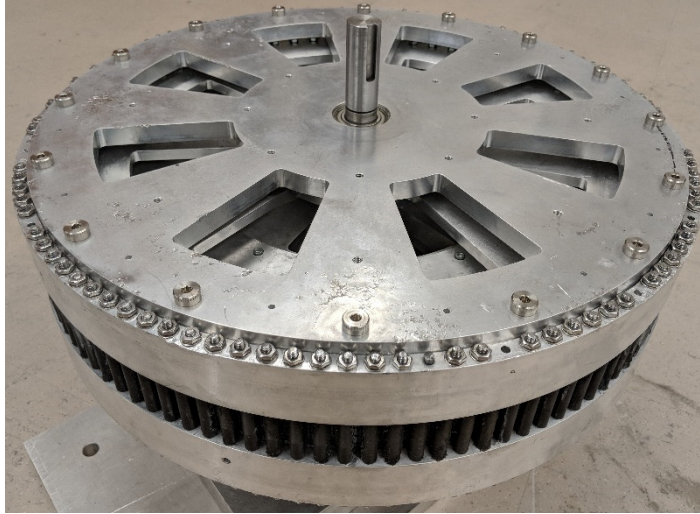
Fig. 4-87. Fully assembled stage 2 MG.

The transient test setup is shown in Fig. 4-88. The low-speed input side of the stage 2 MG was connected to the high-speed output side of the stage 1 MG. The low-speed input side of the stage 1 MG was connected to the 59:1 Sumitomo mechanical gearbox and a motor. Whilst the high-speed output side of the stage 2 MG was also connected to a generator (and then an active front end).

When the input speed of the stage 1 MG was 0.92 RPM, the input and output torque were measured with the load increasing. The input and output torque values are shown in Fig. 4-89. From the torque values, the efficiency was calculated to be 40 % at full load. The high losses were due to the high harmonic content created by the flux-focusing rotor typology as well as the eddy current losses induced in the end plates and support rods. Fig. 4-90 compares the no-load losses for the multistage MG and the stage 1 MG with different input speed (stage 1 is the input and stage 2 is the output).

Motor   59:1 Sumitomo   Torque   Stage 1 Stage 2 Torque   Generator
mechanical gearbox   transducer   MG   MG transducer
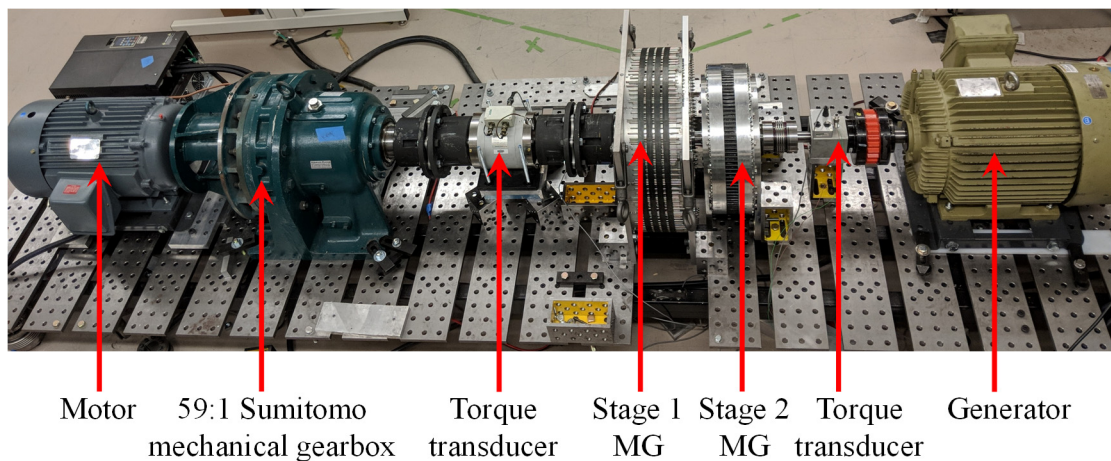
Fig. 4-88. Test setup for the MSMG.
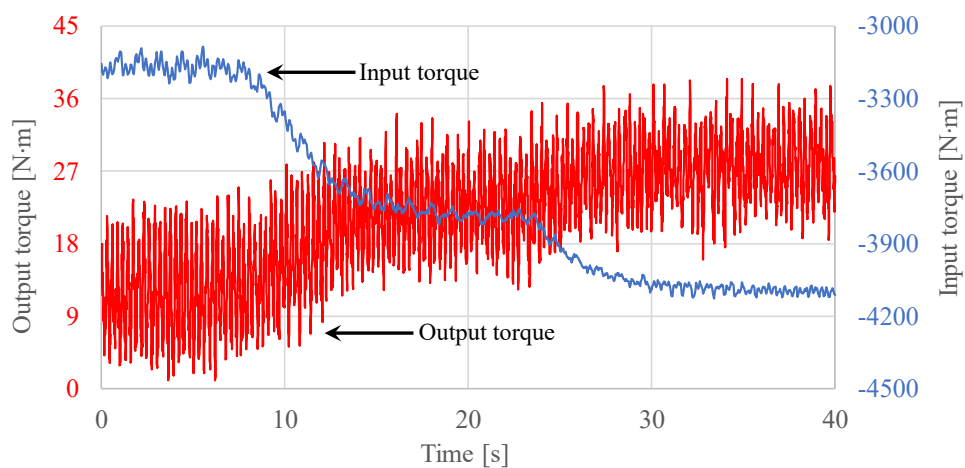
Fig. 4-89. Input and output torque as a function of time when the load was increased.
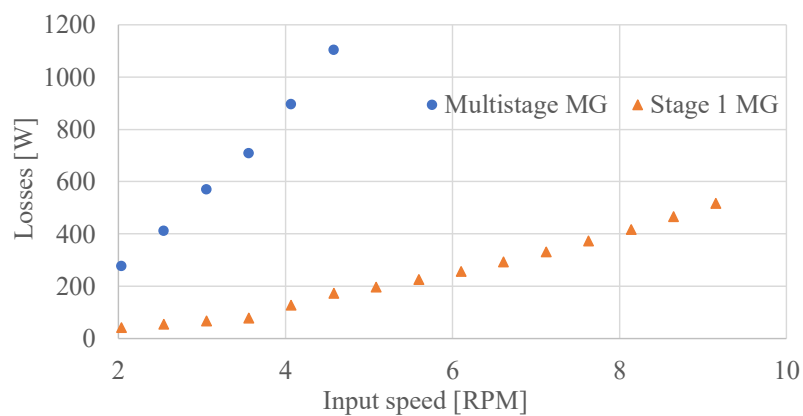
Fig. 4-90. Power loss as a function of input speed for the multistage magnetic gear as well as the stage 1 MG

4.6. CONCLUSION

The performance of a large diameter (0.633 m for the stage 1 MG and 0.507 m for the stage 2 MG) 59:1 magnetic gearbox for a wind turbine application has been presented. The design contains a number of innovations such as utilizing a fully laminated magnetic design with segmented bridged part. The presented stage 1 MG design exhibits a high torque density, while the stage 2 MG has a low torque density due to the small axial length. The torque ripple was shown to be independent of load and the losses were primarily speed and not load dependent.

CHAPTER 5 : A SERIES CONNECTED MULTISTAGE MAGNETIC GEARBOX
GENERATOR FOR A HYDROPOWER APPLICATION

In this chapter, a series connected MSMG with generator has been designed for a hydropower application which has the same working principle as the MSMG discussed in chapter 4. The parameters have been optimized and the performance of this MSMG has been evaluated. A stator has also been added inside the stage 2 MG.

5.1. IDEAL STAGE 1 MAGNETIC GEAR DESIGN ANALYSIS

The inner, cage and outer rotors have p_1, n_2 and p_3 pole pairs, respectively. Conducting the parameter sweeping analysis is very time consuming. Therefore, in this section, a pole pair combination of $p_1 = 12$, $n_2 = 78$ and $p_3 = 66$ has been chosen so that the MG can be modeled with $1/6^{th}$ of its geometry due to symmetric. In this analysis the outer radius was fixed at $r_{o3} = 270$ mm, which is close to the outer radius of the 59:1 Sumitomo mechanical gearbox. The axial length was fixed at $d_1 = 75$ mm and the air gap was chosen as $g = 1$ mm. Table 5-I shows the active material used in this study. The geometry is shown in Fig. 5-1 and Table 5-II. In the following analysis the outer and inner magnet angular lengths were kept equal to the steel lengths:

$$\theta_{1m} = \theta_{1s} \tag{5.1}$$

$$\theta_{3m} = \theta_{3s} \tag{5.2}$$

where subscript m and s denote magnet and steel parts. And also

$$\theta_{2s} = 2\theta_{3s} \tag{5.3}$$

Table 5-I. MATERIALS USED IN THE MG ANALYSIS.

Steel teeth	M19 lamination
Steel rods	Steel 416
Plastic rods and bars	Carbon fiber
Magnets	NMX 40CH
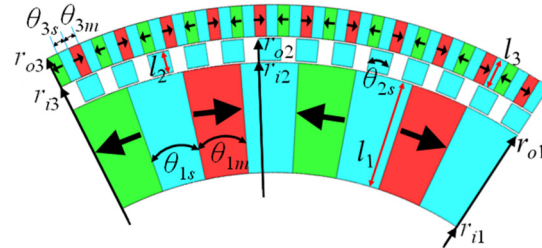
Fig. 5-1. 1/6th model of stage 1 MG with a pole pair combination of p_1 = 12, n_2 = 78 and p_3 = 66.

Table 5-II. GEOMETRIC AND MATERIAL

Description		Value	Unit
Inner rotor	Inner radius, r_{i1}	varied	mm
	Outer radius, r_{o1}	varied	mm
	Pole pairs, p_1	12	-
Cage rotor	Inner radius, r_{i2}	varied	mm
	Outer radius, r_{o2}	varied	mm
	Pole pairs, n_2	78	-
Outer rotor	Inner radius, r_{i3}	varied	mm
	Outer radius, r_{o3}	270	mm
	Pole pairs, p_3	66	-
Air gap, g		1	mm
Axial length, d_1		75	mm

The inner radius of the inner rotor, r_{i1}, the outer radius of the inner rotor, r_{o1}, the radial length of the cage rotor, l_2 and the inner radius of the outer rotor, r_{i3} were all varied in order to obtain the peak torque. The mass and volume torque density plots are shown in Fig. 5-2-Fig. 5-4 when r_{i1} = 220 mm, r_{i1} = 200 mm and r_{i1} = 180 mm. For different values of r_{i1}, the torque density values are clearly grouped. The parameters for each r_{i1} when the peak torque occurs are shown in Table 5-III.

From the figure as shown below, it can be seen that:

1. For one value of the radial length of the cage rotor, l_2, the line looks quite linear.

2. All the lines seem parallel to each other.

3. When l_2 is increasing, the lines are shifted along the y-direction, which means the two boundaries of the plot are the maximum value of l_2 and the minimum value of l_2.

4. When l_2 is increased from 5 mm to 12 mm, the peak value is increasing and then decreasing.
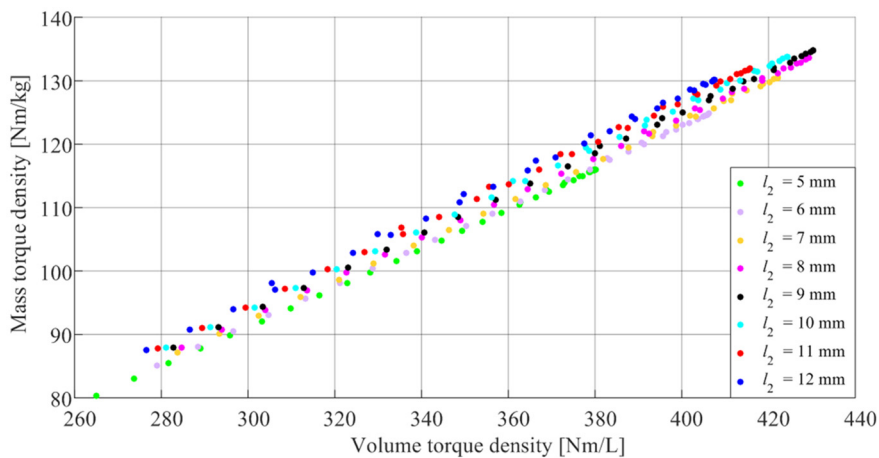
Fig. 5-2. Mass and volume torque densities when r_{i1} = 200 mm.
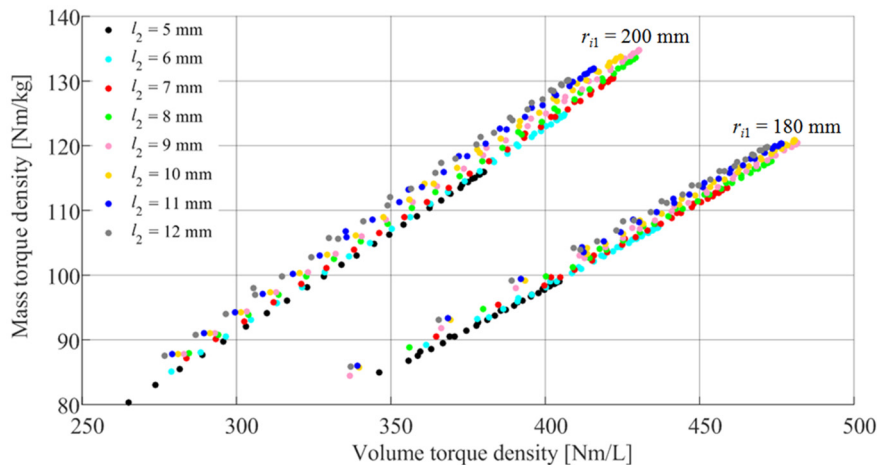
Fig. 5-3. Mass and volume torque densities when r_{i1} = 200 mm and r_{i1} = 180 mm.
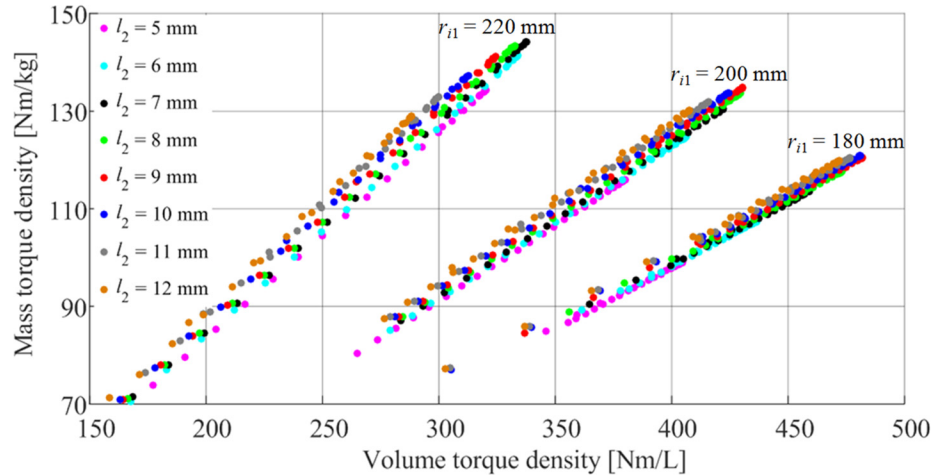
Fig. 5-4. Mass and volume torque densities when r_{i1} = 220 mm, r_{i1} = 200 mm and r_{i1} = 180 mm.

Table 5-III. PARAMETERS OF THE MG AFTER PARAMETER SWEEPING

Description		Value (peak torque) (r_{i1} = 180 mm)	Value (peak torque) (r_{i1} = 200 mm)	Value (peak torque) (r_{i1} = 220 mm)	Unit
Inner rotor	Inner radius, r_{i1}	180	200	220	mm
	Outer radius, r_{o1}	240	243	247	mm
	Pole pairs, p_1		12		-
Cage rotor	Inner radius, r_{i2}	241	244	248	mm
	Outer radius, r_{o2}	250	253	255	mm
	Pole pairs, n_2		78		-
Outer rotor	Inner radius, r_{i3}	251	254	256	mm
	Outer radius, r_{o3}	270	270	270	mm
	Pole pairs, p_3		66		-
Torque, T_2		8275.263	7390.943	5800.268	Nm
Air gap, g			1		mm
Axial length, d_1			75		mm

The inner radius of the inner rotor r_{i1} was varied from 150 mm to 240 mm. At each value of r_{i1}, the peak torque was obtained. The torque density plots are shown in Fig. 5-5 and Fig. 5-6. It can be seen that there is clearly a trade-off between the volume torque density and the mass torque density.
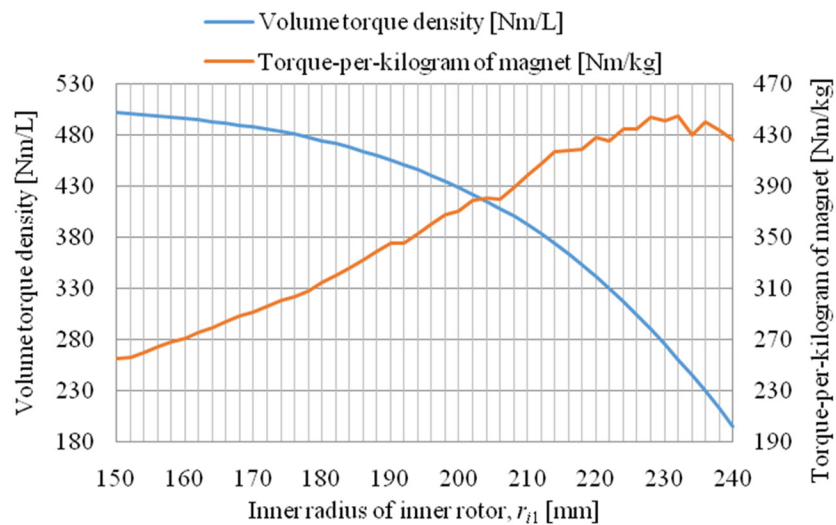
Fig. 5-5. Values of volume and mass torque density when r_{i1} is varied.
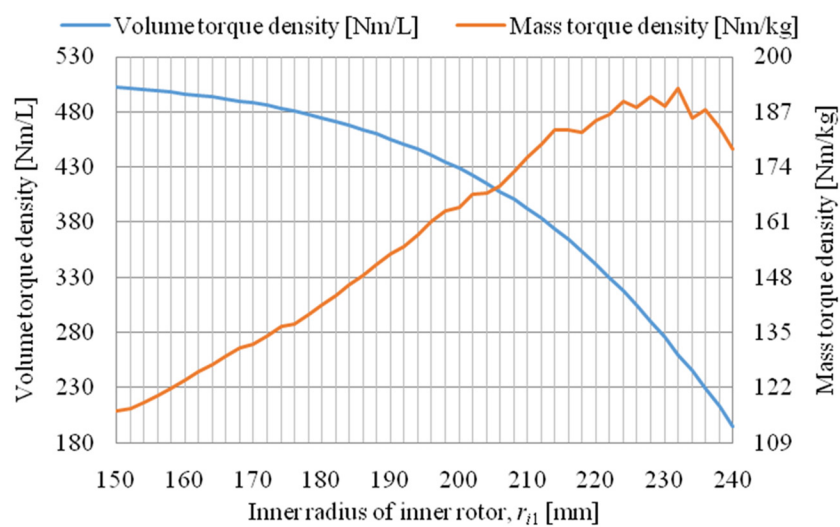
Fig. 5-6. Values of volume and mass torque density when r_{i1} is varied.

The value of r_{i1} was selected as 180 mm in order to get a relatively high mass and volume torque density. The parameters are chosen as shown in Table 5-IV. The corresponding magnetic flux lines are shown in Fig. 5-7.

Table 5-IV. GEOMETRY PARAMETERS

Description		Value	Unit
Inner rotor	Inner radius, r_{i1}	180	mm
	Outer radius, r_{o1}	239	mm
Cage rotor	Inner radius, r_{i2}	240	mm
	Outer radius, r_{o2}	252	mm
Outer rotor	Inner radius, r_{i3}	253	mm
	Outer radius, r_{o3}	270	mm
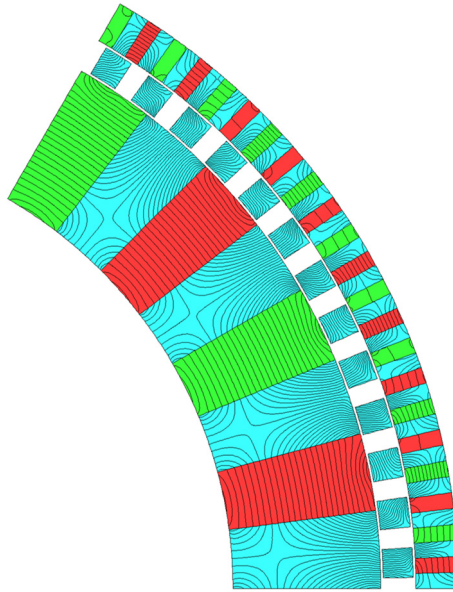
Fig. 5-7. Magnetic flux lines.

The torque plots are shown in Fig. 5-8-Fig. 5-10 when the cage rotor is rotating at 80 RPM and the inner rotor is rotating at 520 RPM. The inner, cage and outer rotors have low torque ripples which are 4.18 %, 0.87 % and 0.27 %, respectively.
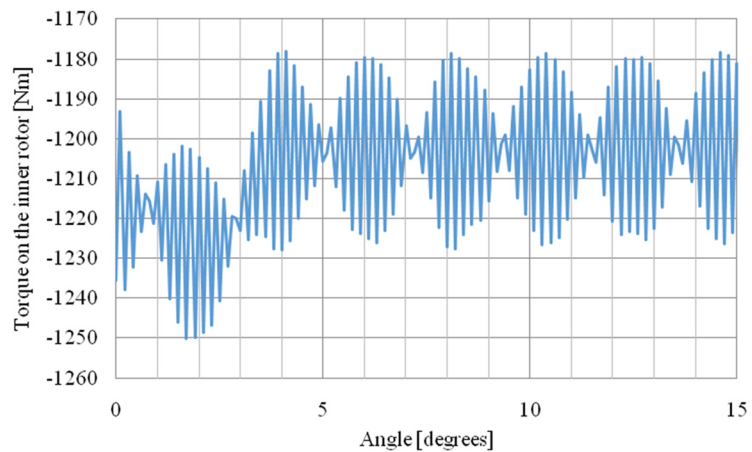
Fig. 5-8. Torque on the inner rotor.
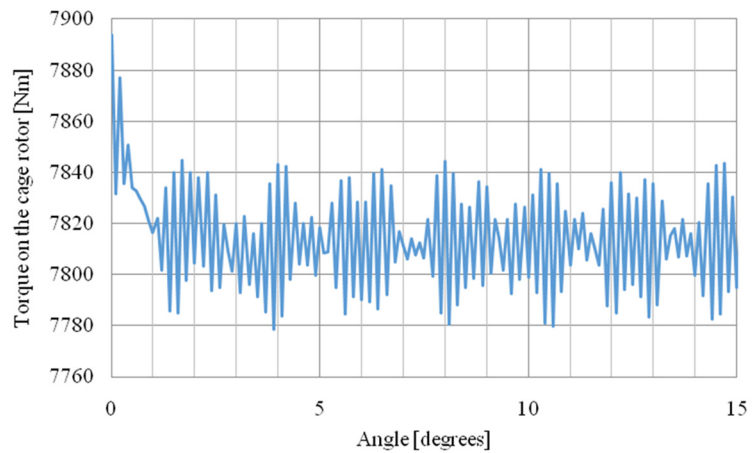
Fig. 5-9. Torque on the cage rotor.
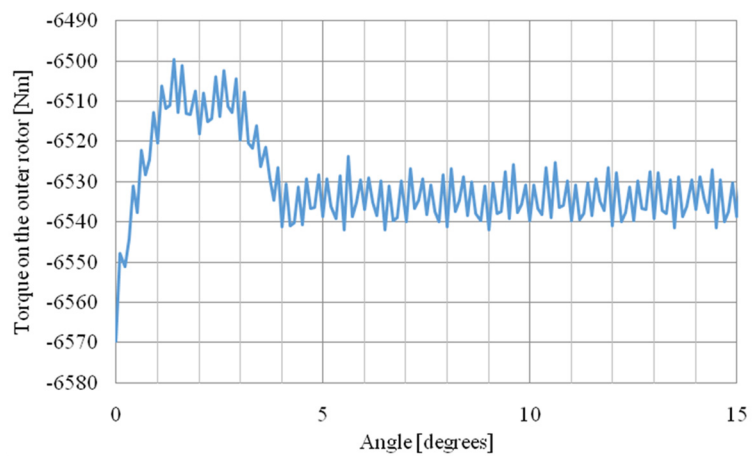
Fig. 5-10. Torque on the outer rotor.

Initially, the radial length of the cage steel bar is $l_2 = 12$ mm in the design shown in Fig. 5-7. In order to make it mechanically strong, l_2 is increased so that the cage bar will provide more support and have smaller deflection. Therefore, r_{i1} was fixed at 180 mm and l_2 was fixed at $l_2 = 15$ mm. Then r_{o1} was varied from 220 mm to 250 mm. The peak torque occurs when $r_{o1} = 236$ mm which is shown in Fig. 5-11. The corresponding volume and mass torque densities are 434.85 Nm/L and 112.13 Nm/kg, respectively.
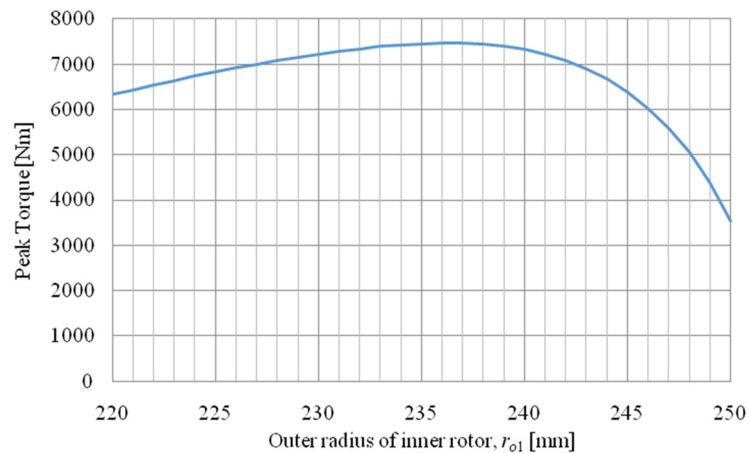
Fig. 5-11. Peak torque when r_{o1} is varied.

The torque plots are shown in Fig. 5-12-Fig. 5-14 when the cage rotor is rotating at 80 RPM and the inner rotor is rotating at 520 RPM. The inner, cage and outer rotors have low torque ripples which are 6.61 %, 1.47 % and 0.97 %, respectively.
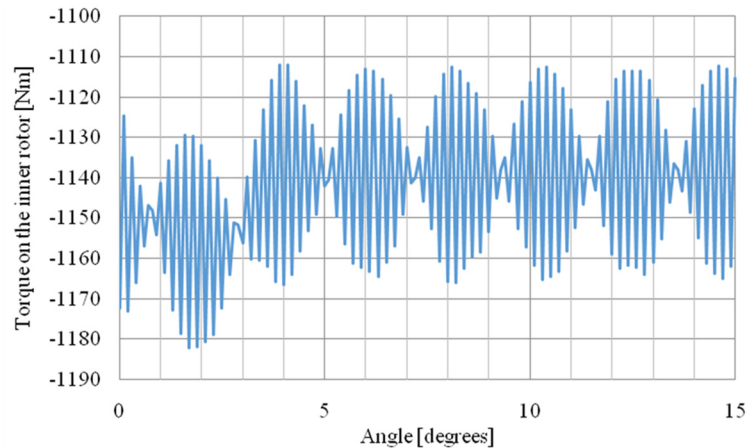
Fig. 5-12. Torque on the inner rotor.
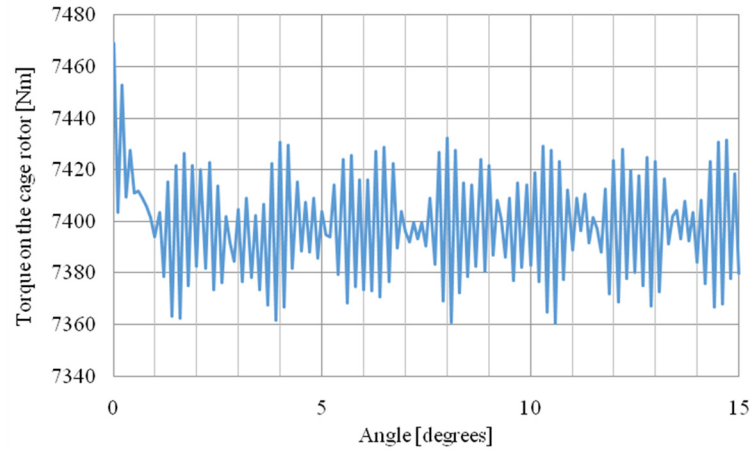
Fig. 5-13. Torque on the cage rotor.
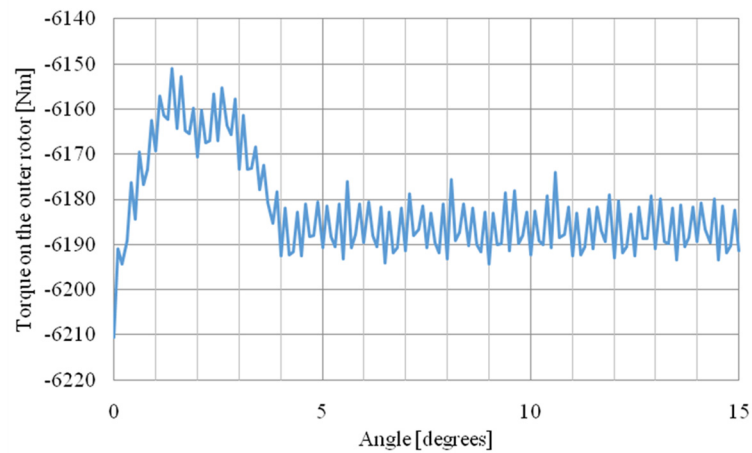
Fig. 5-14. Torque on the outer rotor.

5.2. MAGNETIC GEAR DESIGN WITH FLUX CONCENTRATION

In order to achieve a higher torque, radial magnetized magnets have been added to the inner rotor. Therefore, more magnetic flux will be created in the air gap. The radial length of the inner radial magnets has been varied again in order to achieve peak torque which is shown in Fig. 5-15. The peak torque occurs when the radial length of the radial magnets is 17 mm as shown in Fig. 5-16. The final design with all the supporting rods and magnet retaining lips is shown in Fig. 5-17.
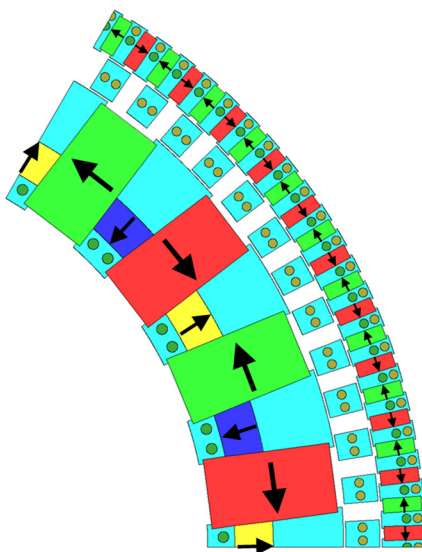
Fig. 5-15. Parameter sweep for the stage 1 MG.
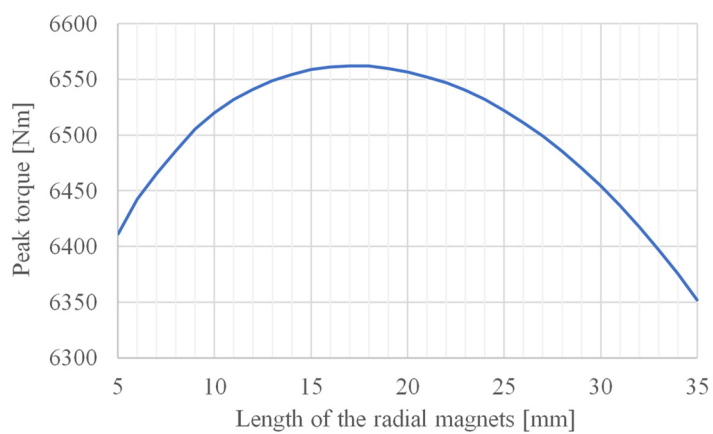
Fig. 5-16. The peak torque with different length of the inner radial magnets.
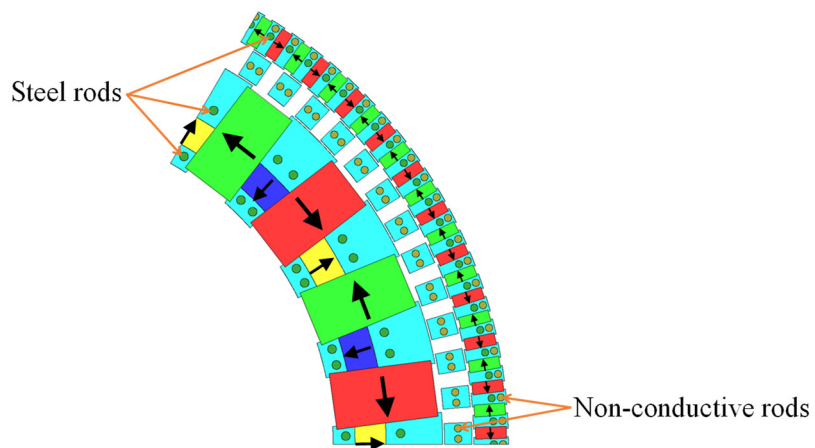
Fig. 5-17. Final design of the stage 1 MG.

When the cage rotor has an angular speed of 80 RPM and the inner rotor has an angular speed of 520 RPM, the total loss as a function a time is plotted in Fig. 5-18. The loss was calculated in a 2-D model and the efficiency is calculated to be 95 %. The contour plot of the loss and current density is shown in Fig. 5-19 and Fig. 5-20. It can be seen that most of the losses are on the outer steel rods and magnets because of the large number of pole pairs. One approach to reduce the losses on the outer rotor is to use axially segmented magnets.
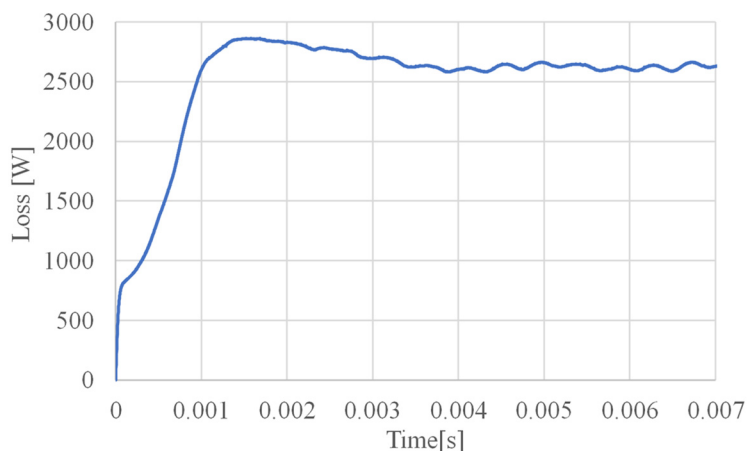
Fig. 5-18. Eddy current losses for stage 1 MG when the cage rotor has an angular speed of 80 RPM.
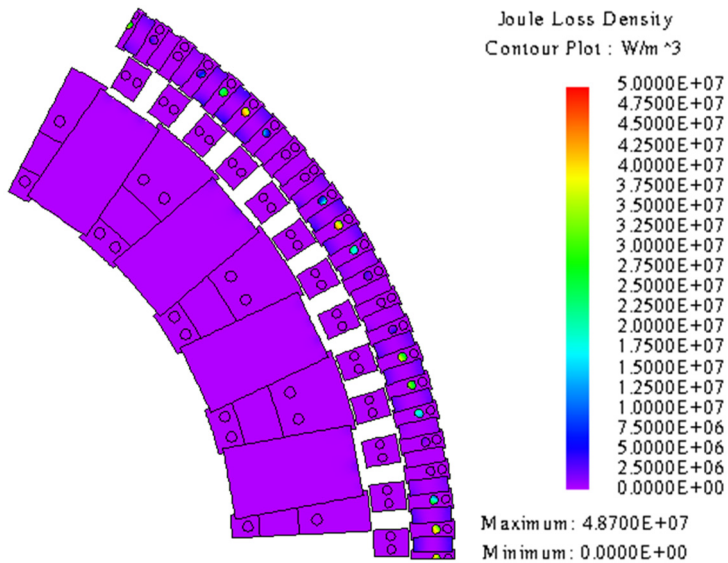
Fig. 5-19. Contour plot of the loss density.
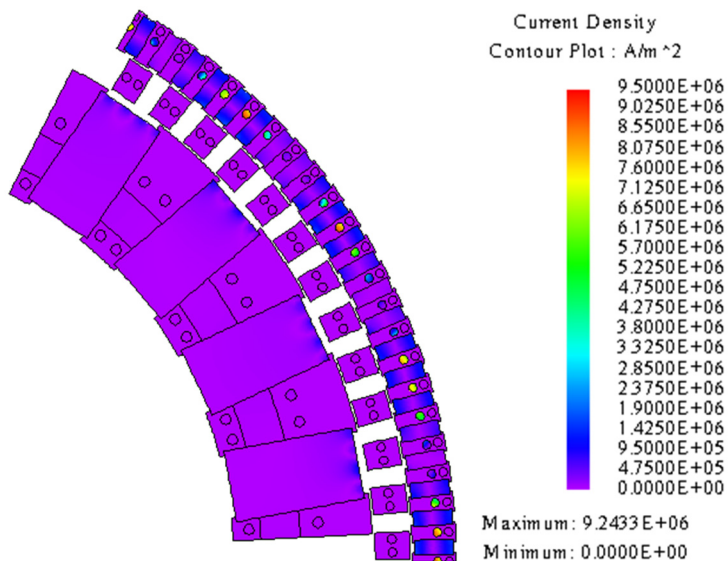
Fig. 5-20. Contour plot of the current density.

The torque plots for the final design are shown in Fig. 5-21-Fig. 5-23. The forces have been calculated on the parts that are shown in Fig. 5-24. The radial and tangential forces have been calculated which are shown in Fig. 5-25-Fig. 5-32. The final geometry parameters are described in Table 5-V and the 2-D calculated volume torque density is 370.84 Nm/L.
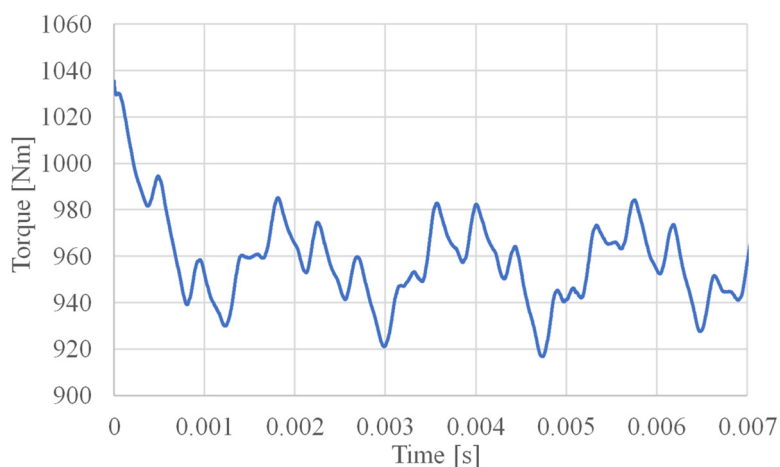
Fig. 5-21. Torque on the inner rotor.
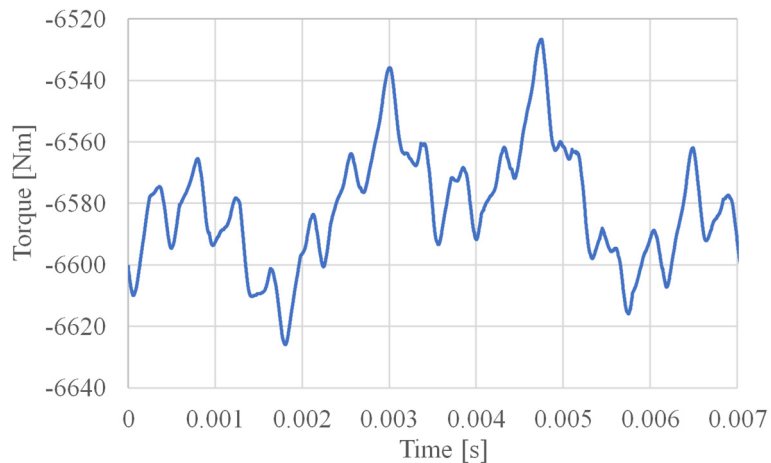
Fig. 5-22. Torque on the cage rotor.
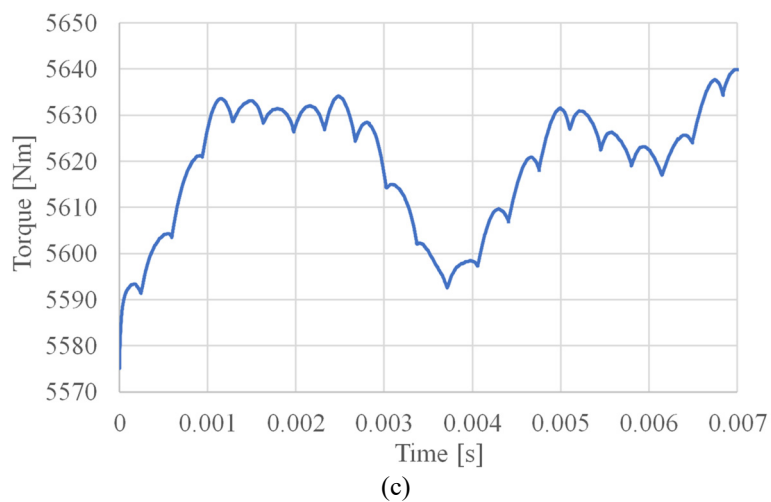
(c)

Fig. 5-23. Torque on the outer rotor.
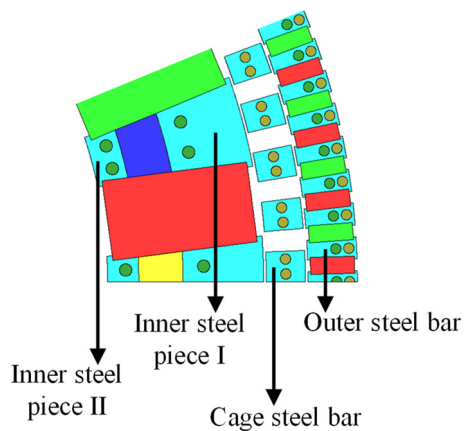
Fig. 5-24. Forces to be calculated on each part.
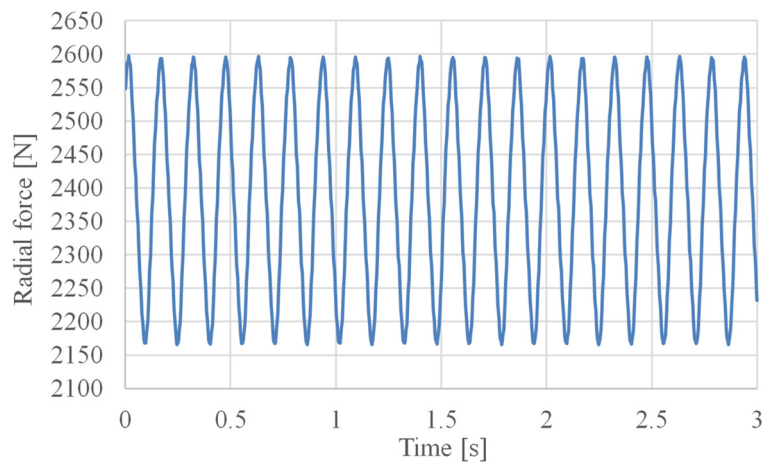
Fig. 5-25. Radial force on inner steel piece I.
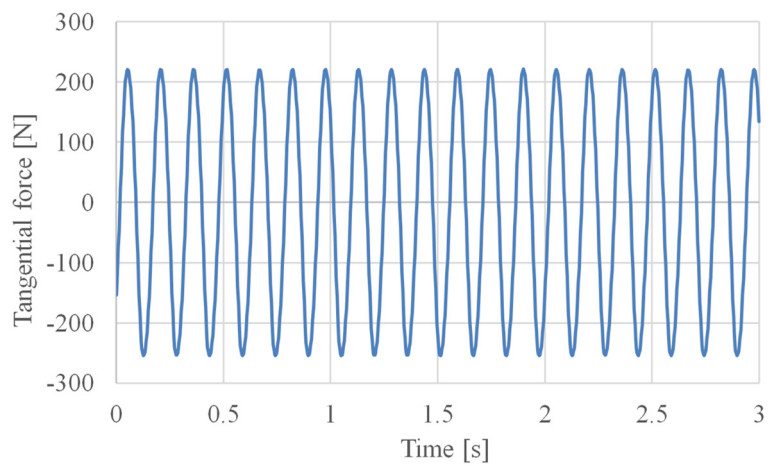
Fig. 5-26. Tangential force on inner steel piece I.
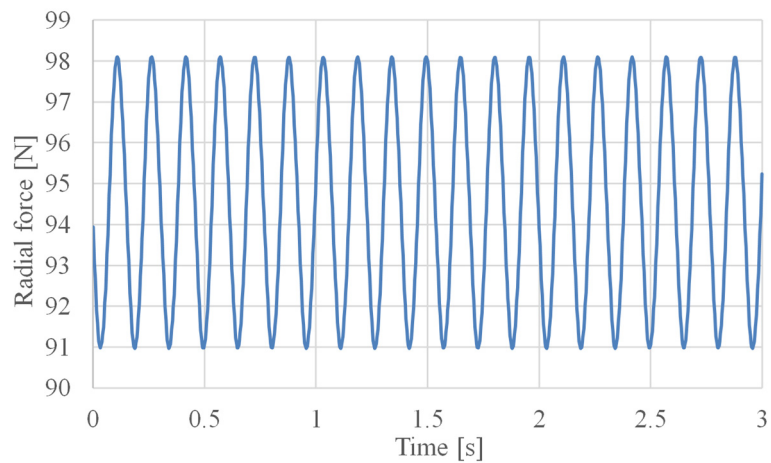
Fig. 5-27. Radial force on inner steel piece II.
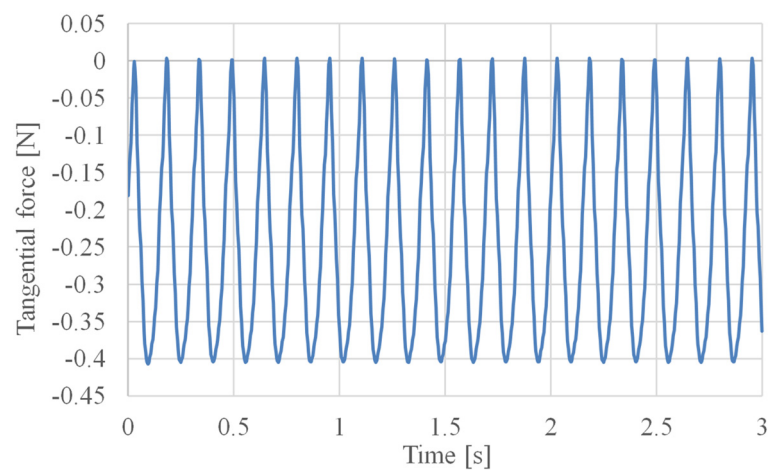
Fig. 5-28. Tangential force on inner steel piece II.
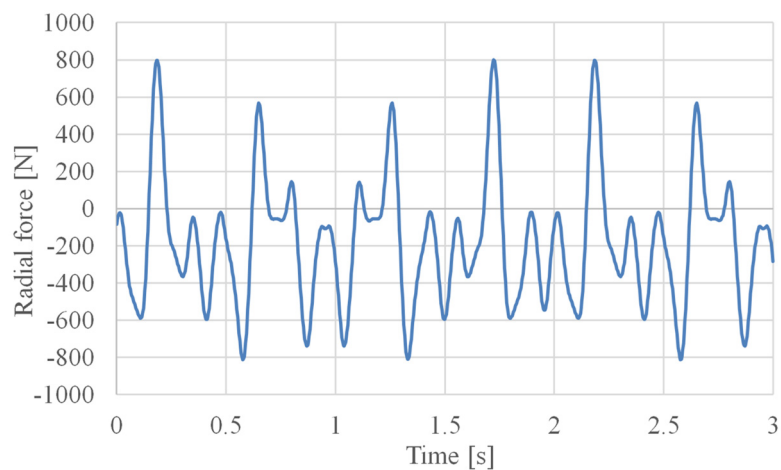
Fig. 5-29. Radial force on cage steel bar.
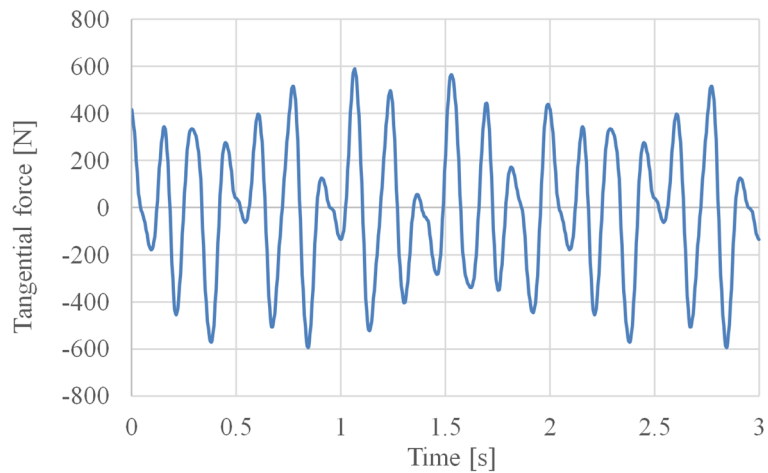
Fig. 5-30. Tangential force on cage steel bar.
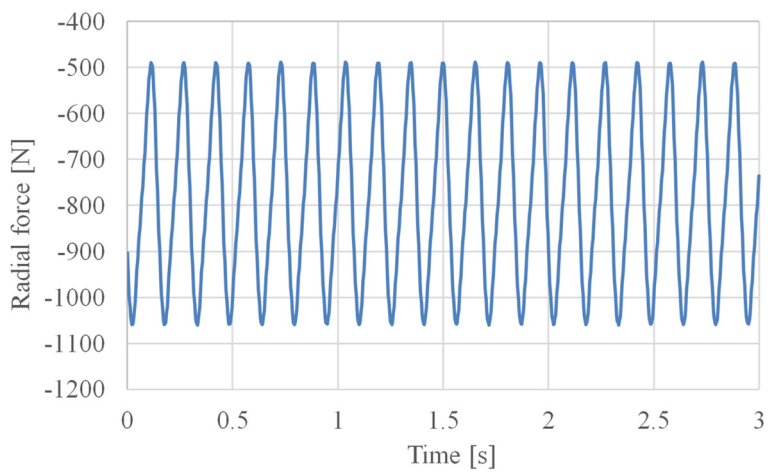
Fig. 5-31. Radial force on outer steel bar.
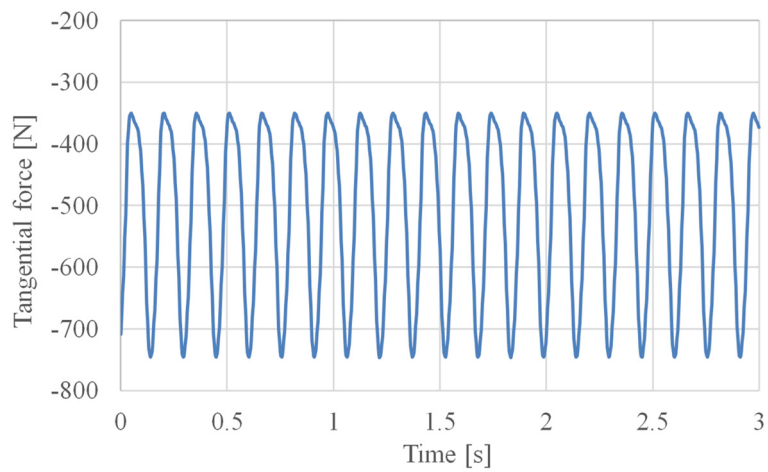
Fig. 5-32. Tangential force on outer steel bar.

Using the calculated force values, the radial deflection of the rods has been calculated and is shown in Fig. 5-33-Fig. 5-36. The maximum deflection of the rods is 0.11 mm which is acceptable compared to the 1 mm air gap. When calculating the deflection, the lamination steels are assumed to provide no support which means the real deflection will be even smaller. Therefore, the air gap will be maintained between each rotor.
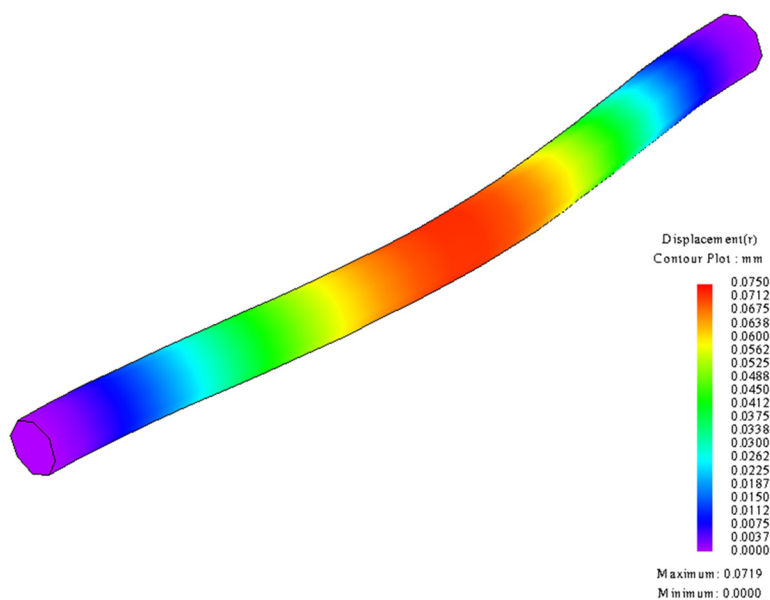
Fig. 5-33. Deflection of the inner rod.
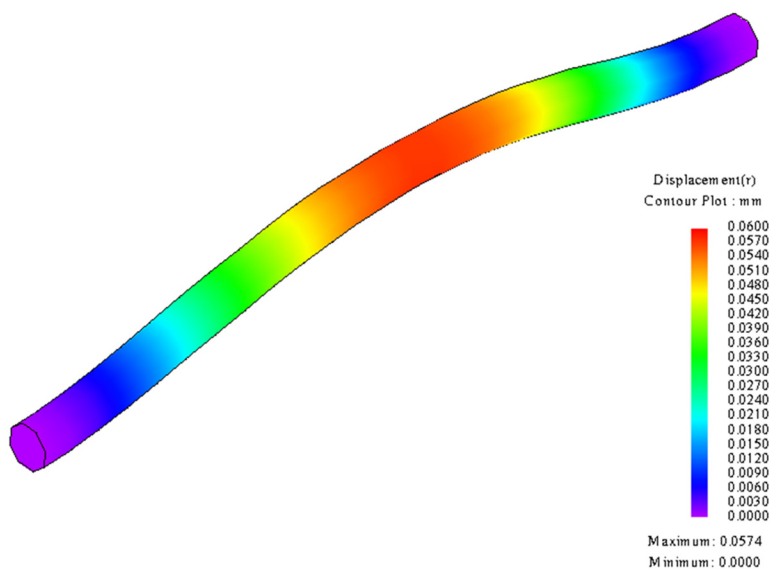
Fig. 5-34. Deflection of the cage rod when deflected outward.

Displacement(r)
Contour Plot : mm

```
 0.0000
-0.0060
-0.0120
-0.0180
-0.0240
-0.0300
-0.0360
-0.0420
-0.0480
-0.0540
-0.0600
-0.0660
-0.0720
-0.0780
-0.0840
-0.0900
-0.0960
-0.1020
-0.1080
-0.1140
-0.1200
```

Maximum: 0.0000
Minimum: -0.1128

Fig. 5-35. Deflection of the cage rod when deflected inward.

Displacement(r)
Contour Plot : mm

```
 0.0000
-0.0048
-0.0095
-0.0142
-0.0190
-0.0238
-0.0285
-0.0333
-0.0380
-0.0428
-0.0475
-0.0523
-0.0570
-0.0617
-0.0665
-0.0713
-0.0760
-0.0808
-0.0855
-0.0902
-0.0950
```

Maximum: 0.0000
Minimum: -0.0908
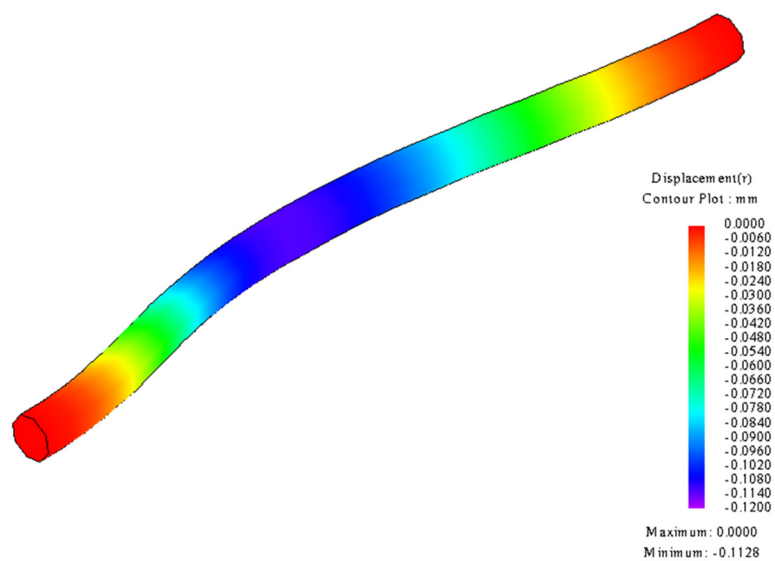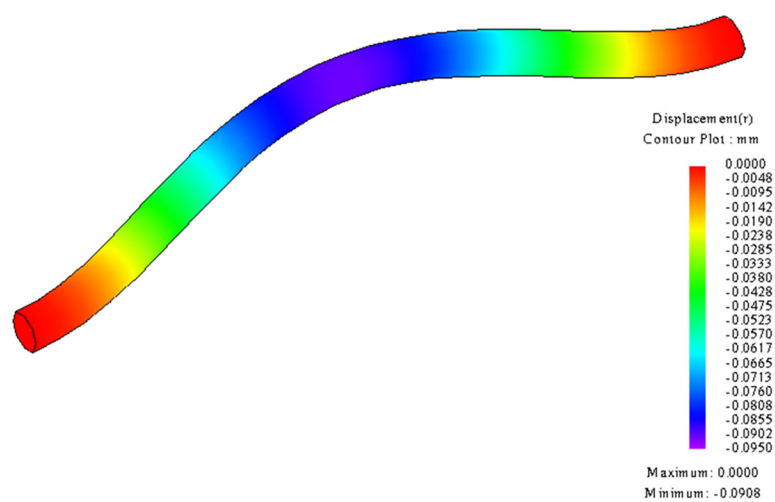
Fig. 5-36. Deflection of the outer rod.

Table 5-V. FINAL GEOMETRY PARAMETERS OF STAGE 1 MG

Description			Unit
Inner rotor	Inner radius, r_{i1}	178	mm
	Outer radius, r_{o1}	238	mm
	Pole pairs, p_1	12	-
	Radial length of the radial magnets	17	mm
Cage rotor	Inner radius, r_{i2}	239	mm
	Outer radius, r_{o2}	254	mm
	Pole pairs, n_2	78	-
Outer rotor	Inner radius, r_{i3}	255	mm
	Outer radius, r_{o3}	274	mm
	Pole pairs, p_3	66	-
Axial length, d_1		75	mm
Air gap, g		1	mm

5.3. DESIGN OF STAGE 2 MG WITHOUT STATOR

The pole pair combination of stage 2 MG has been selected as $p_4 = 6$, $n_5 = 57$ and $p_6 = 51$ which gives a gear ratio of 9.5. The overall gear ratio of the multistage MG becomes 61.75:1 which is still close enough to 59:1 (the gear ratio of the mechanical gearbox). With this pole pair combination, a 1/3 model can be simulated. The parameters for the stage 2 design are defined in Fig. 5-37. The axial length of the stage 2 MG was fixed at $d_2 = 37.5$ mm. The inner radius of the inner rotor was fixed at $r_{i4} = 155$ mm so that a stator could be put inside in the future. The radial length of the cage rotor was fixed at 15 mm so that the steel could provide enough mechanical support to prevent deflection.

The radial length of the inner and outer magnets is defined as:

$$l_4 = r_{o4} - r_{i4} \tag{5.4}$$

and

$$l_6 = r_{o6} - r_{i6} \tag{5.5}$$

The inner magnet length was varied from l_4 = 35 mm to 60 mm and the outer magnets were varied from l_6 = 10 mm to 40 mm. The parameter sweep result is shown in Fig. 5-38.
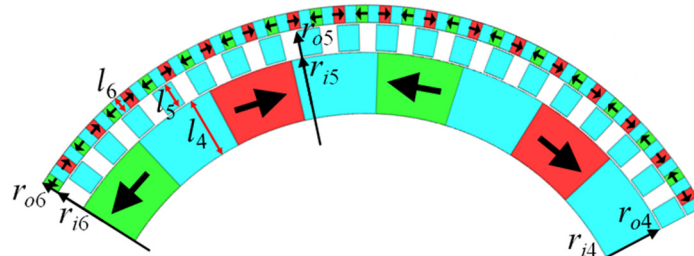
Fig. 5-37. Stage 2 MG with a pole pair combination of p_4 = 6, n_5 = 57 and p_6 = 51.
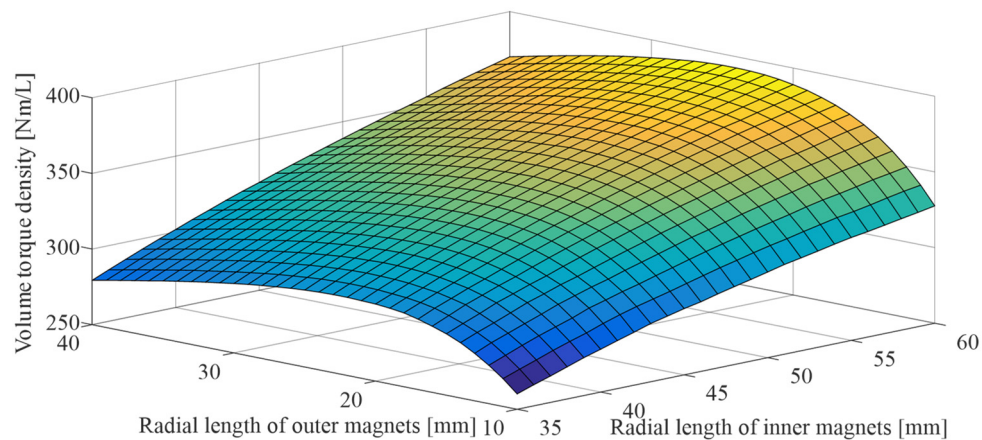
Fig. 5-38. Parameter sweep analysis when the length of the outer and the inner magnets was varied.

From Fig. 5-38 the volume torque density is increasing when the radial length of the inner magnets is increasing. Using too large inner magnets will increase the cost, weight and assembly difficulty. Therefore, the inner radial length was selected to be l_4 = 45 mm. To achieve the peak torque density, the outer radial length was l_6 = 24 mm.

Similar to the stage 1 MG, the radial magnets were added to the inner rotor of the stage 2 MG as shown in Design #1 of Table 5-VI. The peak torque occurred when the radial length of the radial magnets was l_{m4} = 20 mm. 4.5 mm by 5 mm radial magnets were also added to the outer rotor. The performance of a series of alternative designs has

also been compared which are shown in Table 5-VI. These designs try to look at how the mechanical and magnetic performance is traded-off to create a robust and realistic design with a high torque density. Though Design #1 has the highest torque value, it has many steel rods on the outer rotor which creates many losses. The efficiency is also only 79 % when the cage rotor is rotating with an angular speed of ω_4 = 195 RPM. Design #2 has no outer steel rods and the plastic rods will not be strong enough. Design #3 has a low torque. In Design #5, each cage lamination bar has one single rod and there is rectangular plastic bar between each cage lamination piece. The cage rods have also been changed to be round which can have a higher tolerance. Design #6 is the final design as the torque is higher than Design #5.

Table 5-VI. COMPARISON OF DIFFERENT DESIGNS.
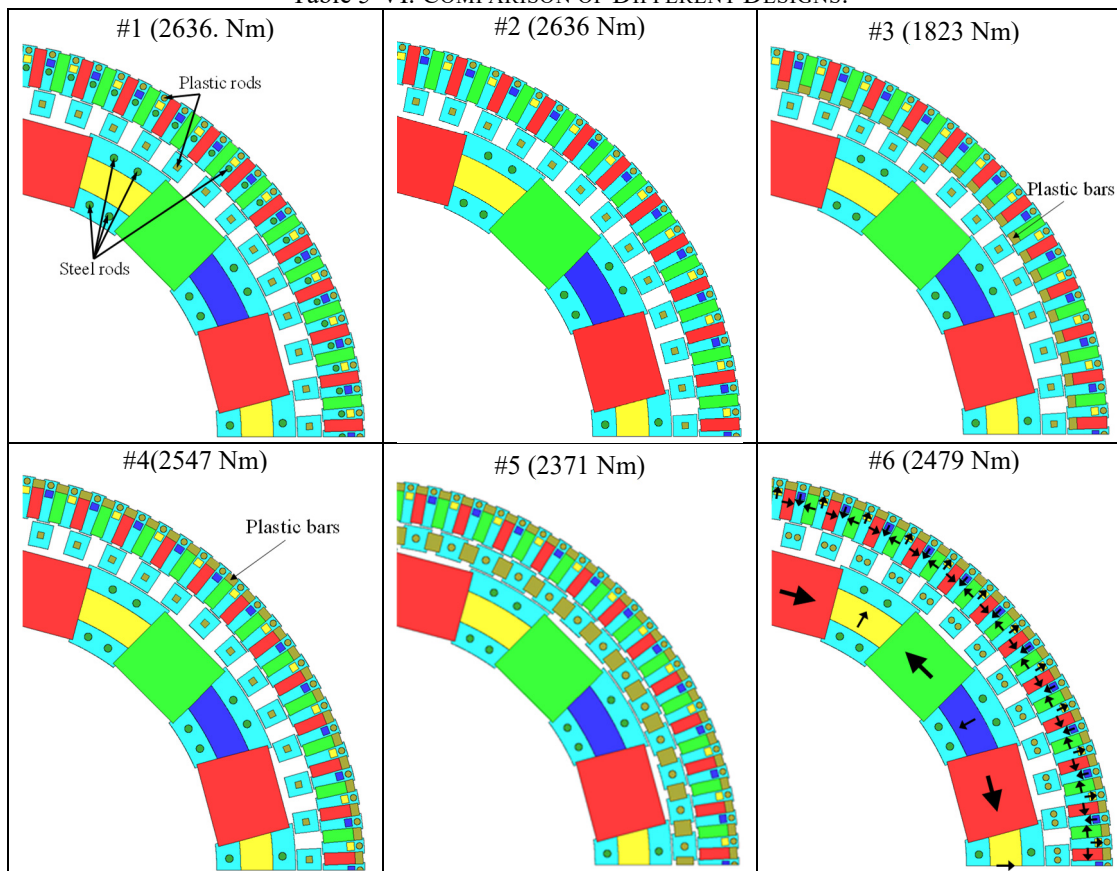
The torque on the three rotors is present in Fig. 5-39-Fig. 5-41. The torque ripple on the cage rotor is 0.28 %. The calculated torque density is 344 Nm/L and the final parameters are shown in Table 5-VII. The efficiency was calculated to be 89 % in 2-D FEA when the cage rotor was rotating at 520 RPM. The loss and loss density are plotted in Fig. 5-42 and Fig. 5-43. Most of the losses are from the outer magnets because of the high frequency.
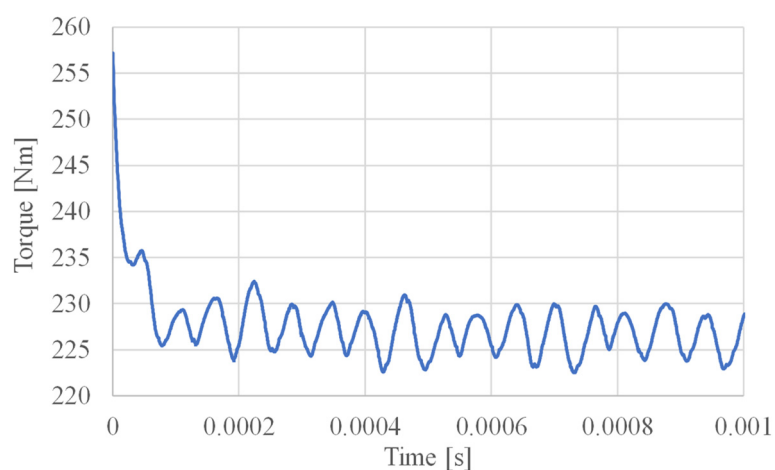
Fig. 5-39. Torque on the inner rotor.
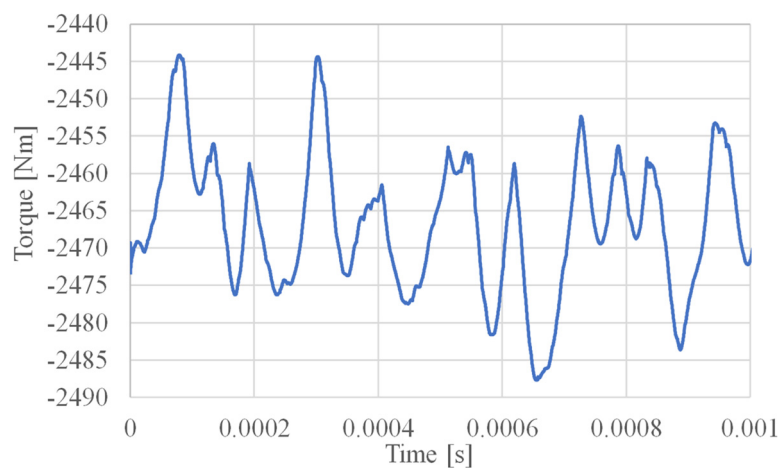
Fig. 5-40. Torque on the cage rotor.
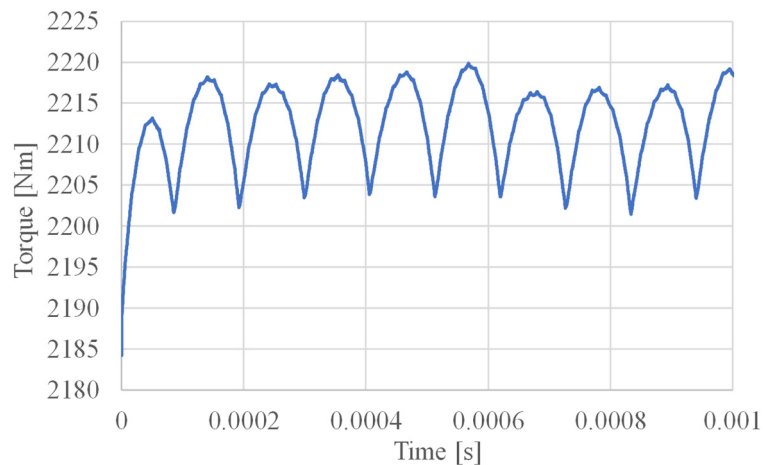
Fig. 5-41. Torque on the outer rotor.

Table 5-VII. FINAL GEOMETRY OF THE STAGE 2 MG

Description			Unit
Inner rotor	Inner radius, r_{i4}	155	mm
	Outer radius, r_{o4}	204	mm
Cage rotor	Inner radius, r_{i5}	205	mm
	Outer radius, r_{o5}	220	mm
Outer rotor	Inner radius, r_{i6}	221	mm
	Outer radius, r_{o6}	247	mm
Axial length, d_2		37.5	mm
Air gap, g		1	mm
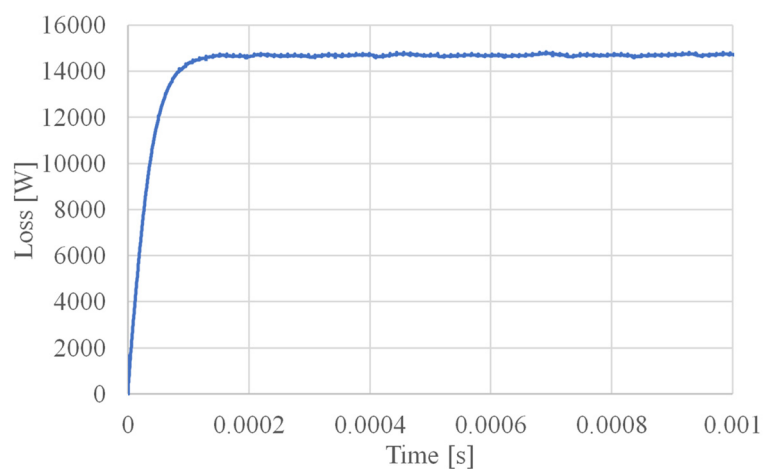
Fig. 5-42. Eddy current loss when the cage rotor was rotating at an angular speed of 520 RPM.

(a)

(b)
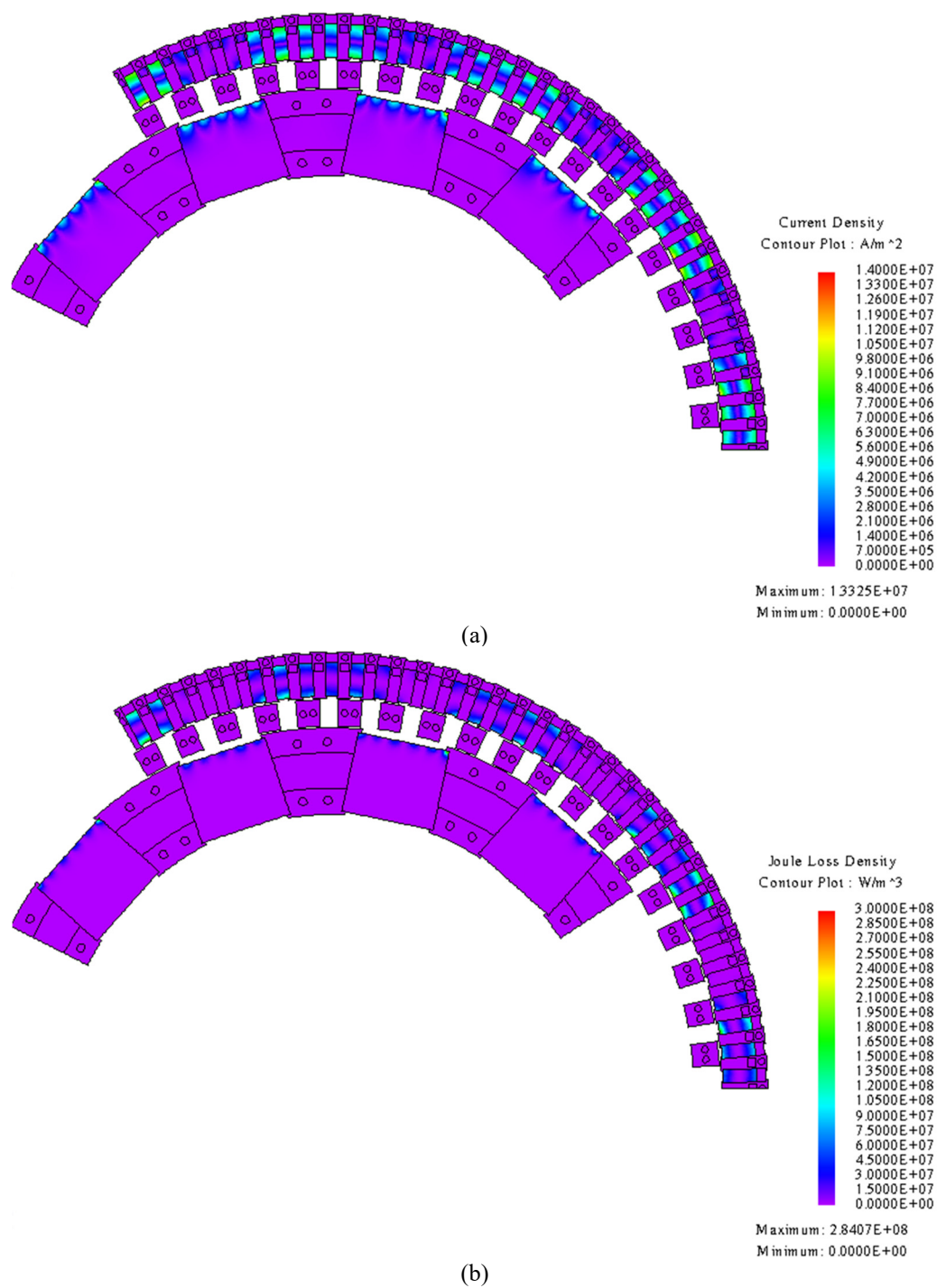
Fig. 5-43. Contour plot of the (a) current density and (b) loss density.

The radial and tangential forces have been calculated on the inner, cage and outer steel

pieces as shown in Fig. 5-44. Based on those magnetic forces, the mechanical deflection

of the rods has been calculated. The radial and tangential forces are present in Fig. 5-45-Fig. 5-52.
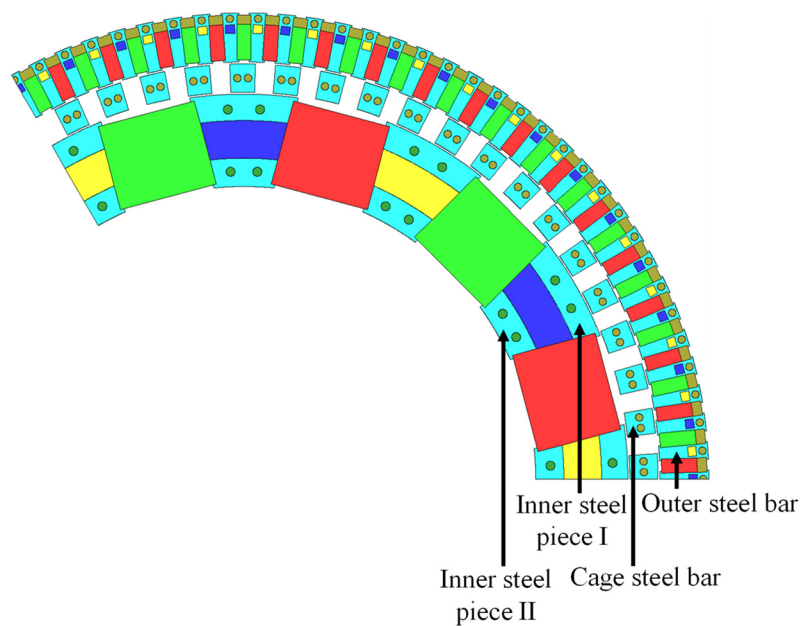
Fig. 5-44. Magnetic forces on steel pieces.
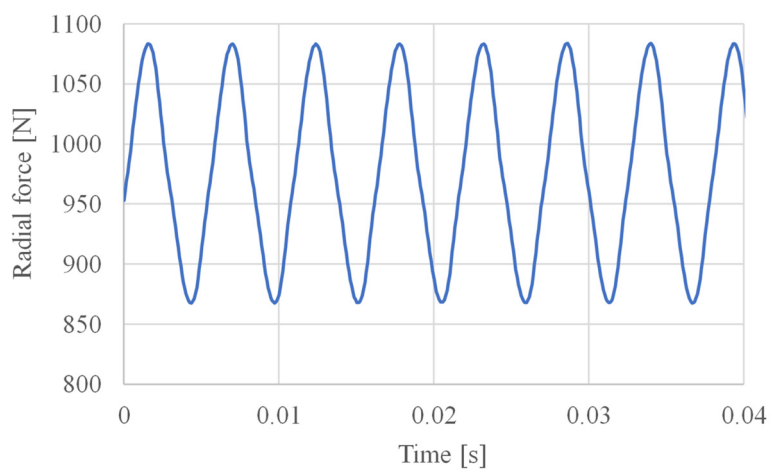
Fig. 5-45. Radial force on inner steel piece I.
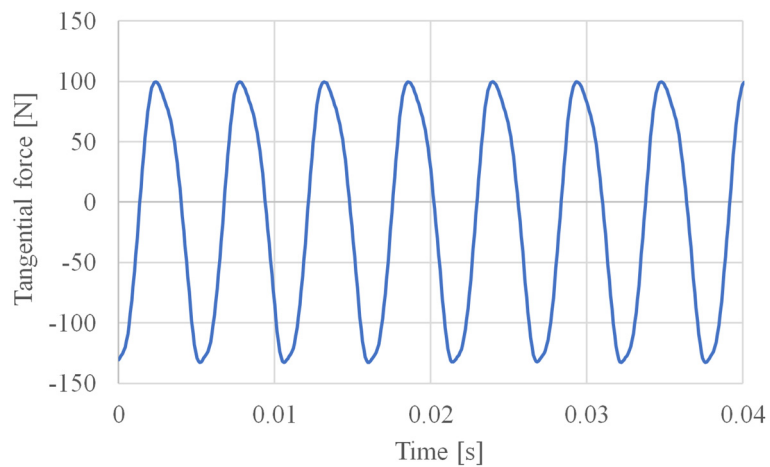
Fig. 5-46. Tangential force on inner steel piece I.
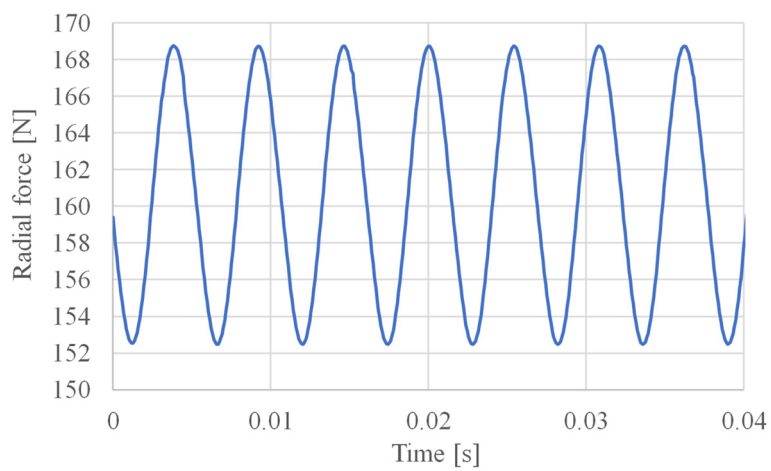
Fig. 5-47. Radial force on inner steel piece II.
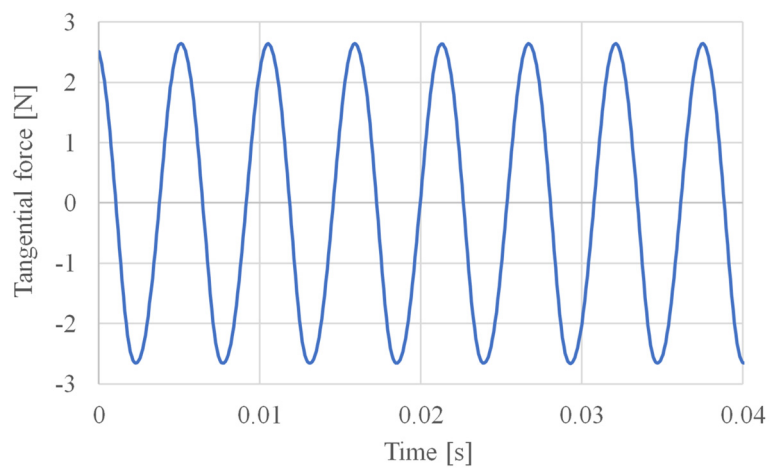
Fig. 5-48. Tangential force on inner steel piece II.
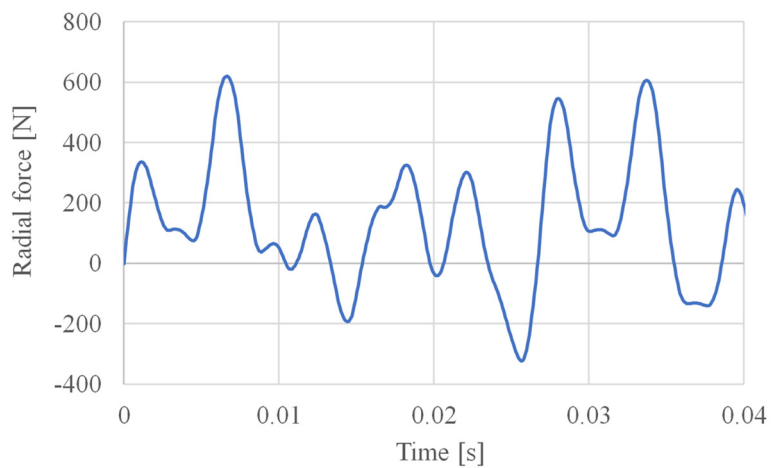
Fig. 5-49. Radial force on cage steel bar.
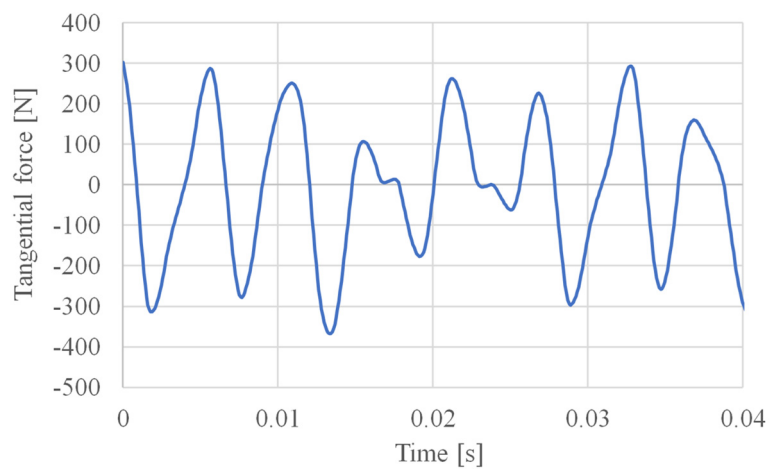
Fig. 5-50. Tangential force on cage steel bar.
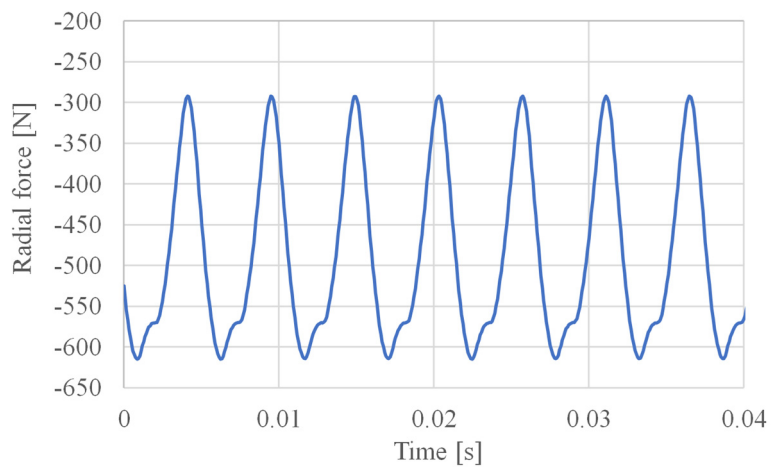
Fig. 5-51. Radial force on outer steel bar.
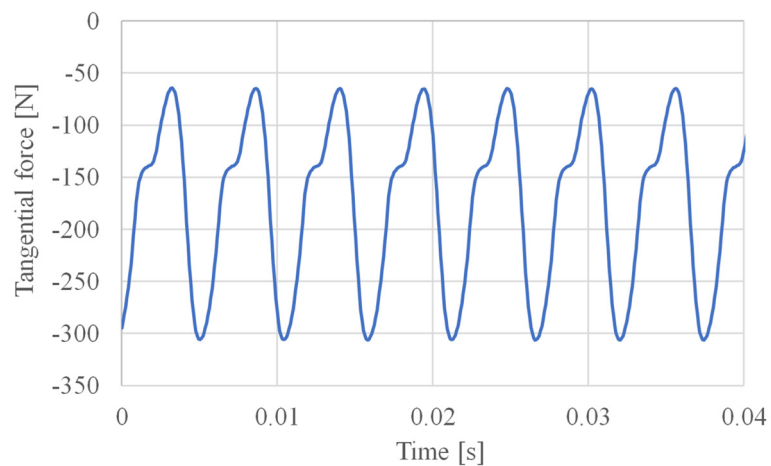
Fig. 5-52. Tangential force on outer steel bar.

Using these magnetic forces, the mechanical deflection of the rods is calculated. From the results shown in Fig. 5-53-Fig. 5-56, the maximum deflection is 0.0093 mm which is very small compared to the 1 mm air gap. Therefore, the air gap will be maintained.
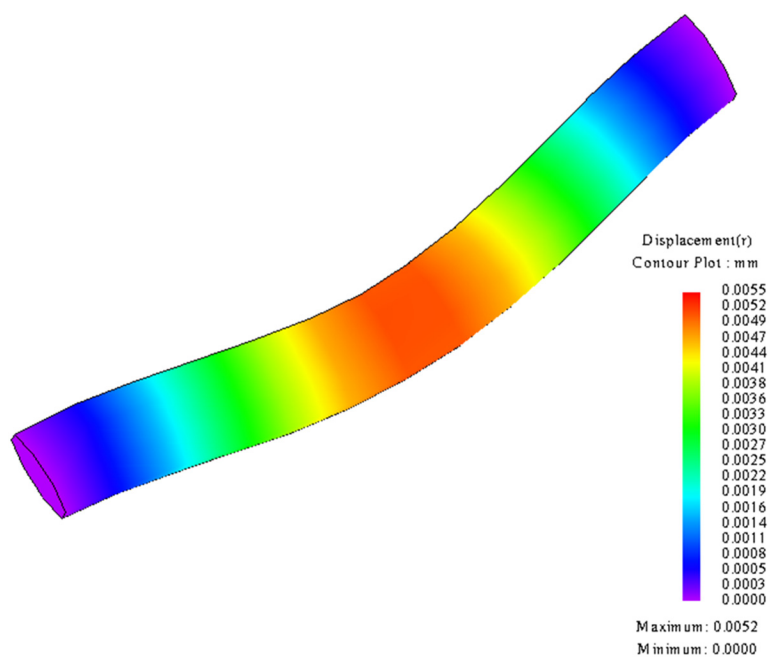
Fig. 5-53. Deflection of the inner rod.
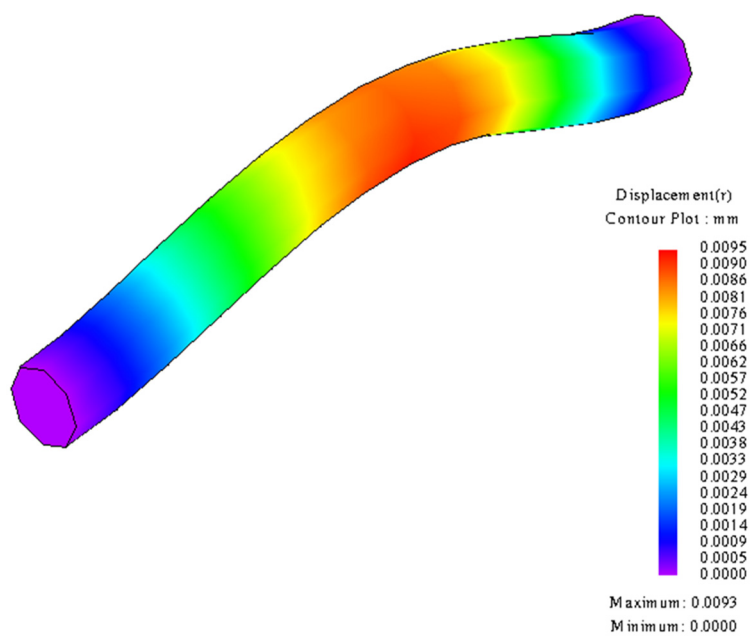
Fig. 5-54. Deflection of the cage rod when deflected outward.
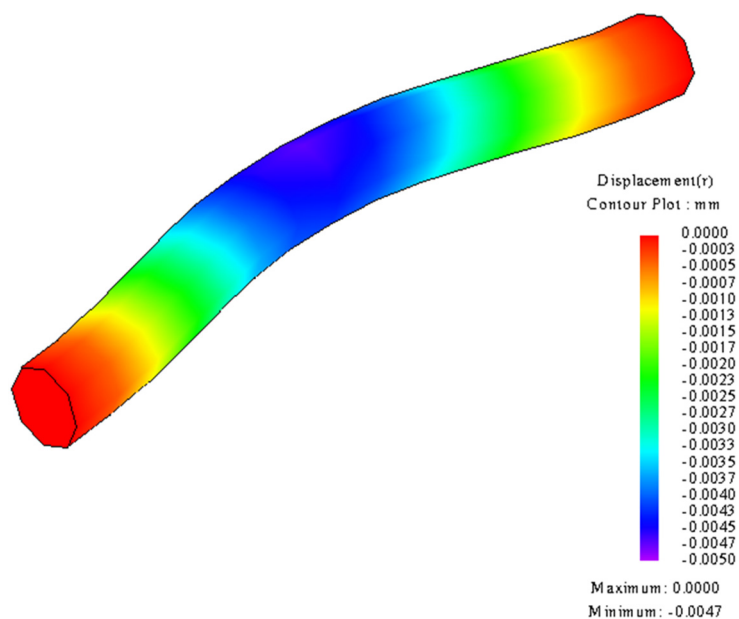
Fig. 5-55. Deflection of the cage rod when deflected inward.
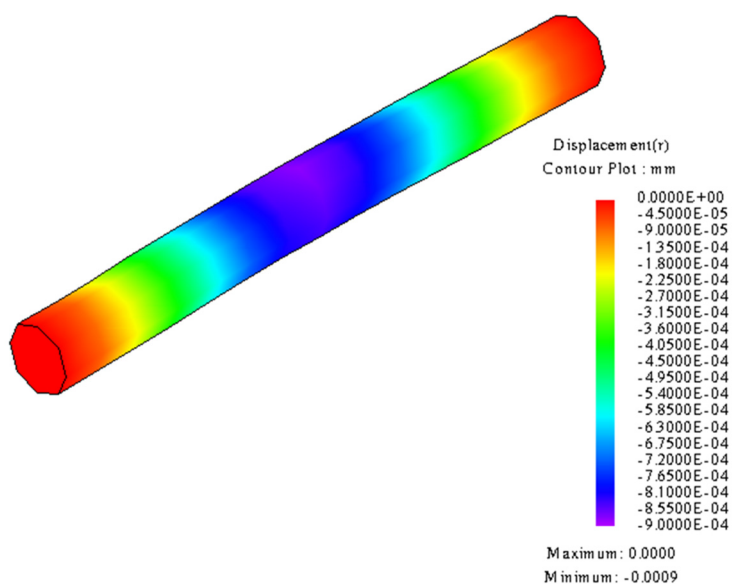
Fig. 5-56. Deflection of the outer rod.

5.4. DESIGN OF STAGE 2 MG WITH STATOR

A stator has been added inside the inner rotor of the stage 2 MG. In this way, it will work as a magnetically geared generator (MGG). The stator has to be able to create 12 poles (6 pole pairs) so that it can interact with the inner rotor and generate a constant

torque. At first, a 45-slot stator was designed which is shown in Fig. 5-57. The distribution of the three-phase distributed winding (phase U, phase W and phase V) is also shown in Fig. 5-57. The phase of the winding was chosen to achieve the highest torque and the corresponding torque on the inner rotor was plotted in Fig. 5-58. The parameters of the stator are described in Table 5-VIII.
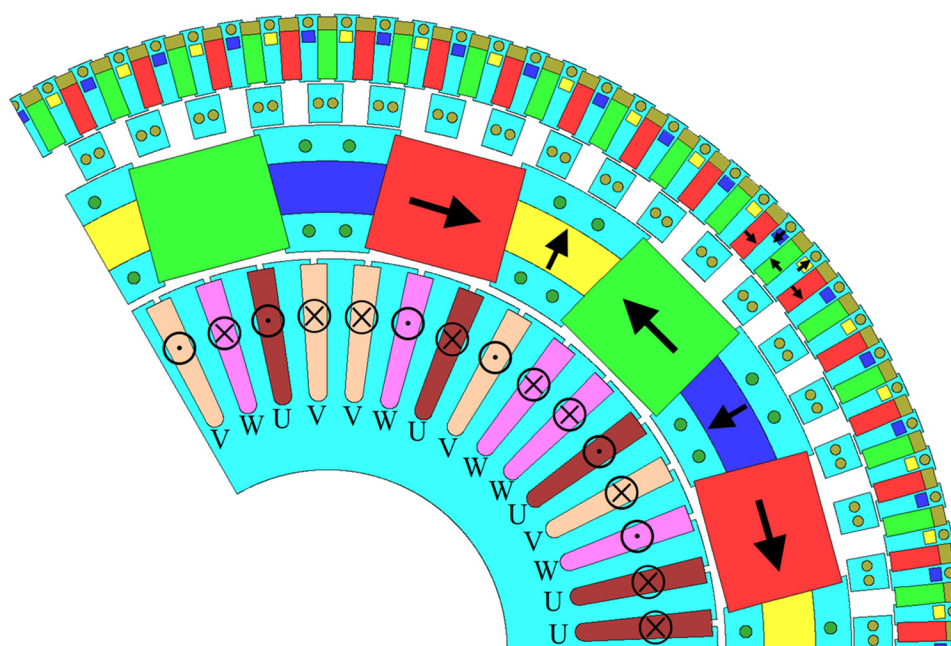
Fig. 5-57. Stage 2 MG with a stator inside which has 45 slots.
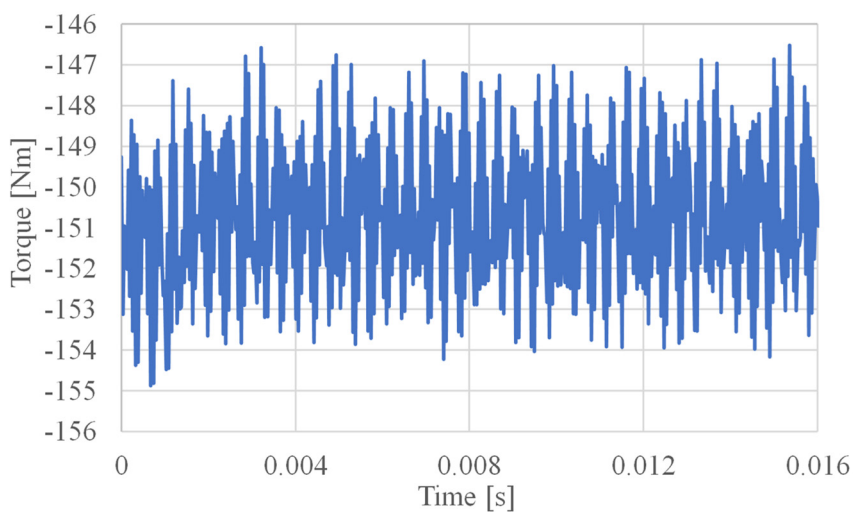
Fig. 5-58. Torque on the inner rotor.

Table 5-VIII. Parameters of the Stator

Parameter	Value	Unit
Outer radius, r_{so}	152	mm
Inner radius, r_{si}	70	mm
Air gap	3	mm
Axial length	37.5	mm
Maximum current density	7.1	A/mm^2
Winding fill factor	0.5	-

Some other fractional winding designs with different number of slots have also been investigated. The slot number was selected to be 17, 37 and 39. The designs and torque on the inner rotor are shown in Fig. 5-59-Fig. 5-66. The performance of different stator designs is summarized in Table 5-IX. The stator with 37 slots can create the highest torque while the stator with 45 slots has the lowest torque ripple on the inner rotor. The 45-slot design has been chosen because of the low torque ripple and as it is the only design which has a symmetric winding distribution.
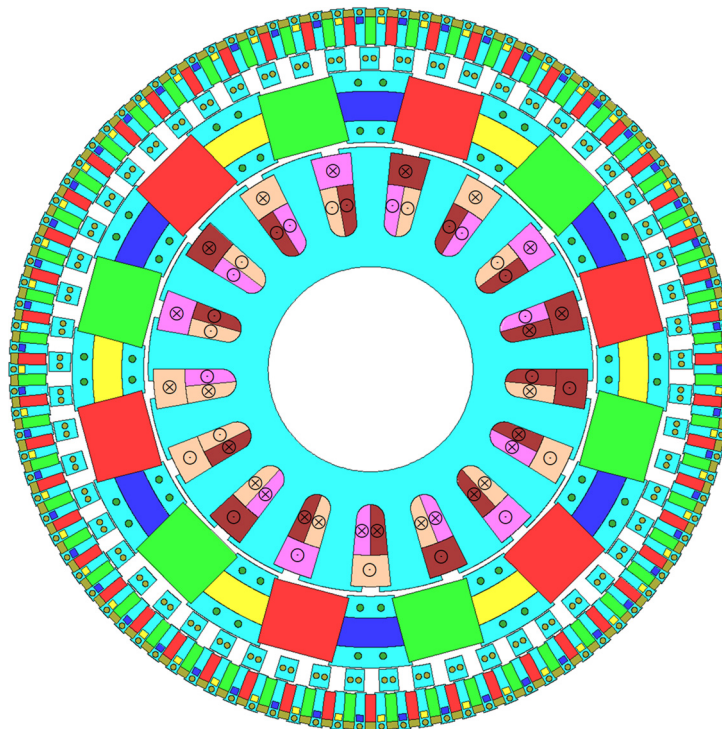
Fig. 5-59. Stage 2 MG with stator which has 17 slots.
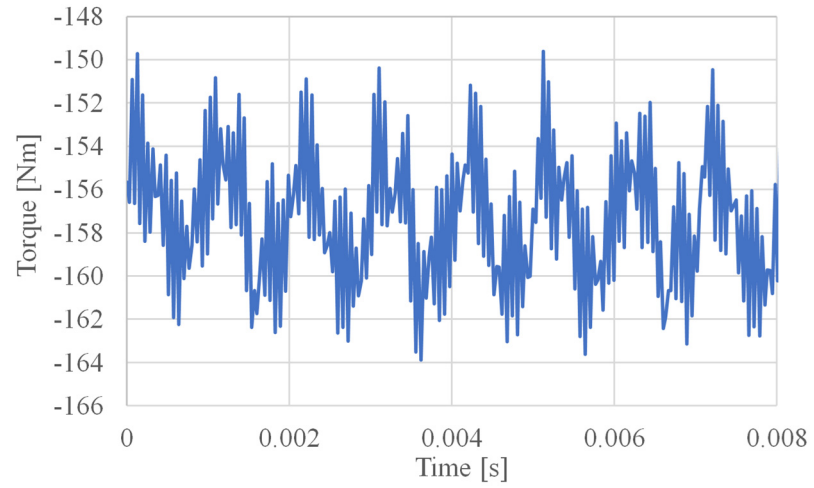
Fig. 5-60. Torque on the inner rotor.
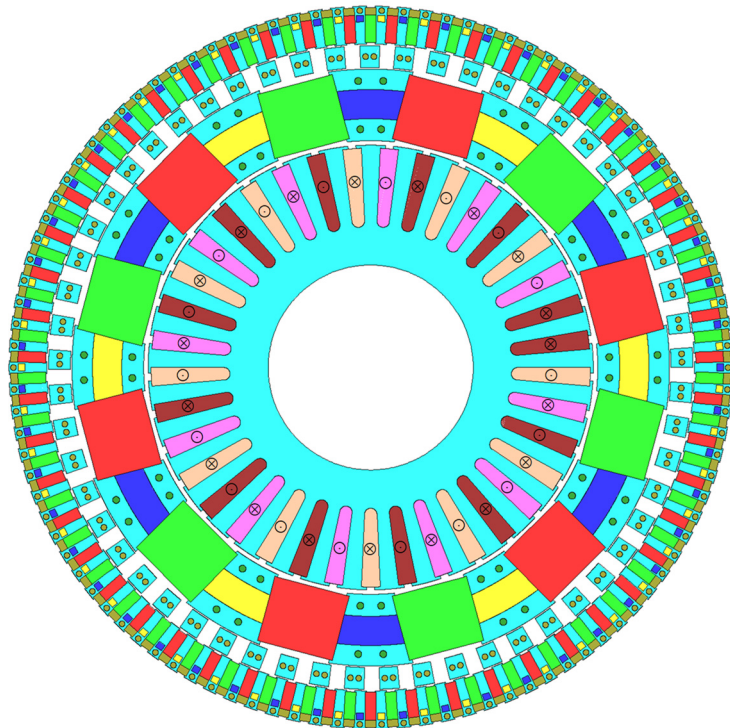
Fig. 5-61. Stage 2 MG with stator which has 37 slots.
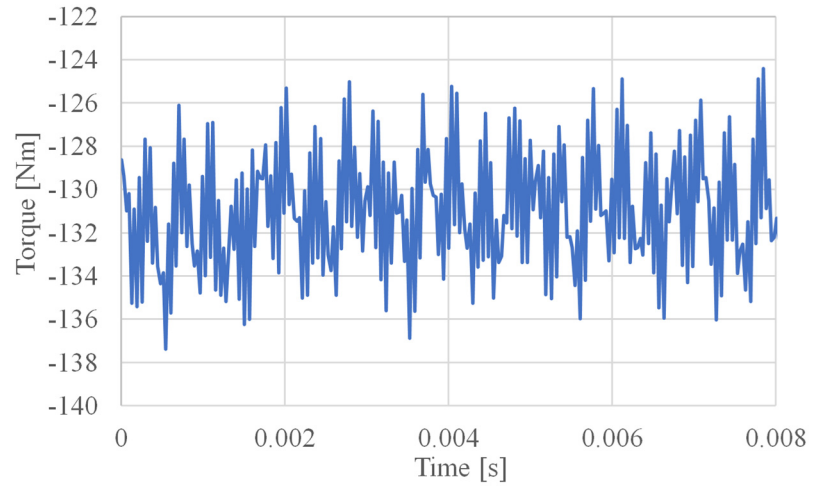
Fig. 5-62. Torque on the inner rotor.
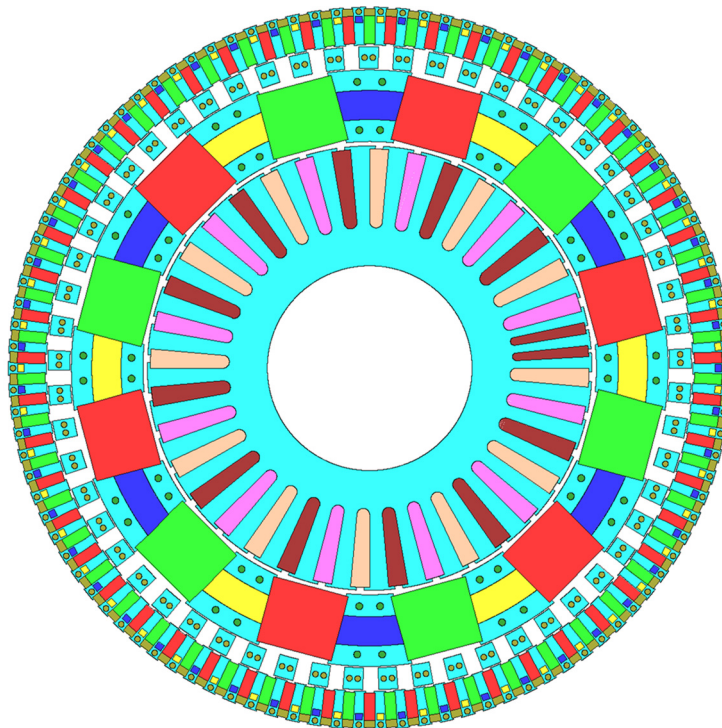
Fig. 5-63. Stage 2 MG with stator which has 37 slots (ununiform teeth).
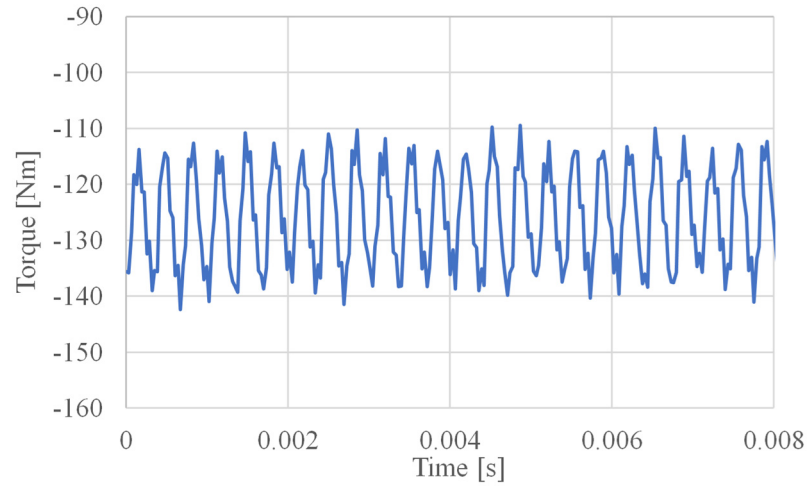
Fig. 5-64. Torque on the inner rotor.
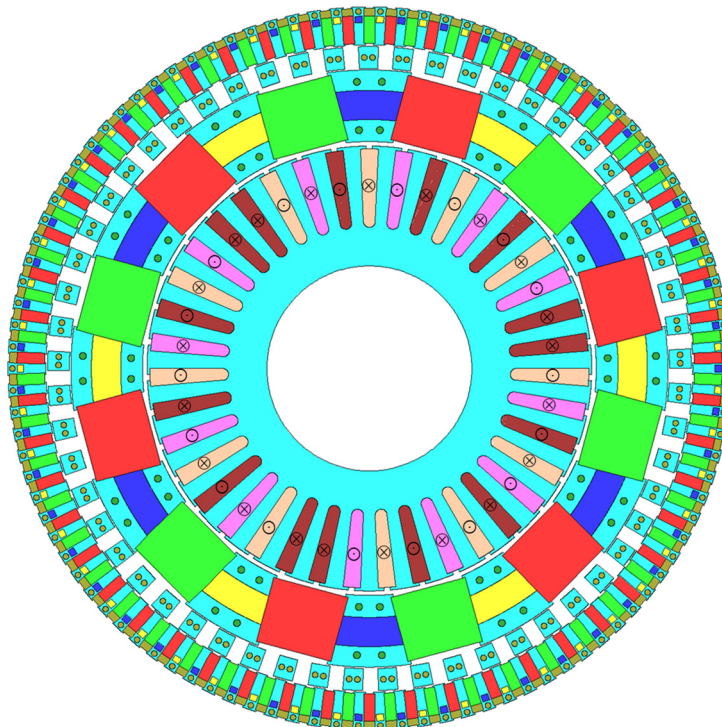
Fig. 5-65. Stage 2 MG with stator which has 39 slots.
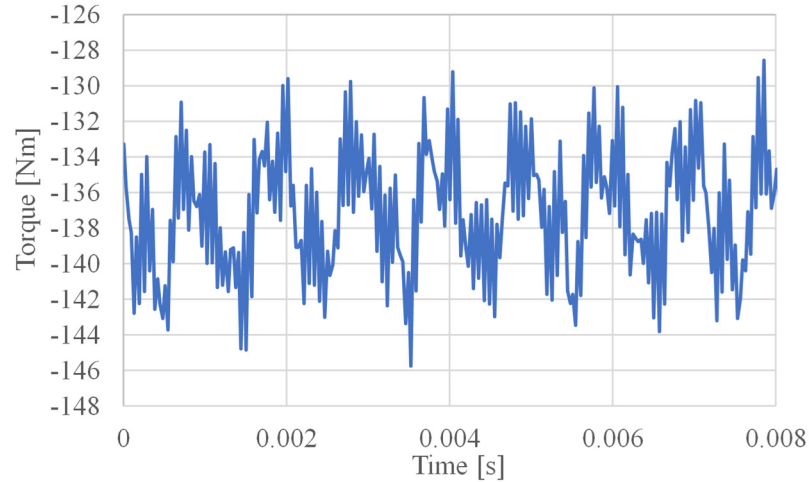
Fig. 5-66. Torque on the inner rotor.

Table 5-IX. COMPARISON OF DIFFERENT DESIGNS OF STATOR.

Number of slots	Peak torque created by stator [Nm]	Torque ripple on the inner rotor [%]
45	95.4	5.55
17	92.5	9.06
37	117.2	9.92
37 (ununiform teeth)	133.1	25.5
39	113.4	12.52

The number of turns in each coil is N_t and the turns function is $n(\theta)$ which gives the total number of turns in a span of θ (starting from 0 degree). The winding function $N(\theta)$, is related to the turns function by

$$N(\theta) = n(\theta) - < n(\theta) > \tag{5.6}$$

where $<n(\theta)>$ is the average of the turns function.

With equation (5.6), the turns functions for the 45-slot design are shown in Fig. 5-67-Fig. 5-69. The winding functions are shown in Fig. 5-70-Fig. 5-72. When $I_W = I_V = -0.5I_U$, the combined winding function is shown in Fig. 5-73. It can be clearly seen that 12 poles (6 pole pairs) is created by this winding distribution. Similarly, the combined winding

functions for 17 slots, 37 slots and 39 slots are shown in Fig. 5-74-Fig. 5-76. All of the designs are able to create 12 poles.
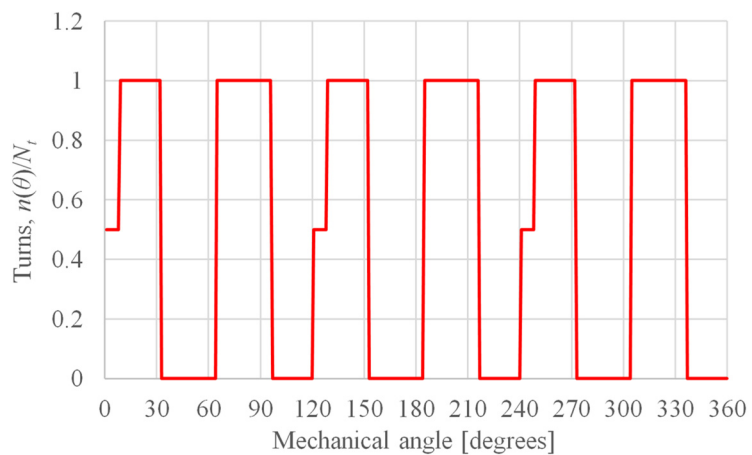
Fig. 5-67. The turns function for phase U with 45 slots.
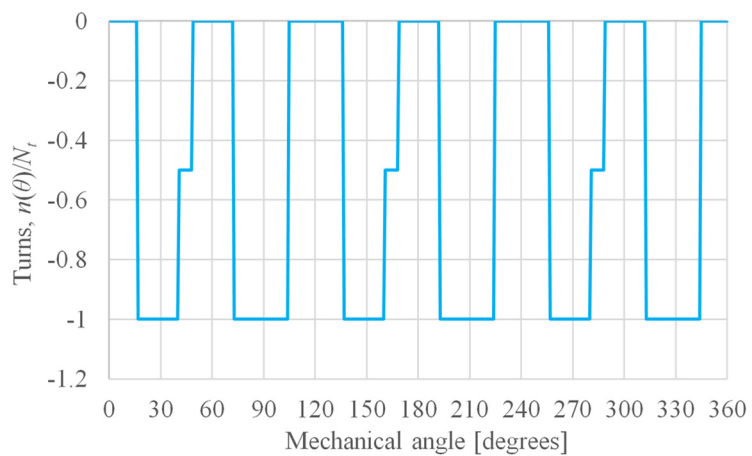
Fig. 5-68. The turns function for phase W with 45 slots.
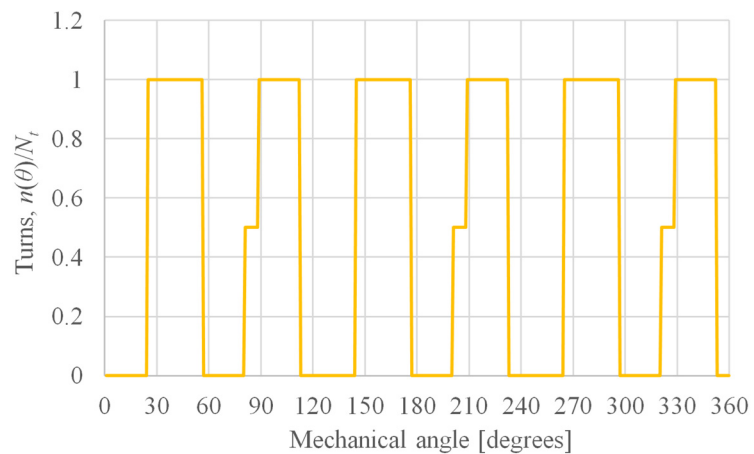
Fig. 5-69. The turns function for phase V with 45 slots.
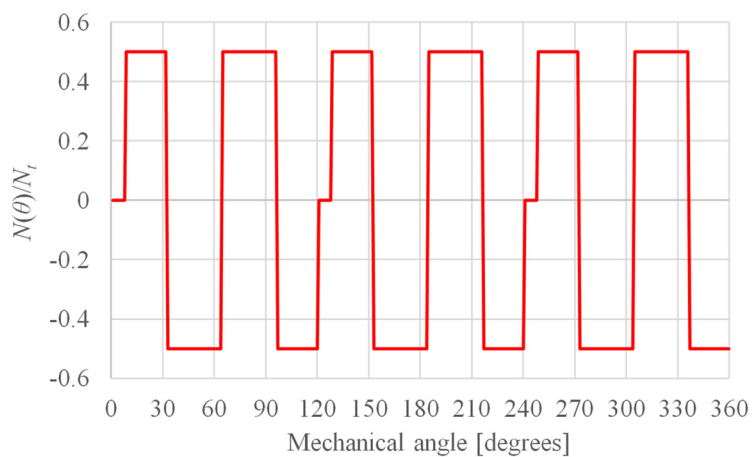
Fig. 5-70. The winding function for phase U with 45 slots.
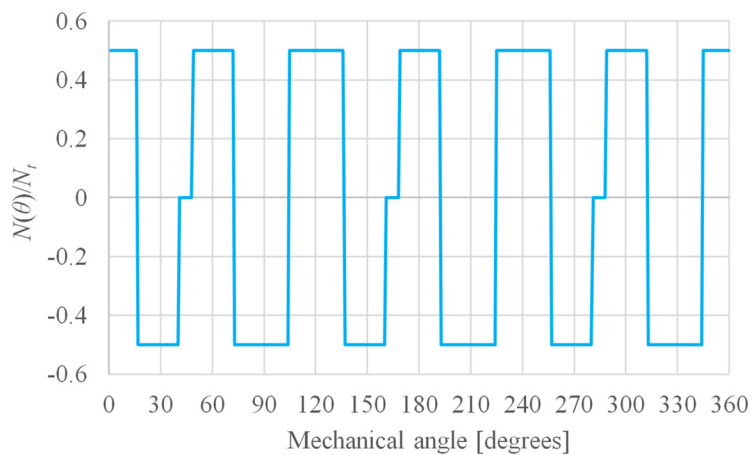
Fig. 5-71. The winding function for phase W with 45 slots.
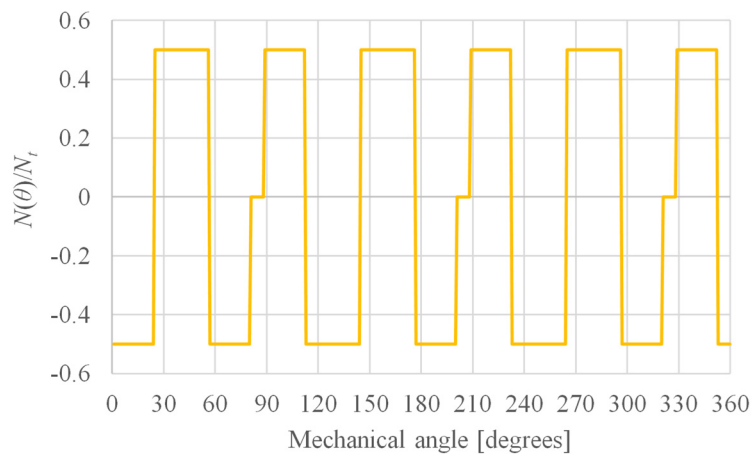
Fig. 5-72. The winding function for phase V with 45 slots.
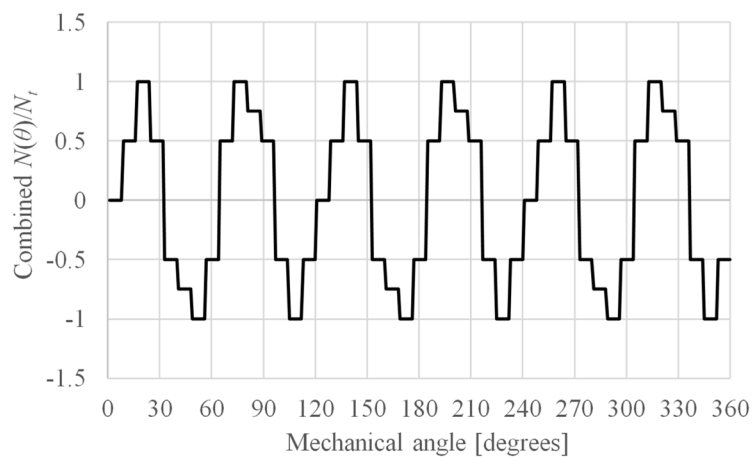
Fig. 5-73. The combined winding function with 45 slots.
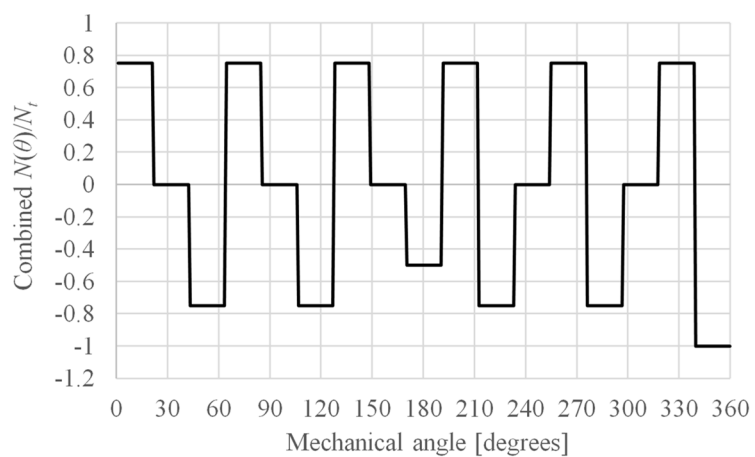
Fig. 5-74. The combined winding function with 17 slots.
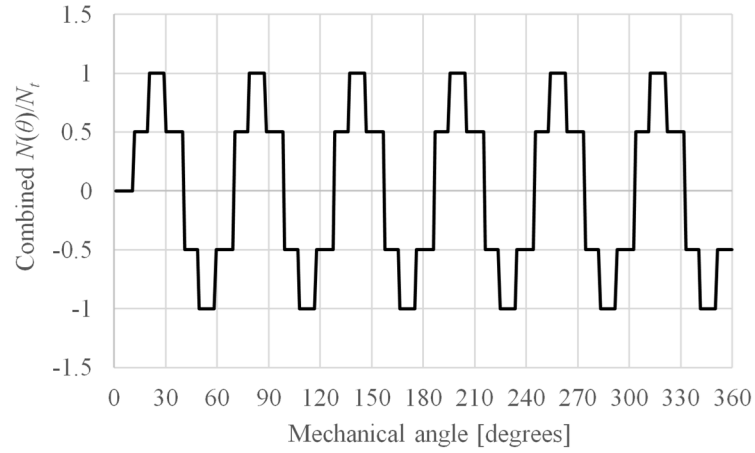
Fig. 5-75. The combined winding function with 37 slots.
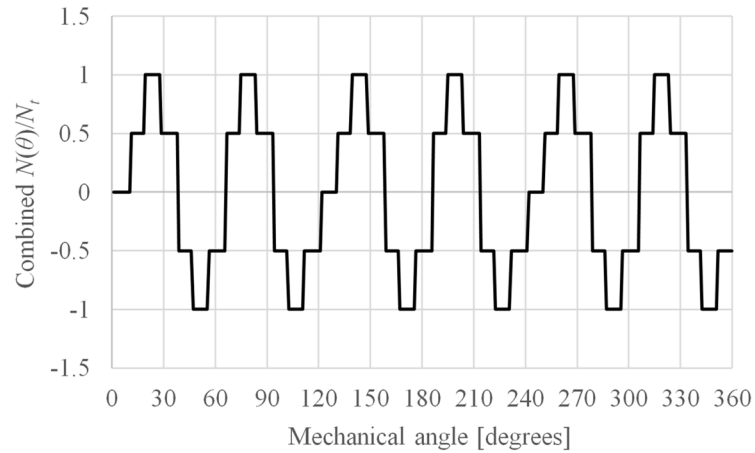
Fig. 5-76. The combined winding function with 39 slots.

For the 45-slot design, the span of the stator teeth lips, θ_s has been varied to evaluate the torque and torque ripple variation. It is illustrated in Fig. 5-77 and the results are shown in Table 5-X. There is no significant difference for the torque and torque ripple values. Therefore, the value of θ_s is kept as 1.5 degrees.
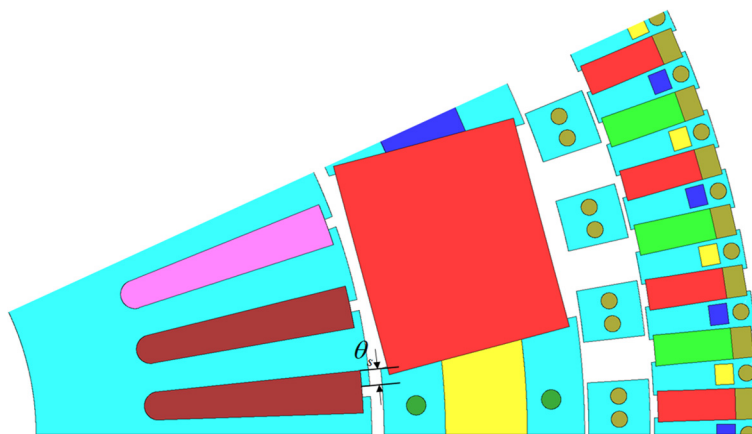
Fig. 5-77. Variation of the lips of the stator teeth.

Table 5-X. Performance Comparison with Different Values of θ_s.

θ_s [degrees]	Peak torque created by stator [Nm]	Torque ripple on the inner rotor [%]
1.8	94.6	6.45
1.5 (original)	95.4	5.55
1.2	97.5	5.29
0.9	97.3	5.15
0.6	96.0	4.95

The performance of magnetic gearboxes has been compared with the mechanical 59:1 Sumitomo gearbox which is shown in Fig. 5-78. The magnetic gear is competitive with a similar size mechanical gearbox.

The scaling analysis has been done to evaluate the possibility to scale up to MW size. In this analysis, the number of pole pairs has been kept the same and the sizes of the rotors and the air gap have been scaled up by a scaling factor γ. The power is calculated when the cage rotor has a speed of 80 RPM and the results are given in Table 5-XI and Fig. 5-79. The MG is capable of achieving more than 3.5 MW when the outer radius is larger than 1.1 m. The volume torque density is almost the same with different scaling factor which means the power and torque are proportional of γ^3.

Stage 1 MG   Stage 2 MG   MSMG   Mechanical gearbox

Fig. 5-78. Comparison between the magnetic gearboxes and mechanical gearbox.
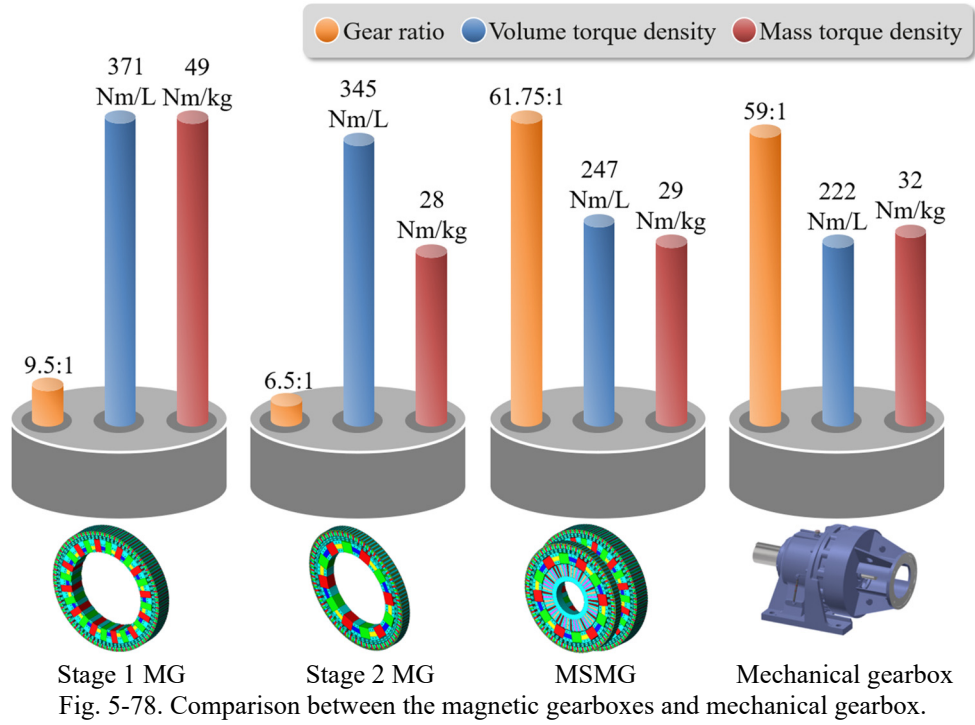
Table 5-XI. SCALING ANALYSIS OF STAGE 1 MG.

γ	Outer radius r_{o3} [mm]	Axial length d_1 [mm]	Air gap g [mm]	Torque [Nm]	Torque density [Nm/L]	Power [kW]
1 (original)	274	75	1	6560	371	55
1.1	301.4	82.5	1.1	8755	372	73
1.2	328.8	90	1.2	11324	370	95
1.3	356.2	97.5	1.3	14380	370	120
1.4	383.6	105	1.4	17979	370	151
1.5	411	112.5	1.5	22121	371	185
2	548	150	2	52349	370	439
3	822	225	3	176944	370	1482
4	1096	300	4	419878	371	3518
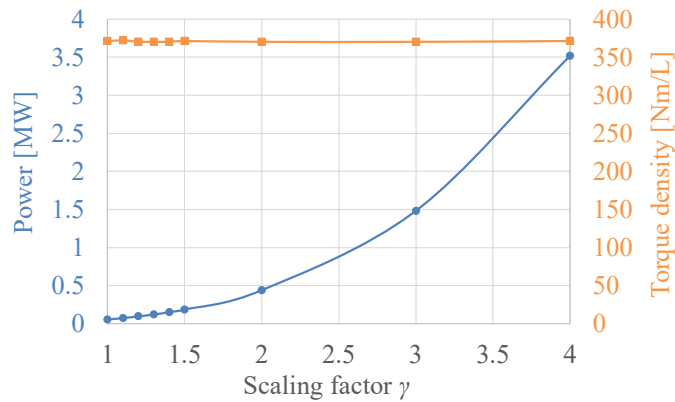
Fig. 5-79. Scaling analysis of the MG.

5.5. CONCLUSION

In this chapter, a series connected MSMG has been designed for a hydropower generator application. The flux concentration topology has been used in order to increase the torque. Different mechanical supports have been designs to make sure that the air gap will be maintained once fully assembled. A stator has also been designed and optimized with fractional winding distribution.

CHAPTER 6 : AN ANALYTICAL BASED MODEL FOR THE AXIAL MAGNETIC COUPLING

A permanent magnetic coupling (PMC) provides a means of spatially transmitting torque without physical contact. It enables components to be isolated and thereby can minimize or eliminate mechanical vibration through magnetic damping [61]. A PMC can act as a torque limiter that can isolate loads when subjected to over torque conditions [62]. A PMC also allows one to insert a mechanical barrier between the drivers allowing torque to be transmitted between separate environments under different pressure differentials [63].

As the PMC is capable of continuously operating at a high sustained magnetic shear stress the study of the mass and volumetric torque densities of PMCs provides insight into the upper performance bound of other magnetic devices, such as magnetic gearboxes.

There are two main types of PMC, axial and radial topologies [64]. This chapter will first focus on deriving exact closed form 3-D torque and field equations for an axial Halbach rotor coupling. In section 6.1 an introduction to the axial magnetic coupling is provided. In section 6.2 the Halbach magnetization vector is determined. In section 6.3 the magnetic scalar field solution for the Halbach axial rotor has been obtained. In section 6.4, the torque expressions are derived. In section 6.5, the magnetic field solution is provided and the presented analytical model is compared with a 3-D FEA model. The presented new 3-D field and torque analysis approach can be extended to model other 3-D axial magnetic devices.

6.1. INTRODUCTION

The fields in an axial PMC are highly dependent on the radial position and therefore in order to accurately model the field profile and consequently torque a full 3-D model is needed. Lubin *et. al.* [65,66] demonstrated that if only a 2-D axial PMC model is used, the error could be up to 30% [65,66].

Wang *et. al.* [67], Shin *et. al.* [68] and Yao *et. al.* [69] utilized the 3-D FEA method to study the performance of an axial PMC. While Dolisy *et. al.* created a 3-D analytic model of a magnetic coupling by ignoring the curvature effects [70,71]. This approach was shown to be quite accurate when the air-gap is not large. Furlani [72] and Waring *et. al.* [73] computed the 3-D field and torque due to two magnetic rotor couplings surrounded by air. In order to create the model, the field contributions were discretized by subdividing the individual segments into magnetic charge regions and then summing up the contributions of each surface. Such an approach is highly accurate [69,72] but the approach is laborious and the final equation is hard to interpret. For instance, Furlani's formula results in the need to evaluate a torque expression that contains six embedded summation terms [72]. Such an approach cannot be extended to problems that contain magnetic steel. Thompson *et. al.* [74,75] used a similar approach. Thompson derived the 3-D field for an axial Halbach rotor by summing up the individual field contributions from individual surface current sheets on each magnet surface. This approach required the evaluation of many double integrals as well as summation terms and the approach also cannot be generalized to model problems that contain magnetic steel. In this chapter, a more computationally efficient 3-D calculation approach is developed. It should be noted that an alternative approximate charge sheet model was developed which is

discussed in Appendix A [76]. This alternative approximate charge sheet model was shown to be only accurate across a limited range of geometry values. This was because the magnetic charge distribution was only defined on the surfaces.

6.2. HALBACH ARRAY MAGNETIZATION VECTOR FIELD SOLUTION

The model of an axial Halbach rotor is shown in Fig. 6-1. It has an inner radius, r_i, and an outer radius, r_o. The axial length is d_a^I. The rotor magnets are magnetized along the axial direction and the Halbach array has 8 segments which is illustrated in Fig. 6-2.
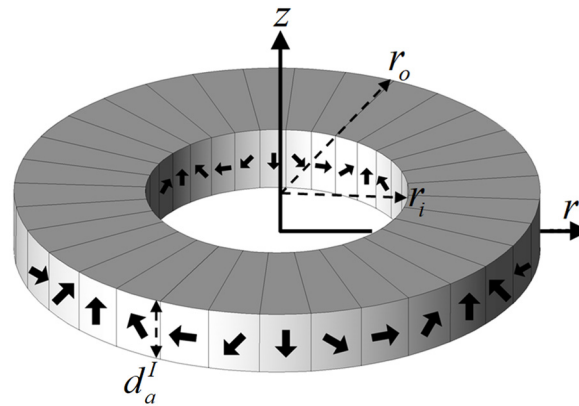
Fig. 6-1. An Axial 8-segment Halbach rotor with $p_I = 4$ pole pairs.
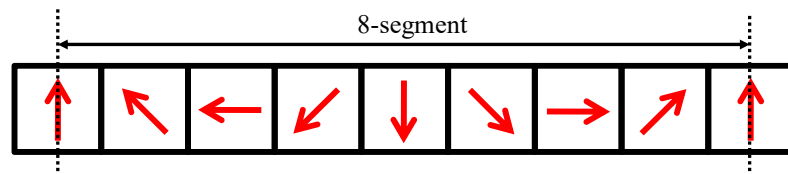
Fig. 6-2. 8-segment Halbach array.

Maxwell's equations for a magnetostatic current-free problem are given by [77]:

$$\nabla \cdot \mathbf{B} = 0 \tag{6.1}$$

$$\nabla \times \mathbf{H} = 0 \tag{6.2}$$

The constitutive equation when a magnetization vector $\mathbf{M}$ is presented is given by:

$$\mathbf{B} = \mu_0 \mu_r \mathbf{H} + \mu_0 \mathbf{M} \tag{6.3}$$

and in the air

$$\mathbf{B} = \mu_0 \mathbf{H} \tag{6.4}$$

The volumetric and surface charge functions are related to the magnetization vector by [72]:

$$\rho_m^b(\theta_I) = -\frac{\nabla \cdot \mathbf{M}}{\mu_r}, \text{ in region } b \tag{6.5}$$

and

$$\sigma_m^a(\theta_I) = \hat{\mathbf{z}} \cdot \mathbf{M}, \text{ on surface } a \tag{6.6}$$

$$\sigma_m^c(\theta_I) = -\hat{\mathbf{z}} \cdot \mathbf{M}, \text{ on surface } c \tag{6.7}$$

where $\hat{z}$ is the normal vector on the top and bottom surface of the axial Halbach rotor. These regions and the normal vectors are defined as shown in Fig. 6-3. Surface S_a is located at $z = d_a^I$ and surface S_c is located at $z = 0$. The volume region is named as volume V_b.
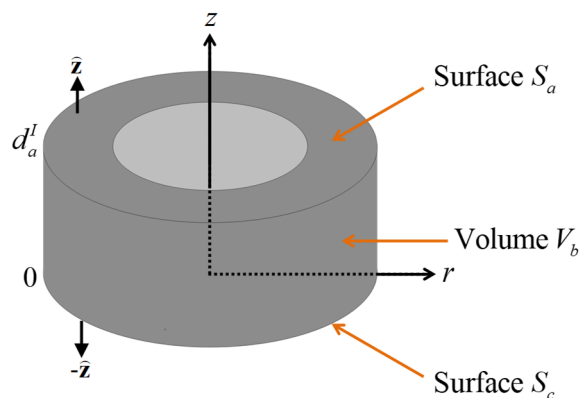
Fig. 6-3. Position and geometry of rotor I.

The Halbach magnetized magnets (8 segments) are modeled as a composition of axially and azimuthally magnetized magnets as shown in Fig. 6-4. The field is directed upwards.
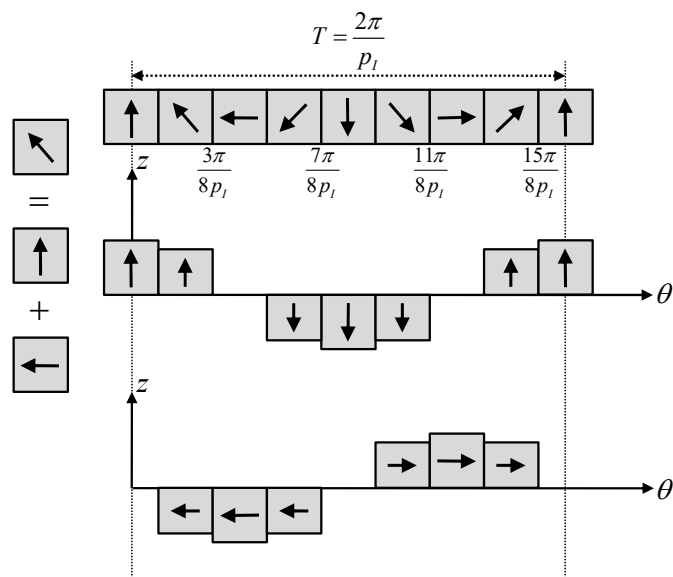
Fig. 6-4. Halbach magnet array expressed in terms of axial and angular direction.

In polar coordinates, the magnetizing distribution in the magnet region can be expressed by the Fourier series:

$$\mathbf{M} = M_z(\theta)\hat{\mathbf{z}} + M_\theta(\theta)\hat{\boldsymbol{\theta}}$$

$$= \sum_{n=1}^{\infty} a_n \cos(np_I\theta)\hat{\mathbf{z}} - \sum_{n=1}^{\infty} b_n \sin(np_I\theta)\hat{\boldsymbol{\theta}} \tag{6.8}$$

where

$$a_n = \frac{4}{T} \int_0^{T/2} M_z(\theta)\cos(np_I\theta)d\theta \tag{6.9}$$

$$b_n = -\frac{4}{T} \int_0^{T/2} M_\theta(\theta)\sin(np_I\theta)d\theta \tag{6.10}$$

$$T = \frac{2\pi}{p_I} \tag{6.11}$$

and p_I is the number of pole pairs. M_z and M_θ are the axial and angular component of $\mathbf{M}$ respectively and are plotted as a function of position in Fig. 6-5 and Fig. 6-6.
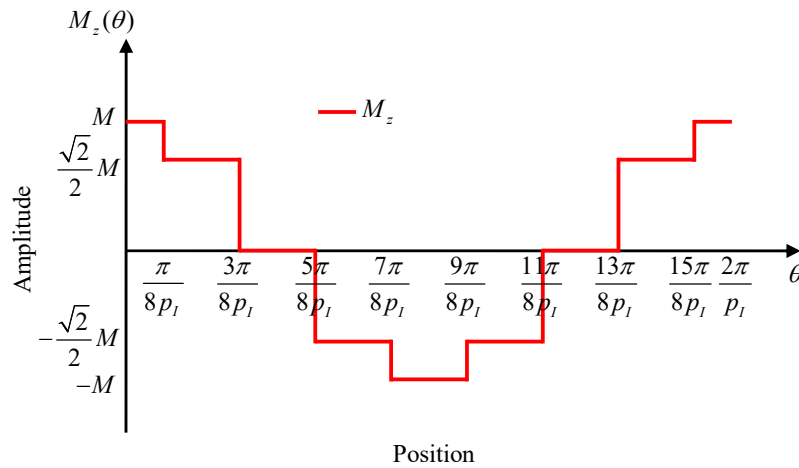
Fig. 6-5. Magnitude of M_z as a function of angular position.

_176_
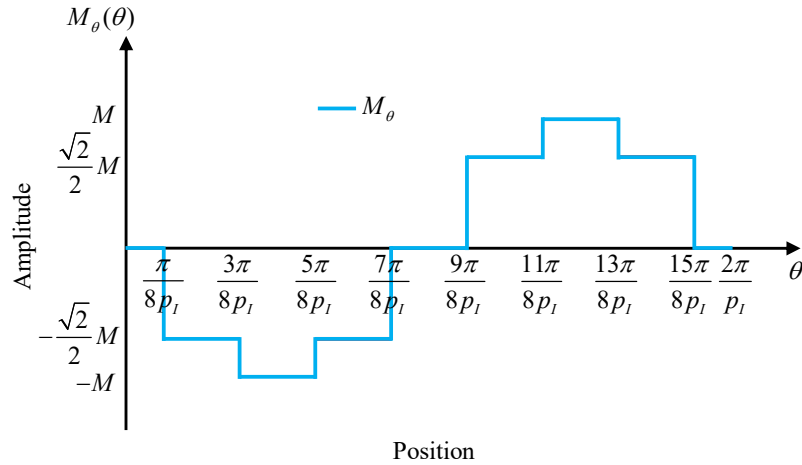
Fig. 6-6. Magnitude of M_θ as a function of angular position.

Noting the values and step changes in Fig. 6-6 (a) allows equation (6.9) to be written as:

$$a_n = \frac{4}{T}\left[\int_0^{\frac{\pi}{8p_I}} M\cos(np_I\theta)d\theta + \int_{\frac{\pi}{8p_I}}^{\frac{3\pi}{8p_I}} \frac{\sqrt{2}}{2}M\cos(np_I\theta)d\theta \right.$$
$$\left. -\int_{\frac{5\pi}{8p_I}}^{\frac{7\pi}{8p_I}} \frac{\sqrt{2}}{2}M\cos(np_I\theta)d\theta - \int_{\frac{7\pi}{8p_I}}^{\frac{\pi}{p_I}} M\cos(np_I\theta)d\theta\right]$$

(6.12)

where

$$M = B_m/\mu_0$$

(6.13)

and B_m is the magnet residual flux density.

Evaluating the integrals in (6.12) one obtains:

$$a_n = \left(\frac{2-\sqrt{2}}{n\pi}\right)M\left[\sin\left(\frac{n\pi}{8}\right)+\sin\left(\frac{7n\pi}{8}\right)\right]+\frac{\sqrt{2}M}{n\pi}\left[\sin\left(\frac{3n\pi}{8}\right)+\sin\left(\frac{5n\pi}{8}\right)\right]$$ (6.14)

Utilizing trigonometric identities allow (6.14) to be simplified to:

$$a_n = \begin{cases} \left(\dfrac{4-2\sqrt{2}}{n\pi}\right) M \sin\left(\dfrac{n\pi}{8}\right) + \dfrac{2\sqrt{2}M}{n\pi}\sin\left(\dfrac{3n\pi}{8}\right) & , n \text{ is odd} \\ 0 & , n \text{ is even} \end{cases} \tag{6.15}$$

Similarly, b_n can be obtained:

$$b_n = \frac{2-\sqrt{2}}{n\pi} M \left[\cos\left(\frac{5n\pi}{8}\right) - \cos\left(\frac{3n\pi}{8}\right)\right] + \frac{\sqrt{2}M}{n\pi}\left[\cos\left(\frac{7n\pi}{8}\right) - \cos\left(\frac{n\pi}{8}\right)\right] \tag{6.16}$$

After simplification, the expression of b_n can be reduced down to:

$$b_n = \begin{cases} \dfrac{4-2\sqrt{2}}{n\pi} M \cos\left(\dfrac{5n\pi}{8}\right) + \dfrac{2\sqrt{2}M}{n\pi}\cos\left(\dfrac{7n\pi}{8}\right) & , n \text{ is odd} \\ 0 & , n \text{ is even} \end{cases} \tag{6.17}$$

The magnetic field is assumed to directed upwards in $+z$ direction. Substituting (6.15) and (6.17) into (6.8) gives:

$$\mathbf{M} = \sum_{n=1}^{\infty}\left[\left(\frac{4-2\sqrt{2}}{(2n-1)\pi}\right) M \sin\left(\frac{(2n-1)\pi}{8}\right) + \frac{2\sqrt{2}M}{(2n-1)\pi}\sin\left(\frac{3(2n-1)\pi}{8}\right)\right]\cos\left[(2n-1)p_I\theta\right]\hat{z}$$
$$- \sum_{n=1}^{\infty}\left[\frac{4-2\sqrt{2}}{(2n-1)\pi} M \cos\left(\frac{5(2n-1)\pi}{8}\right) + \frac{2\sqrt{2}M}{(2n-1)\pi}\cos\left(\frac{7(2n-1)\pi}{8}\right)\right]\sin\left[(2n-1)p_I\theta\right]\hat{\theta} \tag{6.18}$$

Fig. 6-7 shows the absolute magnitude of the different harmonics contained in both M_z and M_θ. When $n = 1$, then from (6.14) and (6.16) one has:

$$\left|a_1\right| = \left|b_1\right| = 0.9745M \tag{6.19}$$

Therefore, if only the fundamental harmonic is considered ($n = 1$), then (6.13) becomes:

$$M_f = c_1 M \tag{6.20}$$

where

$$c_1 = 0.9745 \tag{6.21}$$
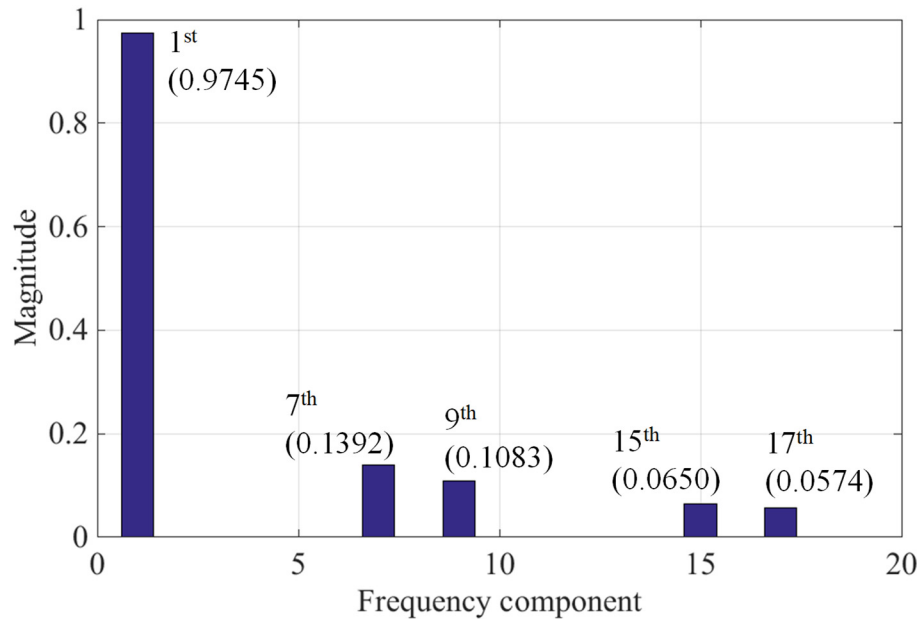
Fig. 6-7. Magnitude of different harmonic components.

In the following sections, M_f will be used to replace M. Such an approximation has been used by Xia [78] and provides an accurate result when the Halbach magnets are highly segmented. In all the analysis, it is assumed that the Halbach field is directed upwards. Similarly, if the Halbach array is made up of 16 segments as shown in Fig. 6-8, the magnitude of the fundamental harmonic is $M_f = 0.9936M$.
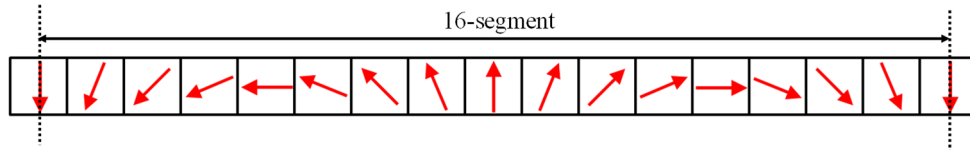
Fig. 6-8. 16-segment Halbach magnet array.

6.3. Magnetic Scalar Field Solution of the Halbach Axial Rotor

The external and internal fields when a magnetization vector is present is given by (6.3). As the fields are magnetostatic, the fields can be described by using the magnetic scalar potential, ϕ. Substituting (6.3) into (6.1) and assume linearity gives:

$$\mu_r \nabla \cdot \mathbf{H} = -\nabla \cdot \mathbf{M} \tag{6.22}$$

From (6.2) the magnetic field intensity can be related to the magnetic scalar potential, since

$$\nabla \times (\nabla \phi) = 0 \tag{6.23}$$

we can therefore define the magnetic scalar potential as [77]

$$\mathbf{B} = -\mu_0 \nabla \phi \tag{6.24}$$

Substituting (6.24) into (6.22) gives

$$\mu_r \nabla^2 \phi = \nabla \cdot \mathbf{M} \tag{6.25}$$

The point charge on the surface S_a and S_c, and in the volume V_b can be separately described as shown in Fig. 6-9, where z_c is located between 0 and d_a^I.
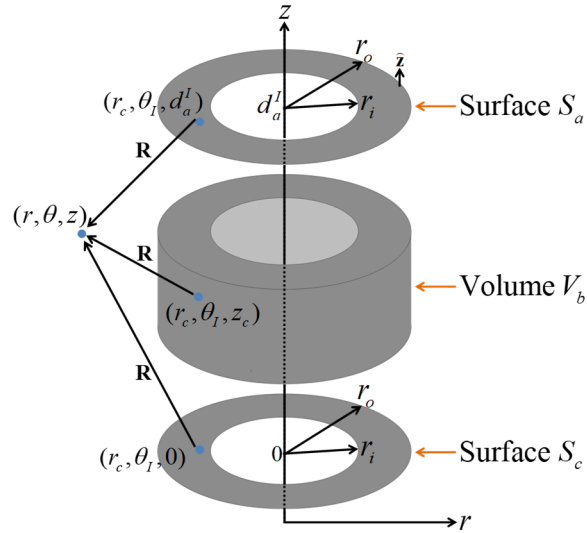
Fig. 6-9. Parameters in the 3-D charge model (the top and bottom surfaces have been separated from the rotor for better illustration).

The external field of the Halbach rotor can then be determined by evaluating the field coming from a magnetic point charge within the volumetric and surface regions of the rotor [72], such that:

$$
\begin{aligned}
\phi^I(r,\theta,z) = {} & \frac{1}{4\pi\mu_0} \frac{\rho_m^b}{R(r,r_c,\theta-\theta_I,z-z_c)} \\
& + \frac{1}{4\pi\mu_0} \frac{\sigma_m^a}{R(r,r_c,\theta-\theta_I,z-d_a^I)} \\
& - \frac{1}{4\pi\mu_0} \frac{\sigma_m^c}{R(r,r_c,\theta-\theta_I,z)}
\end{aligned}
\tag{6.26}
$$

where ρ_m^b is the volume charge density and σ_m^a, σ_m^c are the top and bottom surface charge densities. The distance between the point charge and the field point of interest is described by:

$$
R(r,r_c,\phi,z_c) = \sqrt{C(r,r_c,\phi) + z_c^{\,2}}
\tag{6.27}
$$

where

$$C(a,b,\phi) = a^2 + b^2 - 2ab\cos(\phi) \tag{6.28}$$

is the law of cosines.

If the point charges on the surface and volume are functions then the net field created by all point charges is given by:

$$\begin{aligned}
\phi^I(r,\theta,z) &= \frac{1}{4\pi\mu_0}\int_0^{d_a^I}\int_0^{2\pi}\int_{r_i}^{r_o}\frac{\rho_m^b(\theta_I)}{R(r,r_c,\theta-\theta_I,z-z_c)}r_c\,dr_c\,d\theta_I\,dz_c \\
&+\frac{1}{4\pi\mu_0}\int_0^{2\pi}\int_{r_i}^{r_o}\frac{\sigma_m^a(\theta_I)}{R(r,r_c,\theta-\theta_I,z-d_a^I)}r_c\,dr_c\,d\theta_I \\
&+\frac{1}{4\pi\mu_0}\int_0^{2\pi}\int_{r_i}^{r_o}\frac{\sigma_m^c(\theta_I)}{R(r,r_c,\theta-\theta_I,z)}r_c\,dr_c\,d\theta_I
\end{aligned} \tag{6.29}$$

Since [77]

$$\nabla \cdot \mathbf{M} = \frac{1}{r}M_r + \frac{1}{r}\frac{\partial M_r}{\partial r} + \frac{1}{r}\frac{\partial M_\theta}{\partial \theta} + \frac{\partial M_z}{\partial z} \tag{6.30}$$

Then by substituting (6.8) into (6.30) gives

$$\nabla \cdot \mathbf{M} = -\frac{np_I}{r_c}\sum_{n=1}^{\infty}b_n\cos(np_I\theta_I) \tag{6.31}$$

and this allows (6.5) to be written as:

$$\rho_m^b(\theta_I) = \frac{np_I}{\mu_r r_c}\sum_{n=1}^{\infty}b_n\cos(np_I\theta_I), \text{ in region } b \tag{6.32}$$

Similarly, substituting (6.8) into (6.6) and (6.7) gives

$$\sigma_m^a(\theta_I) = \sum_{n=1}^{\infty} a_n \cos(np_I\theta_I) \tag{6.33}$$

$$\sigma_m^c(\theta_I) = -\sum_{n=1}^{\infty} a_n \cos(np_I\theta_I) \tag{6.34}$$

If we only consider the fundamental component, then (6.32)-(6.34) can be simplified down to

$$\rho_m^b(\theta_I) = \frac{p_I}{\mu_r r_c} M_f \cos(p_I\theta_I) \tag{6.35}$$

$$\sigma_m^a(\theta_I) = M_f \cos(p_I\theta_I) \tag{6.36}$$

$$\sigma_m^c(\theta_I) = -M_f \cos(p_I\theta_I) \tag{6.37}$$

It is interesting to note that only the source field magnitude due to the volumetric region is proportional to the pole pair value. Substituting (6.35)-(6.37) into (6.29) gives:

$$
\begin{aligned}
\phi^I(r,\theta,z) = {} & \frac{M_f}{4\pi\mu_0} \int_0^{2\pi} \int_{r_i}^{r_o} \frac{\cos(p_I\theta_I)}{R(r,r_c,\theta-\theta_I,z,d_a^I)} r_c \, dr_c \, d\theta_I \\
& - \frac{M_f}{4\pi\mu_0} \int_0^{2\pi} \int_{r_i}^{r_o} \frac{\cos(p_I\theta_I)}{R(r,r_c,\theta-\theta_I,z,0)} r_c \, dr_c \, d\theta_I \\
& + \frac{p_I M_f}{4\pi\mu_r\mu_0} \int_0^{d_a^I} \int_0^{2\pi} \int_{r_i}^{r_o} \frac{\cos(p_I\theta_I)}{R(r,r_c,\theta-\theta_I,z,z_c)} dr_c \, d\theta_I \, dz_c
\end{aligned}
\tag{6.38}
$$

The magnetic scalar potential field integral terms in (6.38) can each be evaluated separately by defining:

$$\phi^I(r,\theta,z) = \phi^a(r,\theta,z) + \phi^b(r,\theta,z) - \phi^c(r,\theta,z) \tag{6.39}$$

where ϕ^a, ϕ^c and ϕ^b are the magnetic scalar fields created by the magnetic charge on surface S_a, surface S_c and within volume V_b, respectively. They can be written as:

$$\phi^a(r,\theta,z) = \frac{M_f}{4\pi\mu_0}\int_0^{2\pi}\int_{r_i}^{r_o}\frac{\cos(p_I\theta_I)}{R(r,r_c,\theta-\theta_I,z,d_a^I)}r_c dr_c d\theta_I \tag{6.40}$$

$$\phi^c(r,\theta,z) = \frac{M_f}{4\pi\mu_0}\int_0^{2\pi}\int_{r_i}^{r_o}\frac{\cos(p_I\theta_I)}{R(r,r_c,\theta-\theta_I,z,0)}r_c dr_c d\theta_I \tag{6.41}$$

$$\phi^b(r,\theta,z) = \frac{p_I M_f}{4\pi\mu_r\mu_0}\int_0^{d_a^I}\int_0^{2\pi}\int_{r_i}^{r_o}\frac{\cos(p_I\theta_I)}{R(r,r_c,\theta-\theta_I,z,z_c)}dr_c d\theta_I dz_c \tag{6.42}$$

6.3.1. Magnetic Scalar Field due to Surface Charge

Substituting (6.27) back into (6.40) gives the magnetic surface charge in cylindrical coordinates:

$$\phi^a(r,\theta,z) = \frac{M_f}{4\pi\mu_0}\int_0^{2\pi}\int_{r_i}^{r_o}\frac{\cos(p_I\theta_I)}{\sqrt{r^2+r_c^2-2rr_c\cos(\theta-\theta_I)+(z-d_a^I)^2}}r_c dr_c d\theta_I \tag{6.43}$$

Evaluating the integral in terms of r_c gives

$$\phi^a(r,\theta,z)$$
$$= \frac{M_f}{4\pi\mu_0}\int_0^{2\pi}\cos(p_I\theta_I)\times$$
$$\{R(r,r_o,\theta-\theta_I,z-d_a)+r\cos(\theta-\theta_I)\log[r_o-r\cos(\theta-\theta_I)+R(r,r_o,\theta-\theta_I,z-d_a)]$$
$$-R(r,r_i,\theta-\theta_I,z-d_a)-r\cos(\theta-\theta_I)\log[r_i-r\cos(\theta-\theta_I)+R(r,r_i,\theta-\theta_I,z-d_a)]\}d\theta_I \tag{6.44}$$

Define

$$\theta-\theta_I = \theta_d \tag{6.45}$$

then

$$\theta_I = \theta - \theta_d \tag{6.46}$$

$$d\theta_I = -d\theta_d \tag{6.47}$$

Substituting (6.46) and (6.47) into (6.44) gives

$$
\begin{aligned}
\phi^a(r,\theta,z) \\
= \frac{M_f}{4\pi\mu_0} \int_0^{2\pi} \cos(p_I\theta)\cos(p_I\theta_d) \times \\
\left\{ R(r,r_o,\theta_d,z-d_a) + r\cos(\theta_d)\log\left[r_o - r\cos(\theta_d) + R(r,r_o,\theta_d,z-d_a)\right] \right. \\
\left. - R(r,r_i,\theta_d,z-d_a) - r\cos(\theta_d)\log\left[r_i - r\cos(\theta_d) + R(r,r_i,\theta_d,z-d_a)\right] \right\} d\theta_d
\end{aligned}
\tag{6.48}
$$

Defining

$$
\begin{aligned}
\varphi_1(r,r_A,\theta_d,z_c) \\
= R(r,r_A,\theta_d,z_c) + r\cos(\theta_d)\log\left[r_A - r\cos(\theta_d) + R(r,r_A,\theta_d,z_c)\right]
\end{aligned}
\tag{6.49}
$$

Substituting (6.49) into (6.48) gives

$$
\begin{aligned}
\phi^a(r,\theta,z) \\
= \frac{M_f}{4\pi\mu_0} \int_0^{2\pi} \cos(p_I\theta)\cos(p_I\theta_d)\left[\varphi_1(r,r_o,\theta_d,z-d_a) - \varphi_1(r,r_i,\theta_d,z-d_a)\right] d\theta_d
\end{aligned}
\tag{6.50}
$$

Similarly, the magnetic scalar field on surface S_c can be derived as:

$$
\begin{aligned}
\phi^c(r,\theta,z) \\
= \frac{M_f}{4\pi\mu_0} \int_0^{2\pi} \cos(p_I\theta)\cos(p_I\theta_d)\left[\varphi_1(r,r_o,\theta_d,z) - \varphi_1(r,r_i,\theta_d,z)\right] d\theta_d
\end{aligned}
\tag{6.51}
$$

6.3.2. Magnetic Scalar Field due to Volume Charge

Substituting (6.27), (6.46)-(6.47) into (6.42) gives

$$\phi^b(r,\theta,z) = \frac{p_I M_f}{4\pi\mu_0\mu_r} \int_0^{d_a}\int_0^{2\pi}\int_{r_i}^{r_o} \frac{\cos[p_I(\theta-\theta_d)]}{\sqrt{r^2 + r_c^2 - 2rr_c\cos(\theta_d)+(z-z_c)^2}} dr_c d\theta_d dz_c \qquad (6.52)$$

Using trigonometric identity

$$\cos[p_I(\theta-\theta_d)] = \cos(p_I\theta)\cos(p_I\theta_d) + \sin(p_I\theta)\sin(p_I\theta_d) \qquad (6.53)$$

and noting that the integral of the odd functions in (6.52) is zero, equation (6.52) can be re-written as:

$$\phi^b(r,\theta,z) = \frac{p_I M_f}{4\pi\mu_0\mu_r} \int_0^{d_a}\int_0^{2\pi}\int_{r_i}^{r_o} \frac{\cos(p_I\theta)\cos(p_I\theta_d)}{\sqrt{r^2 + r_c^2 - 2rr_c\cos(\theta_d)+(z-z_c)^2}} dr_c d\theta_d dz_c \qquad (6.54)$$

Evaluating the integral in terms of r_c gives

$$\phi^b(r,\theta,z) = \cos(p_I\theta)\frac{p_I M_f}{4\pi\mu_0\mu_r}\times$$

$$\int_0^{d_a}\int_0^{2\pi}\cos(p_I\theta_d)\log\Big[\big[r_o - r\cos(\theta_d) + R(r,r_o,\theta_d,z-z_c)\big]\Big]d\theta_d dz_c$$

$$-\cos(p\theta)\frac{p_I M_f}{4\pi\mu_0\mu_r}\times \qquad (6.55)$$

$$\int_0^{d_a}\int_0^{2\pi}\cos(p_I\theta_d)\log\Big[\big[r_i - r\cos(\theta_d) + R(r,r_i,\theta_d,z-z_c)\big]\Big]d\theta_d dz_c$$

Defining

$$\varphi_2(r,r_c,\theta_d,z,z_c) = \int \log\Big[\big[r_c - r\cos(\theta_d) + R(r,r_c,\theta_d,z,z_c)\big]\Big]dz_c \qquad (6.56)$$

Evaluating the integral in (6.56) with respect to z_c gives:

$$\varphi_2(r,r_c,\theta_d,z,z_c)$$

$$= -r\left|\sin(\theta_d)\right|\tan^{-1}\left[\frac{z-z_c}{r\left|\sin(\theta_d)\right|}\right]$$

$$+ r\left|\sin(\theta_d)\right|\tan^{-1}\left[\frac{[r_c-r\cos(\theta_d)](z-z_c)}{r\left|\sin(\theta_d)\right|R(r,r_c,\theta_d,z-z_c)}\right] \qquad (6.57)$$

$$- z_c - (z-z_c)\log\left[r_c-r\cos(\theta_d)+R(r,r_c,\theta_d,z-z_c)\right]$$

$$- \left[r_c-r\cos(\theta_d)\right]\log\left[z-z_c+R(r,r_c,\theta_d,z-z_c)\right]$$

Therefore, equation (6.55) can be rewritten as:

$$\phi^b(r,\theta,z) = \cos(p_I\theta)\frac{p_I M_f}{4\pi\mu_0\mu_r}\int_0^{2\pi}\cos(p_I\theta_d)\times$$

$$\left[\varphi_2(r,r_o,\theta_d,z,d_a)-\varphi_2(r,r_o,\theta_d,z,0)\right. \qquad (6.58)$$

$$\left. -\varphi_2(r,r_i,\theta_d,z,d_a)+\varphi_2(r,r_i,\theta_d,z,0)\right]d\theta_d$$

6.3.3. Magnetic Scalar Potential Field for Axial Halbach Rotor

Substituting (6.50), (6.51) and (6.58) into (6.39) gives

$$\phi^I(r,\theta,z) = \frac{M_f\cos(p_I\theta)}{4\pi\mu_0}\int_0^{2\pi}\cos(p_I\theta_d)\left[\varphi_1(r,r_o,\theta_d,z-d_a)-\varphi_1(r,r_i,\theta_d,z-d_a)\right]d\theta_d$$

$$-\frac{M_f\cos(p_I\theta)}{4\pi\mu_0}\int_0^{2\pi}\cos(p_I\theta_d)\left[\varphi_1(r,r_o,\theta_d,z)-\varphi_1(r,r_i,\theta_d,z)\right]d\theta_d$$

$$+\frac{p_I M_f\cos(p_I\theta)}{4\pi\mu_0\mu_r}\int_0^{2\pi}\cos(p_I\theta_d)\times \qquad (6.59)$$

$$\left[\varphi_2(r,r_o,\theta_d,z,d_a)-\varphi_2(r,r_o,\theta_d,z,0)\right.$$

$$\left. -\varphi_2(r,r_i,\theta_d,z,d_a)+\varphi_2(r,r_i,\theta_d,z,0)\right]d\theta_d$$

where

$$\varphi_1(r,r_A,\theta_d,z_c)$$

$$= R(r,r_A,\theta_d,z_c)+r\cos(\theta_d)\log\left[r_A-r\cos(\theta_d)+R(r,r_A,\theta_d,z_c)\right] \qquad (6.49)$$

$$\varphi_2(r, r_c, \theta_d, z, z_c)$$

$$= -r|\sin(\theta_d)|\tan^{-1}\left[\frac{z - z_c}{r|\sin(\theta_d)|}\right]$$

$$+ r|\sin(\theta_d)|\tan^{-1}\left[\frac{[r_c - r\cos(\theta_d)](z - z_c)}{r|\sin(\theta_d)|R(r, r_c, \theta_d, z - z_c)}\right] \tag{6.57}$$

$$- z_c - (z - z_c)\log[r_c - r\cos(\theta_d) + R(r, r_c, \theta_d, z - z_c)]$$

$$- [r_c - r\cos(\theta_d)]\log[z - z_c + R(r, r_c, \theta_d, z - z_c)]$$

This is the exact 3-D magnetic scalar field function for the axial Halbach rotor. With $r_o = 30$ mm, $r_i = 20$ mm, $d_a^I = 30$ mm and $p = 4$, the contour plot of the magnetic scalar field at $z = 35$ mm is shown in Fig. 6-10 by using (6.59).
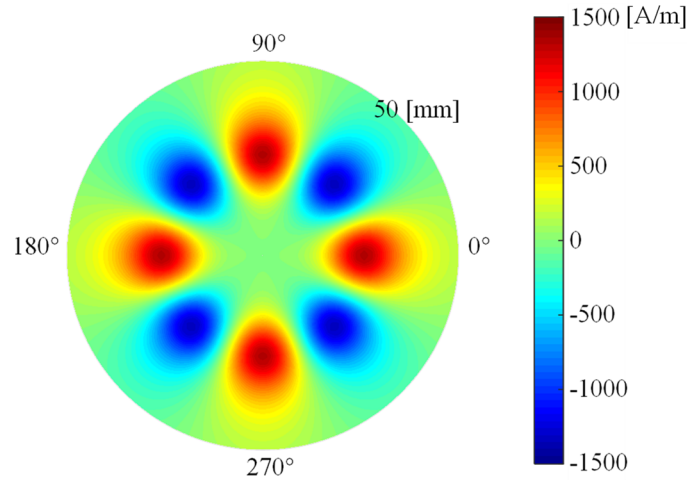
Fig. 6-10. Contour plot of the magnetic scalar potential field.

6.4. TORQUE WITHIN THE AXIAL MAGNETIC COUPLING

The geometry is shown in Fig. 6-11 when both of the rotors are present for the axial magnetic coupling. In this analysis both of the rotors are assumed to have the same axial length and the same number of pole pairs. Therefore,

$$d_a = d_a^I = d_a^{II} \tag{6.60}$$

$$p = p_I = p_{II} \qquad (6.61)$$
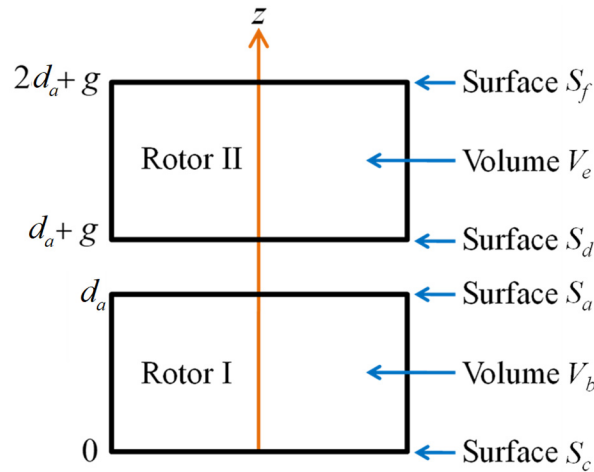
Fig. 6-11. Position and geometry when both rotors present.

As shown in Fig. 6-11, rotor I has one top surface (surface S_a) and one bottom surface (surface S_c). The magnet volume region is defined as V_b. Similarly, Rotor II has one top surface (surface S_f), one bottom surface (surface S_d) and one volume region V_e. The magnetic scalar potential from rotor I is defined by (6.59).

Fig. 6-11 shows two rotors can be decomposed into four surfaces and two volumetric magnetic charge regions. The torque can be computed by evaluating the surface field terms S_f, S_d, S_c, and S_a interaction with each other as well as the fields from the volume regions V_e and V_b. The torque calculation can therefore be split into surface and volume field interactions. The torque between the two rotors is then:

$$
\begin{aligned}
T_A(\theta_t) \\
= T_{ad}^{ss}(\theta_t, g) + T_{af}^{ss}(\theta_t, d_a + g) + T_{cd}^{ss}(\theta_t, d_a + g) + T_{cf}^{ss}(\theta_t, 2d_a + g) \\
+ T_{ae}^{sv}(\theta_t, g) + T_{ce}^{sv}(\theta_t, d_a + g) + T_{bd}^{sv}(\theta_t, g) + T_{bf}^{sv}(\theta_t, d_a + g) \\
+ T_{be}^{vv}(\theta_t)
\end{aligned}
\qquad (6.62)
$$

where subscripts denote the interacting components and θ_t is the offset mechanical angle between the two rotors. The nomenclature for all the torque terms in (6.62) is shown in Table 6-I.

Table 6-I. DESCRIPTIONS OF THE TORQUE TERMS IN EQUATION (6.62).

Torque term	Description
T_{ad}^{ss}	Torque created by surface S_a and surface S_d.
T_{af}^{ss}	Torque created by surface S_a and surface S_f.
T_{cd}^{ss}	Torque created by surface S_c and surface S_d.
T_{cf}^{ss}	Torque created by surface S_c and surface S_f.
T_{ae}^{sv}	Torque created by surface S_a and volume V_e.
T_{ce}^{sv}	Torque created by surface S_c and volume V_e.
T_{bd}^{sv}	Torque created by volume V_b and surface S_d.
T_{bf}^{sv}	Torque created by volume V_b and surface S_f.
T_{be}^{vv}	Torque created by volume V_b and volume V_e.
T_A	The overall torque within the two rotors.

Due to the symmetry of the model in Fig. 6-11, the torque created between surface S_a and surface S_f must be equal to the torque between surface S_c and S_d. Therefore,

$$T_{af}^{ss}(\theta_t, d_a + g) = T_{cd}^{ss}(\theta_t, d_a + g) \tag{6.63}$$

Similarly,

$$T_{ae}^{sv}(\theta_t, g) = T_{bd}^{sv}(\theta_t, g) \tag{6.64}$$

$$T_{ce}^{sv}(\theta_t, d_a + g) = T_{bf}^{sv}(\theta_t, d_a + g) \tag{6.65}$$

Therefore, substituting (6.63)-(6.65) into equation (6.62) gives:

$$T_A(\theta_t) = T_{ad}^{ss}(\theta_t, g) + 2T_{af}^{ss}(\theta_t, d_a + g) + T_{cf}^{ss}(\theta_t) + 2T_{ae}^{sv}(\theta_t, g) + 2T_{ce}^{sv}(\theta_t, d_a + g) + T_{be}^{vv}(\theta_t)$$

$$\tag{6.66}$$

Similarly to (6.35)-(6.37), the charge function for the volume V_e, surface S_d and surface S_f can be written as:

$$\rho_m^e(\theta_{II} - \theta_t) = \frac{pM_f}{\mu_r r_c} \cos(p\theta_{II} - p\theta_t) \tag{6.67}$$

$$\sigma_m^d(\theta_{II} - \theta_t) = M_f \cos(p\theta_{II} - p\theta_t), \text{ on surface } d \tag{6.68}$$

$$\sigma_m^f(\theta_{II} - \theta_t) = -M_f \cos(p\theta_{II} - p\theta_t), \text{ on surface } f \tag{6.69}$$

here the phase angle θ_t has been added in to enable the rotor I and rotor II azimuthal position to be phase shifted. The subscript II denotes the angular position on rotor II.

6.4.1. Surface Torque Components

To calculate the torque terms created by surfaces in equation (6.62), the model shown in Fig. 6-12 has been used. The torque created by surface S_a and surface S_d is derived. The derived equation can be used to compute the torque created between the other surface regions.
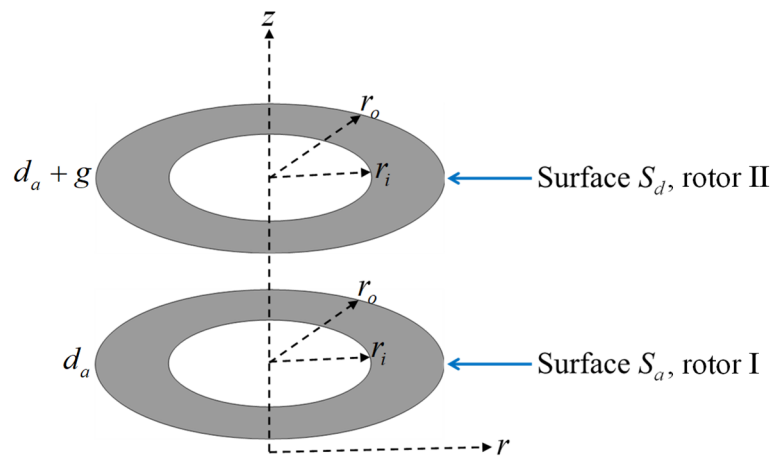
Fig. 6-12. The analytical model to calculate the torque created by magnetic charge surfaces separated axially by a distance g.

The energy present on a charge sheet with charge function σ_m^d and the imparted magnetic scalar potential field ϕ^a is given by [79]

$$W_{ad}^{ss}(\theta_t, g) = \int_0^{2\pi} \int_{r_i}^{r_o} \sigma_m^d(\theta_{II} - \theta_t)\phi^a(r_{II}, \theta_{II}, d+g)r_{II} dr_{II} d\theta_{II} \tag{6.70}$$

where θ_{II} and r_{II} are angular and radial positions on rotor II.

The torque can be computed from [79]

$$T_{ad}^{ss}(\theta_t, g) = \left. \frac{\partial W_{ad}^{ss}}{\partial \theta_{II}} \right|_{\phi^a = \text{constant}} \tag{6.71}$$

Substituting (6.68) into (6.70) and utilizing (6.71) gives

$$T_{ad}^{ss}(\theta_t) = -pM_f \int_0^{2\pi} \int_{r_i}^{r_o} \sin(p\theta_{II} - p\theta_t)\phi^a(r_{II}, \theta_{II}, d_a + g)r_{II} dr_{II} d\theta_{II} \tag{6.72}$$

Then substituting (6.50) into (6.72) one obtains

$$T_{ad}^{ss}(\theta_t, g) = -\frac{pM_f^2}{4\pi\mu_0} \int_0^{2\pi} \int_{r_i}^{r_o} \int_0^{2\pi} \sin(p\theta_{II} - p\theta_t)\cos(p\theta_{II})\cos(p\theta_d) \times \\ \left[\varphi_1(r_{II}, r_o, \theta_d, g) - \varphi_1(r_{II}, r_i, \theta_d, g) \right] r_{II} d\theta_{II} dr_{II} d\theta_d \tag{6.73}$$

Examining (6.73) it can be noted that only the $\sin(p\theta_{II} - p\theta_t)\cos(p\theta_{II})$ terms are function of θ_{II} on the surface S_d of rotor II. Using identity:

$$\sin(p\theta_{II} - p\theta_t)\cos(p\theta_{II}) = \frac{1}{2}\left[\sin(2p\theta_{II} - p\theta_t) - \sin(p\theta_t) \right] \tag{6.74}$$

it can be noted that the integral of (6.74) with respect to θ_{II} is trivial and the first term will be zero. Therefore, (6.73) can be reduced down to:

$$T_{ad}^{ss}(\theta_t, g) = \sin(p\theta_t)\frac{pM_f^2}{4\mu_0}\int\limits_0^{2\pi}\int\limits_{r_i}^{r_o}\cos(p\theta_d)\times$$

$$\left[\varphi_1(r_{II}, r_o, \theta_d, g) - \varphi_1(r_{II}, r_i, \theta_d, g)\right]r_{II}dr_{II}d\theta_d \tag{6.75}$$

The torque between surface S_a on rotor I and surface S_f on rotor II can now also be determined. The only difference in the expression is the separation distance:

$$T_{af}^{ss}(\theta_t, d_a + g) = -\sin(p\theta_t)\frac{pM_f^2}{4\mu_0}\int\limits_0^{2\pi}\int\limits_{r_i}^{r_o}\cos(p\theta_d)\times$$

$$\left[\varphi_1(r_{II}, r_o, \theta_d, d_a + g) - \varphi_1(r_{II}, r_i, \theta_d, d_a + g)\right]r_{II}dr_{II}d\theta_d \tag{6.76}$$

Similarly, for surface S_c and surface S_f one has:

$$T_{cf}^{ss}(\theta_t, 2d_a + g) = \sin(p\theta_t)\frac{pM_f^2}{4\mu_0}\int\limits_0^{2\pi}\int\limits_{r_i}^{r_o}\cos(p\theta_d)\times$$

$$\left[\varphi_1(r_{II}, r_o, \theta_d, 2d_a + g) - \varphi_1(r_{II}, r_i, \theta_d, 2d_a + g)\right]r_{II}dr_{II}d\theta_d \tag{6.77}$$

6.4.2. Surface and Volume Torque Components

To calculate the torque terms created by the surface and the volume region in (6.62), the model shown in Fig. 6-13 has been used. The air gap distance is g between volume V_e and surface S_a.
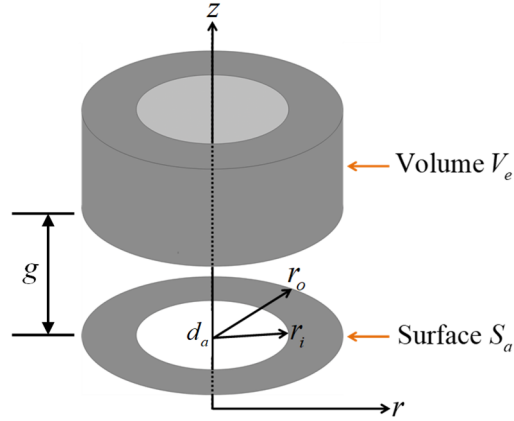
Fig. 6-13. The analytical model to calculate the torque created by the volume region and surfaces.

The energy contained within the volumetric charge region (volume V_e) due to scalar potential field from surface S_a is

$$W_{ae}^{sv}(\theta_t, g) = \int_{d_a+g}^{2d_a+g} \int_0^{2\pi} \int_{r_i}^{r_o} \rho_m^e(\theta_{II} - \theta_t) \phi^a(r_{II}, \theta_{II}, z) r_{II} dr_{II} d\theta_{II} dz \tag{6.78}$$

Holding ϕ^a fixed, the torque can then be computed by [79]

$$T_{ae}^{sv}(\theta_t, g) = \int_{d_a+g}^{2d_a+g} \int_0^{2\pi} \int_{r_i}^{r_o} \frac{\partial \rho_m^e}{\partial \theta_{II}} \phi^a(r_{II}, \theta_{II}, z) r_{II} dr_{II} d\theta_{II} dz \tag{6.79}$$

and then substituting (6.67) into (6.79) gives

$$T_{ae}^{sv}(\theta_t, g) = -\frac{p^2 M_f}{\mu_r} \int_{d_a+g}^{2d_a+g} \int_0^{2\pi} \int_{r_i}^{r_o} \sin(p\theta_{II} - p\theta_t) \phi^a(r_{II}, \theta_{II}, z) dr_{II} d\theta_{II} dz \tag{6.80}$$

Substituting (6.50) into (6.80) gives

$$T_{ae}^{sv}(\theta_t, g) = -\frac{p^2 M_f^2}{4\pi\mu_0\mu_r} \int_{d_a+g}^{2d_a+g} \int_0^{2\pi} \int_{r_i}^{r_o} \int_0^{2\pi} \sin(p\theta_{II} - p\theta_t) \cos(p\theta_{II}) \cos(p\theta_d) \times$$
$$[\varphi_1(r_{II}, r_o, \theta_d, z - d_a) - \varphi_1(r_{II}, r_i, \theta_d, z - d_a)] d\theta_d dr_{II} d\theta_{II} dz \tag{6.81}$$

Utilizing trigonometric identities (6.74) in (6.81) gives

$$
T_{ae}^{sv}(\theta_t, g)
$$
$$
= \sin(p\theta_t) \frac{p^2 M_f^2}{4\mu_0 \mu_r} \int_{r_i}^{r_o} \int_0^{2\pi} \int_{d_a+g}^{2d_a+g} \cos(p\theta_d) \left[\varphi_1(r_{II}, r_o, \theta_d, z - d_a) - \varphi_1(r_{II}, r_i, \theta_d, z - d_a) \right] dz \, d\theta_d \, dr_{II}
$$

$$(6.82)$$

and the sin terms in (6.74) is not present because the integral becomes zero.

Integrating (6.82) with respect to z yields

$$
T_{ae}^{sv}(\theta_t, g) = \sin(p\theta_t) \frac{p^2 M_f^2}{4\mu_0 \mu_r} \int_{r_i}^{r_o} \int_0^{2\pi} \cos(p\theta_d) \times
$$
$$
\left[\varphi_3(r_{II}, r_o, \theta_d, 2d_a + g, d_a) - \varphi_3(r_{II}, r_o, \theta_d, d_a + g, d_a) \right.
$$
$$
\left. - \varphi_3(r_{II}, r_i, \theta_d, 2d_a + g, d_a) + \varphi_3(r_{II}, r_i, \theta_d, d_a + g, d_a) \right] d\theta_d \, dr_{II}
$$

$$(6.83)$$

where

$$
\varphi_3(r_{II}, r_c, \theta_d, z, d_a)
$$
$$
= -\frac{\cos(\theta_d) i \left| \sin(\theta_d) \right| r_{II}^2}{i} \tanh^{-1} \left[\frac{z - d_a}{i r_{II} \left| \sin(\theta_d) \right|} \right]
$$
$$
- \frac{\cos(\theta_d) i \left| \sin(\theta_d) \right| r_{II}^2}{i} \tanh^{-1} \left[\frac{\left[r_{II} \cos(\theta_d) - r_o \right](z - d_a)}{i r_{II} \left| \sin(\theta_d) \right| R(r_{II}, r_c, \theta_d, z - d_a)} \right]
$$
$$
- r_{II} \cos(\theta_d) z + \frac{(z - d_a)}{2} R(r_{II}, r_c, \theta_d, z - d_a)
$$
$$
+ r_{II} \cos(\theta_d)(z - d_a) \log\left[-r_{II} \cos(\theta_d) + r_o + R(r_{II}, r_c, \theta_d, z - d_a) \right]
$$
$$
+ \frac{\left[r_c^2 - r_{II}^2 \cos(2\theta_d) \right]}{2} \log\left[z - d_a + R(r_{II}, r_c, \theta_d, z - d_a) \right]
$$

$$(6.84)$$

where i denotes a complex number.

Similarly,

$$T_{ce}^{sv}(\theta_t, d_a + g)$$

$$= -\sin(p\theta_t)\frac{p^2 M_f^2}{4\mu_0\mu_r}\int\limits_{r_i}^{r_o}\int\limits_{0}^{2\pi}\int\limits_{d_a+g}^{2d_a+g}\cos(p\theta_d)\left[\varphi_1(r_{II}, r_o, \theta_d, z) - \varphi_1(r_{II}, r_i, \theta_d, z)\right]dzd\theta_d dr_{II} \tag{6.85}$$

Equation (6.85) can also be reduced down to two integrals by evaluating the integral with respect to z:

$$T_{ce}^{sv}(\theta_t, d_a + g) = -\sin(p\theta_t)\frac{p^2 M_f^2}{4\mu_0\mu_r}\int\limits_{r_i}^{r_o}\int\limits_{0}^{2\pi}\cos(p\theta_d)\times$$

$$\left[\varphi_3(r_{II}, r_o, \theta_d, 2d_a + g, 0) - \varphi_3(r_{II}, r_o, \theta_d, d_a + g, 0)\right. \tag{6.86}$$

$$\left. -\varphi_3(r_{II}, r_i, \theta_d, 2d_a + g, 0) + \varphi_3(r_{II}, r_i, \theta_d, d_a + g, 0)\right]d\theta_d dr_{II}$$

6.4.3. Volume Torque Components

To calculate the torque term created by the volume charge regions in equation (6.62), the model shown in Fig. 6-14 has been used. The torque created by volume V_b and volume V_e is derived in this section.
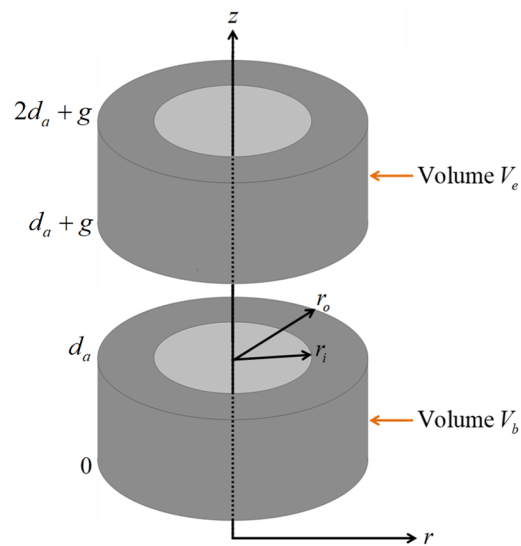
Fig. 6-14. The analytical model to calculate the torque created by volume regions.

The energy contained in volumetric charge region (volume V_b) and volumetric charge region (volume V_e) is

$$W_{be}^{vv} = \int\limits_{d+g}^{2d_a+g} \int\limits_{0}^{2\pi} \int\limits_{r_i}^{r_o} \rho_m^e (\theta_{II} - \theta_t) \phi^b (r_{II}, \theta_{II}, z) r_{II} dr_{II} d\theta_{II} dz \qquad (6.87)$$

The torque can be computed by

$$T_{be}^{vv}(\theta_t) = \int\limits_{d_a+g}^{2d_a+g} \int\limits_{0}^{2\pi} \int\limits_{r_i}^{r_o} \frac{\partial \rho_m^e}{\partial \theta_{II}} \phi^b (r_{II}, \theta_{II}, z) r_{II} dr_{II} d\theta_{II} dz \qquad (6.88)$$

Substituting (6.67) into (6.88) gives

$$T_{be}^{vv}(\theta_t) = -\frac{p^2 M_f}{\mu_r} \int\limits_{d_a+g}^{2d_a+g} \int\limits_{0}^{2\pi} \int\limits_{r_i}^{r_o} \sin(p\theta_{II} - p\theta_t) \phi^b (r_{II}, \theta_{II}, z) dr_{II} d\theta_{II} dz \qquad (6.89)$$

Substituting (6.58) into (6.89) gives

$$\begin{aligned}
T_{be}^{vv}(\theta_t) = \\
-\frac{p^3 M_f^2}{4\pi\mu_0\mu_r^2} \int\limits_{d_a+g}^{2d_a+g} \int\limits_{0}^{2\pi} \int\limits_{r_i}^{r_o} \int\limits_{0}^{2\pi} \sin(p\theta_{II} - p\theta_t)\cos(p\theta_{II})\cos(p\theta_d) \times \\
[\varphi_2(r_{II}, r_o, \theta_d, z, d_a) - \varphi_2(r_{II}, r_o, \theta_d, z, 0) \\
- \varphi_2(r_{II}, r_i, \theta_d, z, d_a) + \varphi_2(r_{II}, r_i, \theta_d, z, 0)] d\theta_{II} dr_{II} d\theta_d dz
\end{aligned} \qquad (6.90)$$

Utilizing (6.74) in (6.90) and simplifying gives

$$\begin{aligned}
T_{be}^{vv}(\theta_t) = \frac{p^3 M_f^2 \sin(p\theta_t)}{4\mu_0\mu_r^2} \int\limits_{d_a+g}^{2d_a+g} \int\limits_{0}^{2\pi} \int\limits_{r_i}^{r_o} \cos(p\theta_d) \times \\
[\varphi_2(r_{II}, r_o, \theta_d, z, d_a) - \varphi_2(r_{II}, r_o, \theta_d, z, 0) \\
- \varphi_2(r_{II}, r_i, \theta_d, z, d_a) + \varphi_2(r_{II}, r_i, \theta_d, z, 0)] dr_{II} d\theta_d dz
\end{aligned} \qquad (6.91)$$

Integrating (6.91) with respect to z yields

$$T_{be}^{vv}(\theta_t) = \sin(p\theta_t)\frac{p^3 M_f^2}{4\mu_0 \mu_r^2}\int_0^{2\pi}\int_{r_i}^{r_o}\cos(p\theta_d)\times$$

$$\begin{aligned}
\big[& \varphi_4(r_{II}, r_o, \theta_d, 2d_a+g, d_a) - \varphi_4(r_{II}, r_o, \theta_d, d_a+g, d_a) \\
& - \varphi_4(r_{II}, r_i, \theta_d, 2d_a+g, d_a) + \varphi_4(r_{II}, r_i, \theta_d, d_a+g, d_a) \\
& - \varphi_4(r_{II}, r_o, \theta_d, 2d_a+g, 0) + \varphi_4(r_{II}, r_o, \theta_d, d_a+g, 0) \\
& + \varphi_4(r_{II}, r_i, \theta_d, 2d_a+g, 0) - \varphi_4(r_{II}, r_i, \theta_d, d_a+g, 0) \big] dr_{II}\, d\theta_d
\end{aligned}$$

(6.92)

where

$$\varphi_4(r_{II}, r_c, \theta_d, z, z_c)$$
$$= \frac{c_3}{4} + \frac{c_4\sqrt{c_3+(z-z_c)^2}}{2} + \frac{(z-z_c)^2}{4} - zz_c - z\sqrt{c_1}(z-z_c)\tan^{-1}\left(\frac{z-z_c}{\sqrt{c_1}}\right)$$

$$+ z\sqrt{c_1}\tan^{-1}\left[\frac{c_4(z-z_c)}{\sqrt{c_1\big[c_3+(z-z_c)^2\big]}}\right] + \frac{c_4^2-c_3-(z-z_c)^2}{2}\log\left[c_4+\sqrt{c_3+(z-z_c)^2}\right]$$

$$+ \frac{c_1}{2}\log\left[c_1+(z-z_c)^2\right] - c_4(z-z_c)\log\left[z-z_c+\sqrt{c_3+(z-z_c)^2}\right]$$

$$+ \frac{\sqrt{c_1}}{2(c_1+c_4^2)}\left[\sqrt{c_1 c_3\left(c_1+c_4^2\right)}+id_a\left(c_1+c_4^2\right)\right]\log\left(\frac{x_1}{y_1}\right)$$

$$+ \frac{\sqrt{c_1}}{2(c_1+c_4^2)}\left[\sqrt{c_1 c_3\left(c_1+c_4^2\right)}-id_a\left(c_1+c_4^2\right)\right]\log\left(-\frac{x_2}{y_2}\right)$$

(6.93)

where i denotes a complex number and

$$c_1 = r_{II}^2 \sin^2(\theta_d) \tag{6.94}$$

$$c_2 = r_{II}\cos(\theta_d) \tag{6.95}$$

$$c_3 = C(r_{II}, r_c, \theta_d) \tag{6.96}$$

$$c_4 = r_c - r_{II}\cos(\theta_d) \tag{6.97}$$

$$x_1 = 2\sqrt{c_1 c_3}\left(c_1 + c_4^2\right) \times$$
$$\left[ic_1\sqrt{c_3} + ic_4\left(c_4\sqrt{c_3} + \sqrt{\left(c_1 + c_4^2\right)\left[c_3 + (z - z_c)^2\right]}\right) + (z - z_c)\sqrt{c_1\left(c_1 + c_4^2\right)}\right] \quad (6.98)$$

$$y_1 = c_4\left[-i\sqrt{c_1 c_3\left(c_1 + c_4^2\right)} + z_c\left(c_1 + c_4^2\right)\right]\left[-i\sqrt{c_1 c_3\left(c_1 + c_4^2\right)} - (z - z_c)\left(c_1 + c_4^2\right)\right] \quad (6.99)$$

$$x_2 = 2\sqrt{c_1 c_3}\left(c_1 + c_4^2\right) \times$$
$$\left[ic_1\sqrt{c_3} + ic_4\left(c_4\sqrt{c_3} + \sqrt{\left(c_1 + c_4^2\right)\left[c_3 + (z - z_c)^2\right]}\right) - (z - z_c)\sqrt{c_1\left(c_1 + c_4^2\right)}\right] \quad (6.100)$$

$$y_2 = c_4\left[i\sqrt{c_1 c_3\left(c_1 + c_4^2\right)} + z_c\left(c_1 + c_4^2\right)\right]\left[i\sqrt{c_1 c_3\left(c_1 + c_4^2\right)} - (z - z_c)\left(c_1 + c_4^2\right)\right] \quad (6.101)$$

Therefore, by comparing (6.75)-(6.77), (6.83), (6.86), the torque equation in (6.66) can be written as:

$$\begin{aligned}
T_A(\theta_t) &= T_{ad}^{ss}(\theta_t, g) - 2T_{ad}^{ss}(\theta_t, d_a + g) + T_{ad}^{ss}(\theta_t, 2d_a + g) \\
&\quad + 2\left[T_{ae}^{sv}(\theta_t, g) - T_{ae}^{sv}(\theta_t, d_a + g)\right] \\
&\quad + T_{be}^{vv}(\theta_t)
\end{aligned} \quad (6.102)$$

By substituting (6.75)-(6.77), (6.83), (6.86) and (6.92) into (6.102), the torque between two rotors can be expressed as:

$$T_A(\theta_t) = \sin(p\theta_t)\cos(p\theta_d)\frac{pM_f^2}{4\mu_0}\int_0^{2\pi}\int_{r_i}^{r_o}\{[\varphi_1(r_{II},r_o,\theta_d,g)-\varphi_1(r_{II},r_i,\theta_d,g)]r_{II}$$

$$-2[\varphi_1(r_{II},r_o,\theta_d,d_a+g)-\varphi_1(r_{II},r_i,\theta_d,d_a+g)]r_{II}$$

$$+[\varphi_1(r_{II},r_o,\theta_d,2d_a+g)-\varphi_1(r_{II},r_i,\theta_d,2d_a+g)]r_{II}$$

$$+\frac{2p}{\mu_r}[\varphi_3(r_{II},r_o,\theta_d,2d_a+g,d_a)-\varphi_3(r_{II},r_o,\theta_d,d_a+g,d_a)$$

$$-\varphi_3(r_{II},r_i,\theta_d,2d_a+g,d_a)+\varphi_3(r_{II},r_i,\theta_d,d_a+g,d_a)]$$

$$-\frac{2p}{\mu_r}[\varphi_3(r_{II},r_o,\theta_d,2d_a+g,0)-\varphi_3(r_{II},r_o,\theta_d,d_a+g,0)$$

$$-\varphi_3(r_{II},r_i,\theta_d,2d_a+g,0)+\varphi_3(r_{II},r_i,\theta_d,d_a+g,0)]$$

$$+\frac{p^2}{\mu_r^2}[\varphi_4(r_{II},r_o,\theta_d,2d_a+g,d_a)-\varphi_4(r_{II},r_o,\theta_d,d_a+g,d_a)$$

$$-\varphi_4(r_{II},r_i,\theta_d,2d_a+g,d_a)+\varphi_4(r_{II},r_i,\theta_d,d_a+g,d_a)$$

$$-\varphi_4(r_{II},r_o,\theta_d,2d_a+g,0)+\varphi_4(r_{II},r_o,\theta_d,d_a+g,0)$$

$$+\varphi_4(r_{II},r_i,\theta_d,2d_a+g,0)-\varphi_4(r_{II},r_i,\theta_d,d_a+g,0)]\}dr_{II}d\theta_d \qquad (6.103)$$

The active volume torque density and mass torque density are defined as:

$$T_{Av} = \frac{T_A}{(2d_a+g)\pi r_o^2} \quad \text{[Nm/L]} \qquad (6.104)$$

$$T_{Am} = \frac{T_A}{2\rho_m\pi d_a(r_o^2-r_i^2)} \quad \text{[Nm/kg]} \qquad (6.105)$$

where ρ_m is the magnet material density and T_A is the peak torque value of the axial

magnetic coupling.

Using equation (6.103), the torque comparison between the analytical model and FEA

model is shown in Table 6-II and Table 6-III. The discrepancy is within 5 %. Fig. 6-15

shows the torque comparison between the analytical model and the FEA model as a

function of angle. The discrepancy plot is shown in Fig. 6-16. A good agreement has been achieved.

When r_o = 100 mm, r_i = 90 mm, d_a = 10 mm and g = 1mm, the calculation time of the analytical model and the FEA model has been compared and is shown in Table 6-IV. It can be seen that the analytical model can reduce the run-time significantly. It was mentioned at the introduction that an alternative approximate charge sheet model [76] was also developed. The accuracy of this model is shown in the last column of Table 6-II. It can be seen that this approximate charge sheet model gives accurate results only at large inner radius values.

Table 6-II. COMPARISON BETWEEN THE ANALYTICAL MODEL AND JMAG (8 SEGMENTS HALBACH ARRAY).

Parameters		Torque			
Outer radius r_o, [mm]	Inner radius r_i, [mm]	Analytical [Nm]	JMAG [Nm]	Discrepancy [%]	Alternative model [Nm]
100	10	909.2	915.0	0.63	1196.7
100	20	896.2	903.0	0.75	1097.5
100	30	858.9	866.4	0.87	992.9
100	40	792.2	800.9	1.09	877.6
100	50	696.1	705.7	1.36	747.5
100	60	572.9	583.6	1.83	600.6
100	70	426.5	436.9	2.38	437.3
100	80	263.5	273.1	3.52	262.8
100	90	100.0	104.7	4.49	95.9
Axial length, d_a [mm]		10			
Air gap, g [mm]		1			
Pole pairs, p		8			

Table 6-III. COMPARISON BETWEEN THE ANALYTICAL MODEL AND JMAG (16 SEGMENTS HALBACH ARRAY).

Parameters			Torque			
Outer radius r_o [mm]	Inner radius r_i [mm]	Axial length d_a [mm]	Analytical [Nm]	JMAG [Nm]	Discrepancy [%]	Alternative model [Nm]
30	20	20	19.2	20.0	4.00	23.3
30	10	30	37.9	38.8	2.32	42.4
50	10	15	146.6	148.6	1.35	168.8
50	40	15	34.1	35.5	3.94	36.8
Air gap, g [mm]			1			
Pole pairs, p			4			
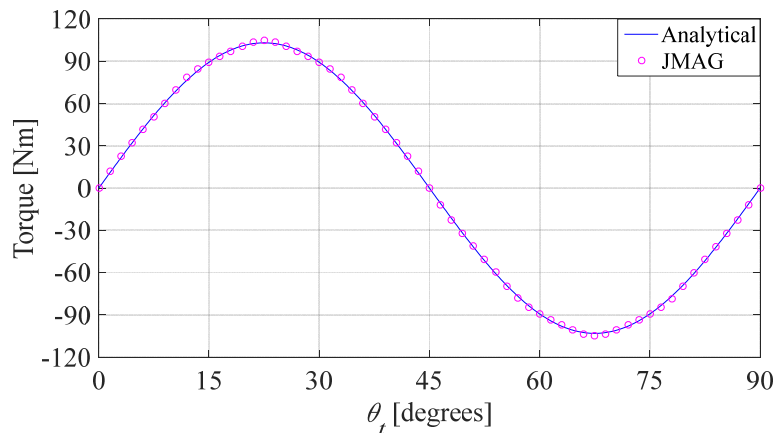
Fig. 6-15. Torque comparison between the analytical model and FEA model when $r_o = 50$ mm, $r_i = 30$ mm, $d_a = 30$ mm and $g = 1$ mm.
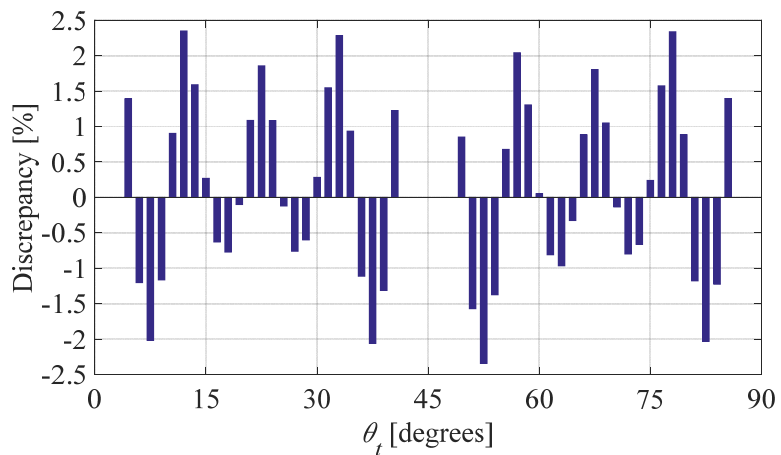
Fig. 6-16. Discrepancy between the analytical and FEA models.

Table 6-IV. RUN-TIME COMPARISON FOR DIFFERENT MODELS

Description	Analytical	JMAG	Unit
Run-time	46	3300	s
Computer model	HP Z620		-

6.5. MAGNETIC FIELD SOLUTION OF THE HALBACH AXIAL ROTOR

From (6.24) it can be noted that

$$\mathbf{B} = -\mu_0 \nabla \phi \tag{6.106}$$

Therefore, the magnetic flux density solution can be determined directly by substituting (6.38) into (6.106) this yields [80]

$$
\begin{aligned}
\mathbf{B}^I(r,\theta,z) = & \frac{p_I M_f}{4\pi\mu_r} \int_0^{d_a^I} \int_0^{2\pi} \int_{r_i}^{r_o} \frac{\cos(p_I \theta_I)\mathbf{R}(r,r_c,\theta,\theta_I,z-z_c)}{\left[r^2 + r_c^2 - 2rr_c \cos(\theta-\theta_I) + (z-z_c)^2 \right]^{\frac{3}{2}}} dr_c d\theta_I dz_c \\
& + \frac{M_f}{4\pi} \int_0^{2\pi} \int_{r_i}^{r_o} \frac{\cos(p_I \theta_I)\mathbf{R}(r,r_c,\theta,\theta_I,z-d_a^I)}{\left[r^2 + r_c^2 - 2rr_c \cos(\theta-\theta_I) + (z-d_a^I)^2 \right]^{\frac{3}{2}}} r_c dr_c d\theta_I \\
& - \frac{M_f}{4\pi} \int_0^{2\pi} \int_{r_i}^{r_o} \frac{\cos(p_I \theta_I)\mathbf{R}(r,r_c,\theta,\theta_I,z)}{\left[r^2 + r_c^2 - 2rr_c \cos(\theta-\theta_I) + z^2 \right]^{\frac{3}{2}}} r_c dr_c d\theta_I
\end{aligned}
\tag{6.107}
$$

where

$$\mathbf{R}(r,r_c,\theta,\theta_I,z-w) = \left[r - r_c \cos(\theta-\theta_I) \right]\hat{\mathbf{r}} + \left[r_c \sin(\theta-\theta_I) \right]\hat{\boldsymbol{\theta}} + (z-w)\hat{\mathbf{z}} \tag{6.108}$$

6.5.1. Axial Magnetic Field Solution, B_z

The axial magnetic flux density can be obtained by substituting (6.108) into (6.107). This gives the B_z component as

$$B_z^I(r,\theta,z) = \frac{p_I M_f}{4\pi\mu_r} \int_0^{d_a^I}\int_0^{2\pi}\int_{r_i}^{r_o} \frac{\cos(p_I\theta_I)(z-z_c)}{\left[r^2 + r_c^2 - 2rr_c\cos(\theta-\theta_I)+(z-z_c)^2\right]^{\frac{3}{2}}} dr_c d\theta_I dz_c$$

$$+ \frac{M_f}{4\pi}\int_0^{2\pi}\int_{r_i}^{r_o} \frac{\cos(p_I\theta_I)(z-d_a^I)}{\left[r^2 + r_c^2 - 2rr_c\cos(\theta-\theta_I)+(z-d_a^I)^2\right]^{\frac{3}{2}}} r_c dr_c d\theta_I \quad (6.109)$$

$$- \frac{M_f}{4\pi}\int_0^{2\pi}\int_{r_i}^{r_o} \frac{\cos(p_I\theta_I)(z)}{\left[r^2 + r_c^2 - 2rr_c\cos(\theta-\theta_I)+z^2\right]^{\frac{3}{2}}} r_c dr_c d\theta_I$$

Evaluating the radial and z-axis integral gives

$$B_z^I(r,\theta,z) = \frac{p_I M_f}{4\pi\mu_r}\int_0^{2\pi}\cos(p_I\theta_I)\Big[R_v(r,r_o,\theta-\theta_I,z-d_a^I)-R_v(r,r_i,\theta-\theta_I,z-d_a^I)$$

$$+ R_v(r,r_i,\theta-\theta_I,z)-R_v(r,r_o,\theta-\theta_I,z)\Big]d\theta_I$$

$$+\frac{M_f(z-d_a^I)}{2\pi}\int_0^{2\pi}\cos(p_I\theta_I)\times\left[\frac{-R_s(r,r_i,\theta-\theta_I,z-d_a^I)+R_s(r,r_o,\theta-\theta_I,z-d_a^I)}{-r^2-2(z-d_a^I)^2+r^2\cos(2\theta-2\theta_I)}\right]d\theta_I \quad (6.110)$$

$$-\frac{M_f z}{2\pi}\int_0^{2\pi}\cos(p_I\theta_I)\times\left[\frac{-R_s(r,r_i,\theta-\theta_I,z)+R_s(r,r_o,\theta-\theta_I,z)}{-r^2-2z^2+r^2\cos(2\theta-2\theta_I)}\right]d\theta_I$$

where

$$R_v(r,r_A,\phi,z-w) = \frac{r_A - r\cos(\phi)}{\sqrt{[r_A - r\cos(\phi)]^2}}\cdot\tanh^{-1}\left[\sqrt{\frac{C(r,r_A,\phi)+(z-w)^2}{(r_A - r\cos\phi)^2}}\right] \quad (6.111)$$

$$R_s(r,r_A,\phi,z-w) = \frac{r^2 + (z-w)^2 - rr_A\cos\phi}{R(r,r_A,\phi,z-w)} \quad (6.112)$$

Equation (6.110) can be simplified by substituting (6.46) and (6.47) into (6.110)

$$B_z^I(r,\theta,z) = -\frac{p_I M_f}{4\pi\mu_r} \int\limits_{\theta}^{\theta-2\pi} \cos(p_I\theta - p_I\theta_d)\Big[R_v(r,r_o,\theta_d,z,d_a^I) - R_v(r,r_i,\theta_d,z,d_a^I)$$

$$+ R_v(r,r_i,\theta_d,z,0) - R_v(r,r_o,\theta_d,z,0)\Big]d\theta_d$$

$$-\frac{M_f(z-d_a^I)}{2\pi} \int\limits_{\theta}^{\theta-2\pi} \cos(p_I\theta - p_I\theta_d)\left[\frac{-R_s(r,r_i,\theta_d,z,d_a^I) + R_s(r,r_o,\theta_d,z,d_a^I)}{-r^2 - 2(z-d_a^I)^2 + r^2\cos(2\theta_d)}\right]d\theta_d \quad (6.113)$$

$$+\frac{M_f z}{2\pi} \int\limits_{\theta}^{\theta-2\pi} \cos(p_I\theta - p_I\theta_d)\left[\frac{-R_s(r,r_i,\theta_d,z,0) + R_s(r,r_o,\theta_d,z,0)}{-r^2 - 2z^2 + r^2\cos(2\theta_d)}\right]d\theta_d$$

Since the integral in (6.113) has a period of 2π, it can be re-written as

$$B_z^I(r,\theta,z) =$$

$$+\frac{p_I M_f}{4\pi\mu_r} \int\limits_{0}^{2\pi} \cos(p_I\theta - p_I\theta_d)\Big[R_v(r,r_o,\theta_d,z,d_a^I) - R_v(r,r_i,\theta_d,z,d_a^I)$$

$$+ R_v(r,r_i,\theta_d,z,0) - R_v(r,r_o,\theta_d,z,0)\Big]d\theta_d$$

$$+\frac{M_f(z-d_a^I)}{2\pi} \int\limits_{0}^{2\pi} \cos(p_I\theta - p_I\theta_d)$$

$$\times\left[\frac{-R_s(r,r_i,\theta_d,z,d_a^I) + R_s(r,r_o,\theta_d,z,d_a^I)}{-r^2 - 2(z-d_a^I)^2 + r^2\cos(2\theta_d)}\right]d\theta_d$$

$$-\frac{M_f z}{2\pi} \int\limits_{0}^{2\pi} \cos(p_I\theta - p_I\theta_d)$$

$$\times\left[\frac{-R_s(r,r_i,\theta_d,z,0) + R_s(r,r_o,\theta_d,z,0)}{-r^2 - 2z^2 + r^2\cos(2\theta_d)}\right]d\theta_d \quad (6.114)$$

Noting that

$$\cos(p_I\theta - p_I\theta_d) = \cos(p_I\theta)\cos(p_I\theta_d) - \sin(p_I\theta)\sin(p_I\theta_d) \quad (6.115)$$

Substituting (6.115) into (6.114) one obtains

$$B_z^I(r,\theta,z) =$$

$$+\frac{p_I M_f}{4\pi\mu_r}\cos(p_I\theta)\int_0^{2\pi}\cos(p_I\theta_d)\Big[R_v(r,r_o,\theta_d,z,d_a^I)-R_v(r,r_i,\theta_d,z,d_a^I)$$

$$+R_v(r,r_i,\theta_d,z,0)-R_v(r,r_o,\theta_d,z,0)\Big]d\theta_d$$

$$-\frac{M_f(z-d_a^I)}{4\pi}\cos(p_I\theta)\int_0^{2\pi}\cos(p_I\theta_d)$$

$$\times\left[\frac{-R_s(r,r_i,\theta_d,z,d_a^I)+R_s(r,r_o,\theta_d,z,d_a^I)}{r^2\sin^2(\theta_d)+(z-d_{a_I})^2}\right]d\theta_d$$

$$+\frac{M_f z}{4\pi}\cos(p_I\theta)\int_0^{2\pi}\cos(p_I\theta_d)$$

$$\times\left[\frac{-R_s(r,r_i,\theta_d,z,0)+R_s(r,r_o,\theta_d,z,0)}{r^2\sin^2(\theta_d)+z^2}\right]d\theta_d \qquad (6.116)$$

The integral associated with the sine term in (6.115) goes to zero when subsititued into (6.114) since it is an odd function with respect to θ_d. Defining

$$b_{sz}(r_A,\theta_d,z,w)=\frac{(z-w)\big[r^2+(z-w)^2-rr_A\cos\theta_d\big]}{R(r,r_A,\theta_d,z,w)\big[r^2\sin^2(\theta_d)+(z-w)^2\big]} \qquad (6.117)$$

Substituting (6.117) into (6.116) gives

$$B_z^I(r,\theta,z) =$$

$$\frac{M_f}{4\pi\mu_r}p_I\cos(p_I\theta)\int_0^{2\pi}\cos(p_I\theta_d)\Big[R_v(r,r_o,\theta_d,z,d_a^I)-R_v(r,r_i,\theta_d,z,d_a^I)$$

$$+R_v(r,r_i,\theta_d,z,0)-R_v(r,r_o,\theta_d,z,0)\Big]d\theta_d \qquad (6.118)$$

$$+\frac{M_f}{4\pi}\cos(p_I\theta)\int_0^{2\pi}\cos(p_I\theta_d)\Big[-b_{sz}(r_i,\theta_d,z,0)+b_{sz}(r_o,\theta_d,z,0)\Big]d\theta_d$$

$$-\frac{M_f}{4\pi}\cos(p_I\theta)\int_0^{2\pi}\cos(p_I\theta_d)\Big[-b_{sz}(r_i,\theta_d,z,d_a^I)+b_{sz}(r_o,\theta_d,z,d_a^I)\Big]d\theta_d$$

In summary, the solution of the B_z magnetic field is given in (6.118) in terms of only one integral.

6.5.2. Azimuthal Magnetic Field Solution, B_θ

The azimuthal magnetic flux density can be determined by substituting (6.108) into (6.107). This gives the B_θ component as

$$
\begin{aligned}
B_\theta^I(r,\theta,z) =\ & \frac{p_I M_f}{4\pi\mu_r} \int_0^{d_a^I} \int_0^{2\pi} \int_{r_i}^{r_o} \frac{\cos(p_I\theta_I)r_c \sin(\theta-\theta_I)}{\left[R(r,r_c,\theta-\theta_I,z-z_c)\right]^{\frac{3}{2}}} dr_c d\theta_I dz_c \\
& + \frac{M_f}{4\pi} \int_0^{2\pi} \int_{r_i}^{r_o} \frac{\cos(p_I\theta_I)\sin(\theta-\theta_I)}{\left[R(r,r_c,\theta-\theta_I,z-d_a^I)\right]^{\frac{3}{2}}} r_c^2 dr_c d\theta_I \\
& - \frac{M_f}{4\pi} \int_0^{2\pi} \int_{r_i}^{r_o} \frac{\cos(p_I\theta_I)\sin(\theta-\theta_I)}{\left[R(r,r_c,\theta-\theta_I,z)\right]^{\frac{3}{2}}} r_c^2 dr_c d\theta_I
\end{aligned}
\tag{6.119}
$$

Substituting (6.46) and (6.47) into (6.119) and evaluating the integral along the radial direction gives

$$B_\theta^I(r,\theta,z)$$

$$= -\frac{p_I M_f}{4\pi\mu_r} \int\limits_0^{d_a^I} \int\limits_0^{2\pi} \cos(p_I\theta - p_I\theta_d)\sin(\theta_d)\times$$

$$\left[\frac{R_s(r,r_i,\theta_d,z-z_c)}{\left[r^2\sin^2(\theta_d)+(z-z_c)^2\right]} - \frac{R_s(r,r_o,\theta_d,z-z_c)}{\left[r^2\sin^2(\theta_d)+(z-z_c)^2\right]}\right]d\theta_d dz_c$$

$$-\frac{M_f}{4\pi}\int\limits_0^{2\pi}\cos(p_I\theta - p_I\theta_d)\sin(\theta_d)$$

$$\times \left\{ \begin{array}{l} \dfrac{\left[r_i(z-d_a^I)^2 - r^2 r_i\cos(2\theta_d) + \left(r^3 + r(z-d_a^I)^2\right)\cos(\theta_d)\right]}{\left[r^2\sin^2(\theta_d)+(z-d_a^I)^2\right]R(r,r_i,\theta_d,z-d_a^I)} \\[3ex] -\dfrac{\left[r_o(z-d_a^I)^2 - r^2 r_o\cos(2\theta_d) + \left(r^3 + r(z-d_a^I)^2\right)\cos(\theta_d)\right]}{\left[r^2\sin^2(\theta_d)+(z-d_a^I)^2\right]R(r,r_o,\theta_d,z-d_a^I)} \\[3ex] +\log\dfrac{\left[r_o - r\cos(\theta_d) + R(r,r_o,\theta_d,z-d_a^I)\right]}{\left[r_i - r\cos(\theta_d) + R(r,r_i,\theta_d,z-d_a^I)\right]} \end{array} \right\} d\theta_d$$

$$+\frac{M_f}{4\pi}\int\limits_0^{2\pi}\cos(p_I\theta - p_I\theta_d)\sin(\theta_d)\times \left\{ \begin{array}{l} \dfrac{\left[r_i z^2 - r^2 r_i\cos(2\theta_d) + \left(r^3 + rz^2\right)\cos(\theta_d)\right]}{\left[r^2\sin^2(\theta_d)+z^2\right]R(r,r_i,\theta_d,z)} \\[3ex] -\dfrac{\left[r_o z^2 - r^2 r_o\cos(2\theta_d) + \left(r^3 + rz^2\right)\cos(\theta_d)\right]}{\left[r^2\sin^2(\theta_d)+z^2\right]R(r,r_o,\theta_d,z)} \\[3ex] +\log\dfrac{\left[r_o - r\cos(\theta_d) + R(r,r_o,\theta_d,z)\right]}{\left[r_i - r\cos(\theta_d) + R(r,r_i,\theta_d,z)\right]} \end{array} \right\} d\theta_d$$

$$(6.120)$$

where $R_s(r, r_A, \phi, z\text{-}w)$ is defined in (6.112).

The above equation can be simplified by defining

$$b_{s\theta}(r,\theta,z,w) = -\frac{M_f}{4\pi} \int_0^{2\pi} \cos[p_I(\theta-\theta_d)]\sin(\theta_d)$$

$$\times \left\{ \begin{array}{l} \dfrac{\left[r_i(z-w)^2 - r^2 r_i \cos(2\theta_d) + \left(r^3 + r(z-w)^2 \right)\cos(\theta_d) \right]}{\left[r^2 \sin^2(\theta_d) + (z-w)^2 \right] R(r,r_i,\theta_d,z-w)} \\[2ex] -\dfrac{\left[r_o(z-w)^2 - r^2 r_o \cos(2\theta_d) + \left(r^3 + r(z-w)^2 \right)\cos(\theta_d) \right]}{\left[r^2 \sin^2(\theta_d) + (z-w)^2 \right] R(r,r_o,\theta_d,z-w)} \\[2ex] +\log\dfrac{[r_o - r\cos(\theta_d) + R(r,r_o,\theta_d,z-w)]}{[r_i - r\cos(\theta_d) + R(r,r_i,\theta_d,z-w)]} \end{array} \right\} d\theta_d \qquad (6.121)$$

Further simplifying and rearranging (6.121) gives

$$b_{s\theta}(r,\theta,z,w) = \frac{M_f}{\pi} \int_0^{2\pi} \cos[p_I(\theta-\theta_d)]\sin(\theta_d)$$

$$\times \left\{ \begin{array}{l} +\dfrac{r_o(z-w)^2 - r^2 r_o \cos(2\theta_d) + [r^3 + r(z-w)^2]\cos(\theta_d)}{\left[r^2 \sin^2(\theta_d) + (z-w)^2 \right] R(r,r_o,\theta_d,z-w)} \\[2ex] -\log[r_o - r\cos(\theta_d) + R(r,r_o,\theta_d,z-w)] \\[2ex] -\dfrac{r_i(z-w)^2 - r^2 r_i \cos(2\theta_d) + [r^3 + r(z-w)^2]\cos(\theta_d)}{\left[r^2 \sin^2(\theta_d) + (z-w)^2 \right] R(r,r_i,\theta_d,z-w)} \\[2ex] +\log[r_i - r\cos(\theta_d) + R(r,r_i,\theta_d,z-w)] \end{array} \right\} d\theta_d \qquad (6.122)$$

Defining

$$b_{s\theta2}(r,z,w,r_A) = \frac{r_A(z-w)^2 - r^2 r_A \cos(2\theta_d) + [r^3 + r(z-w)^2]\cos(\theta_d)}{\left[r^2 \sin^2(\theta_d) + (z-w)^2 \right] R(r,r_A,\theta_d,z-w)}$$
$$- \log[r_A - r\cos(\theta_d) + R(r,r_A,\theta_d,z-w)] \qquad (6.123)$$

and substituting (6.123) into (6.122) gives

$$b_{s\theta}(r,\theta,z,w) = \frac{M_f}{\pi} \int_0^{2\pi} \cos[p_I(\theta-\theta_d)]\sin(\theta_d)[b_{s\theta2}(r,z,w,r_o) - b_{s\theta2}(r,z,w,r_i)]d\theta_d \quad (6.124)$$

Substituting (6.124) into (6.120) gives

$$B_\theta^I(r,\theta,z) = -\frac{p_I M_f}{4\pi\mu_r} \int_0^{d_a^I} \int_0^{2\pi} \cos[p_I(\theta-\theta_d)]\sin(\theta_d)$$

$$\times \left[\frac{R_s(r,r_i,\theta_d,z-z_c)}{\left[r^2\sin^2(\theta_d)+(z-z_c)^2\right]} - \frac{R_s(r,r_o,\theta_d,z-z_c)}{\left[r^2\sin^2(\theta_d)+(z-z_c)^2\right]} \right] d\theta_d dz_c \quad (6.125)$$

$$+ b_{s\theta}(r,\theta,z,d_a^I) - b_{s\theta}(r,\theta,z,0)$$

Finally, substituting (6.123) into (6.125) and one obtains

$$B_\theta^I(r,\theta,z) =$$

$$-\frac{p_I M_f \cos(p_I\theta)}{4\pi\mu_r} \int_0^{d_a^I} \int_0^{2\pi} \cos(p_I\theta_d)\sin(\theta_d) \times$$

$$\left[\frac{R_s(r,r_i,\theta_d,z,z_c)}{\left[r^2\sin^2(\theta_d)+(z-z_c)^2\right]} - \frac{R_s(r,r_o,\theta_d,z,z_c)}{\left[r^2\sin^2(\theta_d)+(z-z_c)^2\right]} \right] d\theta_d dz_c \quad (6.126)$$

$$+\frac{M_f \cos(p_I\theta)}{\pi} \int_0^{2\pi} \cos(p_I\theta_d)\sin(\theta_d)$$

$$\times \left[b_{s\theta2}(r,z,d_a^I,r_o) - b_{s\theta2}(r,z,d_a^I,r_i) - b_{s\theta2}(r,z,0,r_o) + b_{s\theta2}(r,z,0,r_i) \right] d\theta_d$$

The expression of the B_θ magnetic field is given in (6.126) which has two integrals.

6.5.3. Radial Magnetic Field Solution, B_r

Substituting (6.108) into (6.107) gives the B_r component as

$$B_r^I(r,\theta,z) = -\frac{p_I M_f}{4\pi\mu_r} \int_0^{d_a^I} \int_0^{2\pi} \int_{r_i}^{r_o} \frac{\cos(p_I\theta-p_I\theta_d)\left[r-r_c\cos(\theta_d)\right]}{R(r,r_c,\theta_d,z-z_c)^3} dr_c d\theta_d dz_c$$

$$-\frac{M_f}{4\pi} \int_0^{2\pi} \int_{r_i}^{r_o} \frac{\cos(p_I\theta-p_I\theta_d)\left[r-r_c\cos(\theta_d)\right]}{R(r,r_c,\theta_d,z-d_a^I)^3} r_c dr_c d\theta_d \quad (6.127)$$

$$+\frac{M_f}{4\pi} \int_0^{2\pi} \int_{r_i}^{r_o} \frac{\cos(p_I\theta-p_I\theta_d)\left[r-r_c\cos(\theta-\theta_I)\right]}{R(r,r_c,\theta_d,z)^3} r_c dr_c d\theta_d$$

Evaluating the integral in (6.127) with respect to r_c give:

$$B_r^I(r,\theta,z) =$$

$$-\frac{p_I M_f}{4\pi\mu_r} \int_0^{d_a^I}\int_0^{2\pi} \cos(p_I\theta_I)$$

$$\times \left| \frac{2\left[(z-z_c)^2\cos(\theta_d)+rr_c\sin(\theta_d)^2\right]}{R(r,r_c,\theta_d,z-z_c)\left[r^2\left[\cos(2\theta_d)-1\right]-2(z-z_c)^2\right]} \right|_{r_o}^{r_i} d\theta_d dz_c$$

$$+\frac{M_f}{4\pi}\int_0^{2\pi}\cos(p_I\theta - p_I\theta_d)$$

$$\times \left\{ \begin{array}{l} \cos(\theta_d)\log\left[r_i - r\cos(\theta_d)+R(r,r_i,\theta_d,z-d_a^I)\right] \\ -\cos(\theta_d)\log\left[r_o - r\cos(\theta_d)+R(r,r_o,\theta_d,z-d_a^I)\right] \\ +\dfrac{r^2r_i\cos(3\theta_d)-r_i\left[r^2+2(z-d_a^I)^2\right]\cos(\theta_d)+2r\left[r^2+(z-d_a^I)^2\right]\sin^2(\theta_d)}{2\left[r^2\sin^2(\theta_d)+(z-d_a^I)^2\right]R(r,r_i,\theta_d,z-d_a^I)} \\ -\dfrac{r^2r_o\cos(3\theta_d)-r_o\left[r^2+2(z-d_a^I)^2\right]\cos(\theta_d)+2r\left[r^2+(z-d_a^I)^2\right]\sin^2(\theta_d)}{2\left[r^2\sin^2(\theta_d)+(z-d_a^I)^2\right]R(r,r_o,\theta_d,z-d_a^I)} \end{array} \right\} d\theta_d$$

$$-\frac{M_f}{4\pi}\int_0^{2\pi}\cos(p_I\theta - p_I\theta_d)$$

$$\times \left\{ \begin{array}{l} \cos(\theta_d)\log\left[r_i - r\cos(\theta_d)+R(r,r_i,\theta_d,z)\right] \\ -\cos(\theta_d)\log\left[r_o - r\cos(\theta_d)+R(r,r_o,\theta_d,z)\right] \\ +\dfrac{r^2r_i\cos(3\theta_d)-r_i\left[r^2+2z^2\right]\cos(\theta_d)+2r\left[r^2+z^2\right]\sin^2(\theta_d)}{2\left[r^2\sin^2(\theta_d)+z^2\right]R(r,r_i,\theta_d,z)} \\ -\dfrac{r^2r_o\cos(3\theta_d)-r_o\left[r^2+2z^2\right]\cos(\theta_d)+2r\left[r^2+z^2\right]\sin^2(\theta_d)}{2\left[r^2\sin^2(\theta_d)+z^2\right]R(r,r_o,\theta_d,z)} \end{array} \right\} d\theta_d$$

$$(6.128)$$

Defining

$$b_{sr}(r,r_A,z,w) = \cos(\theta_d)\log\left[r_A - r\cos(\theta_d)+R(r,r_A,\theta_d,z-w)\right]$$

$$+\frac{r^2r_A\cos(3\theta_d)-r_A\left[r^2+2(z-w)^2\right]\cos(\theta_d)+2r\left[r^2+(z-w)^2\right]\sin^2(\theta_d)}{2\left[r^2\sin^2(\theta_d)+(z-w)^2\right]R(r,r_A,\theta_d,z-w)} \qquad (6.129)$$

Substituting (6.129) into (6.128) one obtains

$$
B_r^I(r,\theta,z) =
$$

$$
-\frac{p_I M_f}{4\pi\mu_r} \int_0^{d_a^I} \int_0^{2\pi} \cos(p_I\theta - p_I\theta_d)
$$

$$
\times \left[\frac{\left[(z-z_c)^2 \cos(\theta_d) + rr_i \sin^2(\theta_d)\right]}{\sqrt{r^2 + r_i^2 + (z-z_c)^2 - 2rr_i \cos(\theta_d)}\left[-\sin^2(\theta_d)r^2 - (z-z_c)^2\right]} \right.
$$

$$
\left. -\frac{\left[(z-z_c)^2 \cos(\theta_d) + rr_o \sin^2(\theta_d)\right]}{\sqrt{r^2 + r_o^2 + (z-z_c)^2 - 2rr_o \cos(\theta_d)}\left[-\sin^2(\theta_d)r^2 - (z-z_c)^2\right]} \right] d\theta_d dz_c
$$

$$
+\frac{M_f}{4\pi} \int_0^{2\pi} \cos(p_I\theta - p_I\theta_d)
$$

$$
\times \left[b_{sr}(r,r_i,z,d_a^I) - b_{sr}(r,r_o,z,d_a^I) - b_{sr}(r,r_i,z,0) + b_{sr}(r,r_o,z,0) \right] d\theta_d
$$

(6.130)

Noting that

$$
\cos(p_I\theta - p_I\theta_d) = \cos(p_I\theta)\cos(p_I\theta_d) - \sin(p_I\theta)\sin(p_I\theta_d)
$$

(6.131)

Substituting (6.131) into (6.130) gives:

$$B_r^I(r,\theta,z) =$$

$$-\frac{p_I M_f}{4\pi\mu_r} \int\limits_0^{d_a^I}\int\limits_0^{2\pi} \cos(p_I\theta)\cos(p_I\theta_d)$$

$$\times\left[\frac{\left[(z-z_c)^2\cos(\theta_d)+rr_i\sin^2(\theta_d)\right]}{\sqrt{r^2+r_i^2+(z-z_c)^2-2rr_i\cos(\theta_d)}\left[-\sin^2(\theta_d)r^2-(z-z_c)^2\right]} \right.$$

$$\left. -\frac{\left[(z-z_c)^2\cos(\theta_d)+rr_o\sin^2(\theta_d)\right]}{\sqrt{r^2+r_o^2+(z-z_c)^2-2rr_o\cos(\theta_d)}\left[-\sin^2(\theta_d)r^2-(z-z_c)^2\right]} \right]d\theta_d dz_c$$

$$+\frac{p_I M_f}{4\pi\mu_r} \int\limits_0^{d_a^I}\int\limits_0^{2\pi} \sin(p_I\theta)\sin(p_I\theta_d)$$

$$\times\left[\frac{\left[(z-z_c)^2\cos(\theta_d)+rr_i\sin^2(\theta_d)\right]}{\sqrt{r^2+r_i^2+(z-z_c)^2-2rr_i\cos(\theta_d)}\left[-\sin^2(\theta_d)r^2-(z-z_c)^2\right]} \right.$$

$$\left. -\frac{\left[(z-z_c)^2\cos(\theta_d)+rr_o\sin^2(\theta_d)\right]}{\sqrt{r^2+r_o^2+(z-z_c)^2-2rr_o\cos(\theta_d)}\left[-\sin^2(\theta_d)r^2-(z-z_c)^2\right]} \right]d\theta_d dz_c$$

$$+\frac{M_f}{4\pi}\int\limits_0^{2\pi}\cos(p_I\theta)\cos(p_I\theta_d)$$

$$\times\left[b_{sr}(r,r_i,z,d_a^I)-b_{sr}(r,r_o,z,d_a^I)-b_{sr}(r,r_i,z,0)+b_{sr}(r,r_o,z,0) \right]d\theta_d \qquad (6.132)$$

$$-\frac{M_f}{4\pi}\int\limits_0^{2\pi}\sin(p_I\theta)\sin(p_I\theta_d)$$

$$\times\left[b_{sr}(r,r_i,z,d_a^I)-b_{sr}(r,r_o,z,d_a^I)-b_{sr}(r,r_i,z,0)+b_{sr}(r,r_o,z,0) \right]d\theta_d$$

The second and fourth integral terms in (6.132) are zero as they are odd functions with respect to θ_d. Therefore, (6.132) can be reduced down to

$$B_r^I(r,\theta,z) =$$

$$-\frac{p_I M_f}{4\pi\mu_r} \int\limits_0^{d_a^I} \int\limits_0^{2\pi} \cos(p_I\theta)\cos(p_I\theta_d)$$

$$\times \left[\frac{\left[(z-z_c)^2 \cos(\theta_d) + rr_i \sin^2(\theta_d) \right]}{R(r,r_i,\theta_d,z-z_c)\left[-\sin^2(\theta_d)r^2 - (z-z_c)^2 \right]} \right.$$

$$\left. -\frac{\left[(z-z_c)^2 \cos(\theta_d) + rr_o \sin^2(\theta_d) \right]}{R(r,r_o,\theta_d,z-z_c)\left[-\sin^2(\theta_d)r^2 - (z-z_c)^2 \right]} \right] d\theta_d dz_c$$

$$+\frac{M_f}{4\pi} \int\limits_0^{2\pi} \cos(p_I\theta)\cos(p_I\theta_d)$$

$$\times \left[b_{sr}(r,r_i,z,d_a^I) - b_{sr}(r,r_o,z,d_a^I) - b_{sr}(r,r_i,z,0) + b_{sr}(r,r_o,z,0) \right] d\theta_d$$

(6.133)

The solution of the B_r magnetic field is given in (6.133) which has two integrals.

6.6. MAGNETIC FLUX DENSITY VALIDATION

Using equations (6.118), (6.126) and (6.133) the magnetic fields have been calculated

and compared with FEA models. When r_o = 100 mm, r_i = 90 mm, $d_a^I = 10\,\text{mm}$, p_I = 4

and μ_r = 1.05, the fundamental component of B_z has been compared which is shown in

Table 6-V. When r_i = 80 mm, the fundamental component of B_z has been compared

which is shown in Table 6-VI. When r_i = 30 mm, the fundamental component of B_z has

been compared which is shown in Table 6-VII. When r_i = 2 mm, the fundamental

component of B_z has been compared which is shown in Table 6-VIII. The discrepancy is

within 1.5 % for all cases.

Table 6-V. COMPARISON OF B_z VALUE WHEN r_i = 90 mm.

Radius r [mm]	Air gap [mm]	B_z [T] (JMAG)	B_z [T] (Analytical)	Discrepancy [%]
92	1	0.4749	0.4819	-1.47%
94	1	0.5118	0.5195	-1.50%
96	1	0.5112	0.5182	-1.36%
98	1	0.4730	0.4778	-1.01%
92	3	0.3182	0.3216	-1.06%
94	3	0.3646	0.3693	-1.29%
96	3	0.3631	0.3674	-1.17%
98	3	0.3140	0.3163	-0.73%
92	12	0.1030	0.1033	-0.28%
94	12	0.1082	0.1086	-0.36%
96	12	0.1074	0.1078	-0.35%
98	12	0.1007	0.1008	-0.14%

Table 6-VI. COMPARISON OF B_z VALUE WHEN r_i = 80 mm.

Radius r [mm]	Air gap [mm]	B_z [T] (JMAG)	B_z [T] (Analytical)	Discrepancy [%]
84	1	0.5003	0.5058	-1.10%
88	1	0.5064	0.5118	-1.07%
92	1	0.5020	0.5075	-1.09%
96	1	0.4889	0.4940	-1.04%
84	3	0.3869	0.3905	-0.93%
88	3	0.4216	0.4261	-1.07%
92	3	0.4179	0.4222	-1.03%
96	3	0.3765	0.3795	-0.80%
84	12	0.1616	0.1623	-0.45%
88	12	0.1811	0.1821	-0.55%
92	12	0.1791	0.1801	-0.54%
96	12	0.1562	0.1566	-0.26%

Table 6-VII. COMPARISON OF B_z VALUE WHEN r_i = 30 mm.

Radius r [mm]	Air gap [mm]	B_z [T] (JMAG)	B_z [T] (Analytical)	Discrepancy [%]
50	1	0.6283	0.6290	-0.11%
60	1	0.5669	0.5675	-0.11%
70	1	0.5191	0.5199	-0.15%
80	1	0.4873	0.4890	-0.35%
50	3	0.5320	0.5327	-0.14%
60	3	0.4942	0.4949	-0.14%
70	3	0.4609	0.4619	-0.21%
80	3	0.4362	0.4379	-0.39%
50	12	0.2496	0.2499	-0.12%
60	12	0.2639	0.2644	-0.18%
70	12	0.2657	0.2663	-0.23%
80	12	0.2568	0.2578	-0.37%

Table 6-VIII. COMPARISON OF B_z VALUE WHEN r_i = 2 mm.

Radius r [mm]	Air gap [mm]	B_z [T] (JMAG)	B_z [T] (Analytical)	Discrepancy [%]
10	1	0.8037	0.8049	-0.15%
30	1	0.7900	0.7913	-0.16%
50	1	0.6288	0.6295	-0.11%
70	1	0.5181	0.5199	-0.35%
90	1	0.4801	0.4831	-0.62%
10	3	0.3633	0.3638	-0.14%
30	3	0.6019	0.6022	-0.05%
50	3	0.5339	0.5346	-0.13%
70	3	0.4608	0.4620	-0.26%
90	3	0.4185	0.4212	-0.65%
10	12	0.0186	0.0186	0.00%
30	12	0.1790	0.1790	0.00%
50	12	0.2546	0.2549	-0.12%
70	12	0.2662	0.2668	-0.23%
90	12	0.2233	0.2240	-0.31%

With r_o = 30 mm, r_i = 20 mm, $d_a^I = 30\,\text{mm}$ and p = 4, the surface and contour plots of the magnetic flux density at z = 35 mm for the analytical and JMAG models are shown in Fig. 6-17-Fig. 6-22.

(a)   (b)
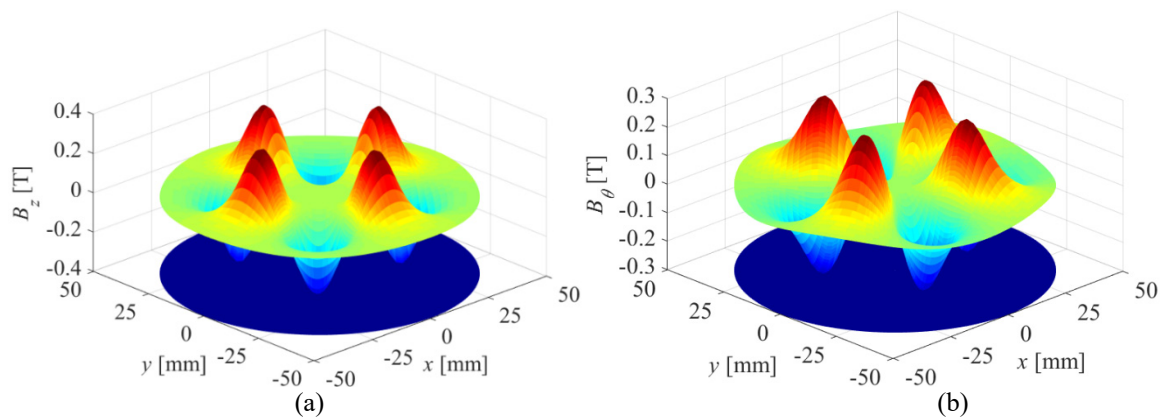
Fig. 6-17. Surface plot for (a) B_z and (b) B_θ from the analytical based model.

(a)   (b)
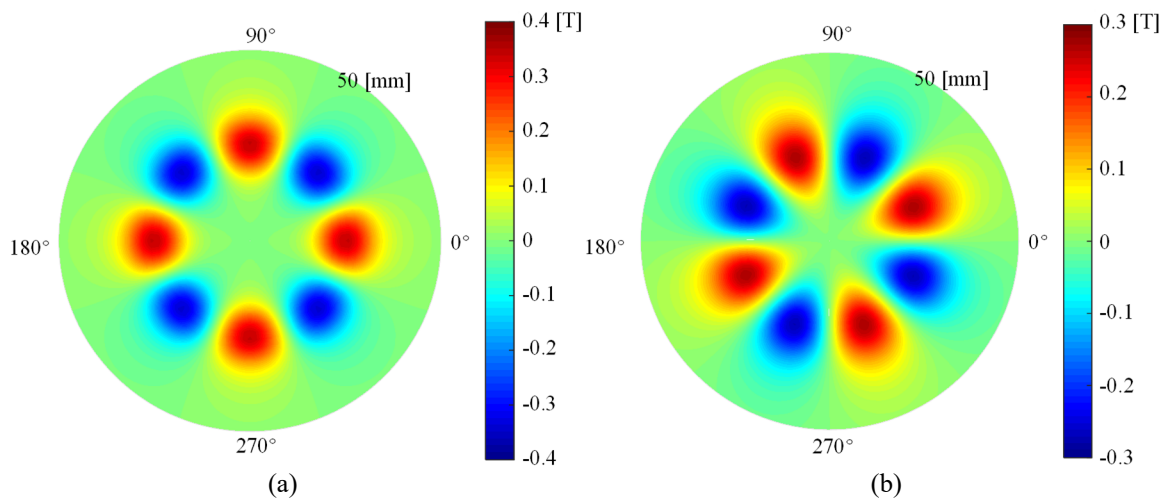
Fig. 6-18. Contour plot for (a) B_z and (b) B_θ from the analytical based model.

(a)   (b)
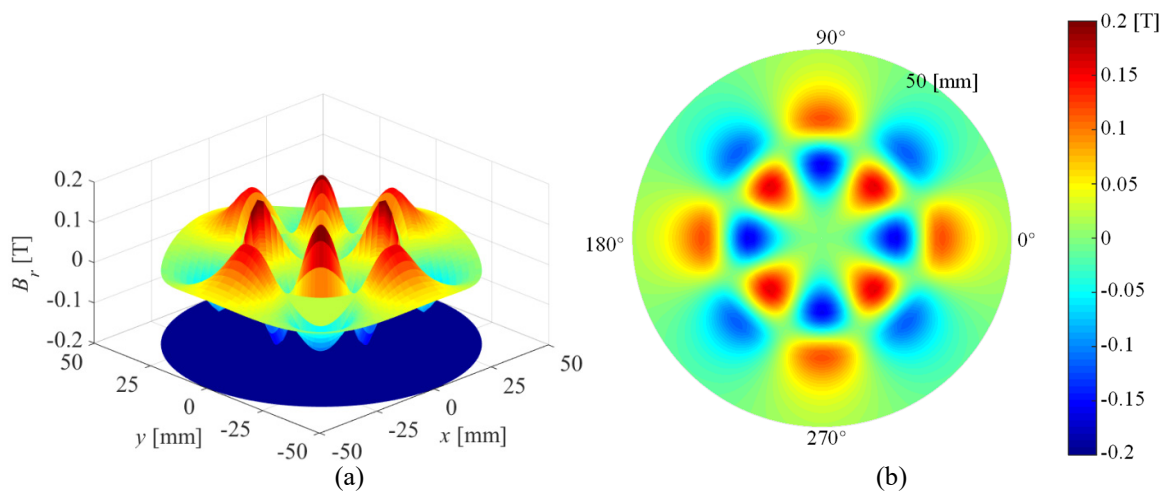
Fig. 6-19. (a) Surface plot and (b) Contour plot for B_r from the analytical based model.
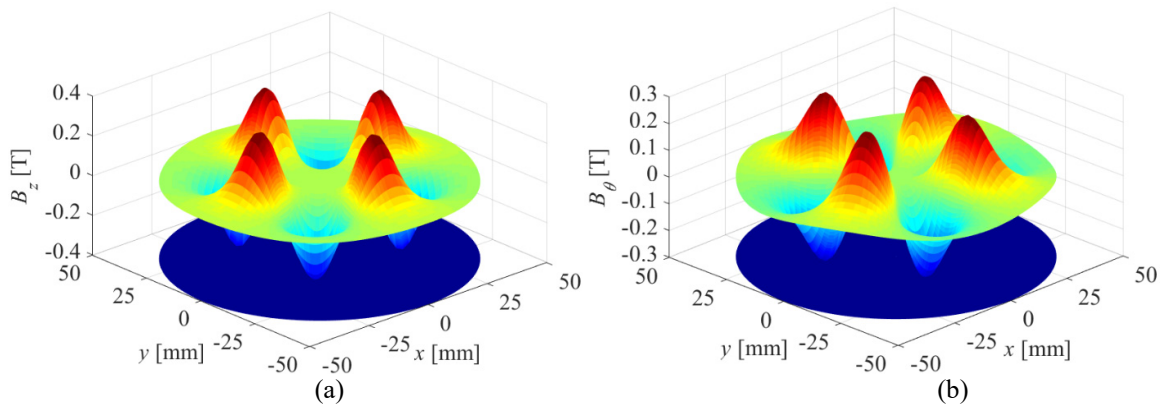
Fig. 6-20. Surface plot for (a) B_z and (b) B_θ from the 3-D JMAG model.
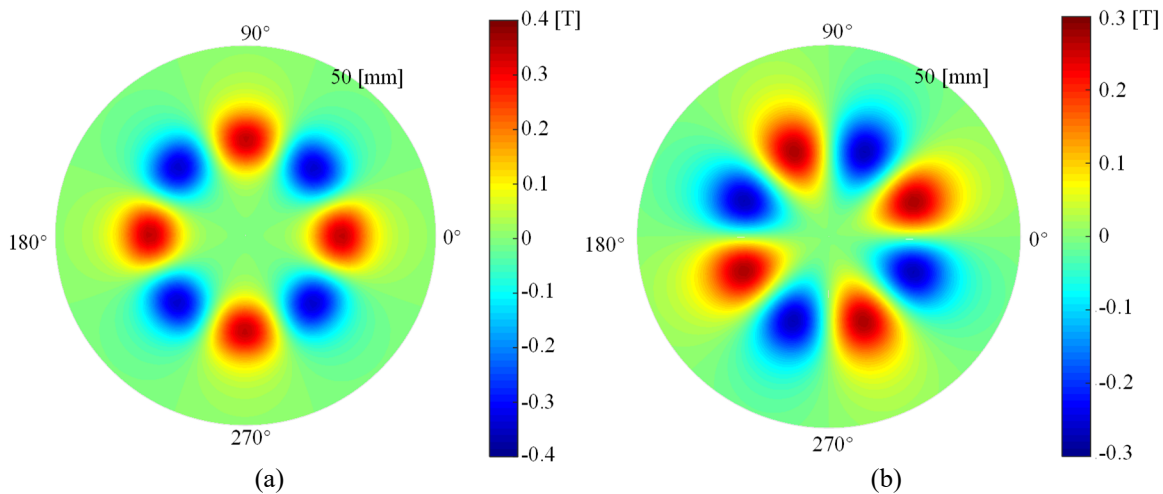
Fig. 6-21. Contour plot for (a) B_z and (b) B_θ from the 3-D JMAG model.
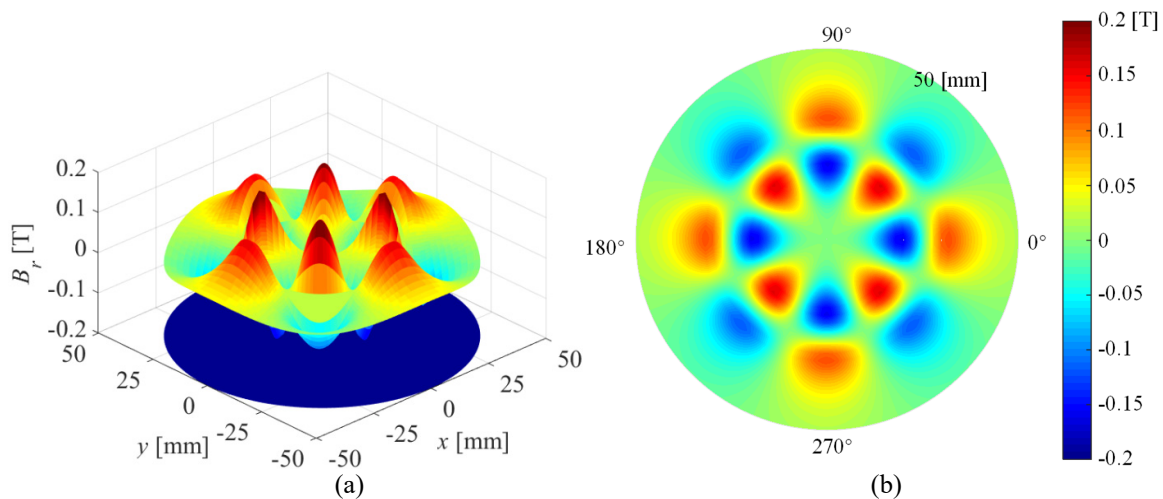
Fig. 6-22. (a) Surface plot and (b) Contour plot for B_r from the 3-D JMAG model.

With different values of geometry parameters, the comparisons between analytical and FEA models are shown in Fig. 6-23-Fig. 6-26 which show an excellent agreement.
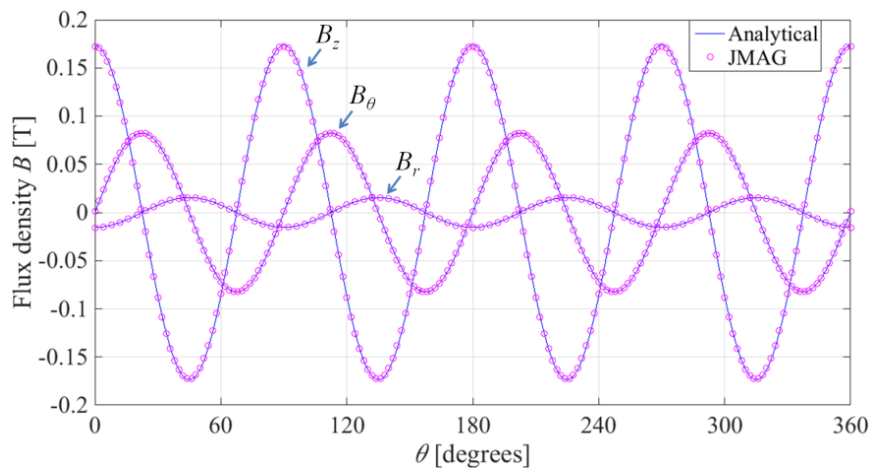
Fig. 6-23. Field comparison when r_o = 100 mm and r_i = 90 mm.
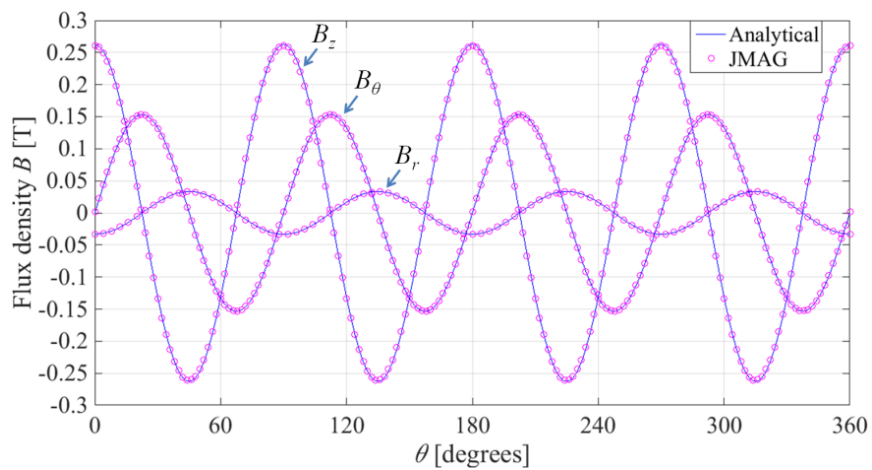
Fig. 6-24. Field comparison when r_o = 100 mm and r_i = 80 mm.
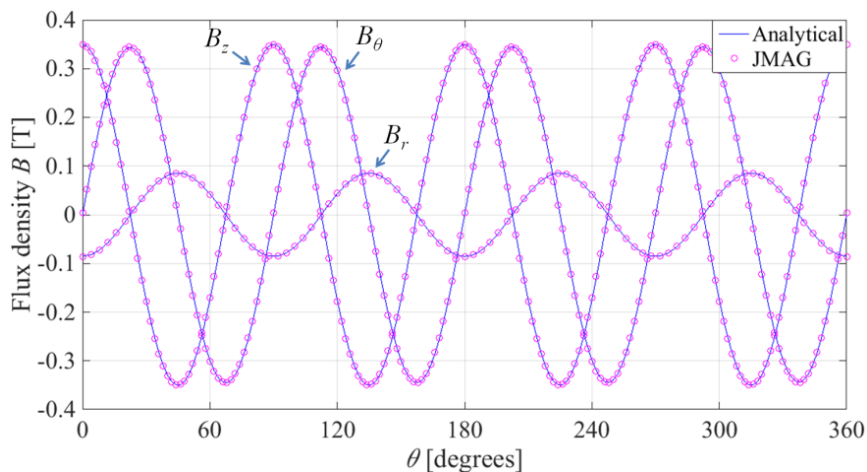
Fig. 6-25. Field comparison when r_o = 100 mm and r_i = 30 mm.
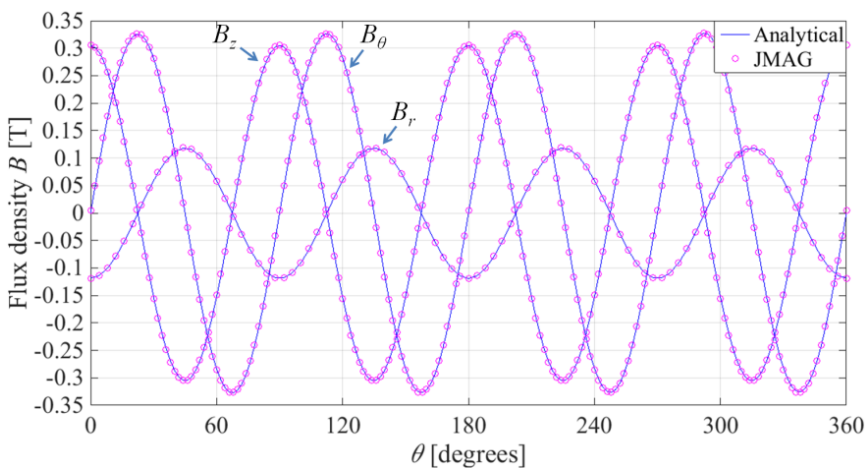
Fig. 6-26. Field comparison when r_o = 100 mm and r_i = 2 mm.

6.7. CONCLUSION

This chapter presents a different type of analytic approach to that presented previously [65,66,70-75]. The resulting torque equation is easy to compute as it only needs two integrals to be evaluated. The benefit of using the presented approach lies in the ability to derive the 3-D field and torque equations from the surface and volume charge functions. The calculation time is significantly reduced by using this analytical model compared to

the FEA models. The field and torque have been validated by FEA models and a good agreement has been achieved.

CHAPTER 7 : AN ANALYTICAL BASED MODEL FOR THE RADIAL MAGNETIC
COUPLING

7.1. GOVERNING EQUATIONS

In this chapter the radial PMC model is developed using a magnetic charge sheet approach that enables the torque equation to be expressed by a single integral without the need for a large number of summations. The radial PMC torque density characteristics are then compared with the performance capabilities of an equivalently sized axial PMC. The accuracy of the magnetic charge modeling approach is validated by using 3-D FEA models. The use of the analytic based modeling and idealized assumptions enable the fundamental geometric scaling parameter relationships to be identified.

Fig. 7-1 shows the 8-segment 4 pole pairs externally directed radial Halbach rotor. It can be noted that at the axial center ($z = 0$) of the radial Halbach rotor, the B_z field component is zero:

$$\mathbf{B}(r,\theta,0) = B_r(r,\theta,0)\hat{\mathbf{r}} + B_\theta(r,\theta,0)\hat{\boldsymbol{\theta}} + 0\hat{\mathbf{z}} \qquad (7.1)$$
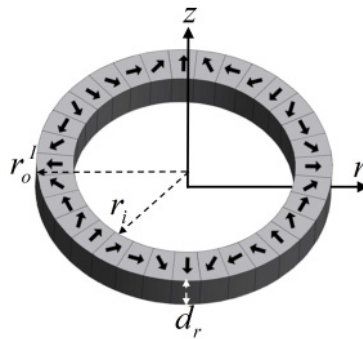
Fig. 7-1. The geometry of the radial Halbach rotor.

The magnetic charge sheet function is [81]:

$$\rho_{Rm}^{I}(\theta_{I}) = 2B_{Rm}^{I}(r_{o}^{I})\cos(p_{I}\theta_{I}) \tag{7.2}$$

where [78]:

$$B_{Rm}^{I}(r) = \frac{2c_{1}B_{m}p(1+\mu_{r})[(r_{i})^{p+1}-(r_{o}^{I})^{p+1}](r_{o}^{I})^{2p}}{r^{p+1}(1+p)[(1-\mu_{r})^{2}(r_{i})^{2p}-(1+\mu_{r})^{2}(r_{o}^{I})^{2p}]} \tag{7.3}$$

$c_{1} = 0.9745$ which is the magnitude of the fundamental component of the 8-segment Halbach magnet array as shown in Fig. 7-1. r_{i} is the inner radius and r_{o} is the outer radius.

The radial 3-D charge sheet model is shown in Fig. 7-2.
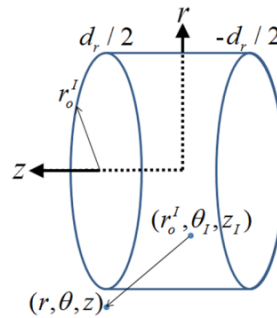
Fig. 7-2. 3-D charge sheet model.

The scalar potential can be calculated using the magnetic surface charge distribution[80,82]:

$$\phi(r,\theta,z) = \frac{1}{4\pi\mu_{0}} \int_{0}^{2\pi} \int_{-d_{r}/2}^{d_{r}/2} \frac{\rho_{Rm}^{I}(\theta_{I})}{R(r,r_{o}^{I},\theta-\theta_{I},z-z_{I})} r_{o}^{I} dz_{I} d\theta_{I} \tag{7.4}$$

Substituting (6.27) and (7.2) into (7.4) one obtains:

$$\phi(r,\theta,z) = \frac{B_{Rm}^{I}}{2\pi\mu_{0}} \int_{0}^{2\pi} \int_{-d_{r}/2}^{d_{r}/2} \frac{\cos(p_{I}\theta_{I})}{\sqrt{r^{2}+(r_{o}^{I})^{2}-2rr_{o}^{I}\cos(\theta-\theta_{I})+(z-z_{I})^{2}}} r_{o}^{I} dz_{I} d\theta_{I} \tag{7.5}$$

Evaluating the integral along the axial direction yields:

$$\phi^I(r,\theta,z) = \frac{B_{Rm}^I r_o^I}{2\pi\mu_0} \int_0^{2\pi} \cos(p_I \theta_I)$$

$$\times \log\left[\frac{z+d_r/2+\sqrt{(z+d_r/2)^2+r^2+(r_o^I)^2-2rr_o^I\cos(\theta-\theta_I)}}{z-d_r/2+\sqrt{(z-d_r/2)^2+r^2+(r_o^I)^2-2rr_o^I\cos(\theta-\theta_I)}}\right] d\theta_I \qquad (7.6)$$

Changing integration variables by defining:

$$\theta_d = \theta - \theta_I \qquad (7.7)$$

Then

$$d\theta_d = -d\theta_I \qquad (7.8)$$

$$\theta_I = \theta - \theta_d \qquad (7.9)$$

Substituting (7.8) and (7.9) into (7.6) gives:

$$\phi^I(r,\theta,z)$$
$$= -\frac{B_{Rm}^I r_o^I}{2\pi\mu_0} \int_\theta^{\theta-2\pi} \cos(p_I\theta - p_I\theta_d)$$

$$\times \log\left[\frac{z+d_r/2+\sqrt{(z+d_r/2)^2+r^2+(r_o^I)^2-2rr_o^I\cos(\theta_d)}}{z-d_r/2+\sqrt{(z-d_r/2)^2+r^2+(r_o^I)^2-2rr_o^I\cos(\theta_d)}}\right] d\theta_d \qquad (7.10)$$

The angular integration limit can also be written as:

$$\phi^I(r,\theta,z)$$

$$=\frac{B_{Rm}^I r_o^I}{2\pi\mu_0}\int_0^{2\pi}\cos(p_I\theta-p_I\theta_d) \tag{7.11}$$

$$\times\log\left[\frac{z+d_r/2+\sqrt{(z+d_r/2)^2+r^2+(r_o^I)^2-2rr_o^I\cos(\theta_d)}}{z-d_r/2+\sqrt{(z-d_r/2)^2+r^2+(r_o^I)^2-2rr_o^I\cos(\theta_d)}}\right]d\theta_d$$

Since

$$\cos(p_I\theta-p_I\theta_d)=\cos(p_I\theta)\cos(p_I\theta_d)-\sin(p_I\theta)\sin(p_I\theta_d) \tag{7.12}$$

Substituting (7.12) into equation (7.11) the scalar potential can be re-written as

$$\phi^I(r,\theta,z)$$

$$=\frac{B_{Rm}^I r_o^I}{2\pi\mu_0}\int_0^{2\pi}\left[\cos(p_I\theta)\cos(p_I\theta_d)-\sin(p_I\theta)\sin(p_I\theta_d)\right] \tag{7.13}$$

$$\times\log\left[\frac{z+d_r/2+\sqrt{(z+d_r/2)^2+r^2+(r_o^I)^2-2rr_o^I\cos(\theta_d)}}{z-d_r/2+\sqrt{(z-d_r/2)^2+r^2+(r_o^I)^2-2rr_o^I\cos(\theta_d)}}\right]d\theta_d$$

The integral associated with the sine term in (7.13) goes to zero since it is an odd function with respect to θ_d. Then the scalar potential can be simplified down to

$$\phi^I(r,\theta,z)$$

$$=\frac{B_{Rm}^I r_o^I}{2\pi\mu_0}\int_0^{2\pi}\cos(p_I\theta)\cos(p_I\theta_d) \tag{7.14}$$

$$\times\log\left[\frac{z+d_r/2+\sqrt{(z+d_r/2)^2+r^2+(r_o^I)^2-2rr_o^I\cos(\theta_d)}}{z-d_r/2+\sqrt{(z-d_r/2)^2+r^2+(r_o^I)^2-2rr_o^I\cos(\theta_d)}}\right]d\theta_d$$

Equation (7.14) will be used in the torque calculation.

7.2. TORQUE ON IDEAL RADIAL MAGNETIC COUPLING

Consider the problem shown in Fig. 7-3 in which two radial Halbach rotors are present. The rotors are separated by a gap g. These two rotors have the same axial length, d_r.

Rotor I has an inner radius of r_i and outer radius r_o^I while rotor II has an inner radius of r_i^{II} and outer radius r_o.

The two Halbach rotors can be replaced with two equivalent magnetic charge sheets as shown in Fig. 7-4.
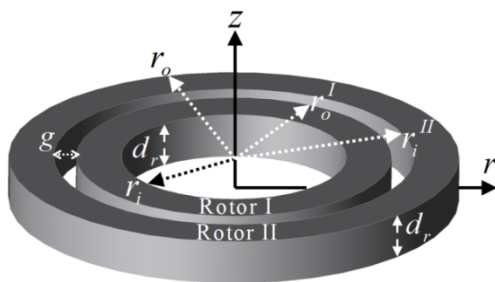
Fig. 7-3. The model of the axial Halbach rotor couplings.
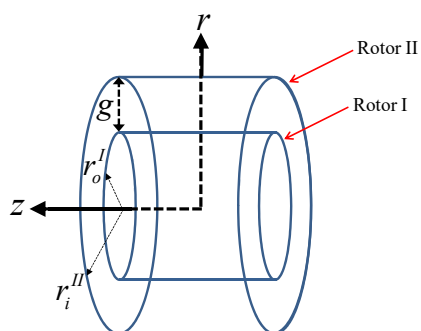
Fig. 7-4. Equivalent magnetic charge sheets.

The torque on the surface of rotor II can be calculated from the magnetic energy [79]:

$$T_R = \frac{\partial W}{\partial \theta_{II}}\bigg|_{\phi^I = \text{constant}} \tag{7.15}$$

where the energy contained in the problem region is given by

$$W = \int_{0}^{2\pi} \int_{-d_r/2}^{d_r/2} \phi^I(r_i^{II},\theta_{II},z_{II})\rho_m^{II}(\theta_{II})r_i^{II}dz_{II}d\theta_{II} \tag{7.16}$$

Substituting (7.16) into (7.15) gives

$$T_R(\theta_t) = \int_{0}^{2\pi} \int_{-d_r/2}^{d_r/2} \phi^I(r_i^{II},\theta_{II},z_{II})\frac{\partial\rho_{Rm}^{II}(\theta)}{\partial\theta}\bigg|_{\theta=\theta_{II}} r_i^{II}dz_{II}d\theta_{II} \tag{7.17}$$

where

$$\rho_{Rm}^{II}(\theta) = 2B_{Rm}^{II}(r_o)\cos(p_I\theta) \tag{7.18}$$

and

$$B_{Rm}^{II}(r) = \frac{2c_1 B_m p(1+\mu_r)[(r_i^{II})^{p+1}-(r_o)^{p+1}](r_o)^{2p}}{r^{p+1}(1+p)[(1-\mu_r)^2(r_i^{II})^{2p}-(1+\mu_r)^2(r_o)^{2p}]} \tag{7.19}$$

Substituting (7.2) into (7.17)gives

$$T_R(\theta_t) = -2B_{Rm}^{II}p_{II}\int_{0}^{2\pi}\int_{-d_r/2}^{d_r/2}\phi^I(r_i^{II},\theta_{II},z_{II})\sin\left[p_{II}(\theta_{II}-\theta_t)\right]r_i^{II}dz_{II}d\theta_{II} \tag{7.20}$$

Substituting (7.14) into (7.20) gives:

$$T_R(\theta_t) = -\frac{B_{Rm}^I B_{Rm}^{II}r_o^I r_i^{II}p_{II}}{\pi\mu_0}\int_{0}^{2\pi}\int_{-d_r/2}^{d_r/2}\int_{0}^{2\pi}\sin(p_{II}\theta_{II}-p_{II}\theta_t)\cos(p_I\theta_{II}-p_I\theta_d)$$

$$\times\log\left[\frac{z_{II}+d_r/2+\sqrt{(z_{II}+d_r/2)^2+(r_i^{II})^2+(r_o^I)^2-2r_i^{II}r_o^I\cos(\theta_d)}}{z_{II}-d_r/2+\sqrt{(z_{II}-d_r/2)^2+(r_i^{II})^2+(r_o^I)^2-2r_i^{II}r_o^I\cos(\theta_d)}}\right]d\theta_{II}dz_{II}d\theta_d \tag{7.21}$$

Uniform torque is only created when $p_I = p_{II} = p$. Using trigonometric identity from equation (6.74), we can rewrite (7.21):

$$
\begin{aligned}
T_R(\theta_t) = &-\frac{B_{Rm}^I B_{Rm}^{II} r_o^I r_i^{II} p}{2\pi\mu_0} \int_0^{2\pi} \int_{-d_r/2}^{d_r/2} \int_0^{2\pi} \sin(2p\theta_{II} - p\theta_t - p\theta_d) \\
&\times \log\left[\frac{z_{II} + d_r/2 + \sqrt{(z_{II} + d_r/2)^2 + (r_i^{II})^2 + (r_o^I)^2 - 2r_i^{II} r_o^I \cos(\theta_d)}}{z_{II} - d_r/2 + \sqrt{(z_{II} - d_r/2)^2 + (r_i^{II})^2 + (r_o^I)^2 - 2r_i^{II} r_o^I \cos(\theta_d)}} \right] d\theta_{II} dz_{II} d\theta_d \\
&+ \frac{B_{Rm}^I B_{Rm}^{II} r_o^I r_i^{II} p}{2\pi\mu_0} \int_0^{2\pi} \int_{-d_r/2}^{d_r/2} \int_0^{2\pi} \sin(p\theta_t - p\theta_d) \\
&\times \log\left[\frac{z_{II} + d_r/2 + \sqrt{(z_{II} + d_r/2)^2 + (r_i^{II})^2 + (r_o^I)^2 - 2r_i^{II} r_o^I \cos(\theta_d)}}{z_{II} - d_r/2 + \sqrt{(z_{II} - d_r/2)^2 + (r_i^{II})^2 + (r_o^I)^2 - 2r_i^{II} r_o^I \cos(\theta_d)}} \right] d\theta_{II} dz_{II} d\theta_d
\end{aligned}
\tag{7.22}
$$

The first term will integrate to zero and the second term's integral with respect to θ_{II} is elementary. The torque equation reduces down to:

$$
\begin{aligned}
T_R(\theta_t) = &\frac{B_{Rm}^I B_{Rm}^{II} r_o^I r_i^{II} p}{\mu_0} \int_0^{2\pi} \int_{-d_r/2}^{d_r/2} \sin(p\theta_t - p\theta_d) \\
&\times \log\left[\frac{z_{II} + d_r/2 + \sqrt{(z_{II} + d_r/2)^2 + (r_i^{II})^2 + (r_o^I)^2 - 2r_i^{II} r_o^I \cos(\theta_d)}}{z_{II} - d_r/2 + \sqrt{(z_{II} - d_r/2)^2 + (r_i^{II})^2 + (r_o^I)^2 - 2r_i^{II} r_o^I \cos(\theta_d)}} \right] dz_{II} d\theta_d
\end{aligned}
\tag{7.23}
$$

Noting that

$$
\sin(p\theta_t - p\theta_d) = \sin(p\theta_t)\cos(p\theta_d) - \cos(p\theta_t)\sin(p\theta_d)
\tag{7.24}
$$

Equation (7.23) can be written as

$$T_R(\theta_t) = \frac{B_{Rm}^I B_{Rm}^{II} r_o^I r_i^{II} p}{\mu_0} \int\limits_0^{2\pi} \int\limits_{-d_r/2}^{d_r/2} \sin(p\theta_t)\cos(p\theta_d)$$

$$\times \log\left[\frac{z_{II} + d_r/2 + \sqrt{(z_{II}+d_r/2)^2 + (r_i^{II})^2 + (r_o^I)^2 - 2r_i^{II}r_o^I\cos(\theta_d)}}{z_{II} - d_r/2 + \sqrt{(z_{II}-d_r/2)^2 + (r_i^{II})^2 + (r_o^I)^2 - 2r_i^{II}r_o^I\cos(\theta_d)}}\right] dz_{II}d\theta_d$$

$$- \frac{B_{Rm}^I B_{Rm}^{II} r_o^I r_i^{II} p}{\mu_0} \int\limits_0^{2\pi} \int\limits_{-d_r/2}^{d_r/2} \cos(p\theta_t)\sin(p\theta_d)$$

$$\times \log\left[\frac{z_{II} + d_r/2 + \sqrt{(z_{II}+d_r/2)^2 + (r_i^{II})^2 + (r_o^I)^2 - 2r_i^{II}r_o^I\cos(\theta_d)}}{z_{II} - d_r/2 + \sqrt{(z_{II}-d_r/2)^2 + (r_i^{II})^2 + (r_o^I)^2 - 2r_i^{II}r_o^I\cos(\theta_d)}}\right] dz_{II}d\theta_d$$

$$(7.25)$$

The second term in (7.25) goes to zero as it is an odd function. Substituting (6.28) into (7.25) gives

$$T_R(\theta_t) = \frac{B_{Rm}^I B_{Rm}^{II} r_o^I r_i^{II} p}{\mu_0} \int\limits_0^{2\pi} \int\limits_{-d_r/2}^{d_r/2} \sin(p\theta_t)\cos(p\theta_d)$$

$$\times \log\left[\frac{z_{II} + d_r/2 + \sqrt{(z_{II}+d_r/2)^2 + C(r_i^{II},r_o^I,\theta_d)}}{z_{II} - d_r/2 + \sqrt{(z_{II}-d_r/2)^2 + C(r_i^{II},r_o^I,\theta_d)}}\right] dz_{II}d\theta_d$$

$$- \frac{B_{Rm}^I B_{Rm}^{II} r_o^I r_i^{II} p}{\mu_0} \int\limits_0^{2\pi} \int\limits_{-d_r/2}^{d_r/2} \cos(p\theta_t)\sin(p\theta_d)$$

$$\times \log\left[\frac{z_{II} + d_r/2 + \sqrt{(z_{II}+d_r/2)^2 + C(r_i^{II},r_o^I,\theta_d)}}{z_{II} - d_r/2 + \sqrt{(z_{II}-d_r/2)^2 + C(r_i^{II},r_o^I,\theta_d)}}\right] dz_{II}d\theta_d$$

$$(7.26)$$

Finally, evaluating the *z*-axis integral term in (7.26) yields:

$$T_R(\theta_t) = \frac{B_{Rm}^I B_{Rm}^{II} r_o^I r_i^{II} p}{\mu_0} \sin(p\theta_t)\int\limits_0^{2\pi} \cos(p\theta_d) \times \left\{\sqrt{C(r_i^{II},r_o^I,\theta_d)} - \sqrt{C(r_i^{II},r_o^I,\theta_d)+(d_r)^2}\right.$$

$$\left. + \frac{d_r}{2}\log\left[\frac{d_r+\sqrt{C(r_i^{II},r_o^I,\theta_d)+(d_r)^2}}{-d_r+\sqrt{C(r_i^{II},r_o^I,\theta_d)+(d_r)^2}}\right]\right\}d\theta_d$$

$$(7.27)$$

The mass torque density, T_{Rm}, and volumetric torque density, T_{Rv}, are defined as:

$$T_{Rm} = \frac{T_R}{\rho_m \pi d_r \left[r_o^2 - (r_i^{II})^2 + (r_o^I)^2 - r_i^2 \right]} \quad [\text{Nm/kg}] \tag{7.28}$$

$$T_{Rv} = \frac{T_R}{d_r \pi r_o^2} \quad [\text{Nm/m}^3] \tag{7.29}$$

where ρ_m is the magnet material density.

The charge sheet model from COMSOL is shown in Fig. 7-5 and the JMAG model is shown in Fig. 7-6. The parameters used to create the analytical based, JMAG and COMSOL models are shown in Table 7-I.

(a)

(b)
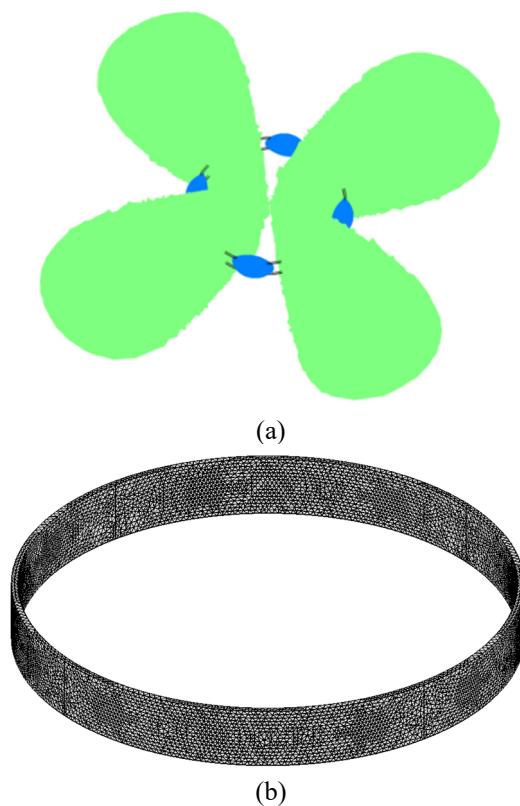
Fig. 7-5. (a) The COMSOL finite element analysis charge sheet model used to calculate the torque and (b) with mesh.

(a)

(b)
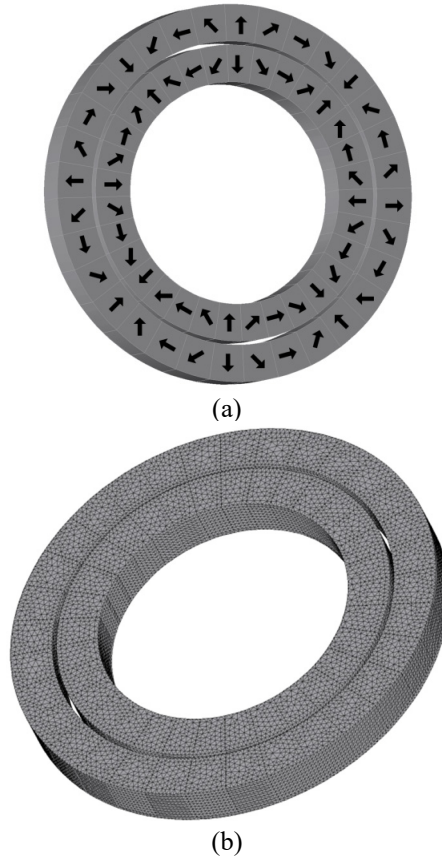
Fig. 7-6. (a) The 4 pole pairs JMAG model used to calculate the torque and (b) with mesh.

Table 7-I. PARAMETERS FOR THE IDEAL RADIAL COUPLING

Description	Value	Unit
Rotor I		
Outer radius, r_o^I	40	mm
Inner radius, r_i^I	30	mm
Axial length, d_r	10	mm
Pole pairs, $p_I=p$	4	-
Rotor II		
Outer radius, r_o^{II}	51	mm
Inner radius, r_i^{II}	41	mm
Axial length, d_r	10	mm
Pole pairs, $p_{II}=p$	4	-
Magnetic permeability, μ_r	1.05	-
Remnant flux density, B_m	1.27	T
Density of magnet, ρ_m	7600	kg/m³
Air gap, g	1	mm

The torque obtained from equation (7.27) is plotted and compared with the COMSOL charge sheet model and JMAG. The results are shown in Fig. 7-7 and Fig. 7-8.
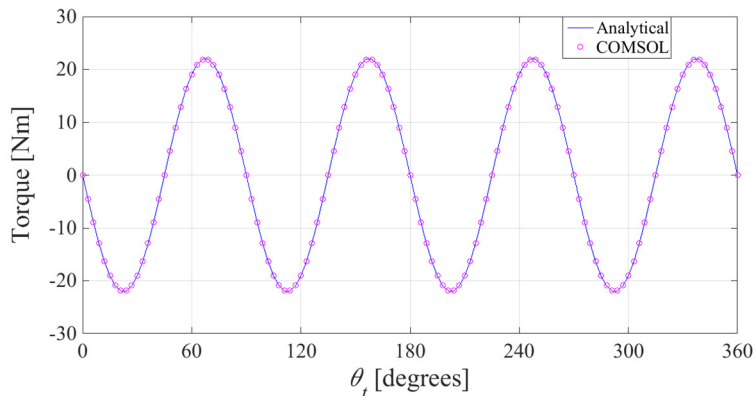
Fig. 7-7. Torque comparison between the analytical based model and the COMSOL charge sheet model.
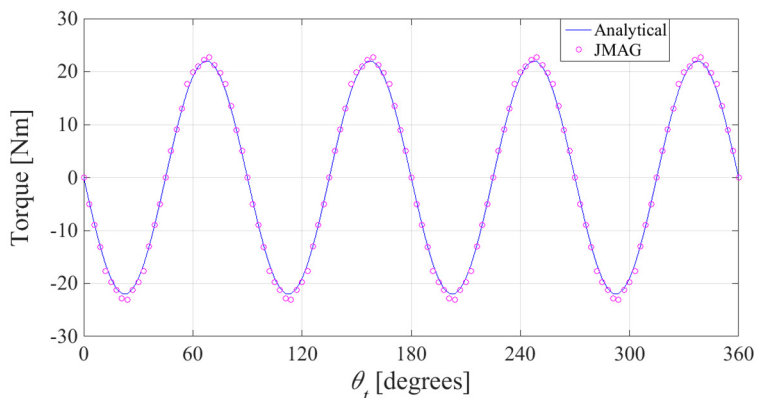
Fig. 7-8. Torque comparison between the analytical based model and the 3-D JMAG model.

The discrepancy between the analytical based model and the FEA models is shown in Fig. 7-9 and Fig. 7-10. The discrepancy shown in Fig. 7-10 may be caused by neglecting the magnet volume region's relative permeability. The magnet's relative permeability was accounted for when assigning the charge density value (in equation (7.3)), but the effect of the field being distorted when passing through the magnet volume region was not accounted for. Another reason that the percentage discrepancy is larger than 5 % at

some positions (near 0, 45, 90 degrees) is because the absolute torque values are small. When comparing at the peak torque positions (22.5 and 67.5 degrees), the discrepancy is within 4 %.
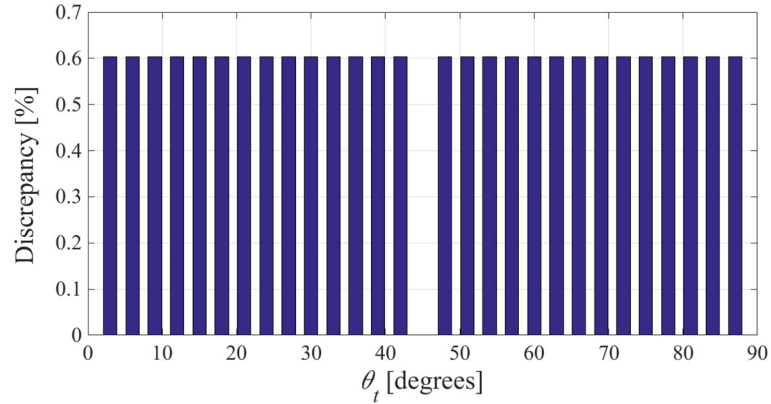
Fig. 7-9. Torque discrepancy between the analytical based model and the COMSOL charge sheet model.
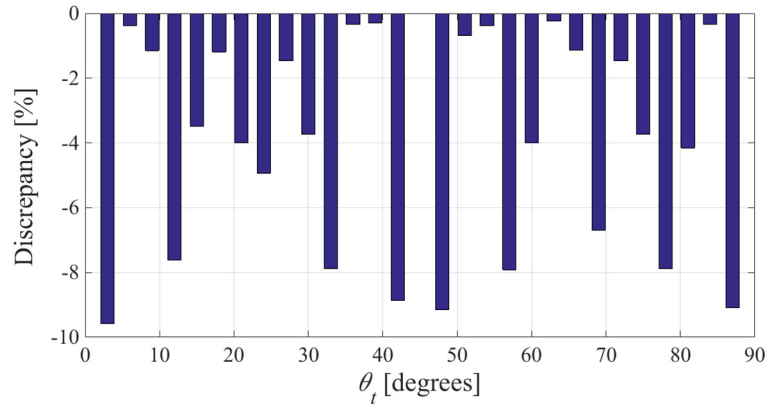
Fig. 7-10. Torque discrepancy between the analytical based model and the 3-D JMAG model.

7.3. MAGNETIC FIELD SOLUTION OF THE HALBACH RADIAL ROTOR

In 3-D the magnetic flux density created by a radial magnetic charge sheet disc is given by:

$$\mathbf{B}(r,\theta,z) = \frac{1}{4\pi} \int_0^{2\pi} \int_{-d_r/2}^{d_r/2} \frac{\rho_{Rm}^I(\theta_I)}{R(r,r_o^I,\theta-\theta_I,z,z_I)^3} r_o^I \mathbf{R}(r,r_o^I,\theta-\theta_I,z-z_I) dz_I d\theta_I \qquad (7.30)$$

Substituting (7.2) and (6.108) into (7.30) one obtains:

$$B_r^I(r,\theta,z) = \frac{1}{2\pi} B_{Rm}^I \int_0^{2\pi} \int_{-d_r/2}^{d_r/2} \frac{\cos(p_I\theta_I)}{R(r,r_o^I,\theta-\theta_I,z,z_I)^3} r_o^I \left[r - r_o^I \cos(\theta-\theta_I) \right] dz_I d\theta_I \qquad (7.31)$$

$$B_\theta^I(r,\theta,z) = \frac{1}{2\pi} B_{Rm}^I \int_0^{2\pi} \int_{-d_r/2}^{d_r/2} \frac{\cos(p_I\theta_I)}{R(r,r_o^I,\theta-\theta_I,z,z_I)^3} r_o^I \left[r_o^I \sin(\theta-\theta_I) \right] dz_I d\theta_I \qquad (7.32)$$

$$B_z^I(r,\theta,z) = \frac{1}{2\pi} B_{Rm}^I \int_0^{2\pi} \int_{-d_r/2}^{d_r/2} \frac{\cos(p_I\theta_I)}{R(r,r_o^I,\theta-\theta_I,z,z_I)^3} r_o^I (z-z_I) dz_I d\theta_I \qquad (7.33)$$

Integrating (7.31)-(7.33) with Mathematica with respect to z_I gives:

$$B_r^I(r,\theta,z) = \int_0^{2\pi} \left(\frac{\dfrac{d_r/2-z}{\sqrt{(d_r/2-z)^2 + C(r,r_o^I,\theta-\theta_I)}} + \dfrac{d_r/2+z}{\sqrt{(d_r/2+z)^2 + C(r,r_o^I,\theta-\theta_I)}}}{C(r,r_o^I,\theta-\theta_I)} \right)$$
$$\times \frac{B_{Rm}^I r_o^I}{2\pi} \cos(p_I\theta_I) \left[r - r_o^I \cos(\theta-\theta_I) \right] d\theta_I \qquad (7.34)$$

$$B_\theta^I(r,\theta,z) = \int_0^{2\pi} \left(\frac{\dfrac{d_r/2-z}{\sqrt{(d_r/2-z)^2 + C(r,r_o^I,\theta-\theta_I)}} + \dfrac{d_r/2+z}{\sqrt{(d_r/2+z)^2 + C(r,r_o^I,\theta-\theta_I)}}}{C(r,r_o^I,\theta-\theta_I)} \right)$$
$$\times \frac{B_{Rm}^I r_o^I}{2\pi} \cos(p_I\theta_I) \left[r_o^I \sin(\theta-\theta_I) \right] d\theta_I \qquad (7.35)$$

$$B_z^I(r,\theta,z) = \int_0^{2\pi} \left(\frac{1}{\sqrt{(d_r/2-z)^2 + C(r,r_o^I,\theta-\theta_I)}} - \frac{1}{\sqrt{(d_r/2+z)^2 + C(r,r_o^I,\theta-\theta_I)}} \right)$$
$$\times \frac{B_{Rm}^I r_o^I}{2\pi} \cos(p_I\theta_I) d\theta_I \qquad (7.36)$$

The analytically calculated magnetic flux density is compared with a magnetic charge FEA model developed in COMSOL and a 3-D JMAG model. Both of the models are shown in Fig. 7-11.

(a)   (b)
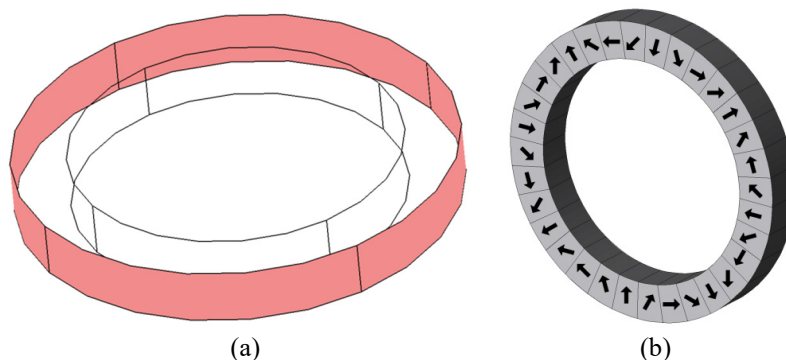
Fig. 7-11. The model used to calculated the magnetic flux density in (a) COMSOL and (b) JMAG.

The parameters for the radial rotor are shown in Table 7-II. The flux density was compared at $(r, z) = (45, 1)$ mm with a JMAG 3-D FEA model and a COMSOL magnetic charge sheet model. The Simpson's rule was used to calculate the flux density in (7.34)-(7.36). The comparison is shown in Fig. 7-12 and Fig. 7-13. A very good match was achieved.

Table 7-II. PARAMETERS FOR THE RADIAL ROTOR

Description	Value	Unit
Outer radius, r_o^I	40	mm
Inner radius, r_i^I	30	mm
Axial length, d_r	10	mm
Pole pairs, $p_I=p$	4	-
Magnetic permeability, μ_r	1.05	-
Remnant flux density, B_m	1.27	T
Density of magnet, ρ	7600	kg/m^3
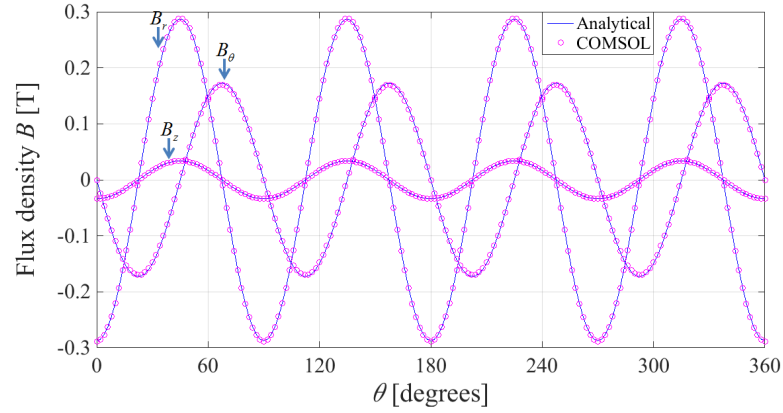
Fig. 7-12. Magnetic flux density comparison between the analytical based model and the COMSOL charge sheet model.
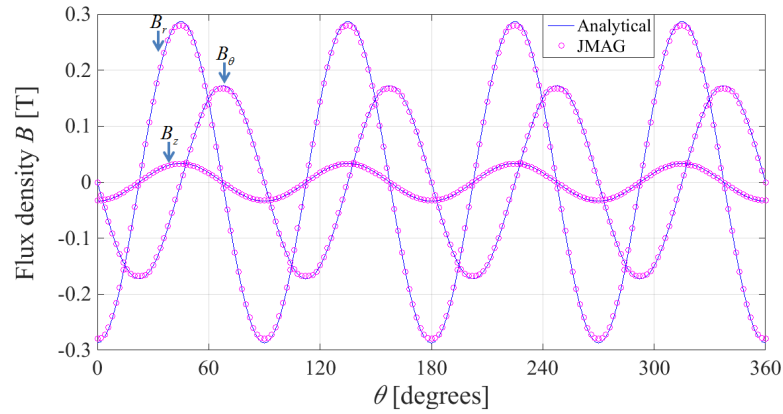
Fig. 7-13. Magnetic flux density comparison between the analytical based model and the 3-D JMAG model.

7.4. PARAMETER ANALYSIS

The inner radius and outer radius ratio is defined as:

$$\Lambda = r_i / r_o \tag{7.37}$$

The air gap radius between rotors is defined as:

$$r_g = r_o^I + g / 2 \tag{7.38}$$

With definition (7.38) the torque density for the radial PMC will be dependent on six parameters, namely, outer PMC radius, r_o, inner PMC radius, r_i, air gap radius, r_g, pole pairs, p, axial length, d_r, and air gap g. These parameters are shown in Table 7-I.

The influence of the air gap length on the torque value is self-evident and will be kept at $g = 1$ mm. This is a very small air gap for a practical PMC. However, the primary purpose is to determine the upper torque density bound for a magnetic device and therefore a 1 mm air gap is not small for many other types of rotary magnetic devices.

The increase in the axial length d_r will result in an increasing torque density. This effect is illustrated in Fig. 7-14. Fig. 7-14 also shows that for a given r_o a further increase in d_r will have a diminishing return. For instance, when $d_r > r_o$ the mass torque density will increase further by only 1% per-mm. Based on this analysis the axial length of the PMC will be scaled with PMC outer radius by keeping $d_r = r_o$.
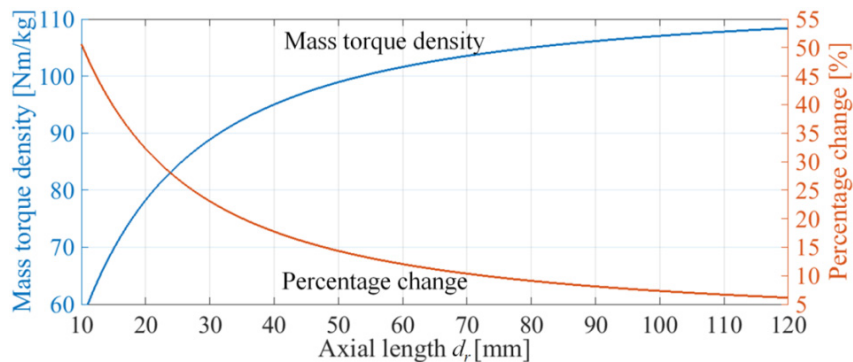
Fig. 7-14. The increase in mass torque density when the axial length d_r is increased while holding other parameters constant.

If the p and r_o are now set to $(p, r_o) = (4, 30$ mm$)$ a torque density plot when r_i and r_g are varied can be created. The resultant plot is shown in Fig. 7-15. From this plot it can be noted that the peak volumetric and mass torque density occurs when $(r_i, r_g) = (0, 21.5)$

mm and $(r_i, r_g) = (15, 23.5)$ mm respectively. These locations are marked in Fig. 7-15 by a black dot.

(a)

(b)
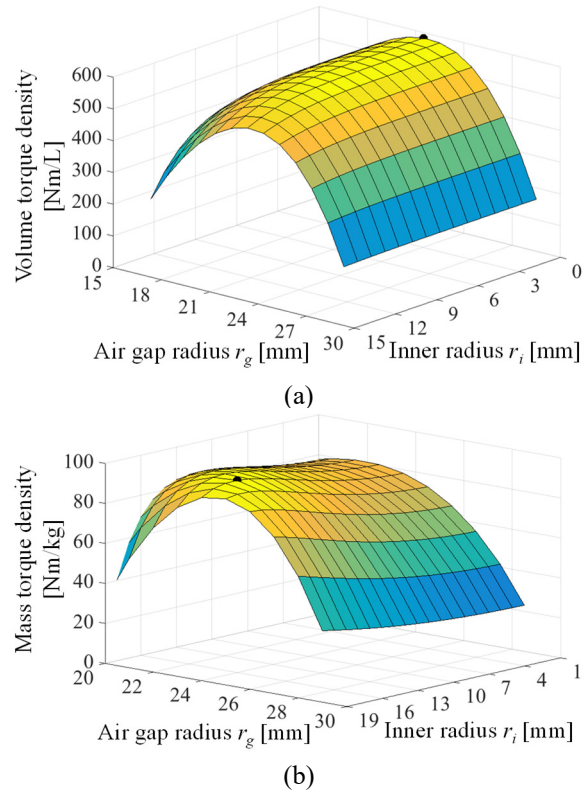
Fig. 7-15. (a) Volumetric and (b) mass torque density when r_g and r_i are both varied and $p = 4$, $g = 1$ mm, r_o = 30 mm, $d_r = r_o$.

The value of (r_i, r_g) that gives the peak mass torque density for each different r_o and p value was then calculated, the resulting peak mass and volumetric torque density plots are shown in Fig. 7-16 (a) and (b) while Fig. 7-16 (c) shows the corresponding r_g used to achieve the peak values.

By studying Fig. 7-16 (c) it was determined that the peak mass torque density always occurs when

$$r_g = (r_i + r_o)/2 \qquad (7.39)$$
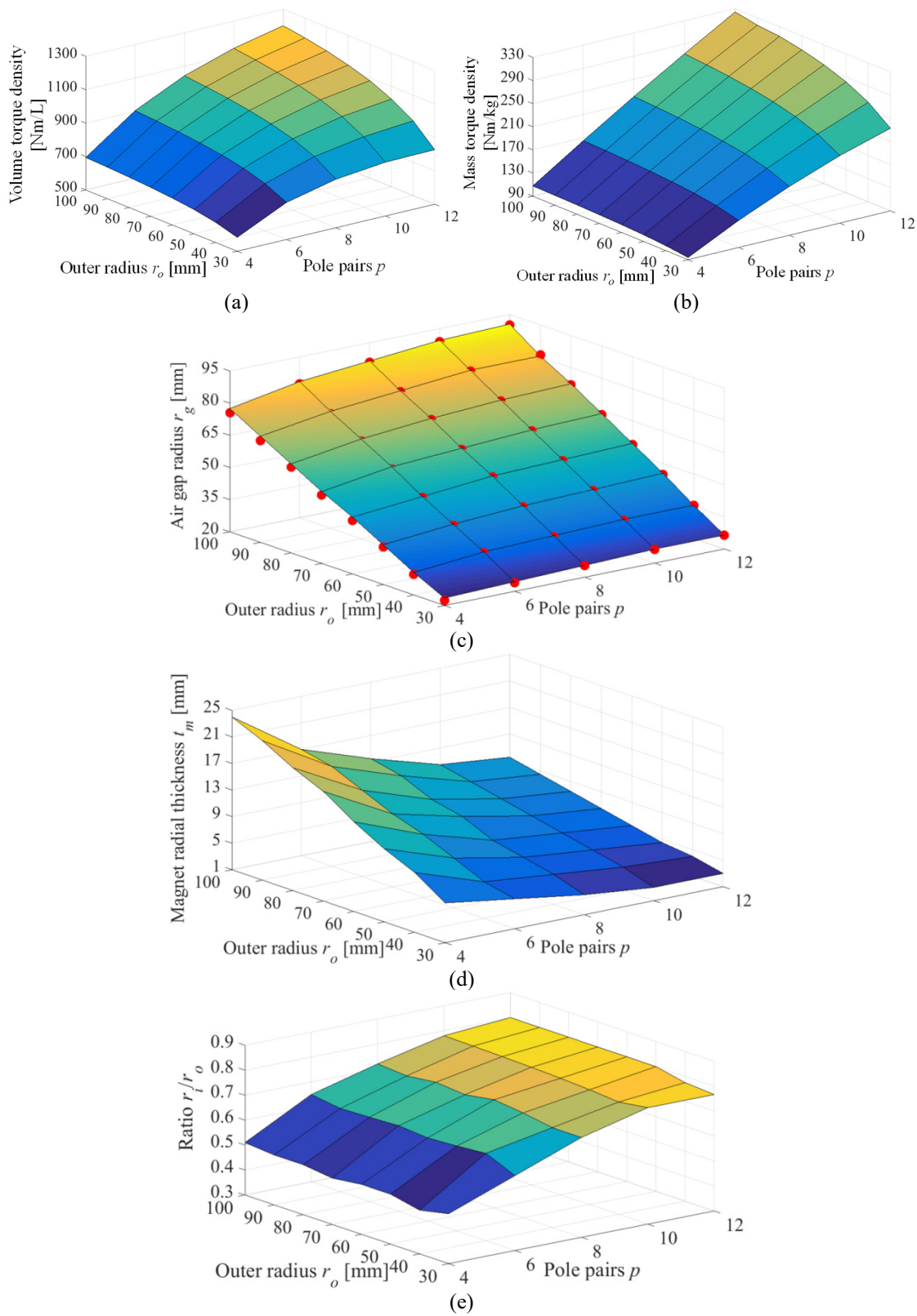
Fig. 7-16. (a) Volumetric and (b) mass torque density for different pole pairs and outer radii also shown is (c) corresponding r_g value, (d) corresponding magnet radial thickness, t_m and (e) inner-to-outer PMC ratio, Λ for the peak mass torque density condition.

With (7.39) satisfied the magnet radial thickness must then be

$$t_m = (r_o - r_i - g)/2 \qquad (7.40)$$

The corresponding magnet thickness value at each peak torque condition is shown in Fig. 7-16 (d). From Fig. 7-16 (d), as p increases the optimal magnet thickness, t_m decreases and this leads to a higher torque density, while Fig. 7-16 (e) shows that the Λ-ratio is a constant with the same value of pole pairs, p. The optimal Λ calculated for different numbers of pole pairs is shown in Fig. 7-17. The Λ-ratio can be curved fitted and is related to the number of pole pairs by

$$\Lambda = 1 - 10/(3 + 5p^{0.9}) \qquad (7.41)$$

By examining Fig. 7-16, and noting that the magnetic shear stress is independent of p, it was determined that at peak mass torque density the following condition is always satisfied

$$r_o - t_m = pt_m\pi/4 \qquad (7.42)$$

The condition given by (7.42) can be confirmed by considering the plot as shown in Fig. 7-18 in which r_o and t_m were both varied whilst hold $p = 4$. The line at which (7.42) is satisfied is also shown in Fig. 7-18, the line clearly traverses the peak.
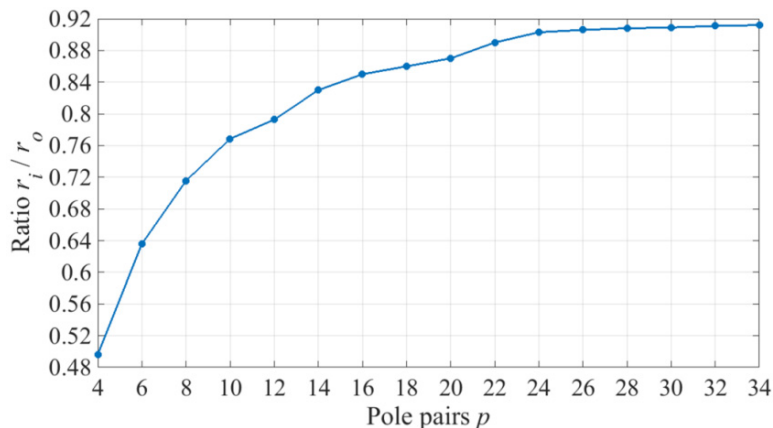
Fig. 7-17. The radial coupling ideal inner-to-outer radii ratio, Λ, that gives the peak mass torque density for different numbers of pole pairs.
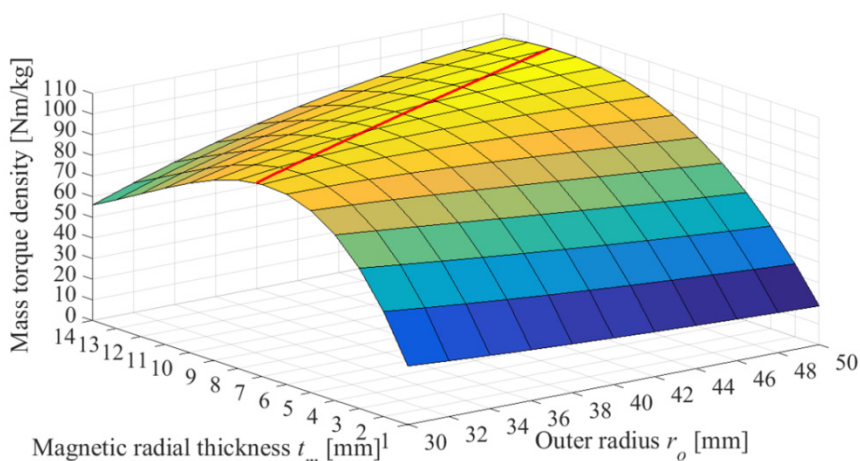
Fig. 7-18. Variation of mass torque density when r_o and t_m are varied and $p=4$, $d_r=r_o$, $g=1$ mm. The line that satisfies (7.42) is superimposed on the plot.

7.5. COMPARISON BETWEEN AXIAL AND RADIAL MAGNETIC COUPLINGS

The performance of the axial and radial PMCs has been compared when they have the same sizes (outer radius r_o and axial length $d_a = d_r = d$). Ideal PMCs models (inner radius $r_i = 0$ mm) were used to compare the volume torque density. The outer radius r_o and the axial length d were varied as well as the number of pole pairs. The corresponding values of torque and volume torque density when $p = 4$ have been calculated and the results are shown in Fig. 7-19-Fig. 7-24.
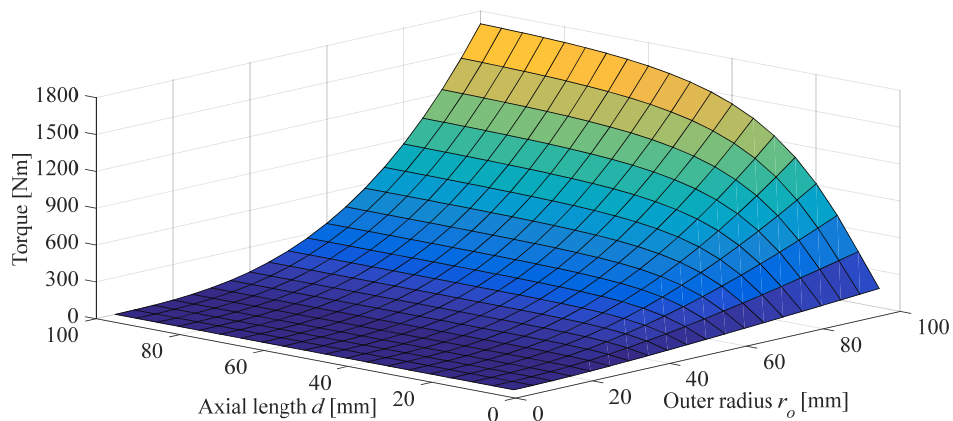
Fig. 7-19. Torque from the axial PMC.
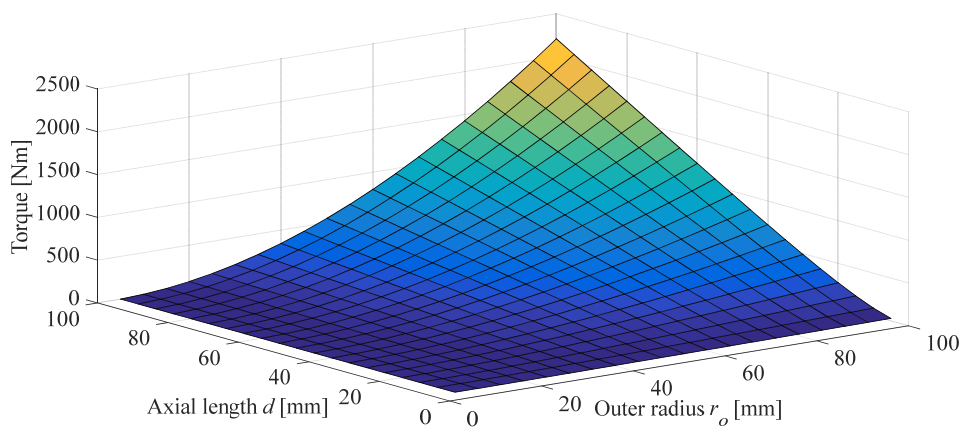
Fig. 7-20. Torque from the radial PMC.
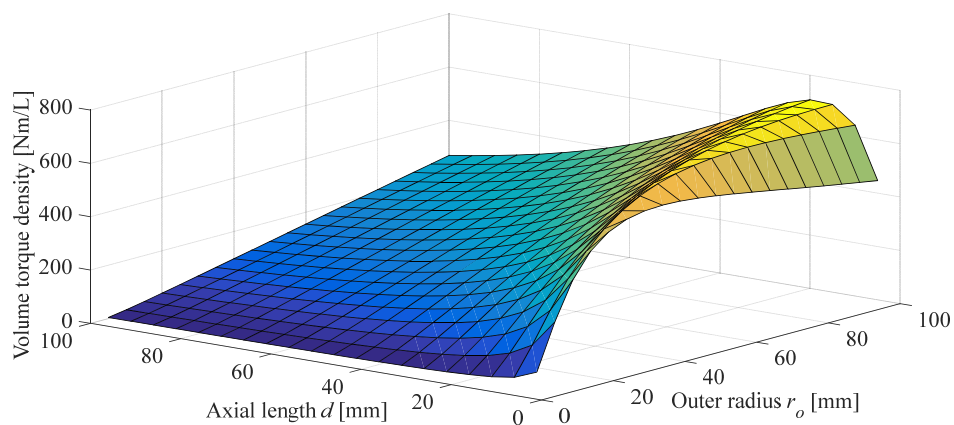
Fig. 7-21. Volume torque density from the axial PMC.
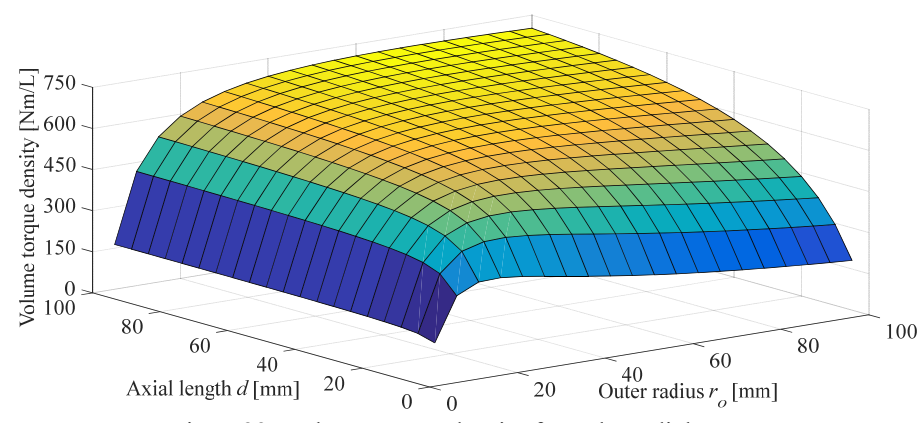
Fig. 7-22. Volume torque density from the radial PMC.
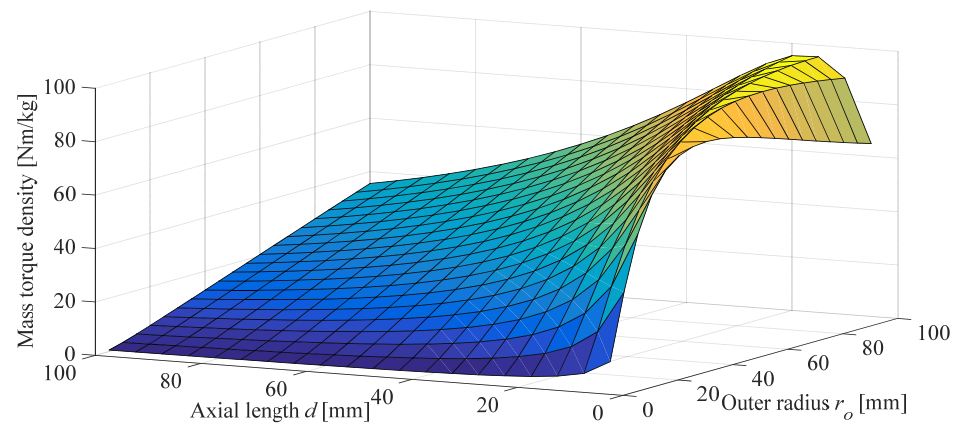
Fig. 7-23. Mass torque density from the axial PMC.

(b)
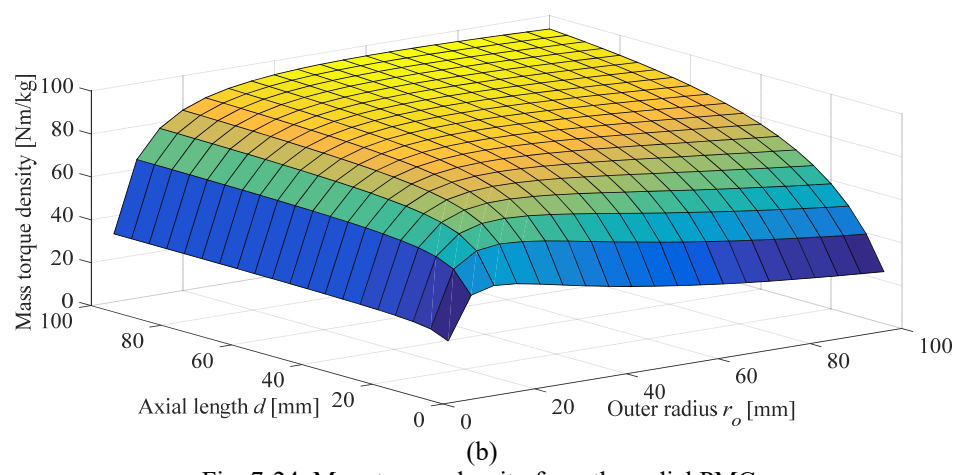
Fig. 7-24. Mass torque density from the radial PMC.

The torque ratio between the axial and radial PMCs is defined as

$$\gamma_T = \frac{T_A}{T_R} \tag{7.43}$$

Similarly, the volume torque density ratio γ_{T_v} and the mass torque density ratio γ_{T_m} are defined as

$$\gamma_{T_v} = \frac{T_{Av}}{T_{Rv}} \tag{7.44}$$

$$\gamma_{T_m} = \frac{T_{Am}}{T_{Rm}} \tag{7.45}$$

The contour plots of the torque density ratio are shown in Fig. 7-25-Fig. 7-27 when p was selected to be 4, 8 and 12. When $p = 4$, for the volume and mass torque densities, it can be noted that the axial and radial PMCs have a similar level of performance when d/r_o is close to 0.4. When d/r_o is larger than 0.5, the radial PMC will have a much better performance, while the axial PMC will have a significant better performance when d/r_o is smaller than 0.3.

When $p = 8$, for the volume and mass torque densities, it can be noted that the axial and radial PMCs have similar level of performance when d/r_o is close to 0.3. When d/r_o is larger than 0.4, the radial PMC will have a much better performance, while the axial PMC will have a significant better performance when d/r_o is smaller than 0.2.

When $p = 12$, for the volume and mass torque densities, it can be noted that the axial and radial PMCs have similar level of performance when d/r_o is close to 0.25. When d/r_o is larger than 0.35, the radial PMC will have a much better performance, while the axial PMC will have a significant better performance when d/r_o is smaller than 0.15.
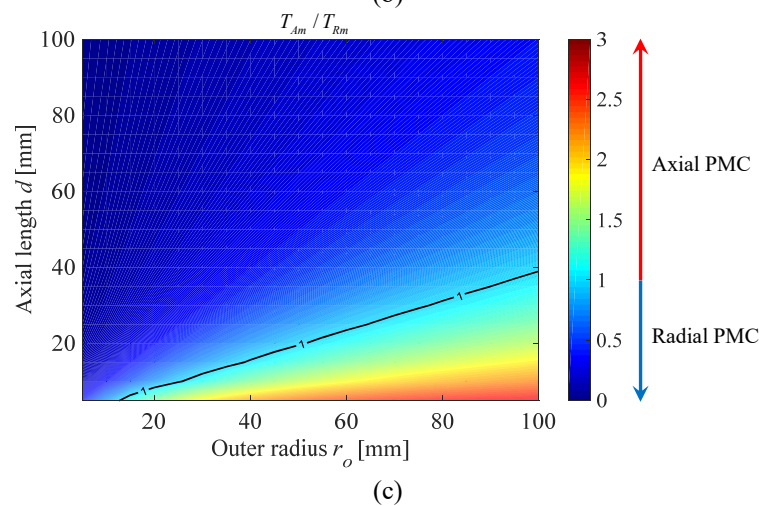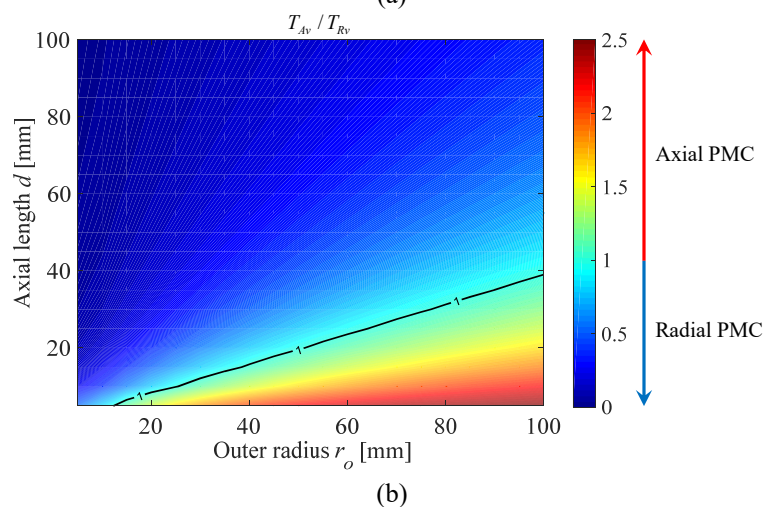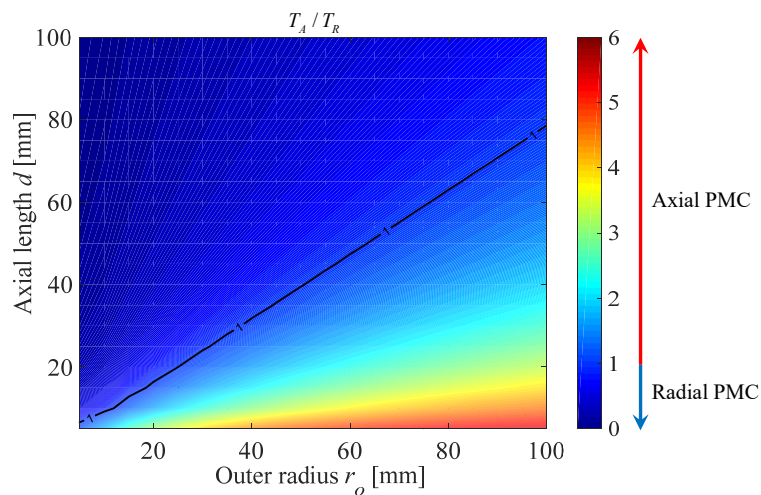
Fig. 7-25. (a) The torque ratio (b) the volume torque density ratio and (c) the mass torque density ratio between the axial and radial PMCs when $p = 4$.
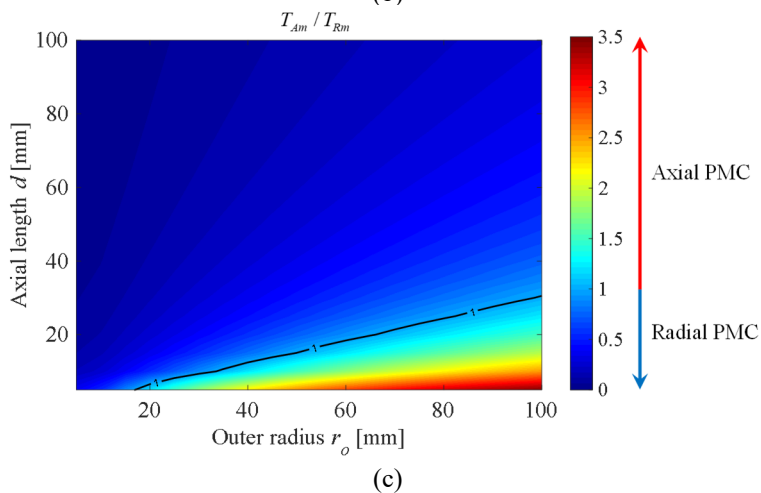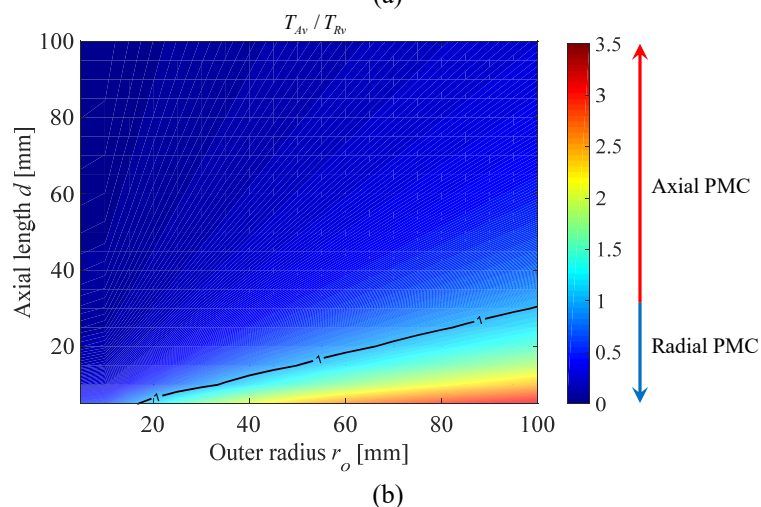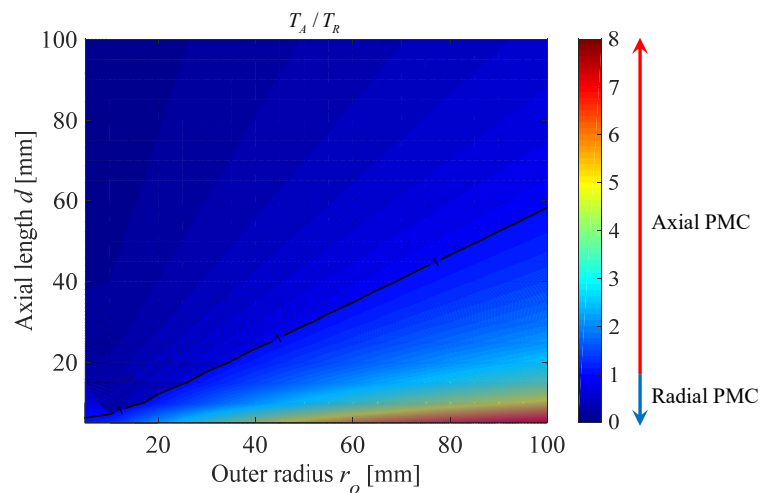
Fig. 7-26. (a) The torque ratio (b) the volume torque density ratio and (c) the mass torque density ratio between the axial and radial PMCs when $p = 8$.

T_A / T_R

T_{Av} / T_{Rv}

T_{Am} / T_{Rm}
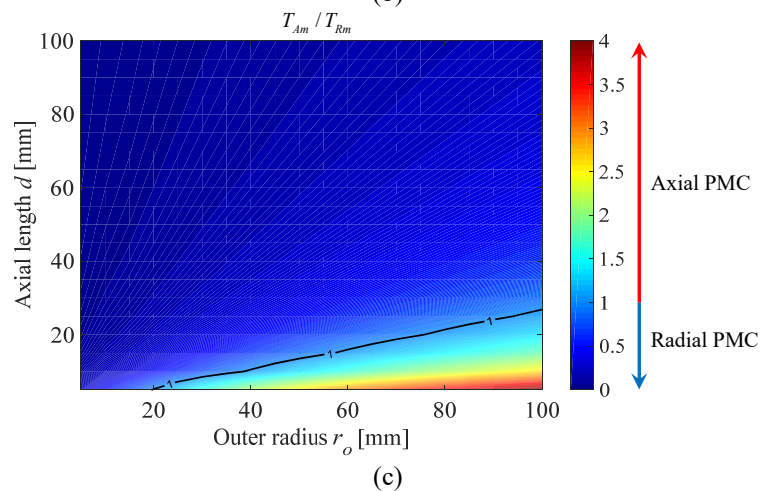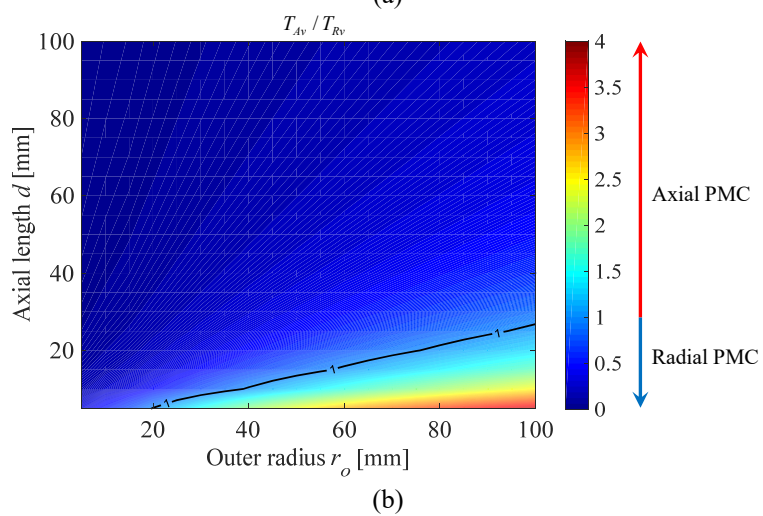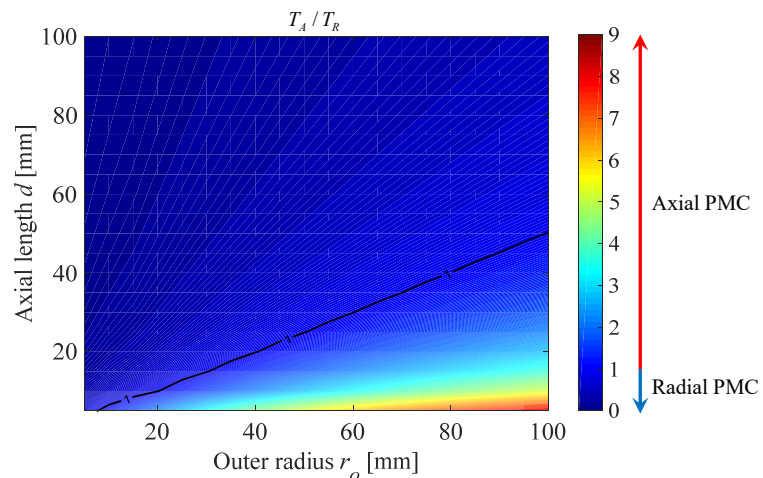
Fig. 7-27. (a) The torque ratio (b) the volume torque density ratio and (c) the mass torque density ratio between the axial and radial PMCs when $p = 12$.

In the above comparison, the axial and radial PMCs have the same sizes. Another comparison for the mass torque density has been done when they have different sizes. The axial length of the radial PMC was fixed at $d_r = r_o/2$ and the inner radius was selected so that the peak mass torque density condition could be reached. Also, the axial length and the inner radius of the axial PMC were selected so as to meet the peak mass torque density condition. The outer radius r_o and the pole pairs p were then varied. The comparison of the performance is shown in Fig. 7-28 and Fig. 7-29. When p is small, the axial and radial PMCs have similar levels of performance. While the radial PMC has a better performance when p is large.

(a)

(b)
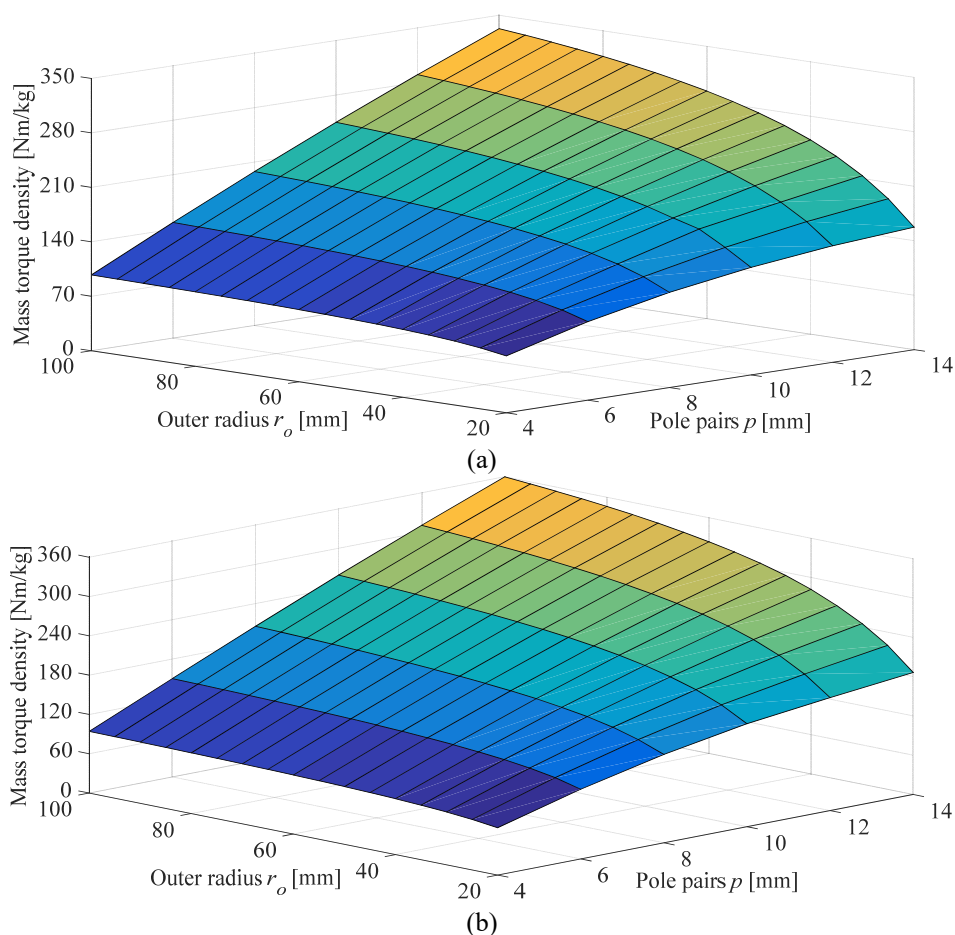
Fig. 7-28. Comparison for the mass torque density for the (a) axial PMC and (b) radial PMC when the peak mass torque density conditions are met.
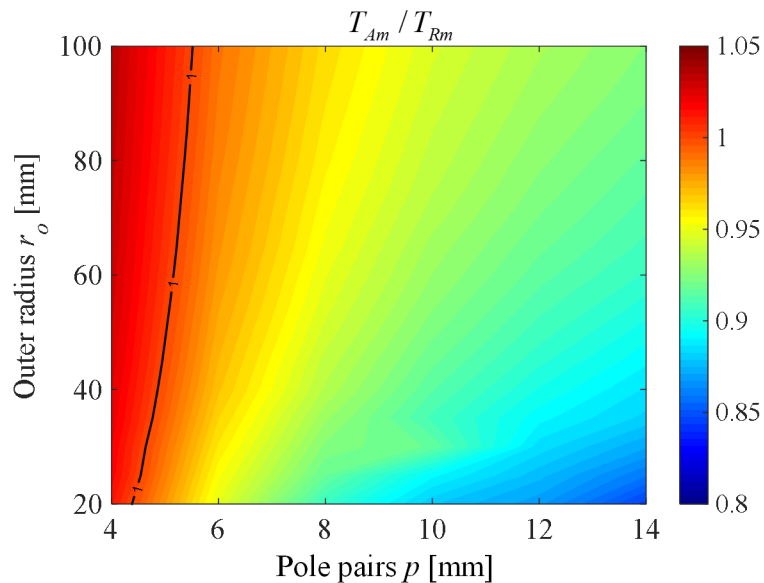
Fig. 7-29. The mass torque density ratio between the axial and radial PMCs.

7.6. CONCLUSION

An accurate 3-D analytical based model for the radial magnetic coupling has been developed by using the charge sheet approach. The analytical based model is much less time consuming. The results have been validated with 3-D FEA models. The performance of the radial PMC has been compared with the axial PMC. The axial PMC tends to only have a better performance when p and d/r_o are small while the radial PMC tends to have a better performance when p and d/r_o are large.

CHAPTER 8 : CONCLUSIONS AND FUTURE WORK

8.1. CONCLUSIONS

The operating principles of the CMG and cycloidal MG have been analyzed in detail. The performance of the flux focusing cycloidal MG and the MSMGs has been investigated and improved. The series connected MSMG has been assembled and tested. 3-D analytical based models for axial and radial magnetic couplings have been developed and the results have been compared with FEA models. The key contributions of this dissertation are:

- A new flux focusing cycloidal MG has been designed which is capable to achieve a 2-D calculated torque density and gear ratio of 260 Nm/L and -20:1 with a low torque ripple of 0.46 %. A parameter sweeping approach was used to obtain the peak torque density. The performance of the flux focusing cycloidal MG was compared with a FFCMG and a surface mounted cycloidal MG. It has been shown that the flux focusing cycloidal MG outperforms the other two designs.

- A nested 59:1 MSMG was designed and analyzed, and the flux concentration topology was used to achieve a high torque density as well as to get a low torque ripple. Different combinations of pole pairs were analyzed in order to reduce the torque ripple further. The final design had a 2-D calculated torque and torque density of 13.7 kNm and 424 Nm/L. This design was not constructed due to complexity of mechanically rotating 4 nested rotors.

- A series connected 59:1 MSMG was designed for the wind turbine and the performance was analyzed. In order to reduce the eddy current losses and to increase the efficiency, laminated steel parts were used and the magnets have been divided

into four segments for the stage 1 MG and five segments for the stage 2 MG along the axial direction so as to reduce the losses. For the stage 1 MG, the 3-D calculated active region torque density was 159 Nm/L and 45 Nm/kg, respectively. The 3-D calculated torque density of 135.Nm/L and 33 Nm/kg was obtained for the stage 2 MG. The experimental peak torque from stage 1 MG is 4.25 kNm. The measured torque densities for stage 1 MG are 141 Nm/L and 40 Nm/kg, respectively.

- Another series connected MSMG was also designed for a hydropower application. Different topologies were used in order to reduce the mechanical deflection and increase the efficiency. A stator was also incorporated inside the stage 2 MG with a fractional slot winding distribution. The 2-D calculated torque densities of the stage 1 MG and stage 2 MG were 371 Nm/L and 344 Nm/L, respectively.

- In order to obtain insight into the upper boundary of magnetic geared devices, 3-D analytical based models have been developed for both the axial and radial PMCs which can reduce the simulation time significantly. FEA models have been used to validate the analytical results. A good match has been achieved. Then the performance of the axial PMC has been compared with the radial PMC using the analytical based models.

8.2. FUTURE WORK

- More analysis of the stator design needs to be done to improve the performance of the magnetically geared generator.

- The impact of the axial segmented magnets needs to be considered when calculating the eddy current losses.

- A thermal analysis is needed to make sure the magnets are not overheated when the gearbox is running at a very high speed.

APPENDIX A : AN ALTERNATIVE CHARGE SHEET MODEL FOR THE AXIAL
MAGNETIC COUPLING

A.1. 2-D Model of an Ideal Axial Halbach Rotor

The model of an axial Halbach rotor is shown in Fig. A- 1. It has an inner radius, r_i,
and an outer radius, r_o. The axial length is d_a^I. The rotor magnets are magnetized along
the axial direction as shown in Fig. A- 1. The field created by the Halbach rotor is first
solved at radius r_c.

$$r_c = \frac{r_i + r_o}{2} \tag{A.1}$$

where r_i and r_o are the inner radius and outer radius of the rotor as shown in Fig. A- 1. It
is assumed that at the position $r = r_c$, the B_r field component is zero.

Therefore, at r_c, it is assumed that the magnetic field is fully described by

$$\mathbf{B}(r_c,\theta,z) = 0\hat{\mathbf{r}} + B_\theta(r_c,\theta,z)\hat{\boldsymbol{\theta}} + B_z(r_c,\theta,z)\hat{\mathbf{z}} \tag{A.2}$$
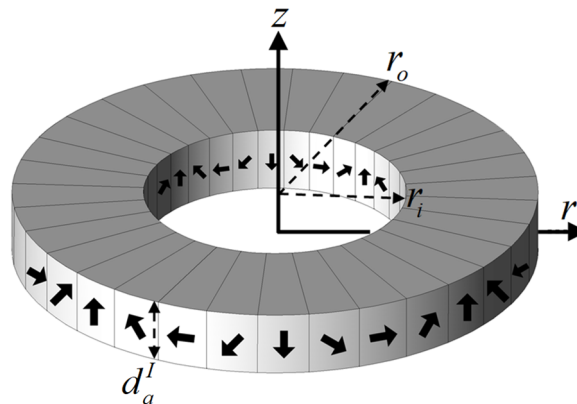
Fig. A- 1. An Axial 8-segment Halbach rotor with $p_I = 4$ pole pairs.

The field at r_c can therefore be solved by solving a 2-D problem in which the magnetic flux density exists on the surface of a cylinder as illustrated in Fig. A- 2. Region Ω_I and Ω_{III} are non-magnetic regions and region Ω_{II} contains the axial magnetized Halbach magnets. By solving for the field in this 2-D model, the magnetic charge value can be obtained to model the 3-D field.
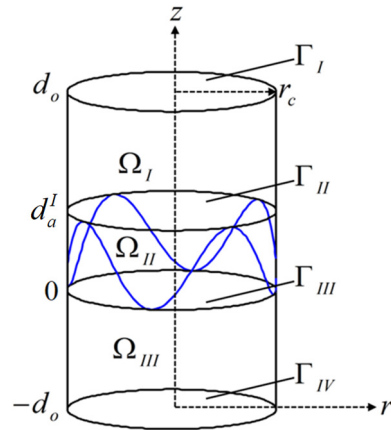
Fig. A- 2. Axial magnetic rotor model.

Maxwell's equations for a magnetostatic current-free problem are given by [77]:

$$\nabla \cdot \mathbf{B} = 0 \qquad\qquad \text{A.3}$$

$$\nabla \times \mathbf{H} = 0 \qquad\qquad \text{A.4}$$

The constitutive equation when a magnetization vector $\mathbf{M}$ is presented is given by:

$$\mathbf{B} = \mu_0 \mu_r \mathbf{H} + \mu_0 \mathbf{M} \qquad\qquad \text{A.5}$$

Substituting A.5 into A.3 and assuming linearity gives:

$$\mu_r \nabla \cdot \mathbf{H} = -\nabla \cdot \mathbf{M} \qquad\qquad \text{A.6}$$

From A.4 the magnetic field intensity is related to the magnetic scalar potential by:

$$\mathbf{H} = -\nabla \phi \qquad \text{A.7}$$

Substituting A.7 into A.6 yields

$$\frac{1}{r_c^2} \frac{\partial^2 \phi^{II}}{\partial \theta^2} + \frac{\partial^2 \phi^{II}}{\partial z^2} = \frac{\nabla \cdot \mathbf{M}}{\mu_r}, \text{ in } \Omega_{II} \qquad \text{A.8}$$

$$\frac{1}{r_c^2} \frac{\partial^2 \phi^{II}}{\partial \theta^2} + \frac{\partial^2 \phi^{II}}{\partial z^2} = -p_I M_f \frac{\cos(p_I \theta)}{\mu_r r_c}, \text{ in } \Omega_{II} \qquad \text{A.9}$$

where

$$M_f = c_1 M \qquad \text{A.10}$$

$$c_1 = 0.9745 \qquad \text{A.11}$$

$$M = B_m / \mu_0 \qquad \text{A.12}$$

In the non-magnetic regions $\mathbf{M} = 0$ and so A.8 becomes:

$$\frac{1}{r_c^2} \frac{\partial^2 \phi^{I}}{\partial \theta^2} + \frac{\partial^2 \phi^{I}}{\partial z^2} = 0, \text{ in } \Omega_{I} \qquad \text{A.13}$$

$$\frac{1}{r_c^2} \frac{\partial^2 \phi^{III}}{\partial \theta^2} + \frac{\partial^2 \phi^{III}}{\partial z^2} = 0, \text{ in } \Omega_{III} \qquad \text{A.14}$$

Utilizing A.7 the magnetic field intensity components are

$$H_\theta = -\frac{1}{r_c} \frac{\partial \phi}{\partial \theta} \qquad \text{A.15}$$

$$H_z = -\frac{\partial \phi}{\partial z}$$ A.16

The boundary conditions at boundary Γ_{II} is given by:

$$B_z^I(\theta, d_I) = B_z^{II}(\theta, d_a^I)$$ A.17

$$H_\theta^I(\theta, d_I) = H_\theta^{II}(\theta, d_a^I)$$ A.18

The boundary conditions at boundary Γ_{III} is given by:

$$B_z^{II}(\theta, 0) = B_z^{III}(\theta, 0)$$ A.19

$$H_\theta^{II}(\theta, 0) = H_\theta^{III}(\theta, 0)$$ A.20

The fields on the outer boundaries are assumed to be zero:

$$H_\theta^I(\theta, d_o) = 0$$ A.21

$$H_\theta^{III}(\theta, -d_o) = 0$$ A.22

Utilizing A.15 and A.16, A.17-A.20 can also be written as:

$$\left.\frac{\partial \phi^I(\theta, z)}{\partial z}\right|_{z=d_a^I} = \left.\frac{\mu_r \partial \phi^{II}(\theta, z)}{\partial z}\right|_{z=d_a^I} - \frac{c_1 B_m \cos(p\theta)}{\mu_0}, \quad \text{on } \Gamma_{II}$$ A.23

$$\left.\frac{\partial \phi^I(\theta, z)}{\partial \theta}\right|_{z=d_a^I} = \left.\frac{\partial \phi^{II}(\theta, z)}{\partial \theta}\right|_{z=d_a^I}, \quad \text{on } \Gamma_{II}$$ A.24

$$\left.\frac{\mu_r \partial \phi^{II}(\theta, z)}{\partial z}\right|_{z=0} - \frac{c_1 B_m \cos(p\theta)}{\mu_0} = \left.\frac{\partial \phi^{III}(\theta, z)}{\partial z}\right|_{z=0}, \quad \text{on } \Gamma_{III}$$ A.25

$$\left. \frac{\partial \phi^{II}(\theta,z)}{\partial \theta} \right|_{z=0} = \left. \frac{\partial \phi^{III}(\theta,z)}{\partial \theta} \right|_{z=0} , \quad \text{on } \Gamma_{III} \tag{A.26}$$

A.2. GENERAL SOLUTION

A.2.1. Outer Regions

Utilizing the separation of variables approach, we can define:

$$\phi^I(\theta,z) = \Theta(\theta)Z(z) \tag{A.27}$$

Then substituting A.27 into A.13 gives:

$$\frac{1}{r_c^2}Z(z)\frac{d^2\Theta}{d\theta^2} + \Theta(\theta)\frac{d^2Z}{dz^2} = 0 \tag{A.28}$$

Then A.28 can be rearranged:

$$\frac{d^2\Theta}{d\theta^2}\frac{1}{\Theta(\theta)} = -\frac{d^2Z}{dz^2}\frac{r_c^2}{Z(z)} = -k^2 \tag{A.29}$$

If $k > 0$, then

$$\frac{d^2\Theta}{d\theta^2} = -k^2\Theta(\theta) \tag{A.30}$$

The solution of A.30 is:

$$\Theta_k(\theta) = A\sin(k\theta) + C\cos(k\theta) \tag{A.31}$$

where k is an integer and A and C are constants. And from A.29

$$\frac{d^2Z}{dz^2} = \frac{k^2}{r_c^2}Z(z) \tag{A.32}$$

Solving A.32 one obtains:

$$Z_k(z) = De^{\frac{kz}{r_c}} + Fe^{-\frac{kz}{r_c}}$$ A.33

where D and F are constants. Substituting A.31 and A.33 into A.27 gives:

$$\phi_k^I(\theta, z) = \left[A\sin(k\theta) + C\cos(k\theta)\right]\left(De^{\frac{kz}{r_c}} + Fe^{-\frac{kz}{r_c}}\right), \quad \text{for } k > 0$$ A.34

If $k = 0$, then from A.30 and A.32:

$$\frac{d^2\Theta}{d\theta^2} = 0$$ A.35

$$\frac{d^2Z}{dz^2} = 0$$ A.36

Integrating A.35 and A.36 gives:

$$\Theta_0(\theta) = G\theta + K$$ A.37

$$Z_0(z) = Nz + U$$ A.38

Substituting A.37 and A.38 into A.27 gives:

$$\phi_0^I(\theta, z) = (G\theta + K)(Nz + U)$$ A.39

where G, K, N and U are constants. Combining A.34 and A.39 gives:

$$\phi_k^I(\theta, z) = (G\theta + K)(Nz + U) + \left[A\sin(k\theta) + C\cos(k\theta)\right]\left(De^{\frac{kz}{r_c}} + Fe^{-\frac{kz}{r_c}}\right), \quad \text{for } k \geq 0 \quad \text{A.40}$$

Due to A.4 the net flux crossing a (charge free) surface in region Γ_I must satisfy:

$$\int_V \nabla \cdot \mathbf{B} = \oint_S \mathbf{B} \cdot d\mathbf{s} = 0 \qquad \text{A.41}$$

where $d\mathbf{s} = \hat{\mathbf{z}}d\theta$. For the 2-D problem, A.41 becomes:

$$\int_0^{2\pi} B_z^I(\theta, d)d\theta = 0 \qquad \text{A.42}$$

Substituting A.40 into A.42 and utilizing A.16 one obtains:

$$\int_0^{2\pi} (GN\theta + KN) + \left[A\sin(k\theta) + C\cos(k\theta)\right]\left(D\frac{k}{r_c}e^{\frac{kz}{r_c}} - F\frac{k}{r_c}e^{-\frac{kz}{r_c}}\right)d\theta = 0 \quad \text{A.43}$$

Then A.43 reduces down to:

$$2\pi\left(\frac{GN\theta^2}{2} + KN\theta\right) = 0 \qquad \text{A.44}$$

Therefore, from A.44 and noting that the scalar potential along a circle is periodic and symmetric:

$$G = K = N = 0 \qquad \text{A.45}$$

By utilizing A.45 and noting that the field must decay as one moves away from the magnetic source A.40 reduces to

$$\phi^I(\theta, z) = \left[A\sin(k\theta) + C\cos(k\theta)\right]e^{-\frac{kz}{r_c}}, \text{ in } \Omega_I \qquad \text{A.46}$$

As the source field is created only by a cosine term, it can be noted that $k = p_I$ and so equation A.46 reduces further down to

$$\phi^I(\theta, z) = C\cos(p_I\theta)e^{\frac{-p_I(z-d_a^I)}{r_c}} \quad , \text{in } \Omega_I \qquad \text{A.47}$$

Similarly, the field in Ω_{III} must decay as $z \to -\infty$. Thus, the field in Ω_{III} is governed

$$\phi^{III}(\theta, z) = V\cos(p_I\theta)e^{\frac{p_I(z)}{r_c}} \quad , \text{in } \Omega_{III} \qquad \text{A.48}$$

where V is a constant.

A.2.2. Magnetic Region

The solution of A.9 is obtained by the superposition of the homogeneous solution (combine A.47 and A.48) and the particular solution [83]. With A.8:

$$\frac{1}{r_c^2}\frac{\partial^2\phi^{II}}{\partial\theta^2} + \frac{\partial^2\phi^{II}}{\partial z^2} = -\frac{p_I M_f}{\mu_r r_c}\cos(p_I\theta) \qquad \text{A.49}$$

Therefore, with A.47 and A.48, noting that source field is created only by a cosine term, the solution in Ω_{II} is:

$$\phi^{II}(\theta, z) = \cos(p_I\theta)\left\{ De^{\frac{p_I(z)}{r_c}} + Fe^{\frac{-p_I(z-d_a^I)}{r_c}} \right\} + W\cos(p_I\theta) \qquad \text{A.50}$$

From A.49:

$$W\frac{p_I^2}{r_c^2} = \frac{p_I M_f}{\mu_r r_c} \qquad \text{A.51}$$

Therefore, with A.10

$$W = \frac{c_1 B_m r_c}{\mu_0 \mu_r p_I} \tag{A.52}$$

Substituting A.52 into A.50 gives:

$$\phi^{II}(\theta, z) = \cos(p_I \theta) \left(De^{\frac{p_I(z)}{r_c}} + Fe^{\frac{-p_I(z - d_a^I)}{r_c}} \right) + \frac{c_1 B_m r_c}{\mu_0 \mu_r p_I} \cos(p_I \theta) \tag{A.53}$$

A.2.3. Flux Density Solutions

Substituting A.47 and A.50 into A.23 gives:

$$-C \frac{p_I}{r_c} \cos(p_I \theta) = D \frac{p_I \mu_r}{r_c} \cos(p_I \theta) e^{\frac{p_I d_a^I}{r_c}} - F \frac{p_I \mu_r}{r_c} \cos(p_I \theta) - \frac{c_1 B_m \cos(p_I \theta)}{\mu_0} \tag{A.54}$$

Substituting A.47 and A.50 into A.24 gives:

$$-p_I C \sin(p_I \theta) = -p_I D \sin(p_I \theta) e^{\frac{p_I d_a^I}{r_c}} - p_I F \sin(p_I \theta) - \frac{c_1 B_m r_c \sin(p_I \theta)}{\mu_0 \mu_r} \tag{A.55}$$

Substituting A.48 and A.50 into A.25 gives:

$$D \frac{p_I \mu_r}{r_c} \cos(p_I \theta) - F \frac{p_I \mu_r}{r_c} \cos(p_I \theta) e^{\frac{p_I d_a^I}{r_c}} - \frac{c_1 B_m \cos(p_I \theta)}{\mu_0} = V \frac{p_I}{r_c} \cos(p_I \theta) \tag{A.56}$$

Substituting A.48 and A.50 into A.26 gives:

$$-p_I D \sin(p_I \theta) - p_I F \sin(p_I \theta) e^{\frac{p_I d_a^I}{r_c}} - \frac{c_1 B_m r_c \sin(p_I \theta)}{\mu_0 \mu_r} = -p_I V \sin(p_I \theta) \tag{A.57}$$

Eliminating V with A.56 and A.57 gives:

$$D = \frac{p_I F(\mu_r + 1)e^{\frac{p_I d_a^I}{r_c}} + \frac{c_1 B_m r_c}{\mu_0 \mu_r}(\mu_r + 1)}{p_I(\mu_r - 1)}$$

A.58

Eliminating C with A.55 and A.56 gives:

$$D = \frac{p_I F(\mu_r - 1) + \frac{c_1 B_m r_c}{\mu_0 \mu_r}(\mu_r - 1)}{p_I(\mu_r + 1)e^{\frac{p_I d_a^I}{r_c}}}$$

A.59

Solving F with A.58-A.59 and noting that it is in Ω_I gives:

$$F = \frac{c_1 B_m r_c e^{-k_I}\left[-e^{k_I}(\mu_r + 1)^2 + e^{-k_I}(\mu_r - 1)^2\right]}{\mu_0 \mu_r p_I \left[e^{2k_I}(1 + \mu_r)^2 - e^{-2k_I}(\mu_r - 1)^2\right]}$$

A.60

where

$$k_I = p_I \frac{d_a^I}{2r_c} = p_I \frac{d_a^I}{r_o + r_i}$$

A.61

Substituting A.60 into A.59 gives:

$$D = \frac{c_1 B_m r_c}{\mu_0 \mu_r p_I} \frac{e^{-k_I}(\mu_r^2 - 1)(e^{k_I} - e^{-k_I})}{\left[e^{2k_I}(\mu_r + 1)^2 - e^{-2k_I}(\mu_r - 1)^2\right]}$$

A.62

Eliminating D with A.54 and A.55 gives:

$$C = \frac{2\mu_0 \mu_r p_I F + 2c_1 B_m r_c}{\mu_0(\mu_r + 1)p_I}$$

A.63

Substituting A.60 into A.63 gives:

$$C = \frac{2c_1 B_m r_c}{\mu_0 p_I} \frac{e^{k_I}(\mu_r+1)(e^{k_I}-e^{-k_I})}{\left[e^{2k_I}(\mu_r+1)^2 - e^{-2k_I}(\mu_r-1)^2\right]}$$

A.64

Substituting A.60 and A.62 into A.56 and simplifying it gives:

$$V = \frac{2c_1 B_m r_c}{\mu_0 p_I} \frac{e^{-k_I}(\mu_r-1)(e^{k_I}-e^{-k_I})}{\left[e^{2k_I}(1+\mu_r)^2 - e^{-2k_I}(\mu_r-1)^2\right]}$$

A.65

Similarly, in Ω_{III} the parameters are:

$$C' = \frac{2c_1 B_m r_c}{\mu_0 p_I} \frac{e^{-k_I}(\mu_r-1)(e^{-k_I}-e^{k_I})}{\left[e^{2k_I}(1+\mu_r)^2 - e^{-2k_I}(\mu_r-1)^2\right]}$$

A.66

$$D' = \frac{c_1 B_m r_c e^{-k_I}\left[e^{k_I}(\mu_r+1)^2 - e^{-k_I}(\mu_r-1)^2\right]}{\mu_0 \mu_r p_I\left[e^{2k_I}(1+\mu_r)^2 - e^{-2k_I}(\mu_r-1)^2\right]}$$

A.67

$$F' = \frac{c_1 B_m r_c}{\mu_0 \mu_r p_I} \frac{e^{-k_I}(\mu_r^2-1)(e^{-k_I}-e^{k_I})}{\left[e^{2k_I}(\mu_r+1)^2 - e^{-2k_I}(\mu_r-1)^2\right]}$$

A.68

$$V' = \frac{2c_1 B_m r_c}{\mu_0 p_I} \frac{e^{k_I}(\mu_r+1)(e^{-k_I}-e^{k_I})}{\left[e^{2k_I}(\mu_r+1)^2 - e^{-2k_I}(\mu_r-1)^2\right]}$$

A.69

If the field is directed upwards into region Ω_I, by substituting A.64 into, A.15, A.16 and A.47, and with the expression of B in region Ω_I will be given:

$$\mathbf{B}^I(\theta, r_c, z) = B_\theta^I(\theta, r_c, z)\hat{\theta} + B_z^I(\theta, r_c, z)\hat{z} = \left[\sin(p_I\theta)\hat{\theta} + \cos(p_I\theta)\hat{z}\right] B_{Am}^I e^{\frac{-p_I(z-d_a^I)}{r_c}}$$

A.70

where

$$B_{Am}^{I} = 2c_1 B_r \frac{(\mu_r + 1)e^{k_I}(e^{k_I} - e^{-k_I})}{e^{2k_I}(\mu_r + 1)^2 - e^{-2k_I}(\mu_r - 1)^2} \qquad \text{A.71}$$

Similarly, if the field is directed downwards into region Ω_{III}, the expression of B in region Ω_{III} will be given:

$$\mathbf{B}^{III}(\theta, r_c, z) = B_{\theta}^{III}(\theta, r_c, z)\hat{\mathbf{\theta}} + B_z^{III}(\theta, r_c, z)\hat{\mathbf{z}} = \left[\sin(p_I\theta)\hat{\mathbf{\theta}} + \cos(p_I\theta)\hat{\mathbf{z}}\right] B_{Am}^{III} e^{\frac{p_I(z)}{r_c}} \quad \text{A.72}$$

where

$$B_{Am}^{III} = 2c_1 B_r \frac{(\mu_r + 1)e^{k_I}(e^{k_I} - e^{-k_I})}{e^{2k_I}(\mu_r + 1)^2 - e^{-2k_I}(\mu_r - 1)^2} \qquad \text{A.73}$$

A.3. GOVERNING EQUATIONS FOR 3-D MODEL

The 2-D model in the previous section does not consider the radial length of the rotor. To take into account the field variation along the radial length an axial 3-D charge sheet model is developed as shown in Fig. A- 3. The charge sheet has an inner radius r_i an outer radius r_o and is located at vertical position:

$$z_I = d_a^I \qquad \text{A.74}$$
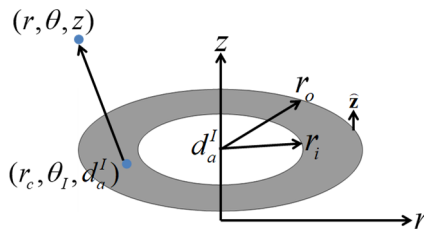
Fig. A- 3. 3-D axial charge sheet model.

The scalar potential due to single magnetic point charge located at (r_c, θ_I, z_I) is given by

$$\phi^I(r,\theta,z) = \frac{1}{4\pi\mu_0} \frac{\rho_{Am}^I}{R(r,r_c,\theta-\theta_I,z-d_a^I)} \qquad \text{A.75}$$

If the magnetic charge is distributed over a disc as shown in Fig. A-3 and the charge over the disc is described by charge function $\rho_{Am}^I(\theta_I)$ then from A.75 the magnetic scalar potential above the magnetic charge disc can be determined by evaluating

$$\phi^I(r,\theta,z) = \frac{1}{4\pi\mu_0} \int_0^{2\pi}\int_{r_i}^{r_o} \frac{\rho_{Am}^I(\theta_I)}{R(r,r_c,\theta-\theta_I,z-d_a^I)} r_c \, dr_c \, d\theta_I \qquad \text{A.76}$$

Substituting equation A.110 into A.76 one obtains:

$$\phi^I(r,\theta,z) = \frac{1}{4\pi\mu_0} \int_0^{2\pi}\int_{r_i}^{r_o} \frac{2B_{Am}^I \cos(p_I\theta_I)r_c}{\sqrt{r^2 + r_c^2 - 2rr_c\cos(\theta-\theta_I)+(z-d_a^I)^2}} \, dr_c \, d\theta_I \qquad \text{A.77}$$

Evaluating the integral along the radial direction yields:

$$\phi^I(r,\theta,z) = \frac{B_{Am}^I}{2\pi\mu_0} \int_0^{2\pi} \cos(p_I\theta_I)$$

$$\times \left\{ \begin{array}{l} -\sqrt{r^2 + r_i^2 + (z-d_a^I)^2 - 2rr_i\cos(\theta-\theta_I)} \\ +\sqrt{r^2 + r_o^2 + (z-d_a^I)^2 - 2rr_o\cos(\theta-\theta_I)} \\ -r\cos(\theta-\theta_I)\log\left[r_i - r\cos(\theta-\theta_I) + \sqrt{r^2 + r_i^2 + (z-d_a^I)^2 - 2rr_i\cos(\theta-\theta_I)}\right] \\ +r\cos(\theta-\theta_I)\log\left[r_o - r\cos(\theta-\theta_I) + \sqrt{r^2 + r_o^2 + (z-d_a^I)^2 - 2rr_o\cos(\theta-\theta_I)}\right] \end{array} \right\} d\theta_I \qquad \text{A.78}$$

Applying (6.46)-(6.47) gives:

$$\phi^I(r,\theta,z) = -\frac{B^I_{Am}}{2\pi\mu_0} \int\limits_{\theta}^{\theta-2\pi} \cos(p_I\theta - p_I\theta_d)$$

$$\times \left\{ \begin{array}{l} -\sqrt{r^2 + r_i^2 + (z-d_a^I)^2 - 2rr_i\cos(\theta_d)} + \sqrt{r^2 + r_o^2 + (z-d_a^I)^2 - 2rr_o\cos(\theta_d)} \\ -r\cos(\theta_d)\log\left[r_i - r\cos(\theta_d) + \sqrt{r^2 + r_i^2 + (z-d_a^I)^2 - 2rr_i\cos(\theta_d)} \right] \\ +r\cos(\theta_d)\log\left[r_o - r\cos(\theta_d) + \sqrt{r^2 + r_o^2 + (z-d_a^I)^2 - 2rr_o\cos(\theta_d)} \right] \end{array} \right\} d\theta_d \qquad \text{A.79}$$

The integration is over period 2π so we can write the integral period as:

$$\phi^I(r,\theta,z)$$
$$= \frac{B^I_{Am}}{2\pi\mu_0} \int\limits_0^{2\pi} \cos[(p_I(\theta-\theta_d)]\left[R(r,r_i,\theta_d,z-d_a^I) - R(r,r_o,\theta_d,z-d_a^I) \right] d\theta_d \qquad \text{A.80}$$
$$+ \frac{B^I_{Am}r}{2\pi\mu_0} \int\limits_0^{2\pi} \cos[(p_I(\theta-\theta_d)]\cos(\theta_d) \times \log\left[\frac{r_i - r\cos(\theta_d) + R(r,r_i,\theta_d,z-d_a^I)}{r_o - r\cos(\theta_d) + R(r,r_o,\theta_d,z-d_a^I)} \right] d\theta_d$$

A.4. TORQUE ON AXIAL MAGNETIC COUPLING

Consider the problem shown in Fig. A- 4 in which two axial Halbach rotors are placed next to each other and aligned along the z direction. The rotors are separated by a gap g. These two rotors have the same inner radius and outer radius. Rotor I has an axial length of d_a^I and p_I pole pairs while rotor II has an axial length of d_a^{II} and p_{II} pole pairs. In order to generate non-zero average torque, the two rotors' pole pairs must be equal. Therefore, it is assumed that pole rotors have the same number of pole pairs:

$$p = p_I = p_{II} \qquad \text{A.81}$$
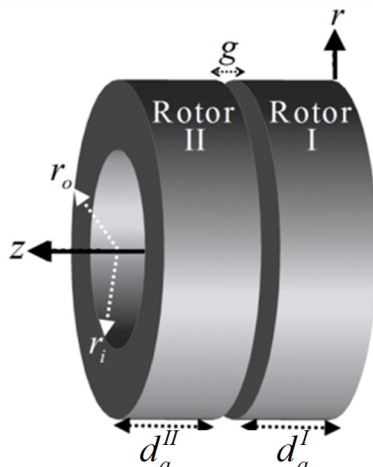
Fig. A- 4. The model of the axial Halbach rotor couplings.

The two Halbach rotors can be replaced with two equivalent magnetic charge discs as shown in Fig. A- 5.
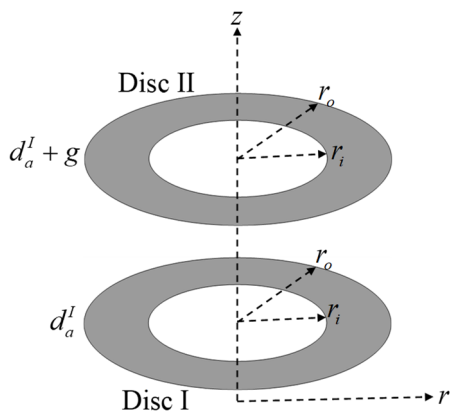
Fig. A- 5. Equivalent magnetic charge discs.

The magnetic charge function for rotor II is defined as

$$\rho_{Am}^{II}(\theta) = 2B_{Am}^{II}\cos(p_{II}\theta) \qquad \text{A.82}$$

where

$$B_{Am}^{II} = 2c_1 B_m \frac{(\mu_r + 1)e^{k_{II}}(e^{k_{II}} - e^{-k_{II}})}{e^{2k_{II}}(\mu_r + 1)^2 - e^{-2k_{II}}(\mu_r - 1)^2} \qquad \text{A.83}$$

$$k_{II} = p_{II} \frac{d_a^{II}}{r_o + r_i} \qquad \text{A.84}$$

The magnetic energy contained within the problem region can be computed from [79]:

$$W = \int_0^{2\pi} \int_{r_i}^{r_o} \rho_{Am}^{II}(\theta_{II}) \phi^I(r_{II}, \theta_{II}, z_{II}) r_{II} \, dr_{II} \, d\theta_{II} \qquad \text{A.85}$$

where ϕ^I is defined in A.80. The torque on the surface of rotor II can be calculated from the magnetic energy by:

$$T_A = \left. \frac{\partial W}{\partial \theta_{II}} \right|_{\phi^{II} = \text{constant}} \qquad \text{A.86}$$

$$
\begin{aligned}
T_A &= \int_0^{2\pi} \int_{r_i}^{r_o} \left. \frac{\partial \rho_{Am}^{II}(\theta)}{\partial \theta} \right|_{\theta = \theta_{II}} \phi^I(r_{II}, \theta_{II}, z_{II}) r_{II} \, dr_{II} \, d\theta_{II} \\
&= -2 B_{Am}^{II} p_{II} \int_0^{2\pi} \int_{r_i}^{r_o} \sin\left[p_{II}(\theta_{II} - \theta_t) \right] \phi^I(r_{II}, \theta_{II}, z_{II}) r_{II} \, dr_{II} \, d\theta_{II}
\end{aligned}
\qquad \text{A.87}
$$

where z_{II} is related to d_a^I by:

$$z_{II} = d_a^I + g \qquad \text{A.88}$$

By substituting A.80 into A.87, the expression of torque is obtained:

$$T_A(\theta_t) = \frac{B_{Am}^I B_{Am}^{II}}{\pi\mu_0} p_I \int_0^{2\pi}\int_{r_i}^{r_o}\{\int_0^{2\pi} \cos(p_I\theta_{II} - p_I\theta_d)[R(r_{II},r_o,\theta_d,z_{II},d_a^I) - R(r_{II},r_i,\theta_d,z_{II} - d_a^I)]d\theta_d\}$$

$$\times \sin\left[p_{II}(\theta_{II} - \theta_t)\right]r_{II}dr_{II}d\theta_{II}$$

$$+ \frac{B_{Am}^I B_{Am}^{II}}{\pi\mu_0} p_I \int_0^{2\pi}\int_{r_i}^{r_o}\{\int_0^{2\pi} \cos(p_I\theta_{II} - p_I\theta_d)\cos(\theta_d)\log\left[\frac{r_o - r_{II}\cos(\theta_d) + R(r_{II},r_o,\theta_d,z_{II} - d_a^I)}{r_i - r_{II}\cos(\theta_d) + R(r_{II},r_i,\theta_d,z_{II} - d_a^I)}\right]d\theta_d\}$$

$$\times \sin\left[p_{II}(\theta_{II} - \theta_t)\right]r_{II}^2dr_{II}d\theta_{II}$$

<div align="right">A.89</div>

As $\sin[p_{II}(\theta_{II} - \theta_o)]$ is not a function of θ_t, it can be put within the integral $d\theta_t$ and then we get:

$$T_A(\theta_t) = \frac{B_{Am}^I B_{Am}^{II}}{\pi\mu_0} p_I \int_0^{2\pi}\int_{r_i}^{r_o}\int_0^{2\pi} [R(r_{II},r_o,\theta_d,z_{II} - d_a^I) - R(r_{II},r_i,\theta_d,z_{II} - d_a^I)]r_{II}$$

$$\times \cos(p_I\theta_{II} - p_I\theta_d)\sin\left[p_{II}(\theta_{II} - \theta_t)\right]d\theta_d dr_{II}d\theta_{II}$$

$$+ \frac{B_{Am}^I B_{Am}^{II}}{\pi\mu_0} p_I \int_0^{2\pi}\int_{r_i}^{r_o}\int_0^{2\pi} \log\left[\frac{r_o - r_{II}\cos(\theta_d) + R(r_{II},r_o,\theta_d,z_{II} - d_a^I)}{r_i - r_{II}\cos(\theta_d) + R(r_{II},r_i,\theta_d,z_{II} - d_a^I)}\right]$$

$$\times \cos(p_I\theta_{II} - p_I\theta_d)\sin\left[p_{II}(\theta_{II} - \theta_t)\right]r_{II}^2\cos(\theta_d)d\theta_d dr_{II}d\theta_{II}$$

<div align="right">A.90</div>

Changing the order of integration and noting that for torque to be created $p_I = p_{II} = p$ we get:

$$T_A(\theta_t) = \frac{B_{Am}^I B_{Am}^{II}}{\pi\mu_0} p \int_0^{2\pi}\int_{r_i}^{r_o}\int_0^{2\pi} [R(r_{II},r_o,\theta_d,z_{II},d_a^I) - R(r_{II},r_i,\theta_d,z_{II} - d_a^I)]r_{II}$$

$$\times \cos(p\theta_{II} - p\theta_d)\sin\left[p(\theta_{II} - \theta_t)\right]d\theta_{II}dr_{II}d\theta_d$$

$$+ \frac{B_{Am}^I B_{Am}^{II}}{\pi\mu_0} p \int_0^{2\pi}\int_{r_i}^{r_o}\int_0^{2\pi} \log\left[\frac{r_o - r_{II}\cos(\theta_d) + R(r_{II},r_o,\theta_d,z_{II} - d_a^I)}{r_i - r_{II}\cos(\theta_d) + R(r_{II},r_i,\theta_d,z_{II} - d_a^I)}\right]$$

$$\times \cos(p\theta_{II} - p\theta_d)\sin\left[p(\theta_{II} - \theta_t)\right]r_{II}^2\cos(\theta_d)d\theta_{II}dr_{II}d\theta_d$$

<div align="right">A.91</div>

Defining

$$D(r_{II},r_o,r_i,\theta_d,z_{II})$$
$$= [R(r_{II},r_o,\theta_d,z_{II}-d_a^I)-R(r_{II},r_i,\theta_d,z_{II}-d_a^I)]r_{II}$$
$$+\cos(\theta_d)\log\left[\frac{r_o-r_{II}\cos(\theta_d)+R(r_{II},r_o,\theta_d,z_{II}-d_a^I)}{r_i-r_{II}\cos(\theta_d)+R(r_{II},r_i,\theta_d,z_{II}-d_a^I)}\right]r_{II}^2 \qquad \text{A.92}$$

Then the torque equation can be written as:

$$T_A(\theta_t)=\frac{B_{Am}^I B_{Am}^{II}}{\pi\mu_0}p\int_0^{2\pi}\int_{r_i}^{r_o}\int_0^{2\pi}\cos(p\theta_{II}-p\theta_d)\sin[p(\theta_{II}-\theta_t)]D(r_{II},r_o,r_i,\theta_d,z_{II})d\theta_{II}dr_{II}d\theta_d$$

A.93

where it can be seen that the sine and cosine terms are the only terms that are functions of θ_{II} we can use a trigonometric identity to write:

$$T_A(\theta_t)=\frac{B_{Am}^I B_{Am}^{II}}{2\pi\mu_0}p\int_0^{2\pi}\int_{r_i}^{r_o}\int_0^{2\pi}\sin(2p\theta_{II}-p\theta_t-p\theta_d)D(r_{II},r_o,r_i,\theta_d,z_{II})d\theta_{II}dr_{II}d\theta_d$$
$$+\frac{B_{Am}^I B_{Am}^{II}}{2\pi\mu_0}p\int_0^{2\pi}\int_{r_i}^{r_o}\int_0^{2\pi}\sin(p\theta_t-p\theta_d)D(r_{II},r_o,r_i,\theta_d,z_{II})d\theta_{II}dr_{II}d\theta_d$$

A.94

The first term will integrate to zero and the second terms integral with respect to θ_{II} is elementary. The torque equation reduces down to:

$$T_A(\theta_t)=\frac{B_{Am}^I B_{Am}^{II}}{\mu_0}p\int_0^{2\pi}\int_{r_i}^{r_o}\sin(p\theta_t-p\theta_d)D(r_{II},r_o,r_i,\theta_d,z_{II})dr_{II}d\theta_d \qquad \text{A.95}$$

Noting that

$$\sin(p\theta_t-p\theta_d)=\sin(p\theta_t)\cos(p\theta_d)-\sin(p\theta_d)\cos(p\theta_t) \qquad \text{A.96}$$

Equation A.95 can be written as:

$$T_A(\theta_t) = \sin(p\theta_t)\frac{B_{Am}^I B_{Am}^{II}}{\mu_0} p \int_0^{2\pi}\int_{r_i}^{r_o} \cos(p\theta_d)D(r_{II},r_o,r_i,\theta_d,z_{II})dr_{II}d\theta_d$$

$$-\cos(p\theta_t)\frac{B_{Am}^I B_{Am}^{II}}{\mu_0} p \int_0^{2\pi}\int_{r_i}^{r_o} \sin(p\theta_d)D(r_{II},r_o,r_i,\theta_d,z_{II})dr_{II}d\theta_d$$

A.97

Equation A.97 shows that the torque oscillation with angular position is governed by the term outside of the integral and the term within the integral must be the torque magnitude term. Substituting A.92 back into A.97 gives:

$$T_A(\theta_t) = \sin(p\theta_t)\frac{B_{Am}^I B_{Am}^{II}}{\mu_0} p \int_0^{2\pi}\int_{r_i}^{r_o} \cos(p\theta_d)[R(r_{II},r_o,\theta_d,z_{II}-d_a^I)-R(r_{II},r_i,\theta_d,z_{II}-d_a^I)]r_{II}dr_{II}d\theta_d$$

$$+\sin(p\theta_t)\frac{B_{Am}^I B_{Am}^{II}}{\mu_0} p \int_0^{2\pi}\int_{r_i}^{r_o} \cos(p\theta_d)\cos(\theta_d)\log\left[\frac{r_o-r_{II}\cos(\theta_d)+R(r_{II},r_o,\theta_d,z_{II}-d_a^I)}{r_i-r_{II}\cos(\theta_d)+R(r_{II},r_i,\theta_d,z_{II}-d_a^I)}\right]$$

$$\times r_{II}^2 dr_{II}d\theta_d$$

$$-\cos(p\theta_t)\frac{B_{Am}^I B_{Am}^{II}}{\mu_0} p \int_0^{2\pi}\int_{r_i}^{r_o} \sin(p\theta_d)[R(r_{II},r_o,\theta_d,z_{II}-d_a^I)-R(r_{II},r_i,\theta_d,z_{II}-d_a^I)]r_{II}dr_{II}d\theta_d$$

$$-\cos(p\theta_t)\frac{B_{Am}^I B_{Am}^{II}}{\mu_0} p \int_0^{2\pi}\int_{r_i}^{r_o} \sin(p\theta_d)\cos(\theta_d)\log\left[\frac{r_o-r_{II}\cos(\theta_d)+R(r_{II},r_o,\theta_d,z_{II}-d_a^I)}{r_i-r_{II}\cos(\theta_d)+R(r_{II},r_i,\theta_d,z_{II}-d_a^I)}\right]$$

$$\times r_{II}^2 dr_{II}d\theta_d$$

A.98

For the third term in A.98, the order of integral is changed and it can be integrated from $-\pi$ to π so then we get:

$$-\cos(p\theta_t)\frac{B_{Am}^I B_{Am}^{II}}{\mu_0} p \int_{r_i}^{r_o}\int_{-\pi}^{\pi} \sin(p\theta_d)[R(r_{II},r_o,\theta_d,z_{II}-d_a^I)-R(r_{II},r_i,\theta_d,z_{II}-d_a^I)]r_{II}d\theta_d dr_{II}$$

A.99

From (99), $R(r_{II},r_o,\theta_d,z_{II}-d_a^I)$ and $R(r_{II},r_i,\theta_d,z_{II}-d_a^I)$ are both even functions with respect to θ_d.

$\sin(p\theta_d)$ is an odd function, then $\sin(p\theta_d)[R(r_{II}, r_o, \theta_d, z_{II} - d_a^I) - R(r_{II}, r_i, \theta_d, z_{II} - d_a^I)]$

is also an odd function with respect to θ_d. Therefore, the integral in A.99 is zero. It is

similar for the fourth term in A.98 which is also zero. Then equation A.98 can be reduced

down to:

$$T_A(\theta_t) = \sin(p\theta_t) \frac{B_{Am}^I B_{Am}^{II}}{\mu_0} p \int_0^{2\pi} \int_{r_i}^{r_o} \cos(p\theta_d)[R(r_{II}, r_o, \theta_d, z_{II} - d_a^I) - R(r_{II}, r_i, \theta_d, z_{II} - d_a^I)]r_{II} dr_{II} d\theta_d$$

$$+ \sin(p\theta_t) \frac{B_{Am}^I B_{Am}^{II}}{\mu_0} p \int_0^{2\pi} \int_{r_i}^{r_o} \cos(p\theta_d) \cos(\theta_d)$$

$$\times \log\left[\frac{r_o - r_{II} \cos(\theta_d) + R(r_{II}, r_o, \theta_d, z_{II} - d_a^I)}{r_i - r_{II} \cos(\theta_d) + R(r_{II}, r_i, \theta_d, z_{II} - d_a^I)}\right] r_{II}^2 dr_{II} d\theta_d$$

A.100

Equation A.100 can be written as:

$$T_A(\theta_t) = \sin(p\theta_t) \frac{B_{Am}^I B_{Am}^{II}}{\mu_0} p \int_0^{2\pi} \int_{r_i}^{r_o} \{\cos(p\theta_d) R_2(r_{II}, r_o, r_i, \theta_d, z_{II} - d_a^I)$$

$$+ \cos(p\theta_d) \cos(\theta_d) r_{II} \log[R_3(r_{II}, r_o, r_i, \theta_d, z_{II} - d_a^I)]\} r_{II} dr_{II} d\theta_d$$

A.101

where

$$R_2(r_{II}, r_o, r_i, \theta_d, z_{II} - d_a^I) = R(r_{II}, r_o, \theta_d, z_{II} - d_a^I) - R(r_{II}, r_i, \theta_d, z_{II} - d_a^I)$$

A.102

$$R_3(r_{II}, r_o, r_i, \theta_d, z_{II} - d_a^I) = \frac{r_o - r_{II} \cos(\theta_d) + R(r_{II}, r_o, \theta_d, z_{II} - d_a^I)}{r_i - r_{II} \cos(\theta_d) + R(r_{II}, r_i, \theta_d, z_{II} - d_a^I)}$$

A.103

The charge sheet model from COMSOL is shown in Fig. A- 6 and the JMAG model is

shown in Fig. A- 7. The parameters used to create the analytical based, JMAG and

COMSOL models are shown in Table A- I.

(a)
         (b)
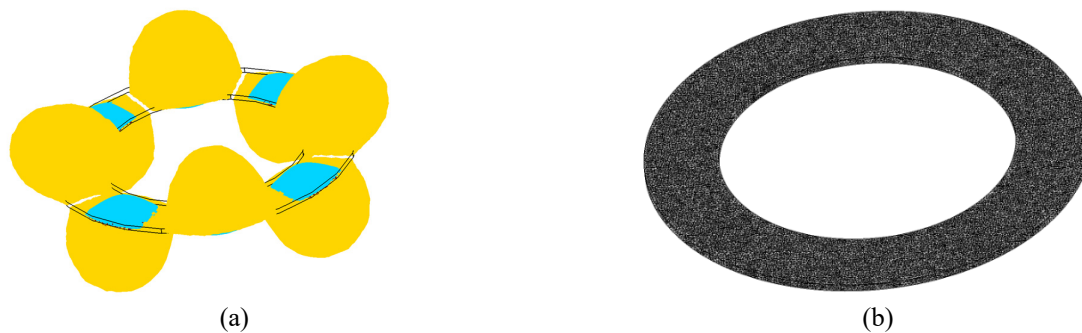
Fig. A- 6. (a) The COMSOL finite element analysis charge sheet model used to calculate the torque and (b) the model with mesh.

(a)
         (b)
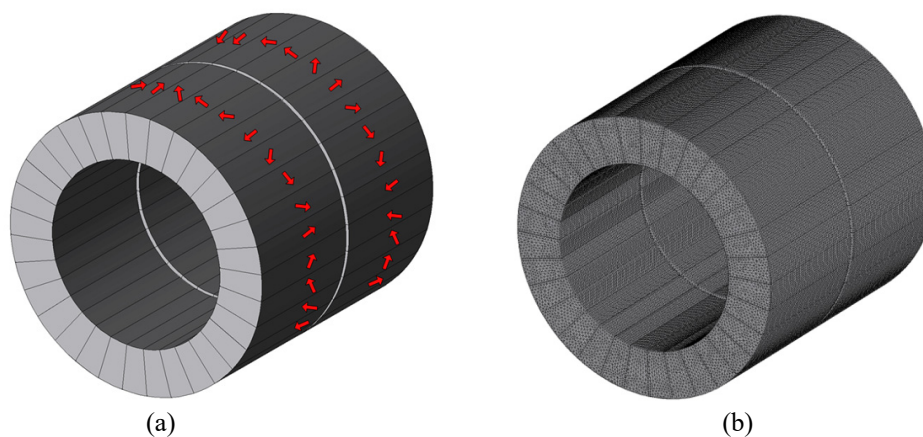
Fig. A- 7. (a) The 4 pole pairs JMAG model used to calculate the torque and (b) the model with mesh.

Table A- I. PARAMETERS FOR THE AXIAL COUPLING

Description	Value	Unit
Rotor I		
Outer radius, r_o	30	mm
Inner radius, r_i	20	mm
Axial length, d_a^I	30	mm
Pole pairs, $p_I = p$	4	-
Rotor II		
Outer radius, r_o	30	mm
Inner radius, r_i	20	mm
Axial length, d_a^{II}	30	mm
Pole pairs, $p_{II} = p$	4	-
Magnetic permeability, μ_r	1.05	-
Remnant flux density, B_m	1.27	T
Density of magnet, ρ_m	7600	kg/m^3
Air gap, g	1	mm

The torque obtained from equation A.101 is plotted and compared with the COMSOL charge sheet model and JMAG. The results are shown in Fig. A- 8 and Fig. A- 9.
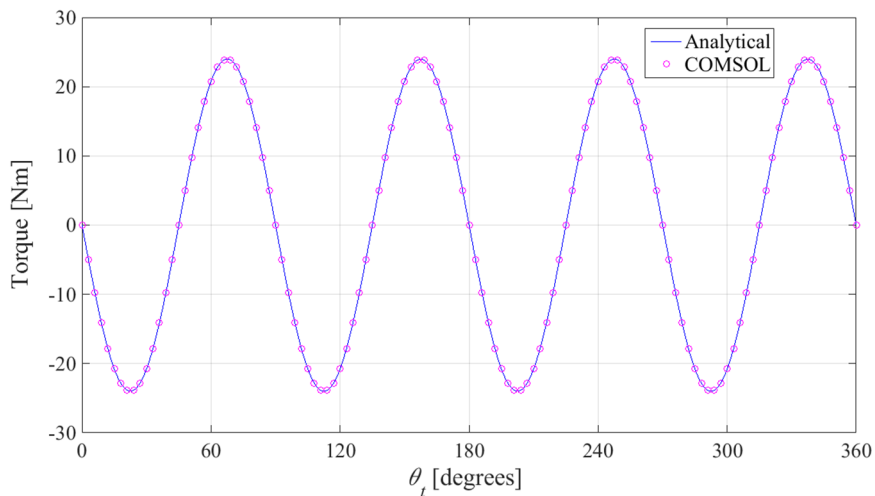
Fig. A- 8. Torque comparison between the analytical based model and the COMSOL charge sheet model.
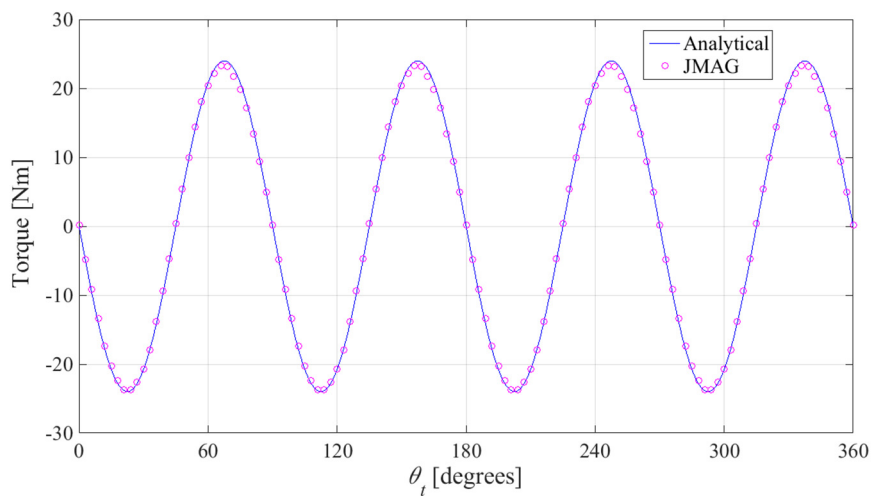
Fig. A- 9. Torque comparison between the analytical based model and the 3-D JMAG model.

The discrepancy plots between the analytical model and the FEA models are shown in Fig. A- 10 and Fig. A- 11.
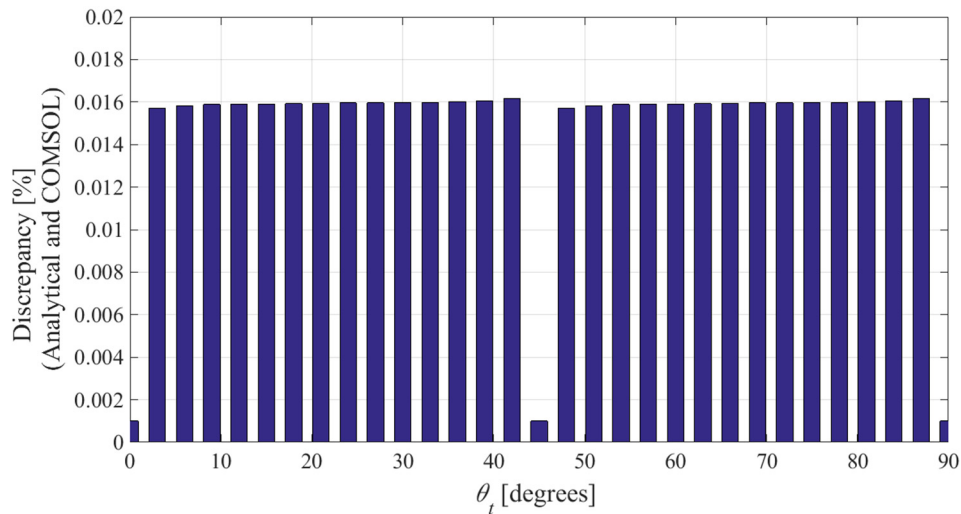
Fig. A- 10. Torque discrepancy between the analytical based model and the COMSOL charge sheet model.
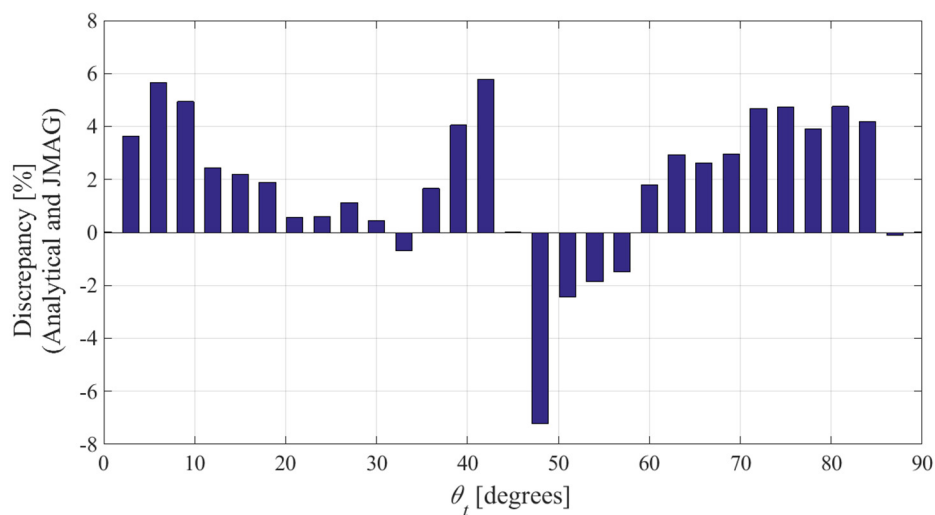
Fig. A- 11. Torque discrepancy between the analytical based model and the 3-D JMAG model.

Using the parameters shown in Table A- II, the axial length of the two rotors, d_a^I and d_a^{II} were both varied in order to understand how they influence mass and volumetric torque density. Fig. A- 12 and Fig. A- 13 shows the normalized mass and volumetric torque density for the case when $r_i = 20$ mm and the axial length d_a^I and d_a^{II} were varied.

It can be noted that for different outer radii, r_o the peak mass and volumetric torque density always occurs when

$$d_a = d_a^I = d_a^{II}$$ A.104

Therefore, in the following analysis the axial length of the inner and outer rotors is kept equal.
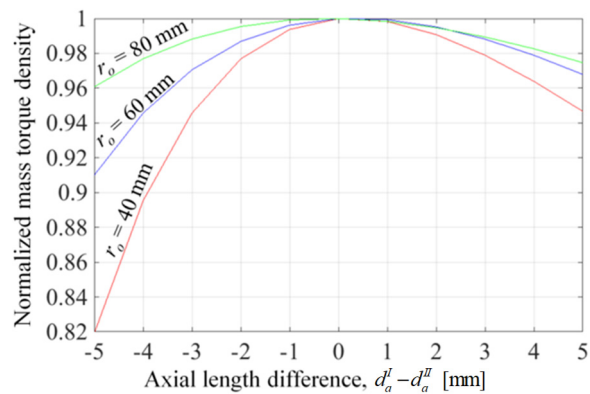
Fig. A- 12. Normalized mass torque density with different axial lengths when $r_i = 20$ mm and $p = 4$.
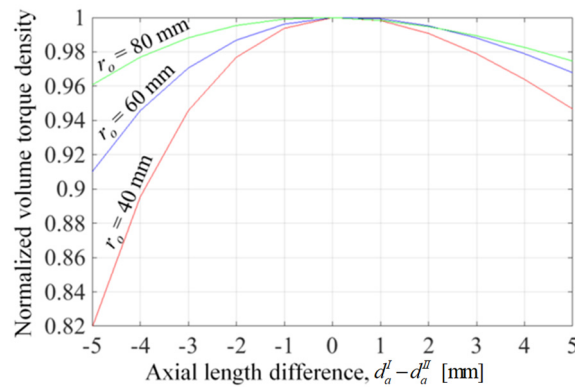
Fig. A- 13. Normalized volume torque density with different axial lengths when $r_i = 20$ mm and $p = 4$.

There are now five geometric variables that influence the torque, namely the inner radius, r_i, the outer radius, r_o, the axial length, d_a the pole pair number, p and the air gap, g. In order to understand how these variables impact the mass and volumetric torque

density a number of plots can be first made. To begin with if the outer radii r_o and pole pairs are fixed at r_o = 60 mm and p = 4, the variation of torque density when the inner radius, r_i and axial length, d_a are varied can be plotted. Such torque density plots for the case when g = 1 mm are shown in Fig. A- 14 and Fig. A- 15. It can be seen that the peak mass and volumetric torque density occur at the same location, (r_i, d_a) = (0, 10) mm. Further analysis showed that the peak mass and volume torque density always occurred when r_i = 0. By keeping r_i = 0 the peak torque density was determined for each d_a and the resultant plot for different values of r_o and p is shown in Fig. A- 18 for the case when the air gap g = 1 mm. Fig. A- 19 shows how the torque density changes when g = 10 mm. Fig. A- 16-Fig. A- 18 show that extremely high torque densities can be created at a very small air gaps and the torque density keeps increasing as the number of pole pairs increases. At the small air gap the torque density is more dependent on pole-number than outer radius. In contrast, Fig. A- 19 shows that with an increased air gap the outer radius has a bigger impact on torque density and the increased pole number decreases torque density (due to the larger flux leakage).
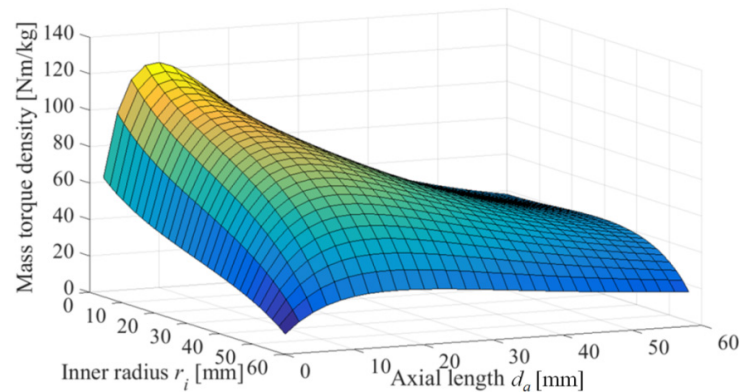
Fig. A- 14. Mass torque density as a function of axial length and inner radius when r_o = 60 mm, g = 1 mm, p = 4.
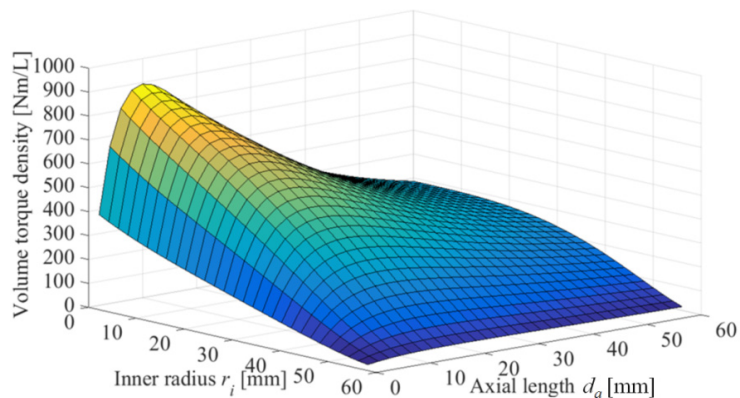
Fig. A- 15. Volumetric torque density as a function of axial length and inner radius when $r_o = 60$ mm, $g = 1$ mm, $p = 4$.
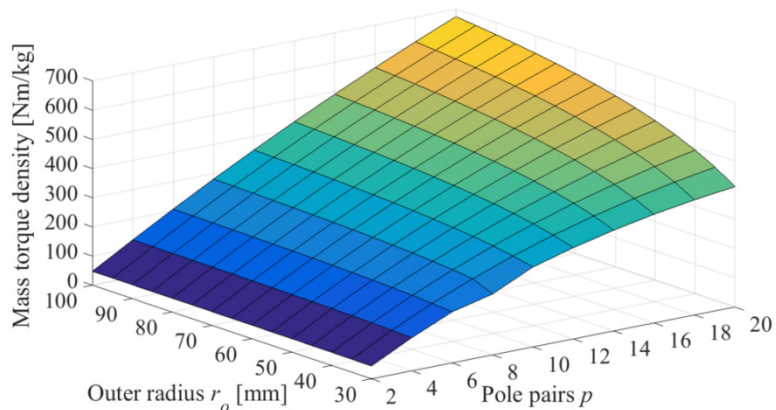
Fig. A- 16. Peak mass torque density as a function of outer radius r_o and pole pairs when $g = 1$ mm.
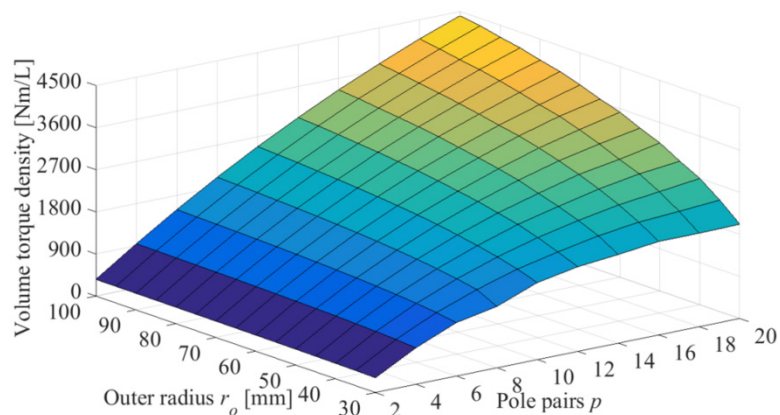
Fig. A- 17. Volumetric torque density as a function of outer radius r_o and pole pairs when $g = 1$ mm.
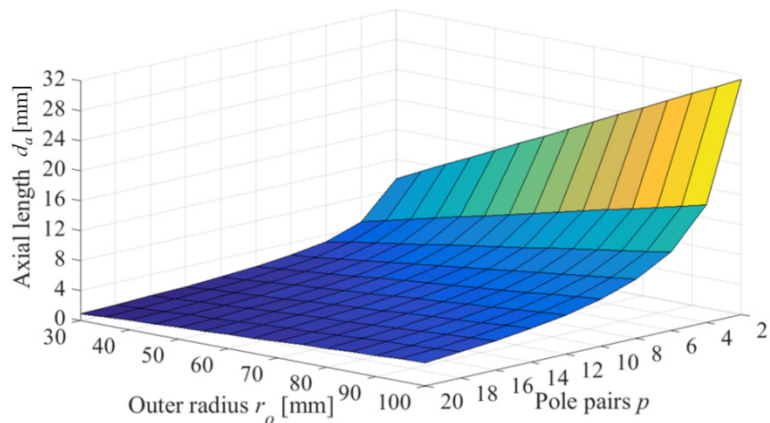
Fig. A- 18. Optimal axial length d_a as a function of outer radius r_o and pole pairs when $g = 1$ mm.

(a)

(b)
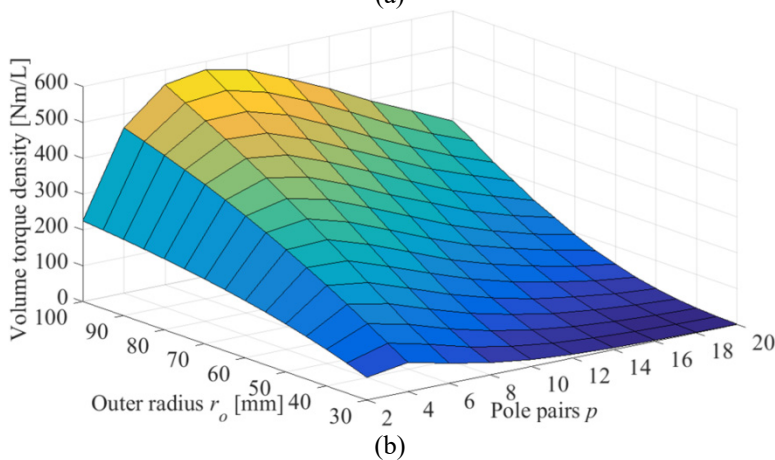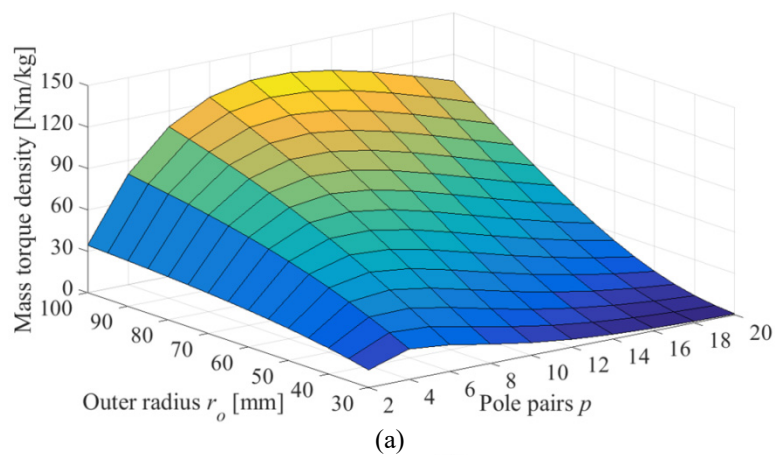
Fig. A- 19. (a) Peak mass torque density and (b) volumetric torque density as a function of outer radius r_o and pole pairs when $g = 10$ mm.

A.5. MAGNETIC FIELD SOLUTION OF THE HALBACH AXIAL ROTOR

The magnetic field solutions have been derived when the field is directed upwards. Substituting A.76 into A.7 the magnetic flux density created by the magnetic charge sheet disc is given by:

$$\mathbf{B}(r,\theta,z) = \frac{1}{4\pi} \int\limits_{0}^{2\pi} \int\limits_{r_i}^{r_o} \frac{\rho_{Am}^{I}(\theta_I)\mathbf{R}(r,r_c,\theta-\theta_I,z-d_a^I)}{R(r,r_c,\theta-\theta_I,z-d_a^I)^3} r_c dr_c d\theta_I \qquad \text{A.105}$$

The boundary interface condition at the location of the charge sheet is defined as [82]

$$\rho_{Am}^{I}(\theta_I) = B_z^{I} - B_z^{II} \qquad \text{A.106}$$

where superscripts *I* and *II* denote the field terms just above and below the magnetic charge sheet respectively. As all the external fields emanate from the charge sheet the field above and below the charge disc, at the boundary, must be equal and opposite:

$$B_z^{I} = -B_z^{II} \qquad \text{A.107}$$

Substituting A.107 into A.106 give [81]:

$$\rho_{Am}^{I}(\theta_I) = 2B_z^{I}(\theta,d_a^I) \qquad \text{A.108}$$

From A.70 the *z*-component magnetic flux density value at $(r, z) = (r_c, d_a^I)$ is

$$B_z^{I}(\theta,d_I) = B_{Am}^{I} \cos(p_I\theta)\hat{\mathbf{z}} \qquad \text{A.109}$$

Substituting A.109 into A.108 gives:

$$\rho_{Am}^{I}(\theta_I) = 2B_{Am}^{I} \cos(p_I\theta_I) \qquad \text{A.110}$$

Substituting A.110 and (6.27) into A.105 and noting that B_m^I is a constant one obtains:

$$B_r^I(r,\theta,z) = \frac{1}{2\pi} B_{Am}^I \int_0^{2\pi} \int_{r_i}^{r_o} \frac{1}{R(r,r_c,\theta-\theta_I,-d_a^I)^3} r_c [r-r_c\cos(\theta-\theta_I)]\cos(p_I\theta_I)dr_c d\theta_I \quad \text{A.111}$$

$$B_\theta^I(r,\theta,z) = \frac{1}{2\pi} B_{Am}^I \int_0^{2\pi} \int_{r_i}^{r_o} \frac{1}{R(r,r_c,\theta-\theta_I,z-d_a^I)^3} r_c^2 \sin(\theta-\theta_I)\cos(p_I\theta_I)dr_c d\theta_I \quad \text{A.112}$$

$$B_z^I(r,\theta,z) = \frac{1}{2\pi} B_{Am}^I (z-d_{a_I}) \int_0^{2\pi} \int_{r_i}^{r_o} \frac{1}{R(r,r_c,\theta-\theta_I,z-d_a^I)^3} r_c \cos(p_I\theta_I)dr_c d\theta_I \quad \text{A.113}$$

Integrating A.111-A.113 with Mathematica gives:

$$B_r^I = \frac{1}{2\pi} B_{Am}^I \int_0^{2\pi} \cos(p_I\theta_I) \times$$

$$\left\{ \begin{array}{l} \cos(\theta-\theta_I)\log[r_i - r\cos(\theta-\theta_I) + R(r,r_c,\theta-\theta_I,z-d_a^I)] \\ -\cos(\theta-\theta_I)\log[r_o - r\cos(\theta-\theta_I) + R(r,r_c,\theta-\theta_I,z-d_a^I)] \\ -\dfrac{r_i[r^2 + 2(z-d_a^I)^2]\cos(\theta-\theta_I) - r^2 r_i \cos 3(\theta-\theta_I) - 2r[r^2 + (z-d_a^I)^2]\sin^2(\theta-\theta_I)}{2[r^2\sin^2(\theta-\theta_I) + (z-d_a^I)^2]R(r,r_c,\theta-\theta_I,z-d_a^I)} \\ -\dfrac{r^2 r_o \cos 3(\theta-\theta_I) - r_o[r^2 + 2(z-d_a^I)^2]\cos(\theta-\theta_I) + 2r[r^2 + (z-d_a^I)^2]\sin^2(\theta-\theta_I)}{2[r^2\sin^2(\theta-\theta_I) + (z-d_a^I)^2]R(r,r_c,\theta-\theta_I,z-d_a^I)} \end{array} \right\} d\theta_I$$

A.114

$$B_\theta^I = \frac{1}{2\pi} B_{Am}^I \int_0^{2\pi} \cos(p_I\theta_I)\sin(\theta-\theta_I)$$

$$\times \left\{ \begin{array}{l} \dfrac{2\left[r_i(z-d_a^I)^2 - r^2 r_i \cos(2\theta-2\theta_I) + \left(r^3 + r(z-d_a^I)^2\right)\cos(\theta-\theta_I)\right]}{2\left[r^2\sin^2(\theta-\theta_I)+(z-d_a^I)^2\right]R(r,r_c,\theta-\theta_I,z-d_a^I)} \\[3ex] -\dfrac{2\left[r_o(z-d_a^I)^2 - r^2 r_o \cos(2\theta-2\theta_I) + \left(r^3 + r(z-d_a^I)^2\right)\cos(\theta-\theta_I)\right]}{2\left[r^2\sin^2(\theta-\theta_I)+(z-d_a^I)^2\right]R(r,r_c,\theta-\theta_I,z-d_a^I)} \\[3ex] +\log\dfrac{\left[r_o - r\cos(\theta-\theta_I) + R(r,r_c,\theta-\theta_I,z-d_a^I)\right]}{\left[r_i - r\cos(\theta-\theta_I) + R(r,r_c,\theta-\theta_I,z-d_a^I)\right]} \end{array} \right\} d\theta_I \qquad \text{A.115}$$

$$B_z^I = \frac{1}{2\pi}(z-d_a^I)B_{Am}^I \int_0^{2\pi} \cos(p_I\theta_I)$$

$$\times \left\{ \dfrac{\left[\dfrac{r^2+(z-d_a^I)^2 - rr_i\cos(\theta-\theta_I)}{R(r,r_i,\theta-\theta_I,z-d_a^I)} - \dfrac{r^2+(z-d_a^I)^2 - rr_o\cos(\theta-\theta_I)}{R(r,r_o,\theta-\theta_I,z-d_a^I)}\right]}{r^2\sin^2(\theta-\theta_I)+(z-d_a^I)^2} \right\} d\theta_I \qquad \text{A.116}$$

A.6. MAGNETIC FLUX DENSITY VALIDATION

In this section, the analytically calculated magnetic flux density is compared with a magnetic sheet FEA model developed in COMSOL and a 3-D JMAG model. Both of the models are shown in Fig. A- 20.

(a)   (b)
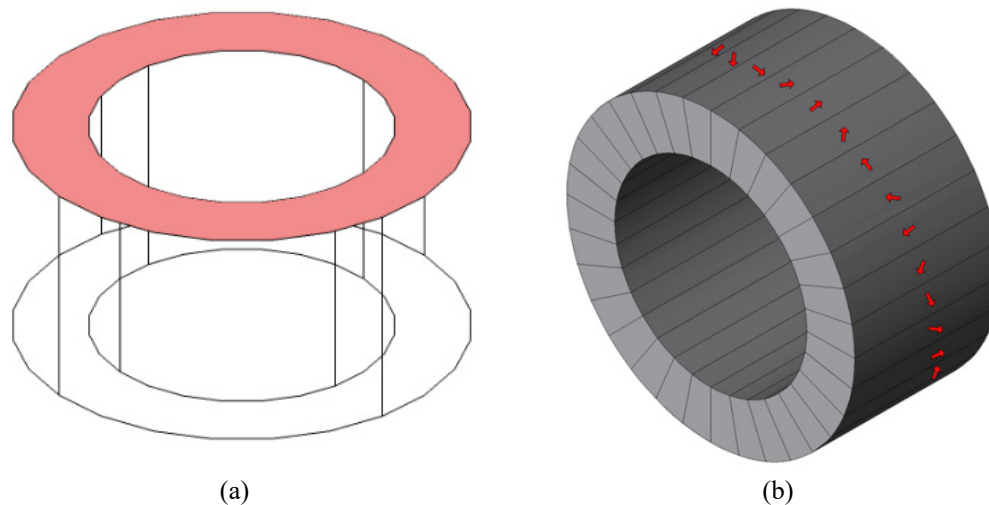
Fig. A- 20. The model used to calculate the magnetic flux density in (a) COMSOL and (b) JMAG.

The parameters and geometry for the axial Halbach rotor are shown in Fig. A- 21 and Table A- II. The flux density was compared at $(r, z) = (24.5, 35)$ mm with the JMAG 3-D model and the COMSOL magnetic charge sheet. The Simpson's rule was used to calculate the flux density in A.114-A.116. The comparison is shown in Fig. A- 22 and Fig. A- 23.
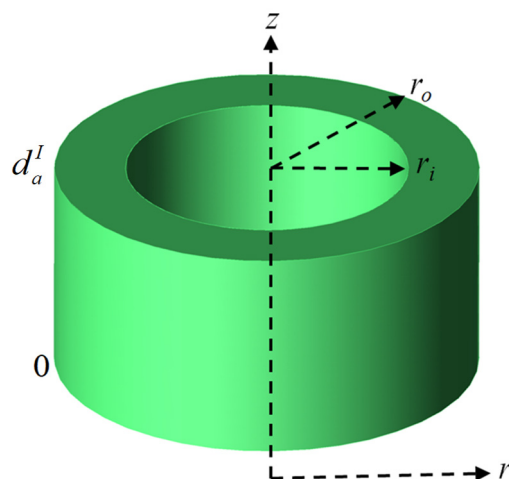
Fig. A- 21. The geometry of the axial rotor.

Table A- II. PARAMETERS FOR theAXIALROTOR

Description	Value	Unit
Outer radius, r_o	30	mm
Inner radius, r_i	20	mm
Axial length, d_a^l	30	mm
Pole pairs, $p_I=p$	4	-
Magnetic permeability, μ_r	1.05	-
Remnant flux density, B_m	1.27	T
Density of magnet, ρ_m	7600	kg/m³
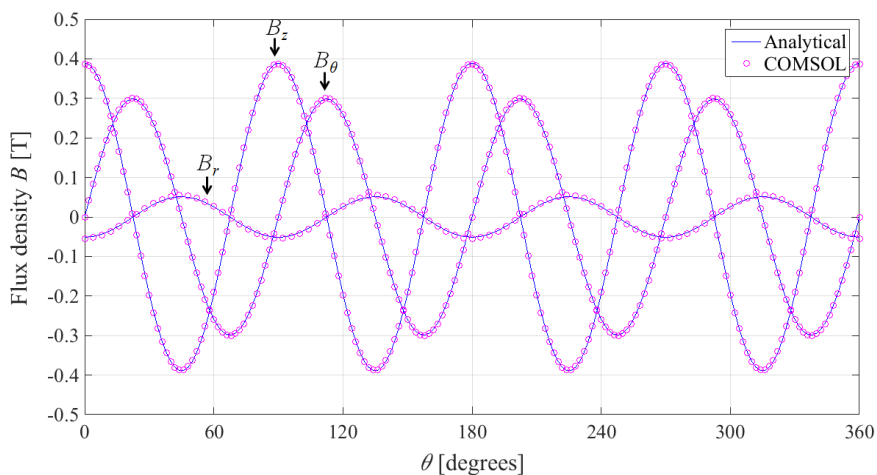
Fig. A- 22. Magnetic flux density comparison between the analytical based model and COMSOL charge sheet model.
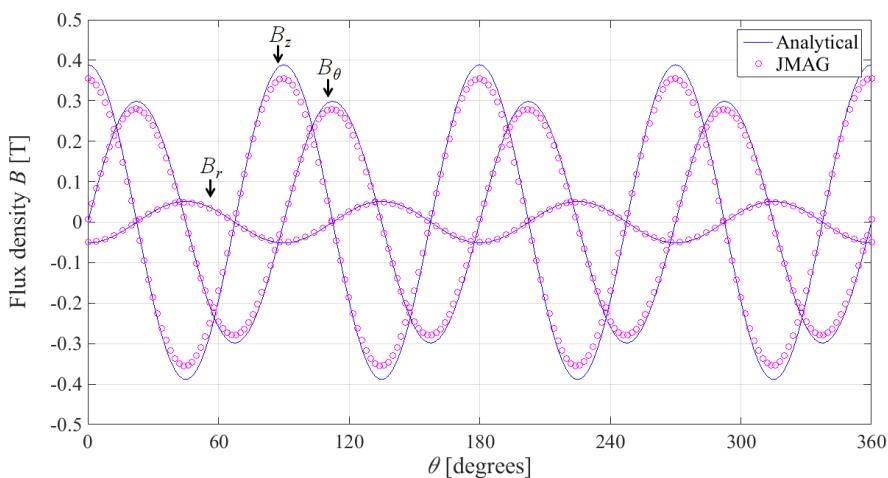
Fig. A- 23. Magnetic flux density comparison between the analytical based model and 3-D JMAG model.

From the result above, there is an acceptable discrepancy between the analytical based model and the JMAG model. And a good agreement is achieved between the analytical model and the COMSOL charge sheet model.

With A.80, the contour plot of the scalar potential at $z = 35$ mm is shown in Fig. A- 24.
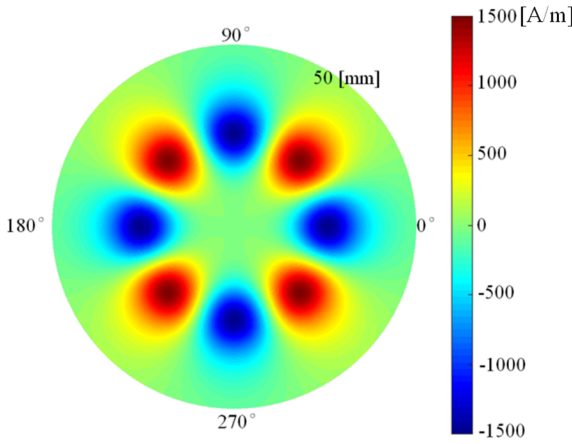
Fig. A- 24. Contour plot of the scalar potential.

The surface and contour plots of the magnetic flux density at $z = 35$ mm for the analytical and JMAG models are shown in Fig. A- 25–Fig. A- 30.

(a)   (b)
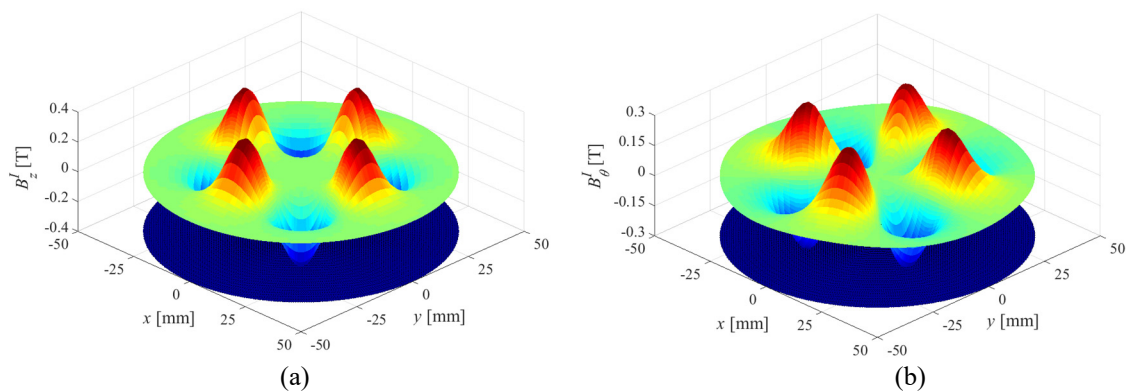
Fig. A- 25. Surface plot for (a) B_z and (b) B_θ from the analytical based model.

(a)   (b)
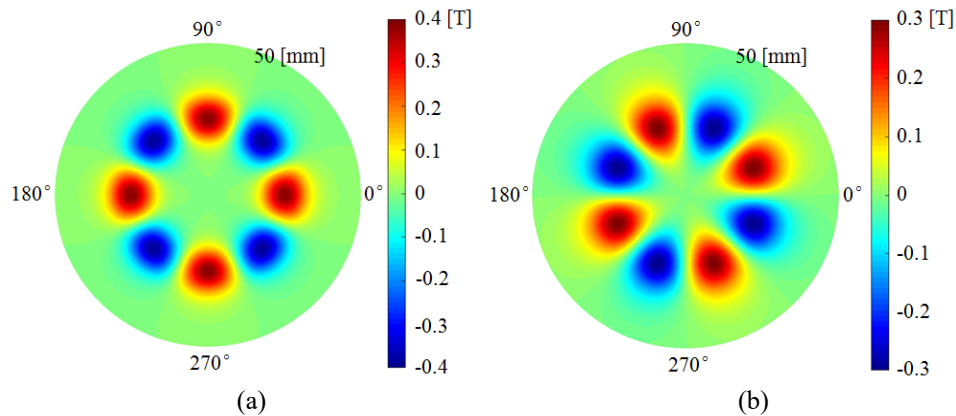
Fig. A- 26. Contour plot for (a) B_z and (b) B_θ from the analytical based model.

(a)   (b)
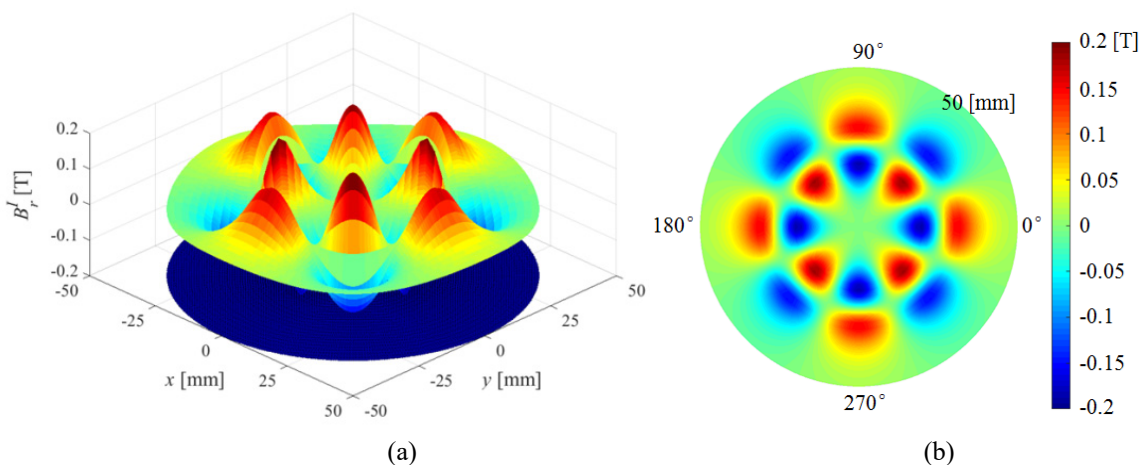
Fig. A- 27. (a) Surface plot and (b) Contour plot Br from the analytical based model.

(a)   (b)
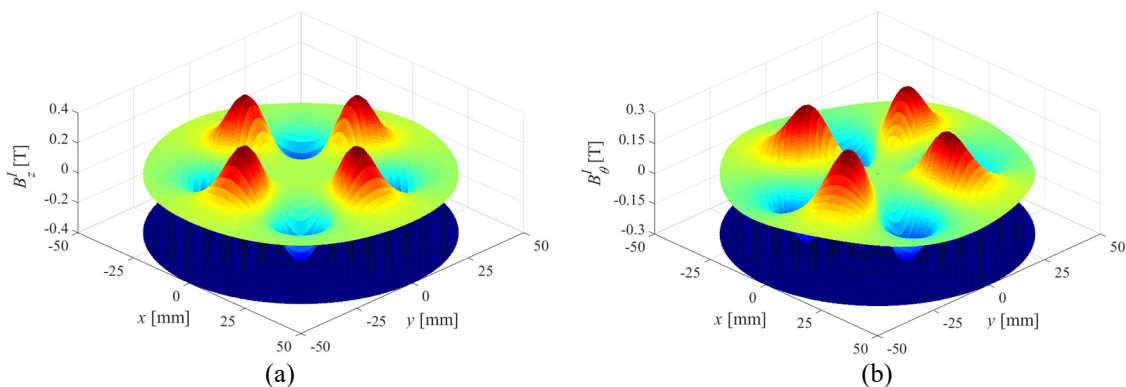
Fig. A- 28. Surface plot for (a) B_z and (b) B_θ from the 3-D JMAG model.
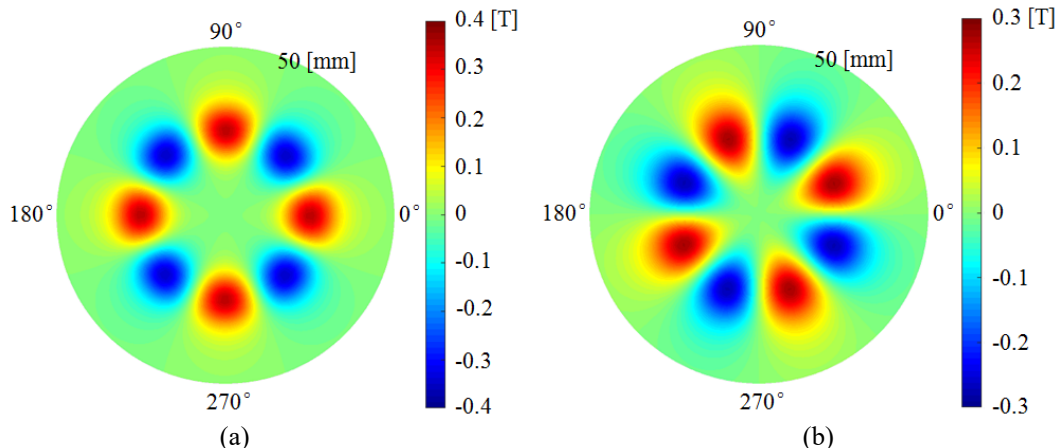
Fig. A- 29. Contour plot for (a) B_z and (b) B_θ from the 3-D JMAG model.
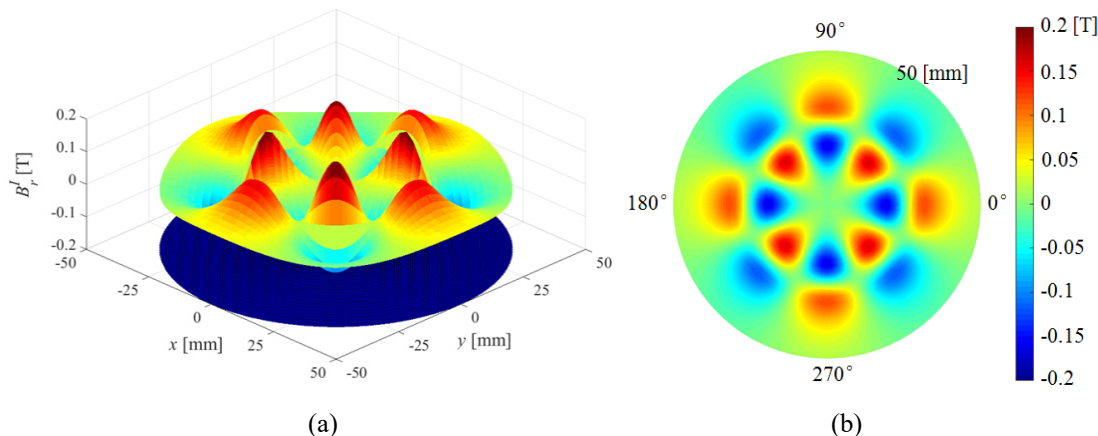
Fig. A- 30. (a) Surface plot and (b) Contour plot for B_r from the 3-D JMAG model.

However, for some other axial PMCs which have different dimensions, the results from the analytical based model are not matching quite well with those from FEA models. This is because the assumption in A.1 is not exactly accurate. The B_r value along the radial direction of a 8-segment 4 pole pairs Halbach rotor is plotted in JMAG as shown in Fig. A- 31 with d_a = 10 mm, r_o = 100 mm and r_i = 20 mm. Therefore, from equation A.1, r_c = 60 mm when B_r = 0. It can be seen from Fig. A- 31 that B_r = 0 occurs at r = 73.5 mm instead of $r = r_c$ =60 mm. Table A- III shows the comparison of the torque values with different inner radius r_i when r_o = 100 mm, p = 8, g = 1 mm and d_a = 10 mm. The

discrepancy is significant when r_i is small. Therefore, more work should be done to understand the discrepancy between the analytical based model and the FEA model so that the analytical model can be more accurate (chapter 6 discusses an improved model with good accuracy).
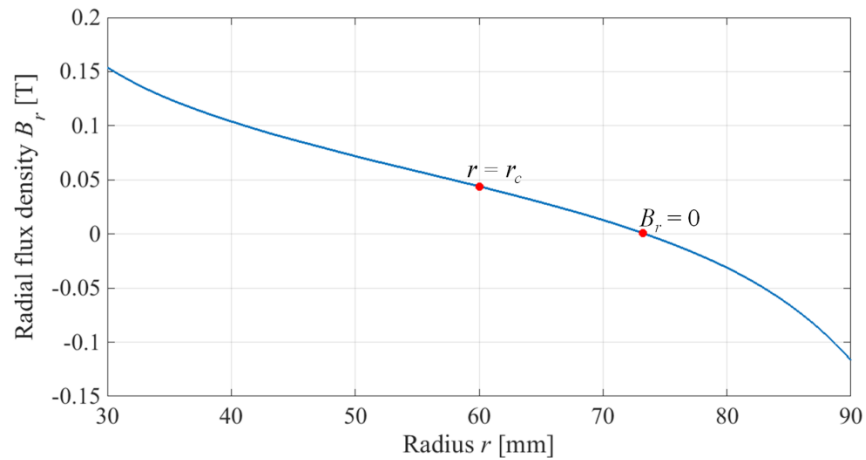
Fig. A- 31. B_r value along the radial direction.

Table A- III. COMPARISON OF TORQUE VALUES WITH DIFFERENT INNER RADIUS

r_i [mm]	Torque from JMAG [Nm]	Torque from the analytical based model [Nm]
10	933	1221
20	916	1119
30	880	1012
40	816	894
50	720	761
60	598	612
70	451	446
80	285	270
90	116	100

A.7. CONCLUSION

The benefit of using the presented approach lies in the ability to derive the 3-D field and torque equations from the magnitude of the field determined from a 2-D solution. It is shown that when the axial PMC air gap is small, the pole pairs have a larger influence

on the torque density. While when the axial PMC air gap is large, the outer radius has a more dominant influence on torque. The inner radius will yield to be zero for achieving peak mass and volume torque density. Therefore, the designing parameters of the axial PMC can be chosen easily with the torque density equation. However, the assumption in the analytical based model is not exactly accurate so that for some dimensions of the axial PMCs, the discrepancy is large. A more accurate model is discussed in chapter 6.

REFERENCES

[1]   D. T. Jelaska, *Gears and gear drives*. Wiley, 2012.

[2]   K. F. Martin, "The efficiency of involute spur gears," *ASME J. Mech. Des.,* vol. 103, pp. 160-169, 1981.

[3]   N. E. Anderson, "Design of spur gears for improved efficiency," *ASME J. Mech. Des.,* vol. 104, pp. 767-774, 1982.

[4]   P. M. Tlali, R. J. Wang, and S. Gerber, "Magnetic gear technologies: a review," in *2014 International Conference on Electrical Machines (ICEM)*, 2014, pp. 544-550.

[5]   *Nabtesco Corporation*. Available: https://www.nabtescomotioncontrol.

[6]   K. Atallah, S. D. Calverley, and D. Howe, "Design, analysis and realisation of a high-performance magnetic gear," *IEE Proceedings - Electric Power Applications,* vol. 151, no. 2, pp. 135-143, 2004.

[7]   K. Atallah and D. Howe, "A novel high-performance magnetic gear," *IEEE Transactions on Magnetics,* vol. 37, no. 4, pp. 2844-2846, 2001.

[8]   P. O. Rasmussen, T. O. Andersen, F. T. Jorgensen, and O. Nielsen, "Development of a high-performance magnetic gear," *IEEE Transactions on Industry Applications,* vol. 41, no. 3, pp. 764-770, 2005.

[9]   T. B. Martin, "Magnetic transmission," USA Patent 3,378,710, 1968.

[10]   K. Tsurumoto and S. Kikuchi, "A new magnetic gear using permanent magnet," *IEEE Transactions on Magnetics,* vol. 23, no. 5, pp. 3622-3624, 1987.

[11]   C. G. Armstrong, "Power transmitting device," USA Patent 687,292, 1901.

[12]   A. H. Neuland, "Apparatus for transmitting power," USA Patent 1,171,351, 1913.

[13]   H. Faus, "Magnet gearing," 2,243,555, 1941.

[14]   F. a. E. P., "Analytical analysis of magnetically coupled multipole cylinders," *Journal of Physics D: Applied Physics,* vol. 33, pp. 28-33, 2000.

[15]   F. T. Jorgensen, T. O. Andersen, and P. O. Rasmussen, "Two dimensional model of a permanent magnet spur gear," in *Fourtieth IAS Annual Meeting. Conference Record of the 2005 Industry Applications Conference, 2005.*, 2005, vol. 1, pp. 261-265 Vol. 1.

[16]   C. C. Huang, M. C. Tsai, D. G. Dorrell, and B. J. Lin, "Development of a magnetic planetary gearbox," *IEEE Transactions on Magnetics,* vol. 44, no. 3, pp. 403-412, 2008.

[17]   L. X. a. X. Zhu, "Magnetic planetary gear drive," *Proc. Inst. Mech. Eng., Part C,* vol. 223, 2009.

[18]   K. Davey, T. Hutson, L. McDonald, C. Ras, R. Weinstein, D. Parks, and R. P. Sawh, "Rotating cylinder planetary gear motor," *IEEE Transactions on Industry Applications,* vol. 52, no. 3, pp. 2253-2260, 2016.

[19]   R. J. Wang, A. Matthee, S. Gerber, and P. Tlali, "Calculation of torque performance of a novel magnetic planetary gear," *IEEE Magnetics Letters,* vol. 7, pp. 1-5, 2016.

[20]   F. T. Jorgensen, T. O. Andersen, and P. O. Rasmussen, "The cycloid permanent magnetic gear," *IEEE Transactions on Industry Applications,* vol. 44, no. 6, pp. 1659-1665, 2008.

[21] J. Rens, K. Atallah, S. D. Calverley, and D. Howe, "A novel magnetic harmonic gear," *IEEE Transactions on Industry Applications,* vol. 46, no. 1, pp. 206-212, 2010.

[22] R. Chicurel-Uziel, "Cycloidal Magnetic Gear Speed Reducer," *Modern Mechanical Engineering,* vol. 3, pp. 147-151, 2013.

[23] K. Li, J. Bird, J. Kadel, and W. Williams, "A flux-focusing cycloidal magnetic gearbox," *IEEE Transactions on Magnetics,* vol. 51, no. 11, pp. 1-4, 2015.

[24] K. Davey, L. McDonald, and T. Hutson, "Axial flux cycloidal magnetic gears," *IEEE Transactions on Magnetics,* vol. 50, no. 4, pp. 1-7, 2014.

[25] L. W. Chubb, "Vernier motor," USA Patent 1,894,979, 1931.

[26] K. Nakamura, M. Fukuoka, and O. Ichinokura, "Performance improvement of magnetic gear and efficiency comparison with conventional mechanical gear," *Journal of Applied Physics,* vol. 115, 17A314, 2014.

[27] L. Shah, A. Cruden, and B. W. Williams, "A variable speed magnetic gearbox using contra-rotating input shafts," *IEEE Transactions on Magnetics,* vol. 47, no. 2, pp. 431-438, 2011.

[28] X. Liu, K. T. Chau, J. Z. Jiang, and C. Yu, "Design and analysis of interior-magnet outer-rotor concentric magnetic gears," *Journal of Applied Physics* vol. 105, 07F101, 2009.

[29] L. Jian, K. T. Chau, Y. Gong, J. Z. Jiang, C. Yu, and W. Li, "Comparison of coaxial magnetic gears with different topologies," *IEEE Transactions on Magnetics,* vol. 45, no. 10, pp. 4526-4529, 2009.

[30] L. Jing, L. Liu, M. Xiong, and D. Feng, "Parameters analysis and optimization design for a concentric magnetic gear based on sinusoidal magnetizations," *IEEE Transactions on Applied Superconductivity,* vol. 24, no. 5, pp. 1-5, 2014.

[31] L. Brönn, R.-J. Wang, and M. J. Kamper, "Development of a shutter type magnetic gear," presented at the Proceedings of the 19th Southern African Univ. Power Eng. Conf., SAUPEC, Johannesburg, 2010.

[32] N. W. Frank and H. A. Toliyat, "Analysis of the concentric planetary magnetic gear with strengthened stator and interior permanent magnet inner rotor," *IEEE Transactions on Industry Applications,* vol. 47, no. 4, pp. 1652-1660, 2011.

[33] N. Niguchi and K. Hirata, "Cogging Torque Analysis of Magnetic Gear," *IEEE Transactions on Industrial Electronics,* vol. 59, no. 5, pp. 2189-2197, 2012.

[34] X. Li, K. T. Chau, M. Cheng, W. Hua, and Y. Du, "An improved coaxial magnetic gear using flux focusing," in *2011 International Conference on Electrical Machines and Systems*, 2011, pp. 1-4.

[35] K. K. Uppalapati, J. Z. Bird, D. Jia, J. Garner, and A. Zhou, "Performance of a magnetic gear using ferrite magnets for low speed ocean power generation," in *2012 IEEE Energy Conversion Congress and Exposition (ECCE)*, 2012, pp. 3348-3355.

[36] K. K. Uppalapati, W. B. Bomela, J. Z. Bird, M. D. Calvin, and J. D. Wright, "Experimental Evaluation of Low-Speed Flux-Focusing Magnetic Gearboxes," *IEEE Transactions on Industry Applications,* vol. 50, no. 6, pp. 3637-3643, 2014.

[37] K. K. Uppalapati, J. Z. Bird, J. Wright, J. Pitchard, M. Calvin, and W. Williams, "A magnetic gearbox with an active region torque density of 239Nm/L," in *2014 IEEE Energy Conversion Congress and Exposition (ECCE)*, 2014, pp. 1422-1428.

[38]   K. Uppalapati, J. Kadel, J. Wright, K. Li, W. Williams, and J. Z. Bird, "A low assembly cost coaxial magnetic gearbox," in *2016 IEEE 2nd Annual Southern Power Electronics Conference (SPEC)*, 2016, pp. 1-6.

[39]   T. Fujita, Y. Ando, K. Nagaya, M. Oka, T. Todaka, M. Enokizono, and K. Sugiura, "Surface magnet gears with a new magnet arrangement and optimal shape of stationary pole pieces," *Journal of Electromagnetic Analysis and Applications,* vol. 5, pp. 243-249, 2013.

[40]   A. Matthee, S. Gerber, and R.-J. Wang, "A high performance concentric magnetic gear," presented at the Proceedings Southern African Universities Power Engineering Conference, Johannesburg, South Africa, 2015.

[41]   W. N. Fu and L. Li, "Optimal design of magnetic gears with a general pattern of permanent magnet arrangement," *IEEE Transactions on Applied Superconductivity,* vol. 26, no. 7, pp. 1-5, 2016.

[42]   Y. Chen, W. N. Fu, and W. Li, "Performance analysis of a novel triple-permanent-magnet- excited magnetic gear and its design method," *IEEE Transactions on Magnetics,* vol. 52, no. 7, pp. 1-4, 2016.

[43]   D. Som, K. Li, J. Kadel, J. Wright, S. Modaresahmadi, J. Z. Bird, and W. William, "Analysis and testing of a coaxial magnetic gearbox with flux concentration halbach rotors," *IEEE Transactions on Magnetics,* vol. 53, no. 11, pp. 1-6, 2017.

[44]   S. Mezani, K. Atallah, and D. Howe, "A high-performance axial-field magnetic gear," *Journal of Applied Physics,* vol. 99, 08R303, 2006.

[45]   M. Johnson, A. Shapoury, P. Boghrat, M. Post, and H. A. Toliyat, "Analysis and development of an axial flux magnetic gear," in *2014 IEEE Energy Conversion Congress and Exposition (ECCE)*, 2014, pp. 5893-5900.

[46]   M. Johnson, M. C. Gardner, and H. A. Toliyat, "Analysis of axial field magnetic gears with Halbach arrays," in *2015 IEEE International Electric Machines & Drives Conference (IEMDC)*, 2015, pp. 108-114.

[47]   V. M. Acharya, M. Calvin, and J. Z. Bird, "A low torque ripple flux focusing axial magnetic gear," in *7th IET International Conference on Power Electronics, Machines and Drives (PEMD 2014)*, 2014, pp. 1-6.

[48]   Y. Li, J. Xing, K. Peng, and Y. Lu, "Principle and simulation analysis of a novel structure magnetic gear," in *2008 International Conference on Electrical Machines and Systems*, 2008, pp. 3845-3849.

[49]   W. Bomela, J. Z. Bird, and V. M. Acharya, "The performance of a transverse flux magnetic gear," *IEEE Transactions on Magnetics,* vol. 50, no. 1, pp. 1-4, 2014.

[50]   D. Zhu, F. Yang, Y. Du, F. Xiao, and Z. Ling, "An axial-field flux-modulated magnetic gear," *IEEE Transactions on Applied Superconductivity,* vol. 26, no. 4, pp. 1-5, 2016.

[51]   S. Peng, W. N. Fu, and S. L. Ho, "A novel triple-permanent-magnet-excited hybrid-flux magnetic gear and its design method using 3-D finite element method," *IEEE Transactions on Magnetics,* vol. 50, no. 11, pp. 1-4, 2014.

[52]   X. Yin, P. D. Pfister, and Y. Fang, "A novel magnetic gear: toward a higher torque density," *IEEE Transactions on Magnetics,* vol. 51, no. 11, pp. 1-4, 2015.

[53]   Y. Chen and W. Fu, "A novel hybrid-flux magnetic gear and its performance analysis using the 3-D finite element method," *Energies,* vol. 8, pp. 3313-3327, 2015.

[54]   K. Atallah, J. Rens, S. Mezani, and D. Howe, "A Novel Pseudo Direct-Drive Brushless Permanent Magnet Machine," *IEEE Transactions on Magnetics,* vol. 44, no. 11, pp. 4349-4352, 2008.

[55]   P. O. Rasmussen, H. H. Mortensen, T. N. Matzen, T. M. Jahns, and H. A. Toliyat, "Motor integrated permanent magnet gear with a wide torque-speed range," in *2009 IEEE Energy Conversion Congress and Exposition*, 2009, pp. 1510-1518.

[56]   P. O. Rasmussen, T. V. Frandsen, K. K. Jensen, and K. Jessen, "Experimental evaluation of a motor integrated permanent magnet gear," in *2011 IEEE Energy Conversion Congress and Exposition*, 2011, pp. 3982-3989.

[57]   T. V. Frandsen, P. O. Rasmussen, and K. K. Jensen, "Improved motor intergrated permanent magnet gear for traction applications," in *2012 IEEE Energy Conversion Congress and Exposition (ECCE)*, 2012, pp. 3332-3339.

[58]   S. Gerber and R. J. Wang, "Torque capability comparison of two magnetically geared PM machine topologies," in *2013 IEEE International Conference on Industrial Technology (ICIT)*, 2013, pp. 1915-1920.

[59]   H. E. Knoepfel, *Magnetic Fields: A Comprehensive Theoretical Treatise for Practical Use*. New York, NY, USA: Wiley, 2000.

[60]   K. Li, J. Wright, S. Modaresahmadi, D. Som, W. Williams, and J. Z. Bird, "Designing the first stage of a series connected multistage coaxial magnetic gearbox for a wind turbine demonstrator," in *2017 IEEE Energy Conversion Congress and Exposition (ECCE)*, 2017, pp. 1247-1254.

[61]   G. S. Highfill and L. A. Halverson, "Lowering total cost of ownership with breakthrough magnetic torque transfer technology," in *IEEE Cement Industry Technical Conference, 2006. Conference Record.*, 2006, p. 15 pp.

[62]   R. Montague, C. Bingham, and K. Atallah, "Servo Control of Magnetic Gears," *IEEE/ASME Transactions on Mechatronics,* vol. 17, no. 2, pp. 269-278, 2012.

[63]   E. P. Furlani, *Permanent magnet and electromechnaical devices materials, analysis, and applications*. San Diego: Academic Press, 2001.

[64]   J. P. Yonnet, "A new type of permanent magnet coupling," *IEEE Transactions on Magnetics,* vol. 17, no. 6, pp. 2991-2993, 1981.

[65]   T. Lubin, S. Mezani, and A. Rezzoug, "Simple Analytical Expressions for the Force and Torque of Axial Magnetic Couplings," *IEEE Transactions on Energy Conversion,* vol. 27, no. 2, pp. 536-546, 2012.

[66]   T. Lubin, S. Mezani, and A. Rezzoug, "Experimental and Theoretical Analyses of Axial Magnetic Coupling Under Steady-State and Transient Operations," *IEEE Transactions on Industrial Electronics,* vol. 61, no. 8, pp. 4356-4365, 2014.

[67]   R. Wang, E. P. Furlani, and Z. J. Cendes, "Design and analysis of a permanent magnet axial coupling using 3D finite element field computations," *IEEE Transactions on Magnetics,* vol. 30, no. 4, pp. 2292-2295, 1994.

[68]   H. J. Shin, J. Y. Choi, S. M. Jang, and K. Y. Lim, "Design and Analysis of Axial Permanent Magnet Couplings Based on 3D FEM," *IEEE Transactions on Magnetics,* vol. 49, no. 7, pp. 3985-3988, 2013.

[69]   Y. Yeong-Der, C. Gwo-Ji, H. Der-Ray, and W. Shyh-Jier, "Theoretical computations for the torque of magnetic coupling," *IEEE Transactions on Magnetics,* vol. 31, no. 3, pp. 1881-1884, 1995.

[70]   B. Dolisy, S. Mezani, T. Lubin, and J. Lévêque, "A New Analytical Torque Formula for Axial Field Permanent Magnets Coupling," *IEEE Transactions on Energy Conversion,* vol. 30, no. 3, pp. 892-899, 2015.

[71]   B. Dolisy, T. Lubin, S. Mezani, and J. Leveque, "Three-dimensional analytical model for an axial-field magnetic coupling," *Progress In Electromagnetics Research M,* vol. 35, pp. 173-182, 2014.

[72]   E. P. Furlani, "Formulas for the force and torque of axial couplings," *IEEE Transactions on Magnetics,* vol. 29, no. 5, pp. 2295-2301, 1993.

[73]   R. Waring, J. Hall, K. Pullen, and M. R. Etemad, "An investigation of face type magnetic couplers," *Proceedings of the Institution of Mechanical Engineers, Part A,* vol. 20, pp. 263-272, 1996.

[74]   D. J. Eichenberg, C. A. Gallo, and W. K. Thompson, "Development and Testing of an Axial Halbach Magnetic Bearing," NASA/TM—2006-214357, Cleveland, OH2006.

[75]   W. K. Thompson, "Three-Dimensional Field Solutions for Multi-Pole Cylinderical Halbach Array in an Axial Orientation," NASA/TM—2006-214359, Cleveland, OH.

[76]   K. Li and J. Z. Bird, "A 3-D analytical model of a Halbach axial magnetic coupling," in *2016 International Symposium on Power Electronics, Electrical Drives, Automation and Motion (SPEEDAM)*, 2016, pp. 1448-1454.

[77]   C. A. Balanis, *Advanced Engineering Electromagnetics*. John Wiley & Sons, 1989.

[78]   Z. P. Xia, Z. Q. Zhu, and D. Howe, "Analytical magnetic field analysis of Halbach magnetized permanent-magnet machines," *IEEE Transactions on Magnetics,* vol. 40, no. 4, pp. 1864-1872, 2004.

[79]   O. D. Jefimenko, *Electricity and Magnetism*. New York: Meredith Publishing Co., 1966.

[80]   H. L. Rakotoarison, J. P. Yonnet, and B. Delinchant, "Using Coulombian Approach for Modeling Scalar Potential and Magnetic Field of a Permanent Magnet With Radial Polarization," *IEEE Transactions on Magnetics,* vol. 43, no. 4, pp. 1261-1264, 2007.

[81]   S. Paul, D. Bobba, N. Paudel, and J. Z. Bird, "Source Field Modeling in Air Using Magnetic Charge Sheets," *IEEE Transactions on Magnetics,* vol. 48, no. 11, pp. 3879-3882, 2012.

[82]   J. P. Selvaggi, S. Salon, O. M. Kwon, M. V. K. Chari, and M. DeBortoli, "Computation of the External Magnetic Field, Near-Field or Far-Field, From a Circular Cylindrical Magnetic Source Using Toroidal Functions," *IEEE Transactions on Magnetics,* vol. 43, no. 4, pp. 1153-1156, 2007.

[83]   D. J. Griffiths, *Introduction to Electrodynamics*. New Jersey: Prentice Hall, 1999.